Doctorate Dissertation

博士論文

Novel properties of the optical conductivity due to electric-dipole-induced magnetic transitions in the Hubbard model

(電気双極子に由来する磁気遷移による新規な光学伝導度)

A Dissertation Submitted for Degree of Doctor of Science
July 2018
平成 30 年 7 月博士（理学）申請

Department of Physics, Graduate School of Science,
The University of Tokyo
東京大学大学院理学系研究科物理学専攻

Adrien Isaac Bolens
ボロンス　アドリアン　イザク

Abstract

In this thesis, we study electron spin resonance (ESR) induced by an AC electric field in the Hubbard model. The weakly correlated and strongly correlated regimes are both considered, but with different approaches which effectively split the thesis into two parts.

In the non-interacting limit, we first investigate spin-flip transitions in the one-dimensional (1D) and two-dimensional (2D) tight-binding models. The synergetic effect of strong spin-orbit coupling (SOC) and Zeeman splitting (ZS) on the spin resonance is studied using the Kubo formula. With both SOC and ZS, the spin resonance can be induced by an AC electric field: the so-called electric dipole spin resonance (EDSR). The resulting contribution to the optical conductivity is analyzed analytically. We show that the electromagnetic absorption spectrum is considerably influenced by the interplay of SOC and ZS, and depends on the relative angle between the SOC vector and the magnetic field direction. In particular, the EDSR is dominant over the traditional magnetic-dipole-induced ESR. Additionally, the spectrum depends on the lattice, the band structure, and the Fermi energy. In 2D systems, we show that spectrum becomes continuous with unexpected singularities.

The effect of the Coulomb repulsion U on the spin resonance is also studied numerically in the 1D model. We find that at half-filling, the resonance is first enhanced for small U but vanishes when the optical gap becomes larger than the kinetic hopping amplitude t.

In the second part of the thesis, we study the low-energy electric-dipole-induced magnetic transitions in the Mott insulating phase, below the optical gap. By treating the inter-site hopping as a perturbation, we show how the electric polarization operator can have non-trivial matrix elements between different low-energy magnetic states through virtual hopping of the electrons. This effective spin-polarization coupling is in general allowed in trimers for the single-band Hubbard model. In addition, we exhaustively derive the possible two-spin effective polarization operators emerging from spin-dependent hopping.

Motivated by terahertz spectroscopy measurements in α-$RuCl_3$, a so-called Kitaev material, multi-orbital Hubbard models are then considered. We develop a theory for magnetoelectric (ME) effects in Mott insulators of d^5 transition metal ions in an octahedral crystal field. For $4d$ and $5d$ compounds, the extended orbitals favor charge fluctuations of the localized electrons to neighboring ions and a significant ME effect from electronic mechanisms is expected. The electric polarization originating from two-spin operators on bonds of nearest-neighbor sites is considered. The allowed coupling is first derived using a symmetry approach. Then, the effective polarization operator in the ground state manifold is evaluated using perturbation theory. We show in particular that the involved lattice structure of Kitaev materials results in a new type of electronic ME coupling.

Finally, we calculate the optical conductivity of ideal Kitaev materials originating from the derived ME coupling. Using exact analytical results of the Kitaev honeycomb spin model, we calculate the continuous terahertz spectrum of the quantum spin liquid originating from Majorana excitations.

Acknowledgements

First of all, I would like to show my gratitude to my supervisor Prof. Seiji Miyashita for his encouragement and support throughout the three years of my PhD. I would like to thank Prof. Masao Ogata and Prof. Hosho Katsura for their valuable contributions to my work. In particular, I am deeply indebted to Prof. Hosho Katsura for the time he spent discussing with me, and for his invaluable insight. I am also grateful to the referees of this thesis, Prof. Naomichi Hatano, Prof. Naoto Nagaosa, Prof. Hidenori Takagi, Prof. Atsushi Fujimori, and Prof. Yusuke Kato.

Furthermore, I thank all the former and present members of the Miyashita group: Dr. Takashi Mori, Dr. Sergio Andraus, Dr. Takafumi Suzuki, Dr. Taichi Hinokihara, Dr. Eriko Kaminishi, Dr. Tatsuhiko Shirai, Mr. Takuya Hatomura, Mr. Hiroki Ikeuchi, Mr. Hayate Nakano, and Mr. Yuta Goto. It was a great pleasure to participate to the different group meetings and exciting discussions throughout the years. I would also like to express my thanks to the secretary of our group, Ms. Keiko Yashima.

Finally, my deepest gratitude belongs to my mother and father for their unconditional support through my life, and my wife to whom I owe more than I can express.

I acknowledge support from the Leading Graduate Course for Frontiers of Mathematical Sciences and Physics (FMSP).

List of Publications

- Part of Chapter 2 was published in

  "Synergetic effect of spin-orbit coupling and Zeeman splitting on the optical conductivity in the one-dimensional Hubbard model",
  Adrien Bolens, Hosho Katsura, Masao Ogata, and Seiji Miyashita, Physical Review **B** 95, 235115 (2017).

- Part of Chapter 5 was published in

  "Mechanism for subgap optical conductivity in honeycomb Kitaev materials",
  Adrien Bolens, Hosho Katsura, Masao Ogata, and Seiji Miyashita, Physical Review **B** 97, 161108(R) (2018).

- Part of Chapter 4 was reported in

  "Theory of electronic magnetoelectric coupling in d^5 Mott insulators",
  Adrien Bolens, arXiv:1805.02488 (2018).

Contents

Chapter 1

Introduction

1.1 Motivation and aim of thesis

Resonance phenomena offer a powerful tool to study a wide variety of properties of condensed matter. For instance, magnetic resonance is fundamental to the study of the quantum mechanical magnetic properties of a system. Historically, the first reported observation of nuclear magnetic resonance (NMR) in condensed media was made in 1946 by the groups of Felix Bloch and Edward Mills Purcell [1–3], who were awarded the 1952 Nobel Prize in Physics. Electron spin resonance (ESR), also called electron paramagnetic resonance (EPR), is a closely related technique also discovered in the 1940s [4] in which the transitions between electronic spin levels are detected, rather than nuclear ones. ESR, while providing a much higher sensitivity than NMR does, is only possible in materials with unpaired electron spins. Such materials, in very general terms (including both metals and insulators), are the focus of this thesis.

When placed in a uniform static magnetic field, the energy of a single electron spin is split into two energy levels separated by a gap Δ_Z due to the Zeeman effect. If the magnetic dipole is perturbed with an oscillatory electromagnetic field of frequency close to $\omega_{\text{res}} = \Delta_Z/\hbar$, a transition between its two energy eigenstates is possible. As the photon frequency approaches ω_{res}, the probability that it gets absorbed increases.

However, an electron is not only a spin, but it is a moving charged particle. Hence, while the magnetic part of the electromagnetic field affects the electron spin, the electric part of the field also affects the electron through its motion. The study of the response of matter to an oscillating electric field, or optical response, is one of the main purposes of the vast branch of physics called optics. Customarily, the spin and charge (i.e., motional) degrees of freedom of electrons are treated independently when considering their response to an electromagnetic wave.

Light interacts with matter through both its magnetic and electric field. The most direct way it can probe a system of electrons is through one-photon absorption processes originating from the linear coupling between the electromagnetic field to the magnetic dipole and electric dipole operators of the system. The AC magnetic field, on the one hand, couples to the spin of each electron and the corresponding absorption spectrum is directly related to the imaginary part of the dynamical spin susceptibility $\chi(\omega)$, which is measured with ESR spectroscopy. The typical magnetic energy range for electronic systems is roughly $0.1 - 10$ meV, which corresponds to resonance frequencies of up to a few THz. The AC electric field, one the other hand, couples to the motion of the electrons and its absorption spectrum is proportional to the real part of the optical conductivity $\sigma(\omega)$. Here, the term "optical" covers the entire frequency range (and is not restricted to visible light) but the frequencies typically considered are much higher than for the magnetic resonance. The nature of the

optical absorption heavily depends on the type of material considered. For instance, a nearly free electron system is well described by the Drude model down to $\omega = 0$, while an insulator has an optical gap below which the optical conductivity vanishes. To be more specific, the distinction between metals and insulators is *defined* by the behavior of $\sigma(\omega)$ as $\omega \to 0$, as we will discuss later in this introductory chapter.

However, this spin-charge dichotomy of the electrons is challenged in certain systems where the spin and charge degrees of freedom are coupled. In this thesis, we investigate how the coupling between the spin and charge degrees of freedom of the electrons can affect the dynamical response to an AC electromagnetic field. More specifically, we study the effect of spin transitions on the optical conductivity in various lattice models of electrons.

The practical use of the spin degree of freedom of the electron in charge-based electronics is at the heart of the field of spintronics [5–8], also known as spin electronics. In conventional electronics, the electrons are controlled with electric fields and their spins are ignored. In 1988, the discovery of the giant magnetoresistance effect [9, 10] in metals triggered the rapid development of spintronics. The central goal of spintronics, whether in metals, semiconductors, or even quantum dots, is to engineer devices where the information is carried by the electron spin rather than by its charge. In order to do so, the ability to actively manipulate and control the spins is necessary. An important phenomenon for spintronics is the spin-charge coupling originating from relativistic spin-orbit coupling (SOC). In particular, it makes electric dipole spin resonance (EDSR) possible. EDSR is the spin-flip resonance of the conduction electrons induced by the electric field of an incoming electromagnetic wave. It was first proposed in 1960 by Emmanuel Rashba [11]. Interest in spin resonance induced by AC electric fields comes from the fact that strong local electric fields are practically easier to obtain than magnetic fields. Hence, with EDSR the electric component of AC fields can be used to control both charge and spin.

More fundamentally, any coupling between magnetic and electric properties of a material is referred to as the magnetoelectric (ME) effect [12]. Historically, the effect was first predicted by Pierre Curie more than 100 years ago [13]. The phenomenological theory of the ME effect was then developed by Landau [14] and Dzyaloshinskii [15]. It was first observed in the antiferromagnet Cr_2O_3 in 1961 [16,17]. The static ME effect is characteristic of so-called multiferroics, for which the magnetization ($\mathbf{M}$) can be induced by an electric field and the electric polarization ($\mathbf{P}$) by a magnetic field [12, 18–24]. For instance, the linear static ME effect arise from the term $\alpha_{ij} M_i P_j$ in the free energy and is only allowed when both time-reversal and inversion symmetries are broken. Multiferroics are attracting a lot of attention in particular due to the potential applications in novel multifunctional devices [25]. Magnetic multiferroics (or type-II multiferroics [23]) such as $TbMnO_3$, for which the ferroelectricity only emerges in the magnetically ordered phase, are especially interesting due to the profound physics behind their properties.

However, the ME effect is not limited to multiferroics. It can appear dynamically in magnetic Mott insulators without long-range ordering. Thus, the dynamical ME effect is possible even without the static ME effect and the accompanying reduction of the symmetry. The dynamical ME coupling influences the charge dynamics of the electrons in the magnetic energy scale, far below the optical gap. Consequently, magnetic excitations (not necessarily simple spin flips) can be probed with an AC electric field and affect the optical conductivity. In particular, a subgap (i.e., below the optical gap) optical conductivity due to ME coupling was observed in some gapless quantum spin liquids [26–29], and understood in terms of an electronic ME mechanism based on ring exchange interaction on triangular and kagome lattices [26, 27].

In this thesis, we extensively consider the coupling of the spin and charge degrees of freedom of electrons in the Hubbard model, and how it affects the optical conductivity through electric-dipole-induced magnetic transitions.

1.1.1 What is new?

Motivated by both the EDSR phenomena in the electron gas (EG) and the ME effect in Mott insulators, we consider the following two limits.

First, there is the nearly free electron picture where each electron carries a spin 1/2 coupled to its movement through relativistic SOC effects. In the lattice model, this is accounted by a spin dependent hopping. In this case, the magnetic transitions are in a sense simple as there are only two magnetic states, up and down, and the transition consists of a spin flip. The effect of strong SOC in a lattice model and its interplay with the Hubbard interaction is interesting, for instance, in the context of iridium-based materials or other $5d$ and $4d$ transition metal (TM) compounds because of the delocalization of the valence electrons and strong SOC. While the EDSR phenomena is known in the quantum wire picture, it has never been studied in the discrete Hubbard model before. We derive the properties of EDSR emerging from the discrete nature of the lattice system and the corresponding band structure. Moreover, our results describe the effect of umklapp scattering (originating from the on-site Coulomb repulsion) on the EDSR spectrum for the first time.

Secondly, we consider Mott insulators where the strongly correlated electrons are localized on the lattice sites. In this case, the magnetic nature of the system is much more complex and described by an effective Hamiltonian of interacting spins. We consider the ME effect arising from the fluctuations of the spin-carrying electrons on neighboring sites (or virtual hopping) and the resulting optical response. The electric-dipole-induced magnetic transitions are not simple spin flips and the response is described in terms of the dynamics of multi-spin operators. The ME effect arising from virtual hopping in the single-band Hubbard model is known to be non-trivial for triangular three-site clusters. However, we focus on much more involved multi-orbital systems which match up with actual strongly correlated TM compounds.

We develop a full theory for the two-site ME coupling in the tight-binding formalism of the Hubbard model. Motivated by experimental results of a subgap optical conductivity in the Kitaev materials α-$RuCl_3$ [30–34], we consider the ME effect in a three-band Hubbard model for the t_{2g} orbitals of d^5 TM ions in an octahedral crystal field (CF). The THz spectroscopy measurement from Ref. [31] is shown in Fig. 1.1. The graph shows the absorption spectrum, as expressed in terms of the optical conductivity, for different temperatures. The authors of Ref. [31] indeed showed that the main weight of the absorption spectrum originates from electric-dipole-induced transitions.

Kitaev materials are d^5 Mott insulators for which the low-energy physics approaches the Kitaev honeycomb model [35] and have been of tremendous interest to both experimentalists and theorists in the recent years. Our final result consists of the actual calculation of the optical response due to electric-dipole induced magnetic transitions in ideal Kitaev materials. We present a novel explanation for the low-energy optical response, whose origin was still unclear before that.

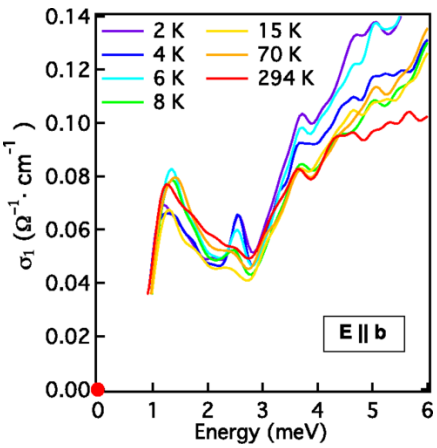

FIGURE 1.1: Subgap optical conductivity of α-$RuCl_3$ measured with THz spectroscopy. Reprinted figure with permission from Ref. [31] Copyright (2017) by the American Physical Society.

1.1.2 Structure of the thesis

This thesis is effectively separated in two parts corresponding to the two limits introduced above. The structure is the following.

First, in the rest of the present chapter, we introduce the basic concepts used throughout the thesis. Those include linear response theory, the optical conductivity and its properties, and the origin of SOC.

Chapter 2 focuses on the EDSR phenomenon. We begin from the original theory of combined resonances in the two-dimensional EG (2DEG) of Rashba and Sheka [11, 36, 37], in which the SOC is treated as a perturbation in the 2DEG with a strong Zeeman coupling. We present the theory of EDSR in one-dimensional (1D) systems where SOC and the Zeeman coupling are of similar strength. In the 1DEG, we also discuss the effects of interaction on the resonance as shown in Ref. [38] using Tomonaga-Luttinger liquid theory. Finally, we present our original results of the EDSR in the Hubbard model in one dimension and calculate the effect of the Hubbard on-site interaction numerically [39]. The chapter ends with the calculation of the EDSR in 2D tight-binding models.

In Chapters 3, 4, and 5, we discuss electric-dipole-induced magnetic transitions in the Mott-insulating phase of various Hubbard models. In Chapter 3, we extensively derive the different ME couplings arising in the single-band Hubbard model. We discuss three-spin coupling on trimers, which was first derived in Ref. [40], and its effect on the optical conductivity. We then derive all the possible two-spin ME couplings which can emerge from spin-dependent hopping integrals, e.g. caused by SOC.

In Chapter 4, we develop a theory for the microscopic mechanisms behind the low-energy electric polarization operator in d^5 Mott insulators originating from the fluctuations of the electronic charge [41]. The ME effect is first discussed from a symmetry point of view, and then calculated from the three-band Hubbard model using perturbation theory in the hopping. Two microscopic mechanisms are introduced and are shown to be particularly relevant for Kitaev materials. Therefore, the results shed light on the origin of the terahertz (THz) optical conductivity observed in α-$RuCl_3$.

In Chapter 5, we calculate the optical conductivity in the effective Kitaev spin model. The Kitaev model is a rare instance of an exactly solvable 2D interacting

quantum spin model. Its ground state is a quantum spin liquid and its excitations are described in terms of Majorana quasiparticles. It thus provides an ideal playground to study the properties of a spin liquid thanks to its analyticity [42–48]. In addition, it can potentially be realized in real materials (Kitaev materials) [49]. For α-$RuCl_3$, even though its low energy physics significantly deviates from the "pure" Kitaev model [50–55], it is often speculated that some of its properties, such as the fractionalized spin excitations, are remnant of the Majorana physics [30–34, 56–61]. Therefore, we calculate the continuous subgap optical conductivity originating from the fractionalized excitations in terms of Majorana fermions combining analytical and numerical methods [62].

1.2 Linear response and Kubo formula

1.2.1 General formalism

Throughout this thesis, we are interested in the linear response of various systems to an electromagnetic field. Let us consider a generic time-independent quantum system described by the Hamiltonian $\mathcal{H}_0$ to which we apply a time-dependent external force $F(t)$ that couples to the system as

$$\mathcal{H} = \mathcal{H}_0 + \mathcal{H}' = \mathcal{H}_0 + BF(t). \tag{1.1}$$

The linear response $\Delta A(t)$ of a physical quantity A to the external force $F(t)$ is defined by

$$\langle A\rangle = \langle A\rangle_0 + \Delta A(t), \tag{1.2}$$

where $\langle A\rangle = \mathrm{Tr}\,\rho A$ and $\langle A\rangle_0 = \mathrm{Tr}\,\rho_0 A$ for the density matrices ρ and ρ_0 corresponding to the Hamiltonians $\mathcal{H}$ and $\mathcal{H}_0$, respectively. The linear response is given by the Kubo formula [63]

$$\begin{aligned}\Delta A(t) &= \int_{-\infty}^{\infty} \chi_{AB}(t-t')F(t')dt' \\ \chi_{AB}(t) &= -i\theta(t)\,\mathrm{Tr}(\rho_0[A(t),B]) = -i\theta(t)\langle[A(t),B]\rangle_0,\end{aligned} \tag{1.3}$$

where the operators are written in the interaction picture, $\theta(t)$ is the Heaviside step function, and we have set $\hbar = 1$. For a periodic force $F(t) = F_0 e^{-i\omega t} + \text{H.c.}$ (henceforth we do not explicitly write the Hermitian conjugate), the response is simply $\Delta A(t) = \mathrm{Re}(2\chi_{AB}(\omega)F_0 e^{-i\omega t})$ with the complex admittance defined by

$$\chi_{AB}(\omega) = \lim_{\delta\to 0^+}\int_0^{\infty} e^{i(\omega+i\delta)t}\chi_{AB}(t)dt, \tag{1.4}$$

where $\delta > 0$ is added to ensure convergence at large times.

The dissipation is calculated from the work associated to the change in energy of the system [64],

$$\frac{dW}{dt} \equiv \frac{d}{dt}\mathrm{Tr}\,\rho\mathcal{H} = \mathrm{Tr}\,\rho\dot{\mathcal{H}} = \mathrm{Tr}\left(\rho B\dot{F}\right) = (\langle B\rangle_0 + \Delta B)\dot{F}, \tag{1.5}$$

where we have used $\dot{\rho} = -i[\mathcal{H}, \rho] = 0$. Averaging over one full period of $F = F_0 e^{-i\omega t}$, the contribution from $\langle B \rangle_0$ vanishes and we have

$$\begin{aligned}\overline{\frac{dW}{dt}} &\equiv \frac{\omega}{2\pi}\int_0^{2\pi/\omega} dt \frac{dW}{dt} = \frac{\omega}{2\pi}\int_0^{2\pi/\omega} dt \int_\infty^\infty \chi_{BB}(t-t')F(t')\dot{F}(t) \\ &= -2\omega\chi''_{BB}(\omega)F_0^2, \end{aligned} \tag{1.6}$$

where $\chi = \chi' + i\chi''$ so that $\chi'' = \mathrm{Im}\,\chi$ is the imaginary part of χ. Here we have used the fact that $\chi'(-\omega) = \chi'(\omega)$ while $\chi''(-\omega) = -\chi''(\omega)$ because $\chi(t)$ is real.

It is often convinient to use a spectral (Lehmann) representation in terms of the eigenstates $|m\rangle$ of $\mathcal{H}_0$. The function $\chi_{BB}(t) = -i\theta(t)\langle [B(t), B(0)]\rangle_0$ is a so-called retarded Green's function for the operator B. A straightforward calculation in the canonical ensemble $\rho_0 = e^{-\beta\mathcal{H}_0}$, where β is the inverse temperature, (see, e.g., [65]) gives

$$\begin{aligned}\chi_{AB}(\omega) &= \frac{1}{Z}\sum_{m,n} e^{-\beta E_m}\left[\frac{\langle m|A|n\rangle\,\langle n|B|m\rangle}{\omega + E_m - E_n + i\delta} - \frac{\langle m|B|n\rangle\,\langle n|A|m\rangle}{\omega + E_n - E_m + i\delta}\right], \\ &= \frac{1}{Z}\sum_{m,n}\left(e^{-\beta E_m} - e^{-\beta E_n}\right)\frac{\langle m|A|n\rangle\,\langle n|B|m\rangle}{\omega + E_m - E_n + i\delta}, \end{aligned} \tag{1.7}$$

which has poles just below the real axis at $\omega = \Delta_{mn} - i\delta$, where $\Delta_{mn} = E_n - E_m$. Here $\mathcal{H}_0|m\rangle = E_m|m\rangle$, and Z is the canonical partition function. Using the relation

$$\frac{1}{\omega - \Delta_{mn} + i\delta} = P\frac{1}{\omega - \Delta_{mn}} - i\pi\delta(\omega - \Delta_{mn}), \tag{1.8}$$

where P is the Cauchy principal value, we obtain

$$\chi''_{AB}(\omega) = -\frac{\pi}{Z}\left(1 - e^{-\beta\omega}\right)\sum_{mn} e^{-\beta E_m}\langle m|A|n\rangle\langle n|B|m\rangle\delta(\omega - \Delta_{mn}). \tag{1.9}$$

Finally, in this thesis we only consider the zero temperature limit for which

$$\chi''_{AB}(\omega > 0) = -\pi\sum_n \langle 0|A|n\rangle\langle n|B|0\rangle\delta(\omega - E_n + E_0), \tag{1.10}$$

where $|0\rangle$ is the ground state of $\mathcal{H}_0$ with energy E_0.

1.2.2 Example: spin susceptibility

An AC magnetic field $\tilde{\mathbf{B}} = \tilde{B}_0 e^{-i\omega t}\hat{\mathbf{e}}_\alpha$ (with $\alpha \in \{x, y, z\}$) couples to the system through the Zeeman effect

$$\mathcal{H}' = -g\mu_B\tilde{\mathbf{B}}\cdot\mathbf{S}, \tag{1.11}$$

where μ_B is the Bohr magneton, g is the Landé g-factor, and $\mathbf{S}$ is the total spin of the system. Hence, the absorption rate per unit of volume is given by

$$I_{\mathrm{MD}}(\omega) = 2\omega(g\mu_B)^2\chi''_{\alpha\alpha}(\omega)\tilde{B}_0^2, \tag{1.12}$$

where MD stands for "magnetic dipole" and $\chi(\omega) \equiv -\frac{1}{V}\chi_{\mathbf{SS}}(\omega)$ is the spin susceptibility tensor,

$$\begin{aligned}\chi_{\alpha\beta}(\omega) &= \frac{i}{V}\int_0^\infty e^{i\omega t}\langle[S^\alpha(t), S^\beta(0)]\rangle_0 dt, \\ &= \frac{\pi}{V}\sum_n \langle 0|S^\alpha|n\rangle\langle n|S^\beta|0\rangle\delta(\omega - E_n + E_0) \qquad (\text{at } T = 0),\end{aligned} \tag{1.13}$$

where V the volume of the system. Here χ is defined with the opposite sign to Eq. (1.3) so that its imaginary part may be positive. Note that in Eq. (1.12) we have assumed that χ has no dissipative off-diagonal elements which is true in isotropic systems.

1.3 Optical conductivity

The optical conductivity $\sigma(\omega) = \int_0^\infty e^{i\omega t}\sigma(t)dt$ is defined by the relation

$$\frac{1}{V}\langle \mathbf{J}(t)\rangle = \int_{-\infty}^{\infty} \sigma(t -' t)\mathbf{E}(t')dt' \tag{1.14}$$

between an external electric field[1] $\mathbf{E}$ and the electric current $\langle\mathbf{J}\rangle$. Here we consider only electric fields and currents homogeneous in space, i.e., at $\mathbf{q} = 0$ so that $\mathbf{J} = \int d^3r\mathbf{J}(\mathbf{r})$ (which is a good approximation due to the large wavelength of light compared to the system). The interaction between the charged particles of the system and the electromagnetic wave is given by

$$\mathcal{H}' = -\mathbf{J}\cdot\mathbf{A}(t), \tag{1.15}$$

where $\mathbf{A}(t)$ is the vector potential and we have used the Coulomb gauge $\nabla\cdot\mathbf{A} = 0$, so that the scalar potential $\phi = 0$. Alternatively, the coupling of the electric field can also be written $\mathcal{H}' = -\mathbf{E}\cdot\mathbf{P}$, where $\mathbf{P} = e\mathbf{r}$ is the polarization operator, which we will discuss in Sec. 1.3.1. Henceforth, we consider a time-periodic electric field $\tilde{\mathbf{E}}(t) = \tilde{E}_0 e^{-i\omega t}\hat{\mathbf{e}}_\alpha$ so that

$$\tilde{\mathbf{A}}(t) = \frac{-i}{\omega}\tilde{\mathbf{E}}(t). \tag{1.16}$$

Hence, we can already infer from the definition of $\sigma(\omega)$ and the calculation that lead to Eq. (1.6) (with an extra i/ω factor) that the absorption rate from the electric dipole (ED) processes is given by

$$I_{\mathrm{ED}}(\omega) = 2\sigma'_{\alpha\alpha}(\omega)\tilde{E}_0^2, \tag{1.17}$$

where $\sigma' = \mathrm{Re}\,\sigma$ is the real part of the optical conductivity.

There are subtleties in the definition of the optical conductivity. The physical current $\mathbf{J}$ (the actual current measured by experimentalists) is given in a semi-classical way by $\mathbf{J} = e\sum_i \mathbf{v}_i$ where $\mathbf{v}_i$ is the velocity of each electron [65]. When quantizing the particle velocity, it becomes $\mathbf{v}_i = \frac{1}{m}[\mathbf{k}_i - e\mathbf{A}(\mathbf{r}_i)]$. Using second quantization, the physical current operator for free spinless particles (at $\mathbf{q} = 0$) is

$$\mathbf{J} = \frac{e}{m}\sum_{\mathbf{k}} c^\dagger_{\mathbf{k}}[\mathbf{k} - e\mathbf{A}]c_{\mathbf{k}} \equiv \mathbf{j} - \frac{e^2N}{m}\mathbf{A}, \tag{1.18}$$

[1] Here, to be precise, $\mathbf{E}$ contains both the applied or external field and the internal electric field created by the induced currents [65].

where **j** is the so-called paramagnetic current (henceforth just "current"), and the second term in the right hand side originating from **A** is often called the gauge current or diamagnetic current. For a general Hamiltonian $\mathcal{H}$, the total current is defined as $J_\alpha = -\frac{\partial \mathcal{H}}{\partial A_\alpha}$ and the paramagnetic current is $j_\alpha = J_\alpha\big|_{\mathbf{A}=0}$. Generally, for a Hamiltonian whose kinetic part is $\mathcal{H}_{\text{kin}} = \sum_{\mathbf{k}} \epsilon(\mathbf{k}) c^\dagger_{\mathbf{k}} c_{\mathbf{k}}$, the current operator is

$$j_\alpha = e \sum_{\mathbf{k}} \frac{\partial \epsilon(\mathbf{k})}{\partial k_\alpha} c^\dagger_{\mathbf{k}} c_{\mathbf{k}}, \tag{1.19}$$

and the diamagnetic tensor $\tau_{\alpha\beta}$ [66] is

$$\tau_{\alpha\beta} = \sum_{\mathbf{k}} \frac{\partial \epsilon(\mathbf{k})}{\partial k_\alpha k_\beta} c^\dagger_{\mathbf{k}} c_{\mathbf{k}}, \tag{1.20}$$

so that that $J_\alpha = j_\alpha - e^2 \sum_\beta \tau_{\alpha\beta} A_\beta + O(A^2)$.

Therefore, the optical conductivity obtained from the linear response reads

$$\begin{aligned} \sigma_{\alpha\beta}(\omega) &= \frac{1}{\omega V} \int_0^\infty dt e^{i\omega t} \langle [j_\alpha(t), j_\beta(0)] \rangle + \frac{ie^2}{\omega V} \langle \tau_{\alpha\beta} \rangle, \\ &= \frac{i}{\omega V} \Big[\chi_{j_\alpha j_\beta}(\omega) + e^2 \langle \tau_{\alpha\beta} \rangle \Big], \end{aligned} \tag{1.21}$$

where χ_{jj} is the current response function defined by Eq. (1.4). For free electrons we have $\tau_{\alpha\beta}/V = \frac{n_0}{m}\delta_{\alpha\beta}$, where $n_0 = N/V$ is the particle density. In lattice systems, the $\langle \tau \rangle$ term can be interpreted as the thermal expectation value of the kinetic energy of the system.

We are interested in the real part of $\sigma(\omega)$ at $T = 0$. Replacing $\omega \to \omega + i\delta$ and using Eq. (1.10), we find

$$\sigma'(\omega) = \frac{-1}{\omega V} \chi''_{jj}(\omega) + D\delta(\omega) \equiv \sigma_{\text{reg}}(\omega) + D\delta(\omega). \tag{1.22}$$

where σ_{reg} is the "regular" part of $\sigma'(\omega)$ and

$$D = \frac{\pi}{V} \Big[\chi'_{jj}(\omega \to 0) + e^2 \langle \tau \rangle \Big] = -\lim_{\omega \to 0} [\omega \sigma''(\omega)] \tag{1.23}$$

is the so-called Drude weight. We discuss the physical meaning of D in Sec. 1.3.2.

1.3.1 Optical conductivity from the electric polarization operator

In the Hubbard model, especially in the Mott insulating phase, it will prove useful to have an expression of the optical conductivity in terms of the electric polarization operator **P**. Indeed, while the current operator is typically diagonal in momentum space, the polarization, related to **j** by $\partial_t \mathbf{P} = \mathbf{j}$, commutes with the position operator. It is thus diagonal in terms of the discrete spatial representation of localized electrons used in the tight-binding formalism.

Starting from the coupling $-\tilde{\mathbf{E}} \cdot \mathbf{P}$, we obtain from Eq. (1.3)

$$\sigma_{\alpha\beta}(\omega) = \frac{-1}{V} \chi_{j_\alpha P_\beta} = \frac{i}{V} \int_0^\infty e^{i\omega t} \langle [j_\alpha(t), P_\beta(0)] \rangle. \tag{1.24}$$

In general, the dynamical response function χ_{AB} defined in Eq. (1.4) obeys the following identities [67],

$$\chi_{AB}(\omega) = \frac{1}{\omega}\langle[A,B]\rangle + \frac{i}{\omega}\chi_{(\partial_t A)B}(\omega), \tag{1.25}$$

$$= \frac{1}{\omega}\langle[A,B]\rangle - \frac{i}{\omega}\chi_{A(\partial_t B)}(\omega). \tag{1.26}$$

Identifying Eq. (1.24) with Eq. (1.26) by setting $A = j_\alpha$ and $B = P_\beta$ (hence $\partial_t B = j_\beta$), we recover the already derived expression for $\sigma(\omega)$ in Eq. (1.21) provided that $[j_\alpha, P_\beta] = -ie^2\tau_{\alpha\beta}$. This is easily verified by using the fact that the one-body operator $\mathbf{P}_1 = e\mathbf{r} = ie\nabla_{\mathbf{k}}$ so that

$$[j_\alpha, P_\beta] = \sum_{\mathbf{k}\mathbf{k}'}\langle\mathbf{k}'|[e(\partial_{k_\alpha}\epsilon), ie\partial_{k_\beta}]|\mathbf{k}\rangle c^\dagger_{\mathbf{k}'}c_{\mathbf{k}} = -ie^2\sum_{\mathbf{k}}\frac{\partial\epsilon(\mathbf{k})}{\partial k_\alpha \partial k_\beta}c^\dagger_{\mathbf{k}}c_{\mathbf{k}} = -ie^2\tau_{\alpha\beta}. \tag{1.27}$$

Finally, using Eq. (1.25) with $A = P_\alpha$ and $B = P_\beta$ (so that $[A,B] = 0$), we obtain

$$\sigma_{\alpha\beta}(\omega) = \frac{\omega}{V}\int_0^\infty e^{i\omega t}\langle[P_\alpha(t), P_\beta(0)]\rangle. \tag{1.28}$$

1.3.2 Optical conductivity in metals and insulators

The Drude weight D, also called charge stiffness, was introduced by W. Kohn in 1984 [68] as a criterion to differentiate between ideal conducting and insulating behaviors at $T = 0$ in the context of the Mott metal-insulator transition. In clean metallic systems, D is finite and $\sigma'(\omega)$ diverges at $\omega = 0$. This is characteristic of integrable systems with ballistic transport (i.e., a freely accelerating system) which is possible due to the lack of disorder. Without disorder and at $T = 0$, D is actually finite for *both* metals and superconductors [69], while it vanishes for insulators. In fact, the theoretical definition of an insulator is

$$\lim_{T\to 0}\lim_{\omega\to 0}\lim_{\mathbf{q}\to 0}\sigma'(\omega,\mathbf{q}) = 0. \tag{1.29}$$

In a system of non-interacting electrons, or any system well described with band structure theory, the $\sigma_{\text{reg}}(\omega)$ contribution in Eq. (1.22) only corresponds to $\mathbf{q} = 0$ interband transitions. For the multi-band Hamiltonian $\mathcal{H} = \sum_n\sum_{\mathbf{k}}\epsilon_n(\mathbf{k})c^\dagger_{\mathbf{k},n}c_{\mathbf{k},n}$, where n is the band index, the retarded response function can be written in terms of the single-particle states $|\mathbf{k},n\rangle = c^\dagger_{\mathbf{k},n}|0\rangle$ (where $c_{\mathbf{k},n}|0\rangle = 0$ for all $\mathbf{k}$ and n) as

$$\sigma'(\omega > 0) = \frac{\pi}{V\omega}\sum_k\sum_{n\neq m}|\langle\mathbf{k},n|j|\mathbf{k},m\rangle|^2\left(\langle n_{\mathbf{k},m}\rangle - \langle n_{\mathbf{k},n}\rangle\right)\delta(\omega - \epsilon_n(\mathbf{k}) + \epsilon_m(\mathbf{k})), \tag{1.30}$$

where now $\langle\cdot\rangle$ denotes the grand canonical ensemble average such that $\langle n_{\mathbf{k},m}\rangle = n_F(\epsilon_m(\mathbf{k}))$ (n_F is the Fermi-Dirac distribution). Therefore, a simple single-band model of non-interacting spinful electrons ($n = \uparrow,\downarrow$) has $\sigma_{\text{reg}} = 0$ unless the current has matrix element operators non-diagonal in spin. Such magnetic transitions can be induced by SOC and are thus electric-dipole-induced spin resonances. This kind of systems is the focus of Chapter 2. Thus, for a single electron band, the only contribution to $\sigma'(\omega)$ is $D\delta(\omega)$ which vanishes if the band is full (i.e., the system is a band insulator).

1.3.3 In metals

Nevertheless, in a clean metallic system with interactions such as the Hubbard model away from half-filling, in addition to the δ function at $\omega = 0$, there is a finite frequency part that vanishes as $\omega \to 0$, typically with a power law dependence [70–72]. However, note that in a spatially continuous system without SOC, the current is proportional to the center-of-mass momentum so that it commutes with the electron-electron interactions, which conserve the total momentum (hence the interactions do not affect χ_{jj}) [67]. This is sometimes known as the Kohn theorem [73]. In the presence of a lattice, the momentum is only conserved modulo a vector of the reciprocal lattice. The processes with a jump of the reciprocal vector, called umklapp scattering, lead to an intrinsic finite resistivity [72]. This types of physics is particularly interesting in the study of the Mott metal-insulator transition in the Hubbard model.

However, at finite T, or with the inclusion of disorder at $T = 0$, the weak scattering of the conduction electrons allows intraband processes which can be understood, for instance, by the classical Drude theory or by the classical Bolztmann equation [74]. In a few words, the intraband processes are modelled by introducing a relaxation time τ (which depends on the scattering mechanism and is in general temperature dependent), and

$$\sigma_{\text{Drude}}(\omega) = \frac{n_0 e^2 \tau}{m(1 - i\omega\tau)}, \tag{1.31}$$

so that its real part is a Lorentzian centered at $\omega = 0$ which tends to $\sigma'(\omega) = D\delta(\omega)$ for $\tau \to 0$. Thus, in this case, there is no δ function at $\omega = 0$ anymore (no Drude weight per se) but $\sigma'(\omega = 0) \equiv \sigma_{dc}$ is finite while it vanishes for insulators. In addition, the free carriers can also be excited collectively (a density wave) which are the results of additional poles in χ_{jj} induced by interactions through the screening effect. Finally, other phenomena can affect the optical response of metals at $\mathbf{q} = 0$, such as vibration modes of the lattice (optical phonons) or interband processes at higher frequencies.

In this thesis, we only consider metallic systems in Chapter 2 and focus on the magnetic resonance. This means that we do not consider disorder or any contributions to $\sigma'(\omega)$ other than the spin transitions induced by $\mathbf{j}$ in χ_{jj}. Magnetic transitions correspond to frequencies in the meV energy range, far below the range of frequencies used for usual optical response experiments in metals (typically $\hbar\omega \approx 1$ eV).

1.3.4 In insulators

In insulators, the principal contribution to the optical conductivity comes from interband processes which are only possible for frequencies above a certain gap. This gap in the optical conductivity, the optical gap, is the minimum amount of energy needed for photon to be absorbed. Note that there is a distinction between the optical gap and the electronic band gap (defined by the energy needed to add one electron) because the number of electrons is conserved during the optical absorption. The optical gap is typically smaller than the band gap. For instance, bound electron-hole pairs (or excitons) can be created for an energy less than the band gap. Note that in insulators too, optical phonons can lead to a finite response, even below the optical gap.

In the Mott insulating phase of the Hubbard model, the optical gap separates the so-called upper and lower Hubbard bands and the optical excitations are at the energy scale $\omega \sim U$ [75–78], where U is the on-site Coulomb repulsion. In the large

U limit, the optical gap is well approximated by $\Delta_{\text{opt}} \simeq U - 4t + 8\ln(2)t^2/U$ [79], where t is the hopping integral, and the optical conductivity at $T = 0$ is finite at frequencies between $\omega \simeq U - 4t$ and $\omega \simeq U + 4t$ [75]. Such excitations are inter-site as an electron moves from one site to another at the energy cost of U.

In actual Mott insulating materials, such as some TM compounds with d orbitals, we distinguish two types of optical absorption [80]. First, there are the charge transfer processes, where electrons hop between different ions. The Coulomb repulsion U has to be paid for a TM-TM hopping, but processes from a ligand orbital to the upper Hubbard band are also possible. In this case, the so-called charge-transfer gap Δ has to be overcome.

Secondly, local on-site transitions are characterized by the creation of an electron-hole pair on the same TM ion such that the repulsion energy is not modified. Now, such a local transition corresponds to a change in the electronic orbital of the electron (a d-d transition) and is forbidden for an isolated atom by symmetry. Nevertheless, the actual wave function of the electrons contains an additional mixture of the "orbital tails" coming from the neighboring ligands and TM ions [80]. Therefore, local electric dipole transitions can be made possible by the residual dispersion of the electrons. In other words, local transitions which should be forbidden for isolated atoms may be allowed by the inter-ion hopping Hamiltonian. This leads to the notion of an electric dipole operators with finite matrix elements between sates inside the lower Hubbard band. The energy needed is thus determined by the splitting induced by local potentials. Typically, the d orbitals are split by CF and SOC in the $\omega \approx$ 0.1-1 eV energy range. By treating the hopping as a perturbation, the electric polarization operator can be written in terms of local operators.

Finally, the same principles can be applied for magnetic transitions, i.e., including the spin degree of freedom, and is the focus of Chapters 3, 4, and 5. Then, the effective polarization operator is written of in terms of local spin operators and correspond to the ME effect. There are two potential origins for the coupling between spin and charge of the electrons: one is explicit, the SOC, and the other is intrinsic to any system, the Pauli exclusion principle. These notions will be concretely addressed in Chapter 3 for the single-band Hubbard model and in Chapter 4 for a more complex multi-band Hubbard model.

1.4 Spin-orbit coupling

The main theme of this thesis is the interplay between the spin and charge degrees of freedom of electrons. SOC is thus central to most of the phenomena considered. In this section, we derive the following three types of SOC Hamiltonians used in this thesis.

1. The Rashba [81] and Dresselhaus [82] SOC Hamiltonian are proportional to the momentum of the electrons,

$$\mathcal{H}_R(k) = \alpha_R(k_x\sigma_y - k_y\sigma_x), \tag{1.32}$$
$$\mathcal{H}_D(k) = \alpha_D(k_x\sigma_x - k_y\sigma_y), \tag{1.33}$$

   where σ_x, σ_y, and σ_z are Pauli matrices representing the electron spin, and α_R and α_D are the Rashba and Dresselhaus coupling constants, respectively.

2. The corresponding Hamiltonian on lattice models becomes a spin-dependent hopping Hamiltonian,

$$\mathcal{H}_{\mathrm{SO}} = i\lambda \sum_{\langle ij \rangle} \left[\mathbf{c}_i^\dagger (\hat{\mathbf{d}}_{ij} \cdot \boldsymbol{\sigma}) \mathbf{c}_j - \mathrm{H.c.} \right], \tag{1.34}$$

where i and j are nearest neighbor sites, $\boldsymbol{\sigma} = (\sigma_x, \sigma_y, \sigma_z)$, the $\hat{\mathbf{d}}_{ij}$ vectors are lattice-dependent unit vectors, $\mathbf{c}_i^\dagger = (c_{i\uparrow}^\dagger, c_{i\downarrow}^\dagger)$, and $\mathbf{c}_i = (c_{i\uparrow}, c_{i\downarrow})^\intercal$, where $c_{is}^\dagger$ and c_{is} are the electron creation and annihilation operators with spin s at site i.

3. The on-site intrinsic SOC Hamiltonian originating from the relativistic coupling between the orbital angular momentum $\mathbf{L}$ and spin angular momentum $\mathbf{S}$ of an electron is

$$\mathcal{H}_{\mathrm{SO}} = \lambda \mathbf{S} \cdot \mathbf{L}. \tag{1.35}$$

It only appears in the multi-orbital systems considered in Chapters 4 and 5.

Spin-orbit coupling is a relativistic effect which arises from the non-relativistic limit of the Dirac equation with electromagnetic coupling. The Dirac equation is

$$\mathcal{H}\psi = i\frac{\partial}{\partial t}\psi = c\boldsymbol{\alpha} \cdot (\mathbf{p} - e\mathbf{A}) + c^2\beta m + e\phi, \tag{1.36}$$

$$\{\alpha_i, \alpha_j\} = 2\delta_{ij}, \quad \{\alpha_i, \beta\} = 0, \tag{1.37}$$

where $\mathbf{A}$ and ϕ are the vector and scalar electromagnetic potentials, and α_i (with $i = 1, 2,$ and 3) and β are 4×4 Hermitian matrices. In the non-relativistic limit ($\mathcal{H}_0 = \mathcal{H} - mc^2 \ll mc^2$), the Hamiltonian becomes

$$\mathcal{H}_0\psi = \left(\frac{1}{2m}(\mathbf{p} - e\mathbf{A})^2 + e\phi - \frac{e}{2m}\boldsymbol{\sigma} \cdot \mathbf{B} - \frac{\mathbf{p}^4}{8m^3c^2} - \frac{e}{8m^2c^2}\nabla \cdot \mathbf{E} - \frac{e}{4m^2c^2}\boldsymbol{\sigma} \cdot (\mathbf{E} \times \mathbf{p}) \right)\psi. \tag{1.38}$$

The first three terms constitute the usual non-relativistic Hamiltonian. The fourth term is a relativistic correction to the kinetetic energy. The fifth term is the so-called Darwin term. Finally, the last term,

$$\mathcal{H}_{\mathrm{SO}} = -\frac{e}{4m^2c^2}\boldsymbol{\sigma} \cdot (\mathbf{E} \times \mathbf{p}) = -\frac{\mu_B}{2mc^2}\boldsymbol{\sigma} \cdot (\mathbf{E} \times \mathbf{p}) = -\frac{1}{2}\mu_B \boldsymbol{\sigma} \frac{\mathbf{E} \times \mathbf{v}}{c^2}, \tag{1.39}$$

is identified as the spin-orbit coupling (with the correct Thomas precession factor). It can be seen as the non-relativistic Zeeman coupling (third term in the right hand side of Eq. (1.38)) from the magnetic field arising after a Lorentz transformation of the electric field to the rest frame of the particle.

1.4.1 Rashba and Dresselhaus SOC

In systems lacking inversion symmetry, the Rashba effect [81], caused by structural inversion asymmetry, and the Dresselhaus effect [82], caused by bulk asymmetry of the system, are usual instances of SOC. Typically, the Rashba SOC arises in a 2D system (e.g., at an interface) due to the lack of reflection symmetry across the 2D plane. For example, by simply applying an external field $\mathbf{E} = E\hat{\mathbf{z}}$ in the z direction we obtain

$$\mathcal{H}_R = -\frac{\mu_B E}{2mc^2}(\mathbf{k} \times \boldsymbol{\sigma})_z \equiv \alpha_R(k_x\sigma_y - k_y\sigma_x). \tag{1.40}$$

The Dresselhaus effect is observed in systems which lack inversion symmetry and was first described in systems with the zinc blende structure [82]. In general, for the energy dispersion $E_s(\mathbf{k})$ with $s =\uparrow,\downarrow$, the time reversal symmetry imposes $E_\uparrow(\mathbf{k}) = E_\downarrow(-\mathbf{k})$ and the inversion symmetry imposes $E_s(\mathbf{k}) = E_s(-\mathbf{k})$, so that there is a two-fold degeneracy throughout the Brillouin zone when both symmetries are preserved. Without the inversion symmetry, the degeneracy is lifted and the spin operators $\boldsymbol{\sigma}$ can couple to odd powers of the momentum $\mathbf{k}$. For 3D materials with the T_d point group symmetry (e.g., with the zinc blende structure), there are no linear terms and the Dresselhaus Hamiltonian is obtained from symmetry considerations,

$$\mathcal{H}_D = \gamma_D \boldsymbol{\kappa} \cdot \boldsymbol{\sigma}, \tag{1.41}$$

where

$$\kappa_x = k_x(k_y^2 - k_z^2), \qquad \kappa_x = k_y(k_z^2 - k_x^2), \qquad \kappa_z = k_z(k_x^2 - k_y^2), \tag{1.42}$$

and x, y, and z are the crystallographic axes. In 2D systems (say with a finite width in the z direction), the symmetry is lowered and both linear and cubic terms are commonly considered. They are obtained from Eq. (1.42) by replacing k_z and k_z^2 with their averaged values $\langle k_z\rangle = 0$ and $\langle k_z^2\rangle \neq 0$, so that

$$\mathcal{H}_D = \gamma_D\langle k_z^2\rangle(-k_x\sigma_x + k_y\sigma_y) + \gamma_D(k_x k_y^2\sigma_x - k_y k_x^2\sigma_y). \tag{1.43}$$

In this thesis, we limit ourselves to the linear Hamiltonian which thus has the form

$$\mathcal{H}_D = \alpha_D(k_x\sigma_x - k_y\sigma_y), \tag{1.44}$$

where $\alpha_D = -\langle k_z^2\rangle\gamma_D$.

1.4.2 Lattice SOC

In the tight-binding language, the single-electron states are localized Wannier functions. The effect of SOC is akin to a spin rotation during the hopping processes and is responsible for the Dzaloshinskii-Moriya (DM) [83, 84] interaction in effective spin systems. This is understood starting from the 2D Hamiltonian quadratic in momentum with Rashba and Dresselhaus SOC, which can be rewritten as

$$\frac{\mathbf{k}^2}{2m} + \mathcal{H}_R + \mathcal{H}_D = \frac{1}{2m}(k_x + m\alpha_R\sigma_y + m\alpha_D\sigma_x)^2 + (k_y - m\alpha_R\sigma_x - m\alpha_D\sigma_y)^2 + \text{const.} \tag{1.45}$$

In a lattice system, the SOC can hence be seen as a SU(2) gauge field [85], i.e., a spin dependent phase which is commonly called the Aharonov-Casher phase [86]. The phase factor that an electron acquires by taking a step of length a between two sites, say in the $\hat{\mathbf{x}}$ direction, is $\exp\left(-i\theta\hat{\mathbf{d}}\cdot\boldsymbol{\sigma}/2\right)$ where $\theta = 2ma\sqrt{\alpha_R^2 + \alpha_D^2}$ is the spin rotation angle accompanying each hopping and $\hat{\mathbf{d}} = (\alpha_D, \alpha_R, 0)/\sqrt{\alpha_R^2 + \alpha_D^2}$. In general, θ and the direction of $\hat{\mathbf{d}}$ depends on the orientation of the hopping and on α_R and α_D. Therefore, starting from the hopping Hamiltonian

$$\mathcal{H}_{\text{hop}} = -t_0\sum_{\langle ij\rangle}\left[\mathbf{c}_i^\dagger\mathbf{c}_j + \text{H.c.}\right], \tag{1.46}$$

the effect of SOC is obtained by replacing $t_0 \to t_0 \exp\left(-i\theta\hat{\mathbf{d}}\cdot\boldsymbol{\sigma}/2\right)$. The Hamiltonian then reads

$$\mathcal{H} = -t\sum_{\langle ij\rangle}\left[\mathbf{c}_i^\dagger\mathbf{c}_j + \text{H.c.}\right] + i\lambda\sum_{\langle ij\rangle}\left[\mathbf{c}_i^\dagger(\hat{\mathbf{d}}_{ij}\cdot\boldsymbol{\sigma})\mathbf{c}_j - \text{H.c.}\right] \tag{1.47}$$

where the new parameters t and λ satisfy

$$t = t_0\cos(\theta/2), \qquad \lambda = t_0\sin(\theta/2). \tag{1.48}$$

The second term is identified as the SOC Hamiltonian,

$$\mathcal{H}_{\text{SO}} = i\lambda\sum_{\langle ij\rangle}\left[\mathbf{c}_i^\dagger(\hat{\mathbf{d}}_{ij}\cdot\boldsymbol{\sigma})\mathbf{c}_j - \text{H.c.}\right], \tag{1.49}$$

and $\hat{\mathbf{d}}_{ij}$ will henceforth be called the "SOC vector". In particular, in 1D systems, $\hat{\mathbf{d}}_{ij} = \hat{\mathbf{d}}$ is constant throughout the system.

1.4.3 Local SOC

In the case of a centrally symmetric electric potential $V(r)$,

$$e\mathbf{E} = -\frac{dV}{dr}\frac{\mathbf{r}}{r}, \tag{1.50}$$

the SOC Hamiltonian reduces to a familiar expression,

$$\mathcal{H}_{\text{SO}} = -\frac{e}{4m^2}\boldsymbol{\sigma}\cdot(\mathbf{E}\times\mathbf{p}) = \frac{1}{2m^2}\frac{1}{r}\frac{dV}{dr}\mathbf{S}\cdot\mathbf{L} \equiv \lambda\mathbf{S}\cdot\mathbf{L}, \tag{1.51}$$

where $\mathbf{S} = \boldsymbol{\sigma}/2$ and $\mathbf{L} = \mathbf{r}\times\mathbf{p}$. This is the form that the SOC Hamiltonian adopts when considering an electron localized on an ion with a given orbital angular momentum. SOC is particularly strong in heavy TM compounds with $4d$ and $5d$ elements (for instance, $\lambda \approx 400$ meV in iridates), which leads to emergent quantum phases and other interesting phenomena [87–90].

Chapter 2

Electric dipole spin resonance

In this chapter, we study in detail the phenomenon known as electric dipole spin resonance (EDSR). In particular, we consider how it is affected when considering a lattice model (as opposed to a continuum model) and introducing interaction by using the Hubbard model.

2.1 Introduction

The EDSR was originally predicted by Rashba in Ref. [11]. It was studied in the context of semi-conductors and was first observed in InSb [91–93]. The EDSR can be understood as an extension of the standard ESR for which the AC magnetic field is replaced by an AC electric field. ESR is a well-known phenomenon extensively used by experimentalists to study the magnetic moments of electrons in a system. Under a magnetic field, each non-interacting electron is characterized by one of two Hamiltonian eigenstates: spin parallel or anti-parallel to the magnetic field, whose energies are separated by the so-called Zeeman gap. Then, applying an AC magnetic field polarized perpendicular to the static magnetic field induces transitions between the two energy levels when the frequency of the field matches the Zeeman gap. For a pristine non-interacting system of free electrons, there is not much more to say. The energy dispersion depends on the spin of the electrons only through the magnetic field, and thus the gap Δ between the two spin branches is momentum independent. In this sense, the charge and spin degrees of freedom of the electrons are unrelated, and the ESR corresponds to the same spin-flip transition regardless of the motion of the electrons. In this case, the ESR spectrum is a single Dirac-delta peak at the Zeeman gap.

As carefully shown in Ref. [94], the addition of any SU(2)-invariant term leaves the ESR signal unaffected. For example, charge-charge interactions (i.e., only depending on the positions of the electrons) do not modify the ESR spectrum. Thus, for the Hubbard model at half-filling, the signal is independent of U, the on-site Coulomb repulsion. Even in the $U \to \infty$ limit, the effective spin Heisenberg model (which is SU(2)-invariant) with the extra magnetic field has the same ESR spectrum as the free electrons. However, SU(2)-breaking terms do modify the ESR spectrum. The most obvious example is *de facto* the external magnetic field. SOC is another term which is common in materials. It appears in several forms, as explained in Sec. 1.4.

In this chapter, we study the synergetic effects of SOC and the static magnetic field. As shown in detail below, SOC affects the general band dispersion so that the gap Δ between the two spin branches deviates from the Zeeman gap as a function of momentum: $\Delta = \Delta(k)$. Therefore the resonance frequency ω_{res} corresponds to the gap near the Fermi surface. As the gap is not uniform, the ESR spreads out (even

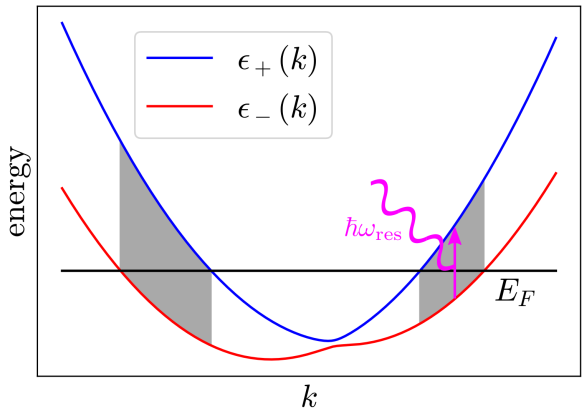

FIGURE 2.1: Sketch of the band dispersion of the 1D electron gas with SOC and Zeeman coupling. The horizontal black line indicates the Fermi energy E_F.

at zero temperature) to match the energy gaps in a small region around the Fermi surface. This is illustrated in Fig 2.1 in the case of a parabolic dispersion in 1D, for which the effect of SOC is to shift the two branches left and right (in momentum space) while the magnetic field splits them up and down (in energy space). The black line indicates the fermi energy E_F and the shaded regions show all the possible transitions (only considering the zero-temperature limit). The resonance frequencies then match the inter-band gap in the shaded regions and thus correspond to two finite-width peaks in the resonance spectrum. The corresponding resonance amplitude can be calculated with the Kubo formula. For the ESR, it is obtained from the spin-spin dynamical correlation function, also called the spin susceptibility, as mentioned in Sec. 1.2. In two dimensions, instead of two peaks the resonance spectrum is continuous for frequencies matching $\Delta(\mathbf{k})$ for $\mathbf{k}$ in a small region around the Fermi surface, as shown in Sec. 2.5.

SOC has another important effect on the spin resonance: the transitions can now be induced by an AC electric field. Indeed, the (Rashba and/or Dresselhaus) SOC creates an effective magnetic field that is proportional to the electron momentum. The irradiated light can thus excite electrons from the lower branch to the upper branch through both magnetic and electric periodic fields, corresponding to magnetic-dipole and electric-dipole transitions, respectively. The later is the so-called EDSR. The absorption rate originating from the electric-dipole-induced transitions is measured through the optical conductivity, as explained in Sec. 1.3.

Therefore, in a metal with SOC, both the optical conductivity and the spin susceptibility are related to the light absorption rate at the resonance frequency $\omega_{\rm res}$. We know from Eqs. (1.12) and (1.17) that the absorption rate of the irradiated light with frequency $\omega_{\rm res}$ and electric and magnetic field amplitudes $\tilde{E}_0$ and $\tilde{B}_0$, respectively, is

$$I(\omega_{\rm res}) = 2\sigma'(\omega_{\rm res})\tilde{E}_0^2 + 2\omega_{\rm res}(g\mu_B)^2\chi''(\omega_{\rm res})\tilde{B}_0^2, \tag{2.1}$$

where $\sigma'(\omega)$ is the real part of the optical conductivity, $\chi''(\omega)$ is the imaginary part of the spin susceptibility (along the direction of the AC magnetic field), g is the Landé factor and $\mu_B = \frac{e\hbar}{2m_0}$ is the Bohr magneton (e is the charge and m_0 is the mass of the electron in a vaccuum). The relative strength of the magnetic-dipole contribution and the electric-dipole contribution is such that the EDSR amplitude (the first term

in Eq. (2.1) is much stronger than the ESR amplitude (the second term in Eq. (2.1) by several orders of magnitude [73, 95].

This can be understood from a dimensional analysis. The SOC, in general terms, defines a coupling between the momentum and the spin of each electron. The coupling constant is written α and has units of velocity. Given a typical wavelength of the system a (e.g., the De Broglie wavelength $2\pi/k_F$ for free electrons, or the inter-site spacing for a lattice system), the SOC defines the energy scale λ_{SO},

$$\alpha \sim \frac{1}{\hbar} a \lambda_{\mathrm{SO}}. \tag{2.2}$$

From a dimensional analysis point of view (i.e., by associating current and spin as $j \sim 2e\alpha S/\hbar$), we can relate $\sigma' \sim (4e^2\alpha^2/\omega)\chi''$ in Eq. (2.1). In SI units, the electric and magnetic field amplitudes are related by $\tilde{E}_0 = c\tilde{B}_0$ (c is the speed of light) so that

$$I(\omega_{\mathrm{res}}) \sim 2\omega_{\mathrm{res}}\chi''(\omega_{\mathrm{res}})\left[\frac{4e^2\alpha^2}{\omega_{\mathrm{res}}^2} + \frac{(g\mu_B)^2}{c^2}\right]\tilde{E}_0^2. \tag{2.3}$$

Thus when SOC is of the same order as the Zeeman splitting and $\hbar\omega_{\mathrm{res}} \sim \lambda_{\mathrm{SO}}$, the ratio of the EDSR and magnetic-dipole ESR contributions is of the order $(a/\lambda\!\!\!^{-}_C)^2$, where $\lambda\!\!\!^{-}_C = \hbar/m_0 c$ is the reduced Compton length of the electron ($\approx 3.86 \times 10^{-13}$ m), much smaller than other characteristic length scales of the electrons (e.g. a lattice spacing is typically $a \approx 5 \times 10^{-10}$ m).

As explained in Sec. 1.3.2, in a non-interacting single-band electron system without SOC, the optical conductivity has only a Drude weight contribution at $\omega = 0$ and vanishes for $\omega > 0$, $\sigma(\omega) = D\delta(\omega)$. In the presence of SOC, the only contribution to $\sigma(\omega > 0)$ is the EDSR.

The EDSR only describes the spin-flip-like excitations through electric dipoles. Strictly speaking, once SOC is introduced, the excitations is not exactly a spin flip, as the direction of the spin depends on momentum. Therefore we more generally refer to them as *magnetic* transitions. Importantly, their frequencies are the same as the magnetic-dipole ESR ones. Only their intensities differ.

Originally, EDSR was studied in 2D semi-conductors. In addition to the Zeeman effect, the orbital effect of the magnetic field was also studied. Indeed, electric-dipole transitions are allowed between different Landau levels, at multiples of the cyclotron frequency, and are affected by SOC. The phenomenon is summarized in the next section. After that, we do not further consider orbital effects from the magnetic field in this thesis. In 1D systems, they simply do not occur. In the 2D case considered at the end of this chapter, there are no orbital effects for an in-plane magnetic field.

In this chapter, we study the EDSR in the single-band Hubbard model. However, we first revisit the electron gas formulation in two dimensions with Landau levels in Sec. 2.2, and in a generic 1DEG system in Sec. 2.3. Following the recent work of Ref. [38], we also discuss the effects of interaction in the 1DEG using the Tomonaga-Luttinger liquid theory in Sec. 2.3.3. Our results generalize the previously known results as explained in Sec. 2.3.3.

Then, we present the most important results of this chapter in Secs. 2.4 and Secs. 2.5.

In Sec. 2.4, we present our original results for the EDSR in the 1D single-band Hubbard model. First we highlight the effect of the lattice in the non-interacting case. We show that the EDSR spectrum strongly depends on the position of the Fermi level in the electronic band. At half-filling, we subsequently discuss the effect of the Hubbard interaction on the EDSR when an optical gap grows and the system

become a Mott insulator. We show using exact diagonalization that when the optical gap is larger than the kinetic hopping, the umklapp scattering suppresses the EDSR.

On a separated note, in the 1D Hubbard model in the strong-coupling limit at half-filling, i.e., the Mott-insulating phase, we also show in Sec. 2.4.2 how the magnetic field and SOC affect the optical conductivity above the optical gap. This is not related to the ESR and EDSR, but it underscores the synergetic effect of SOC and Zeeman effect on the optical resonance at a different energy scale.

Finally, in Sec. 2.5, we consider the ESR and EDSR in 2D single-band systems with strong SOC and magnetic field. We show that the spectrum is continuous due to the varying effective Zeeman field along the Fermi surface. In addition, there are unexpected square root Van Hove-like singularities in the spectrum. Moreover, we show that the optical conductivity is highly anisotropic, and that the number of singularities and their positions greatly depend on the electronic band structure, the Fermi level, and the lattice shape.

2.2 Combined resonances in the Zeeman limit

In the original work of E. Rashba [11, 36], SOC is introduced as a perturbation and the resonance occurs at the Zeeman gap (neglecting changes in the resonance frequency). However, it is pointed out that for 2D systems with an out-of-plane magnetic field, cyclotron resonances are also affected by the SOC, and new resonances combining attributes of spin and cyclotron resonances are possible. In this section, we present the phenomenon as extensively reviewed by Rashba and Sheka in Ref. [37].

Resonance phenomena in a 2DEG can be separated into electric resonances, such as the electron cyclotron resonance and magnetic resonances, such as the ESR. When SOC is introduced, the dichotomy breaks, and a more general type of electron resonance is defined. The so-called combined resonances are characterized by (1) the electric mechanism of the resonance, (2) a change in the spin quantum state. The EDSR corresponds to the special case for which the orbital motion is left unchanged, and the resonance frequency is the spin frequency. A combined resonance which modifies the orbital motion, through a combination of spin resonance and cyclotron resonance, occurs at linear combinations of spin and cyclotron frequencies, or combinational frequencies. This latter case is referred to as 'combinational frequency resonance'. In other words, both EDSR and combinational frequency resonances are combined resonances. In EDSR only the spins are affected, whereas for combinational frequency resonances there is a change in the Landau levels.

Electric resonances are inherently orders of magnitude stronger than magnetic ones. Without SOC, an electron under a magnetic field $\mathbf{B}$ performs two motions associated with its orbital and spin degrees of freedom, corresponding to the spin and cyclotron resonances, respectively. The spin resonance is determined by the spin frequency $\hbar\omega_s = g\mu_B B$, where $B = \|\mathbf{B}\|$. The length associated with the transition is the Compton wavelength $\lambda\!\!\!^{-}_C$, which is small due to the relative $1/c$ factor between magnetic and electric field amplitudes. The cyclotron rotation is characterized by the frequency

$$\omega_c = \frac{eB}{m^*}, \tag{2.4}$$

where m^* is the effective mass. The corresponding characteristic spatial scale of the orbital motion is the magnetic length

$$r_B = \sqrt{\frac{\hbar}{eB}}. \tag{2.5}$$

Then, the electric dipole moment associated with a cyclotron transition induced by an AC electric field is roughly er_B, and the ratio between cyclotron resonance and ESR is approximated by $(r_B/\lambda\!\!\!^{-}_C)^2 \sim 10^{10}$, for typical values of r_B. Compared to magnetic resonances, all purely electric resonances are intrinsically large. For example, the paraelectric resonance is characterized by the atomic length, namely, the Bohr radius $a_0 \approx 5.3 \times 10^{-11} m$, and the ratio of the intensities is $(a_0/\lambda\!\!\!^{-}_C)^2 \sim 10^4$.

Electric resonances being considerably stronger than magnetic ones, it is expected that even a weak SOC, which couples orbital and spin resonances, will be important for electric-dipole induced spin resonances.

But just how weak can the SOC be? As we saw in Sec. 1.4, SOC is present in all systems as a relativistic correction,

$$\mathcal{H}_{\mathrm{SO}} = -\frac{\mu_B}{2m_0c^2}\boldsymbol{\sigma}(\mathbf{E}\times\mathbf{p}) = -\frac{1}{2}\mu_B\boldsymbol{\sigma}\frac{\mathbf{E}\times\mathbf{v}}{c^2}, \tag{2.6}$$

where $\boldsymbol{\sigma}$ are the spin Pauli matrices, $\mathbf{E}$ is any electric field, $\mathbf{p}$ the momentum of the electron and $\mathbf{v} = \mathbf{p}/m_0$ is the velocity of the electron. For the AC electric field $\tilde{\mathbf{E}}$ of an electromagnetic wave with frequency ω_s, Eq. (2.6) is similar to an additional Zeeman coupling with the effective $\tilde{B}_{\mathrm{eff}} = (v/c^2)\tilde{E} = (v/c)\tilde{B}$ AC magnetic field. Through this direct SOC mechanism, the intensity ratio $I_{\mathrm{EDSR}}/I_{\mathrm{ESR}} \sim (v/c)^2$ which is vanishing in the non-relativistic limit of condensed matter systems. This explains why EDSR is not systematically observed in all materials but requires sufficiently strong source of SOC. In crystals, the SOC can be substantially stronger due to the existence of a different field $\mathbf{E}$ in Eq. (2.6) (e.g., Rashba or Dresselhaus SOC). In the following, we calculate the intensity of the combined resonances, including EDSR.

We consider a general Hamiltonian split as

$$\mathcal{H} = \mathcal{H}_0 + \mathcal{H}_{\mathrm{SO}}. \tag{2.7}$$

The resonances are possible thanks to the coupling of the system to the AC electric fields $\tilde{\mathbf{E}}$ through the magnetic vector potential $\tilde{\mathbf{A}}$,

$$\tilde{\mathcal{H}}_e = -e\mathbf{v}\cdot\tilde{\mathbf{A}}, \tag{2.8}$$

where $\mathbf{v}$ is the velocity operator,

$$\mathbf{v} = \frac{i}{\hbar}[\mathcal{H}, \mathbf{r}], \tag{2.9}$$

and $\mathbf{r}$ is the position operator. The interaction between electrons and the AC field can also be described by the scalar potential $-e\tilde{\mathbf{E}}\cdot\mathbf{r}$, and the combined resonance intensity is equivalently expressed by matrix elements of $\mathbf{r}$ and $\mathbf{v}$ as we have

$$\langle f|\mathbf{v}|i\rangle = i\omega_{i\to f}\langle f|\mathbf{r}|i\rangle, \tag{2.10}$$

where $\omega_{i\to f}$ is the resonance frequency from state $|i\rangle$ to state $|f\rangle$. To compare the relative intensity of combined resonances and magnetic-dipole ESR, we also introduce the coupling to the AC magnetic field $\tilde{\mathcal{H}}_m = \frac{1}{2}g\mu_B\tilde{\mathbf{B}}\cdot\boldsymbol{\sigma}$. Using $\tilde{\mathbf{B}} = \boldsymbol{\nabla}\times\tilde{\mathbf{A}} = i\mathbf{q}\times\tilde{\mathbf{A}}$,

the total coupling to an AC electromagnetic field of wavelength $\mathbf{q}$ with $\tilde{\mathbf{A}} = \tilde{A}\hat{\mathbf{e}}$ is expressed as

$$\tilde{\mathcal{H}} = \tilde{\mathcal{H}}_e + \tilde{\mathcal{H}}_m \equiv -e\mathbf{u}\cdot\tilde{\mathbf{A}} = -\left[e\mathbf{v}\cdot\hat{\mathbf{e}} + i\frac{g\mu_B}{2}(\boldsymbol{\sigma}\times\mathbf{q})\cdot\hat{\mathbf{e}}\right]\tilde{A}. \tag{2.11}$$

The general velocity $\mathbf{u}$ contains both the electric-dipole contribution through $\mathbf{v}$ and the paramagnetic contribution of ESR.

In the framework of the effective mass approximation with quadratic dispersion, originally used to describe combined resonances in semiconductors, the Hamiltonian $\mathcal{H}_0$ is

$$\mathcal{H}_0 = \frac{\hbar^2\mathbf{k}^2}{2m^*} + \frac{1}{2}g\mu_B\mathbf{B}\cdot\boldsymbol{\sigma}. \tag{2.12}$$

For now, we use a general SOC Hamiltonian written as

$$\mathcal{H}_{\mathrm{SO}} = \lambda\sum_i f_i(\mathbf{k})\sigma_i, \tag{2.13}$$

where λ is the SO coupling constant, and the $f_i(\mathbf{k})$ are polynomials over powers of k_j, the coordinates of $\mathbf{k}$. Here, the notation differs from Sec. 1.3, and $\mathbf{k}$ directly refers to the magnetic field quasimomentum

$$\mathbf{k} = -i\nabla_r - \frac{e}{\hbar}\mathbf{A}. \tag{2.14}$$

In the Zeeman limit, in which SOC is treated as a perturbation, only terms linear in $\mathcal{H}_{\mathrm{SO}}$ are kept. The matrix elements (2.10) are conveniently calculated using the eigenstates of $\mathcal{H}_0$. This can be done by eliminating $\mathcal{H}_{\mathrm{SO}}$ from the Hamiltonian through an adequate unitary transformation defined as

$$\mathcal{H} \to e^{\hat{T}}\mathcal{H}e^{-\hat{T}} = \mathcal{H}_0, \tag{2.15}$$

which is also applied to the other operators. In the first order approximation, $\hat{T}$ is linear in $\mathcal{H}_{\mathrm{SO}}$ and

$$\mathcal{H}_{\mathrm{SO}}(\mathbf{k}) + [\hat{T}, \mathcal{H}_0] = 0, \tag{2.16}$$

$$\hat{T} = -i\int_0^\infty \mathcal{H}_{\mathrm{SO}}(t)dt, \tag{2.17}$$

$$\mathbf{k}(t) = e^{i\mathcal{H}_0 t}\mathbf{k}e^{-i\mathcal{H}_0 t}. \tag{2.18}$$

Similarly, the velocity operator used to calculate the matrix elements becomes

$$\tilde{\mathbf{v}} = \frac{i}{\hbar}[\mathcal{H}_0, \tilde{\mathbf{r}}], \tag{2.19}$$

where we defined

$$\tilde{\mathbf{r}} = e^{\hat{T}}\mathbf{r}e^{-\hat{T}} \approx \mathbf{r} + [\hat{T}, \mathbf{r}] \equiv \mathbf{r} + \mathbf{r}_{\mathrm{SO}}. \tag{2.20}$$

The SOC Hamiltonian (2.13) is written in the reference system A, usually set by the crystallographic axes, in which $\mathbf{B}$ points in an arbitrary direction characterized by its polar and azimuthal angles, θ and ϕ, respectively. The vectors in system A are written in the basis $\mathcal{B} = \{\hat{\mathbf{x}}, \hat{\mathbf{y}}, \hat{\mathbf{z}}\}$. We now introduce the reference system A′ associated with the magnetic field so that its Z direction points along $\mathbf{B}$. Moreover, the vectors are written in the circular basis defined by $\mathcal{B}' = \{\hat{\mathbf{E}}_-, \hat{\mathbf{Z}}, \hat{\mathbf{E}}_+\}$ where $\hat{\mathbf{E}}_\pm = (\hat{\mathbf{X}} \pm i\hat{\mathbf{Y}})/\sqrt{2}$

and $\hat{\mathbf{Z}} \parallel \mathbf{B}$. In system A, the basis $\mathcal{B}$ is used and lowercase letters are employed to denote vectors (e.g. $\mathbf{r}$, $\mathbf{v}$ and $\mathbf{k}$). In system A′, vectors written in the $\mathcal{B}'$ basis are denoted by capital letters. For instance, the velocity is written as

$$\mathbf{V} = (V_-, V_Z, V_+) = (V_{\bar{1}}, V_0, V_1), \tag{2.21}$$

where

$$V_\pm = \frac{V_X \pm iV_Y}{\sqrt{2}}. \tag{2.22}$$

In the circular basis of A′, Greek indices are used $\alpha, \beta \in \{-1, 0, 1\}$ ($\bar{1} \equiv -1$) to label the coordinates, whereas roman letters $i, j \in \{1, 2, 3\}$ are used in A. We use the same notation for the Pauli matrices: $\sigma_i = \hat{\mathbf{e}}_i \cdot \boldsymbol{\sigma}$ where $\hat{\mathbf{e}}_i \in \mathcal{B}$ and $\sigma_\alpha = \hat{\mathbf{E}}_\alpha \cdot \boldsymbol{\sigma}$ where $\hat{\mathbf{E}}_\alpha \in \mathcal{B}'$.

Let the 3×3 unitary matrix corresponding to the change of basis transformation A′ → A be $\hat{M} = \hat{M}(\theta, \phi)$ such that

$$\mathbf{k} = \hat{M}\mathbf{K} \tag{2.23}$$

$$\hat{\mathbf{r}} = \hat{M}\hat{\mathbf{R}} \tag{2.24}$$

$$\sigma_i = \sum_\alpha \hat{M}^\dagger_{\alpha i} \sigma_\alpha. \tag{2.25}$$

In system A, the magnetic quasimomentum follow the commutation relation

$$[k_a, k_b] = \epsilon_{abc} i \frac{e}{\hbar} B_c, \tag{2.26}$$

where ϵ_{abc} is the three-dimensional Levi-Civita tensor. Translated in system A′, K_Z must be a scalar and

$$[K_-, K_+] = \frac{eB}{\hbar} = \frac{1}{r_B^2} \tag{2.27}$$

Then, we define ladder operator $a^\dagger$ and a for the Landau levels,

$$\mathbf{K} \equiv \frac{\boldsymbol{a}}{r_B} = \frac{1}{r_B}(a, \xi, a^\dagger), \tag{2.28}$$

where $\xi = r_B K_Z$ is a scalar, and $\{a, a^\dagger\} = 1$. In the circular basis, we also have

$$[K_\alpha, R_\beta] = -i\delta_{\alpha,\beta}. \tag{2.29}$$

We are now ready to calculate the intensity of the combined resonances. In the reference system A′, the Hamiltonian is conveniently written as

$$H_0 = \hbar\omega_c \left(a^\dagger a + \frac{1}{2}[\beta(\hat{\mathbf{Z}} \cdot \boldsymbol{\sigma}) + \xi^2 + 1] \right), \tag{2.30}$$

with eigenvalues

$$\varepsilon_{N,\sigma} = \hbar\omega_c \left(N + \frac{1}{2}(\beta\sigma + \xi^2 + 1) \right), \tag{2.31}$$

where $\sigma = \pm 1$ for the $|\uparrow\rangle$ and $|\downarrow\rangle$ spinors quantized along $\mathbf{B}$, $N = 0, 1, \ldots$, and

$$\beta = \frac{g\mu_B B}{\hbar\omega_c} = \frac{gm^*}{2m_0}. \tag{2.32}$$

The spin frequency ω_s and the cyclotron frequency ω_c are related by $\omega_s = \beta\omega_c$. The

spinor part of the matrix elements of $\hat{T}$ are found by explicitly calculating the integral in Eq. (2.12) using the equality

$$K_\alpha(t) = e^{i\alpha\hbar\omega_c t} K_\alpha. \tag{2.33}$$

The polynomials $f_i(\mathbf{k})$ defining $\mathcal{H}_{\rm SO}$ in (2.13) are written as

$$f_j(\mathbf{k}) = \sum_{\{i\}} F^{(j)}_{i_1,\ldots,i_l} k_{i_1} \ldots k_{i_l}, \tag{2.34}$$

where $l = l(j)$ depends on j. Noticing that $\langle\downarrow|\sigma_j|\uparrow\rangle = \sqrt{2}M^\dagger_{\bar{1}j}$, the matrix elements of $\hat{T}$ becomes

$$\langle\downarrow|\hat{T}|\uparrow\rangle = \lambda\frac{\sqrt{2}}{\hbar\omega_c}\sum_j M^\dagger_{\bar{1}j}\sum_{\{i\},\{\alpha\}}\frac{F^{(j)}_{i_1,\ldots,i_l}M_{i_1\alpha_1}\cdots M_{i_l\alpha_l}}{\alpha_1+\cdots+\alpha_l-\beta}K_{\alpha_1}\cdots K_{\alpha_l}. \tag{2.35}$$

Finally, the commutation of $\hat{T}$ with R_τ in Eq. (2.20), which is needed to calculate $R_{{\rm SO},\tau}$, just reduces to a total derivative with respect to K_τ because $[K_{\alpha_1}\cdots K_{\alpha_l}, R_\tau] = -i\frac{\partial}{\partial K_\tau}(K_{\alpha_1}\ldots K_{\alpha_l})$. In order for $\langle N'\downarrow|R_{{\rm SO},\tau}|N\uparrow\rangle$ to be finite, the condition $\alpha_1+\cdots+\alpha_l = N'-N-\tau$ must be satisfied. The corresponding resonance frequency is $\hbar\omega_{\rm res} = \varepsilon_{N',\downarrow}-\varepsilon_{N,\uparrow}$ so that, from Eq. (2.10),

$$\begin{aligned}&\langle N'\downarrow\big|\tilde{V}_\tau\big|N\uparrow\rangle = i\omega_{\rm res}\langle N'\downarrow\big|R_{{\rm SO},\tau}\big|N\uparrow\rangle\\ &= \lambda\frac{\sqrt{2}}{\hbar}\frac{N'-N-\beta}{N'-N-\beta-\tau}\sum_{j,\{i\},\{\alpha\}}M^\dagger_{\bar{1}j}F^{(j)}_{i_1,\ldots,i_l}M_{i_1\alpha_1}\cdots M_{i_l\alpha_l}\langle N'\big|\frac{\partial}{\partial K_\tau}(K_{\alpha_1}\cdots K_{\alpha_l})\big|N\rangle.\end{aligned} \tag{2.36}$$

Let us now investigate the combined resonance theory with the concrete Rashba SOC Hamiltonian,

$$\mathcal{H}_{\rm SO} = \alpha(\mathbf{k}\times\boldsymbol{\sigma})\cdot\hat{\mathbf{z}}. \tag{2.37}$$

In order to compare the electric-dipole-induced and magnetic-dipole-induced transitions, it is instructive to look at the general velocity operator define in Eq. (2.11), which now reads

$$\mathbf{u} = \frac{\hbar\mathbf{k}}{m^*} - (\frac{\alpha}{\hbar}\hat{\mathbf{z}} + i\frac{g\mu_B}{2e}\mathbf{q})\times\boldsymbol{\sigma} \tag{2.38}$$

$$= \frac{\hbar\mathbf{k}}{m^*} - \frac{\alpha}{\hbar}(\hat{\mathbf{z}} + i\mathbf{q}')\times\boldsymbol{\sigma}, \qquad \text{where} \quad \mathbf{q}' = \frac{\hbar g\mu_B}{2e\alpha}\mathbf{q} = \frac{\hbar^2\beta}{2m^*\alpha}\mathbf{q}. \tag{2.39}$$

The first term of the right hand side of Eq. (2.39) describes the pure cyclotron resonance transitions, the second term is the combined resonances (including EDSR), made possible by SOC, and the third term is the ESR through the conventional magnetic-dipole-induced resonance. In order to compare the combined resonances and ESR, we set $\mathbf{q}\parallel\hat{\mathbf{z}}$ so that their respective terms in the velocity differ only by a numerical factor. Their respective intensities are thus related to each other as

$$I_{\rm ESR}/I_{\rm COR} = (\mathbf{q}')^2, \tag{2.40}$$

where COR stands for "combined resonance". The maximum wavelength at which magnetic absorption experiments are carried out reaches about $100\,\mu m$ ($\sim$ 12.4 meV $\sim$ 3 THz) which, for typical semiconductors, corresponds to $q' \lesssim 10^{-3}$ and the combined resonances thus dominate over ESR.

Without magnetic field, the energy eigenvalues are $\varepsilon_\pm = \hbar^2\mathbf{k}^2/2m^* \pm \alpha k_\perp$, where $k_\perp$ is the momentum projected in the xy plane. The energy minimum defines an energy $\Delta \equiv |\varepsilon_{\min}| = m^*\alpha^2/2\hbar^2$. For $\mathbf{B} \parallel \hat{\mathbf{z}}$, the Hamiltonian can be diagonalized analytically and the its eigenvalues are

$$\varepsilon_{M,\sigma} = \hbar\omega_c\left[M + \sigma\left(\frac{1}{4}(1-\beta)^2 + \frac{4\Delta}{\hbar\omega_c}M\right)\right] + \frac{\hbar^2 k_z^2}{2m^*}, \tag{2.41}$$

for $M > 0$, where $\sigma = \pm 1$ is the branch index. For $M = 0$ there is only one energy corresponding to $\sigma = +1$,

$$\varepsilon_0 = \frac{1}{2}\hbar\omega_c(1-\beta) + \frac{\hbar^2 k_z^2}{2m^*}. \tag{2.42}$$

In the Zeeman limit, the Δ term becomes negligible and the σ index is interpreted as the spin of the electron ($S_Z = \hbar\sigma/2$). By relabeling the states such that $(M,+) \to (N,-)$ and $(M,-) \to (N+1,+)$, we recover the spectrum of Eq. (2.31),

$$\varepsilon_{N,\sigma} = \hbar\omega_c\left(N + \frac{1}{2}\right) + \sigma\frac{1}{2}\hbar\omega_s + \frac{\hbar^2 k_z^2}{2m^*}. \tag{2.43}$$

Finally, the combined resonance amplitudes can be calculated using Eq. (2.31) in the Zeeman limit. The Rashba SOC Hamiltonian corresponds to $F_2^{(1)} = -1$ and $F_1^{(2)} = 1$. Due to the linear form of the SOC, the combined resonance velocity V_τ is independent of momentum and thus $N \neq N'$ matrix elements vanish in Eq. (2.31) because $\langle N'|N\rangle = \delta_{N,N'}$. In other words, only the EDSR contributes to the combined resonances, and the combinational frequency resonance contributions vanish. Any violation of the harmonicity of $\mathcal{H}_0$ (e.g., additional terms $\propto \mathbf{k}^4$, or away from the Zeeman limit) will allow some combinational frequency resonances [37], but we do not consider them here. The expression for the velocity matrix elements becomes

$$\langle N\downarrow|\tilde{V}_\tau|N\uparrow\rangle = \frac{\sqrt{2}\lambda}{\hbar}\frac{\beta}{\beta+\tau}\left(M_{\bar{1}2}^\dagger M_{1\tau} - M_{\bar{1}1}^\dagger M_{2\tau}\right). \tag{2.44}$$

We now allow the magnetic field to point in any direction and study the effect of the angle θ between $\mathbf{B}$ and the $\hat{\mathbf{z}}$ axis. The transformation matrix $\hat{M}$ from system A' (in a circular basis) to system A (in a cartesian basis) with $\phi = 0$ and polar angle θ (so that $\hat{\mathbf{X}} = \cos\theta\hat{\mathbf{x}} - \sin\theta\hat{\mathbf{z}}$, $\hat{\mathbf{Y}} = \hat{\mathbf{y}}$, and $\hat{\mathbf{Z}} = \sin\theta\hat{\mathbf{x}} + \cos\theta\hat{\mathbf{z}}$) is

$$\hat{M}(\theta,0) = \begin{pmatrix} \frac{1}{\sqrt{2}}\cos\theta & \sin\theta & \frac{1}{\sqrt{2}}\cos\theta \\ \frac{-i}{\sqrt{2}} & 0 & \frac{i}{\sqrt{2}} \\ -\frac{1}{\sqrt{2}}\sin\theta & \cos\theta & -\frac{1}{\sqrt{2}}\sin\theta \end{pmatrix}, \tag{2.45}$$

so that we find

$$\langle N\uparrow|\tilde{V}_-|N\downarrow\rangle = -i\sqrt{2}\frac{\lambda}{\hbar}\frac{\beta}{\beta-1}\cos\theta, \tag{2.46}$$

$$\langle N\uparrow|\tilde{V}_Z|N\downarrow\rangle = -i\frac{\lambda}{\hbar}\sin\theta, \tag{2.47}$$

$$\langle N\uparrow|\tilde{V}_+|N\downarrow\rangle = 0. \tag{2.48}$$

In the Cartesian coordinates X, Y and Z attached to the magnetic field $\mathbf{B}$, the matrix elements read

$$\langle N\uparrow|\tilde{V}_X|N\downarrow\rangle = -i\frac{\lambda}{\hbar}\frac{\beta}{\beta-1}\cos\theta, \tag{2.49}$$

$$\langle N\uparrow|\tilde{V}_Y|N\downarrow\rangle = \frac{\lambda}{\hbar}\frac{\beta}{\beta-1}\cos\theta, \tag{2.50}$$

$$\langle N\uparrow|\tilde{V}_Z|N\downarrow\rangle = -i\frac{\lambda}{\hbar}\sin\theta. \tag{2.51}$$

Then intensity of the EDSR therefore depends on both the direction of the AC electric field $\hat{\mathbf{e}}$ relatively to the $\mathbf{B}$, and the relative angle θ between $\mathbf{B}$ and the Rashba direction $\hat{\mathbf{z}}$.

Henceforth, we do not consider the orbital effect of the magnetic field anymore. In a 2D system, this is only justified when the magnetic field $\mathbf{B}$ is in the xy plane, in which case $\theta = \pi/2$ and only the component of the velocity along the magnetic field yield a finite matrix element: from Eq. (2.51), $|\langle\uparrow|\tilde{\mathbf{v}}|\downarrow\rangle|^2 = (\mathbf{B}\cdot\tilde{\mathbf{v}}/B\tilde{v})^2\lambda^2/\hbar^2$.

Moreover, for a 1D system oriented in a direction $\hat{\mathbf{u}}_{1D}$ in the xy plane of the 2D system, $\mathbf{k} = k\hat{\mathbf{u}}_{1D}$ and the Rashba Hamiltonian becomes $\mathcal{H}_{SO} = \alpha k\hat{\mathbf{d}}\cdot\boldsymbol{\sigma}$ where $\hat{\mathbf{d}} \perp \hat{\mathbf{u}}_{1D}$ in the xy plane. Thus, because $\tilde{\mathbf{v}}$ is along $\hat{\mathbf{u}}_{1D}$, the EDSR intensity is proportional to $\sin^2\varphi$ where φ is the angle between $\mathbf{B}$ and $\hat{\mathbf{d}}$. This property is recurrent in the following sections and is proved for a general SOC Hamiltonian (linear in k) away from the Zeeman limit.

2.3 1D systems

In the following, the systems considered differ from the model used in the previous section concerning the followings points:

1. The "orbital effects" are not considered. Namely, the momentum operator $\mathbf{k}$ does not include the magnetic potential $\mathbf{A}$. This is possible because of the lower dimensionality. For a 1D system under a constant $\mathbf{B}$ field, it is always possible to choose a gauge where the component of $\mathbf{A}$ along the direction of the system vanishes. For 2D systems, this is only possible if $\mathbf{B}$ lies in the 2D plane.

2. The SOC is not treated as a perturbation and its energy scale is similar to the Zeeman gap, which is in contrast to the first studies of EDSR [11, 37, 96, 97].

3. Other bands are considered. In particular, we study the effect of the spatially periodic potential of the crystal lattice, which we implement by studying a tight-binding model.

4. Electron-electron interaction is considered.

For the 1D system, we proceed in two steps. First, the 1DEG is considered (with quadratic dispersion) and the effect of interactions is discussed with a Tomonaga-Luttinger liquid theory. Secondly, the tight-binding model is considered. The EDSR in the Hubbard model, including the on-site interaction, is studied numerically using exact diagonalization (ED).

As all the systems considered are translationally invariant (either continuously or discretely, by multiples of the lattice constant), the general non-interacting single-band 1D model (with spin) is uniquely defined by the energy dispersion relations of its upper and lower branches, $\epsilon_+(k)$ and $\epsilon_-(k)$, respectively. In the case of a spatially

discrete model, the dispersion is furthermore periodic in k with period $2\pi/a$, where a is the inter-site spacing. The general 1D model is thus

$$\mathcal{H} = \sum_k \mathbf{c}_k^\dagger \mathcal{H}(k) \mathbf{c}_k + \mathcal{H}_{\text{int}}, \tag{2.52}$$

where $\mathbf{c}_k^\dagger = (c_{k\uparrow}^\dagger, c_{k\downarrow}^\dagger)$ and $\mathbf{c_k} = (c_{k\uparrow}, c_{k\downarrow})^\intercal$, $c_{ks}^\dagger$ and c_{ks} are the electron creation and annihilation operators with momentum k and spin s, $\mathcal{H}(k)$ is a 2×2 Hermitian matrix with eigenvalues $\epsilon_\pm(k)$ and $\mathcal{H}_{\text{int}}$ is an additional two-electron interaction Hamiltonian that we leave unspecified for now. For the Hamiltonian (2.52), three different factors affect the spin resonances at zero temperature:

1. The band Hamiltonian $\mathcal{H}(k)$. Note that the dispersions themselves are not enough as we need the full Hamiltonian to properly calculate other quantities such as the current operator and the direction of the eigen-spinor at a given momentum.

2. The electron density or, equivalently, the Fermi energy. It defines the Fermi surface.

3. The interaction Hamiltonian $\mathcal{H}_{\text{int}}$.

2.3.1 Generic system

In the non-interacting regime, the EDSR spectrum is fully characterized by the energy dispersions of its two branches. The generic Hamiltonian is written as

$$\mathcal{H}(k) = \epsilon_0(k)\sigma_0 + \Delta(k)\hat{\mathbf{n}}_k \cdot \boldsymbol{\sigma}, \tag{2.53}$$

where σ_0 and $\boldsymbol{\sigma}$ denote the identity and the Pauli matrices, respectively. Here $\hat{\mathbf{n}}_k$ is a momentum-dependent unit vector and $\Delta(k)$ is half the gap between the two branches at a given momentum k. The branch splitting includes the contributions from both the magnetic field and SOC, and explicit expressions will be considered in subsequent sections of this chapter. For a given momentum k, the energy dispersions of the two eigenstates $|k\pm\rangle$ are

$$\epsilon_\pm(k) = \epsilon_0(k) \pm \Delta(k). \tag{2.54}$$

The spin resonance corresponds to transitions from $|k-\rangle$ to $|k+\rangle$ and thus can be understood as a momentum-dependent (pseudo-)spin-flip, in the sense that the "flipping" eigen-spinors point in a k-dependent direction, $\hat{\mathbf{n}}_k$ which is not a fixed quantization axis for the whole system.

As mentioned in the introduction of this chapter, the resonance is expected at frequencies matching $2\Delta(k)$ for k close to the two Fermi points $k_F^{L/R}$ (L and R stand for *left* and *right*, respectively), and correspond to the shaded regions in Fig. 2.1. This is clearly understood from the expression of the optical conductivity derived in the Chapter 1,

$$\sigma'(\omega) = \frac{\pi}{L\omega} \sum_k |\langle k+|j|k-\rangle|^2 \left(\langle n_{k-}\rangle - \langle n_{k+}\rangle\right) \delta(\omega - 2\Delta(k)), \tag{2.55}$$

where we have set $\hbar = 1$. Here, j is the current operator and $\langle\cdot\rangle$ denotes the grand canonical ensemble average. Therefore $\langle n_{k\pm}\rangle = n_F(\epsilon_\pm(k))$, where n_F is the Fermi-Dirac

distribution. With Eq. (2.55), we can calculate the optical conductivity of any non-interacting single-band model with translational invariance.

Let us derive an expression for the matrix elements $\langle k+|j|k-\rangle$. The diagonaliztion of $\mathcal{H}(k)$ is made explicit by the SU(2) rotation U_k defined by

$$U_k^\dagger(\hat{\mathbf{n}}_k \cdot \boldsymbol{\sigma})U_k = \sigma_z. \tag{2.56}$$

The eigen-operators $\tilde{\mathbf{c}}_k = (\tilde{c}_{k+}, \tilde{c}_{k-})$, which annihilate fermions with energy given in Eq. (2.54), are

$$\tilde{\mathbf{c}}_k = U_k^\dagger \mathbf{c}_k. \tag{2.57}$$

The single-particle states are clearly $|k\pm\rangle = \tilde{c}_{k,\pm}^\dagger |0\rangle$, where $|0\rangle$ is the vacuum state (i.e. with no electrons). Technically, the definition of U_k in Eq. (2.56) is ambiguous, as the axis of the rotation is left unspecified, but the exact definition will not matter in the end.

The operator j is analogous to the (group) velocity of the electrons, $j = ev$, and is related to the Hamiltonian as $j(k) = e\frac{\partial}{\partial k}\mathcal{H}(k)$ with

$$j = \sum_k \mathbf{c}_k^\dagger j(k) \mathbf{c}_k, \tag{2.58}$$

as explained in more details in Chapter 1. Henceforth, we set $e = 1$. The current operator reads

$$\begin{aligned} j(k) =& \frac{\partial}{\partial k}\epsilon_0(k)\sigma_0 + \frac{\partial}{\partial k}(\Delta(k)\hat{\mathbf{n}}_k)\cdot\boldsymbol{\sigma} \\ \equiv& j_{\mathrm{K}}(k)\sigma_0 + j_{\mathrm{SO}}(k)\hat{\mathbf{d}}_k \cdot \boldsymbol{\sigma}. \end{aligned} \tag{2.59}$$

Only the spin-orbit induced current (j_{SO}) gives rise to the EDSR signal, while both the "kinetic" current (j_{K}) and the SO current contribute to the Drude part of the conductivity. In terms of energy eigenstates, the current operator reads

$$U_k^\dagger j(k) U_k = j_{\mathrm{K}}(k)\sigma_0 + j_{\mathrm{SO}}(k)\hat{\mathbf{d}}_k' \cdot \boldsymbol{\sigma}, \tag{2.60}$$

where $\hat{\mathbf{d}}_k' = U_k^\dagger \hat{\mathbf{d}}_k U_k$. The transformation defined by U_k correspond to an SO(3) rotation in $\mathbb{R}^3$ which preserves angles. Therefore, we have the relation

$$\hat{\mathbf{d}}_k' \cdot \hat{\mathbf{z}} = \hat{\mathbf{d}}_k \cdot \hat{\mathbf{n}}_k \equiv \cos\phi_k, \tag{2.61}$$

where ϕ_k can be interpreted as the angle between the eigen-spinors of the Hamiltonian and those of the current operator.

Using Eqs. (2.60) and (2.61), off-diagonal matrix elements for the current operator arise from the x and y components of $\hat{\mathbf{d}}_k'$ and are given by

$$\begin{aligned} |\langle k+|j|k-\rangle|^2 &= j_{\mathrm{SO}}(k)^2\left[1 - (\hat{\mathbf{d}}_k' \cdot \hat{\mathbf{z}})^2\right] \\ &= j_{\mathrm{SO}}(k)^2\left[1 - (\hat{\mathbf{d}}_k \cdot \hat{\mathbf{n}}_k)^2\right] \\ &= j_{\mathrm{SO}}(k)^2 \sin^2\phi_k. \end{aligned} \tag{2.62}$$

The importance of both the Zeeman coupling and SOC in 1D systems can be understood as follows. For a static magnetic field $\mathbf{B}$, the spin-dependent part of the

Hamiltonian (2.53) can be generically decomposed as

$$\Delta(k)\hat{\mathbf{n}}_k \cdot \boldsymbol{\sigma} = (\mathbf{D}(k) - \mathbf{b}) \cdot \boldsymbol{\sigma}, \tag{2.63}$$

where $\mathbf{b} = (g\mu_B/2)\mathbf{B}$. Here $\mathbf{D}(k)$ represents the k-dependent effective magnetic field originating from SOC. In 1D systems, the direction of $\mathbf{D}(k)$ is often constant and set by the system direction, as will be explicitly shown shortly in two models. In this case, $\mathbf{D}(k) = D(k)\hat{\mathbf{d}}$ where $\hat{\mathbf{d}}$ is identified as $\hat{\mathbf{d}}_k$ in Eq. (2.59) and is k-independent. Furthermore,

$$[\mathcal{H}(k), j(k)] = [\big(D(k)\hat{\mathbf{d}} - \mathbf{b}\big) \cdot \boldsymbol{\sigma}, \partial_k D(k)\hat{\mathbf{d}} \cdot \boldsymbol{\sigma}] = [-\mathbf{b} \cdot \boldsymbol{\sigma}, \partial_k D(k)\hat{\mathbf{d}} \cdot \boldsymbol{\sigma}], \tag{2.64}$$

so that without either Zeeman coupling or SOC, j is constant in time and

$$\sigma'(\omega > 0) \neq 0 \iff \langle [j(t), j(0)] \rangle \neq 0 \iff \quad B \neq 0 \quad \text{and} \quad \lambda \neq 0. \tag{2.65}$$

Note that in the occurrence where the direction of $\mathbf{D}(k)$ depends on k, EDSR can be finite even without the static magnetic field, because in general $[\partial_k \mathbf{D}(k) \cdot \boldsymbol{\sigma}, \mathbf{D}(k) \cdot \boldsymbol{\sigma}] \neq 0$. This is the case for the 2D systems considered in Sec. 2.5.

2.3.2 1D electron gas

Quantum nanowires are commonly described using an 1DEG model with a quadratic dispersion, for which the EDSR has been studied in Ref. [98] for instance. The SOC is caused by inversion asymmetry of the system: Rashba SOC [81] and Dresselhaus SOC [82] as discussed in Sec. 1.4.

In one dimension, the SOC Hamiltonian can always be written as

$$\mathcal{H}_{\mathrm{SO}}(k) = \alpha k(\hat{\mathbf{d}} \cdot \boldsymbol{\sigma}), \tag{2.66}$$

where α and the direction $\hat{\mathbf{d}}$ depends on Rashba and Dresselhaus parameters α_R and α_D, and on the orientation of the system. For instance, for Rashba SOC only, $\hat{\mathbf{d}}$ is perpendicular to the direction of the 1D system. The full non-interacting Hamiltonian reads

$$\mathcal{H}(k) = \frac{k^2}{2m^*} + (\alpha k - b_\parallel)\hat{\mathbf{d}} \cdot \boldsymbol{\sigma} - \mathbf{b}_\perp \cdot \boldsymbol{\sigma}, \tag{2.67}$$

where we have decomposed the magnetic field into its components with respect to the SOC axis $\hat{\mathbf{d}}$, i.e, $\mathbf{b} = b_\parallel \hat{\mathbf{d}} + \mathbf{b}_\perp$ and φ is defined as the angle between $\hat{\mathbf{d}}$ and $\mathbf{b}$: $b_\parallel = b\cos\varphi$ ($b = \|\mathbf{b}\|$). The energy eigenvalues $\epsilon_\pm(k) = \epsilon_0(k) \pm \Delta(k)$ are given by

$$\epsilon_0(k) = \frac{k^2}{2m^*} \qquad \Delta(k) = \sqrt{(\alpha k - b_\parallel)^2 + \mathbf{b}_\perp^2}, \tag{2.68}$$

and the energy eigen-spinor direction $\hat{\mathbf{n}}_k$ is given by

$$\hat{\mathbf{n}}_k = \frac{(\alpha k - b_\parallel)\hat{\mathbf{d}} - \mathbf{b}_\perp}{\sqrt{(\alpha k - b_\parallel)^2 + \mathbf{b}_\perp^2}}. \tag{2.69}$$

The Fermi surface is made of two points for each branch, corresponding to right and left movers. The four Fermi momenta are denoted by $k_{r,\sigma}$, where $r = R$ (L) denotes the right (left) movers and σ labels the spin branches [see Fig. 2.2]. The effect of $\mathbf{b}_\perp$ is to split the two branches while $b_\parallel$ causes a $k \leftrightarrow -k$ reflection asymmetry.

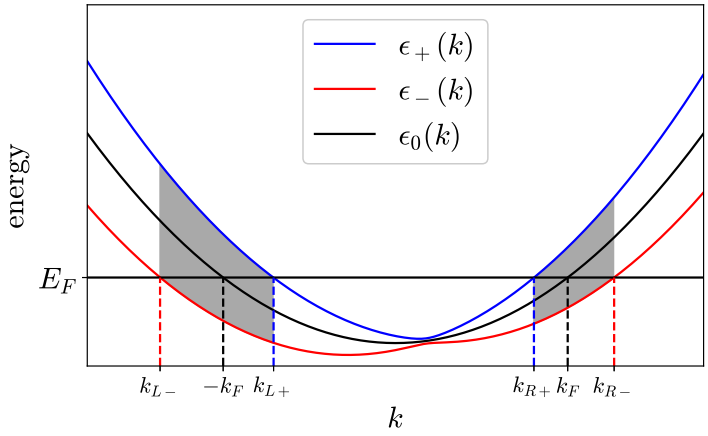

FIGURE 2.2: Sketch of the parabolic band dispersion of the 1DEG with SOC and Zeeman coupling with the different Fermi momenta indicated.

For a typical experimental setup, the Fermi energy E_F is considerably larger than the Zeeman gap and SOC gap at the Fermi surface, so that $\alpha \ll v_F$ and $b \ll E_F$, where $v_F = k_F/m^*$. Here, $k_F = \pi n/2$ (n is the electron density) is the Fermi momenta without magnetic field nor SOC which satisfies $k_F = \sqrt{2m^*E_F}$. The actual Fermi momenta differ only slightly from rk_F so that $k_{r,\sigma} = rk_F + \delta k_{r,\sigma}$. Keeping only linear terms in α/v_F and b/E_F, we have

$$k_{r,\sigma} \approx rk_F - \sigma r \frac{m^*\Delta(rk_F)}{k_F}. \tag{2.70}$$

As can be seen in Fig. 2.2, the spin resonance spectrum (for both ESR and EDSR) corresponds to momenta in the $(k_{L,-}, k_{L,+})$ and $(k_{R,+}, k_{R,-})$ intervals (shaded regions) and is thus generally made two peaks around $\omega = 2\Delta(\pm k_F)$. States in the $(k_{L,+}, k_{R,+})$ intervals are doubly occupied and do not contribute to the resonance at zero temperature. If $b_\parallel = 0$, $\Delta(k) = \Delta(-k)$ and the two peaks merge into one.

The width of the peaks scales as the square of SOC and the magnetic field, and is thus rapidly shrinking for large Fermi velocity. This can be seen more clearly in the limit of small magnetic field $b \ll \alpha k_F$. At second order in $b/\alpha k_F$, the inter-branch gap is given by

$$2\Delta(k) \approx 2\left|\alpha k - b_\parallel\right| + \frac{\mathbf{b}_\perp^2}{\left|\alpha k - b_\parallel\right|}, \tag{2.71}$$

and the Fermi momenta are approximated by

$$k_{r,\sigma} \approx rk_F - \sigma m^*\left[r\alpha - \frac{b_\parallel}{k_F} + \frac{\mathbf{b}_\perp^2}{2k_F(r\alpha k_F - b_\parallel)}\right]. \tag{2.72}$$

Because $\Delta(k)$ is a monotonic function of k near rk_F, the width δ_w of the peaks becomes

$$\delta_w = 2\left|\Delta(k_{+,r}) - \Delta(k_{-,r})\right| \approx 4m^*\frac{\alpha\Delta(rk_F)}{k_F} + O\left(\frac{b}{\alpha k_F}\right)^2 = 4m^*\alpha(\alpha - r\frac{b_\parallel}{k_F}) + O\left(\frac{b}{\alpha k_F}\right)^2. \tag{2.73}$$

Therefore, the spin transitions occur at energies centered around $2\Delta(rk_F)$ in a narrow region of width $\delta_w \ll \Delta(rk_F)$. For a smaller Fermi energy ($v_F \sim \alpha$), however, the width becomes substantial.

The intensity of the EDSR is found using Eq. (2.55). The finite contribution comes from the SOC driven current in Eq. (2.62) with $j_{\mathrm{SO}}(k) = \alpha$, and

$$\begin{aligned} \cos\phi_k = \hat{\mathbf{d}}\cdot\hat{\mathbf{n}}_k &= \frac{\alpha k - b_\parallel}{\sqrt{(\alpha k - b_\parallel)^2 + b_\perp^2}} \\ \Rightarrow \sin\phi_k &= \frac{\pm\|\mathbf{b}_\perp\|}{\sqrt{(\alpha k - b_\parallel)^2 + \mathbf{b}_\perp^2}} = \pm\frac{\|\mathbf{b}_\perp\|}{\Delta(k)}. \end{aligned} \tag{2.74}$$

The optical conductivity then reads

$$\sigma'(\omega) = \frac{4\pi\alpha^2\mathbf{b}_\perp^2}{L\omega^3}\sum_k \left(\langle n_{k-}\rangle - \langle n_{k+}\rangle\right)\delta(\omega - 2\Delta(k)), \tag{2.75}$$

and two peaks have a boxlike shape between $\omega = 2\Delta(k_{r-})$ and $\omega = 2\Delta(k_{r+})$ when $T = 0$.

Note that because the spinor direction of j_{SO} is constant, the optical conductivity is directly proportional to the spin susceptibility $\chi''(\omega)$ in the $\hat{\mathbf{d}}$ direction ($\propto \int dt\, e^{i\omega t}\langle[\hat{\mathbf{d}}\cdot\boldsymbol{\sigma}(t), \hat{\mathbf{d}}\cdot\boldsymbol{\sigma}(0)]\rangle$). In an experimental setup where the AC electric field $\tilde{\mathbf{E}}$ is directed along the wire, and the AC magnetic field $\tilde{\mathbf{B}}$ is directed along $\hat{\mathbf{d}}$, the intensities of EDSR and ESR are directly related and Eq. (2.3) holds exactly (independently of the direction of $\mathbf{b}$). The maximum ESR intensity corresponds to a setup where $\tilde{\mathbf{B}}$ is roughly perpendicular to the effective magnetic field at the Fermi momenta (i.e., perpendicular to $\hat{\mathbf{n}}_k$ at $k = \pm k_F$), in which case the ESR does not vanish even when $\mathbf{b}_\perp = 0$. Therefore, EDSR is dominant over ESR unless $\mathbf{b}_\perp \approx 0$.

The necessity of both finite α and $\mathbf{b}_\perp$ for the EDSR is explicit in Eq. (2.75). The dependence on the angle φ between the SOC direction $\hat{\mathbf{d}}$ and $\mathbf{b}$ comes through both the prefactor $\mathbf{b}_\perp^2 = b^2\sin^2\varphi$ and the resonance frequency $\omega = 2\Delta(k)$, which depends on φ even in the limit $v_F \gg \alpha, b/k_F$. Additionally, a "gap density of state" factor proportional to $|\partial_k\Delta(k)|^{-1}$ arises from the k integral. In the Zeeman limit, $\omega = 2\Delta(k) \approx 2b$ uniformly, so that the EDSR intensity depends on φ as $\sin^2\varphi$. This property was already derived from the results of Sec. 2.2 [see Eq. (2.51) and the following discussion] in the 2DEG with Landau levels by setting the magnetic field in the plane ($\theta = \pi/2$).

Later in this chapter, we derive an equation similar to Eq. (2.75) for the tight-binding model, for which we additionally plot the corresponding $\sigma'(\omega)$ for different parameters. In the next section, we introduce interaction in the model following the Tomonaga-Luttinger (TL) liquid formalism.

2.3.3 Tomonaga-Luttinger liquid

In this subsection, we consider the EDSR in the context of the TL liquid theory. The effects of interactions in a quantum wire with SOC under a magnetic field has been studied with a TL liquid approach in Refs. [99, 100]. The calculations presented in this chapter are mostly based on Ref. [38] but are more general as Tretiakov *et al.* assume the magnetic field to be much smaller than SOC and strictly perpendicular to it (i.e., $b_\parallel = 0$), which we do not. In fact, it was shown that when $b_\parallel = 0$, the system develops a spin-density wave state and is not well described by the TL liquid theory [99–101]. It is thus important to consider the situation $b_\parallel \neq 0$ in order to study EDSR in the TL liquid.

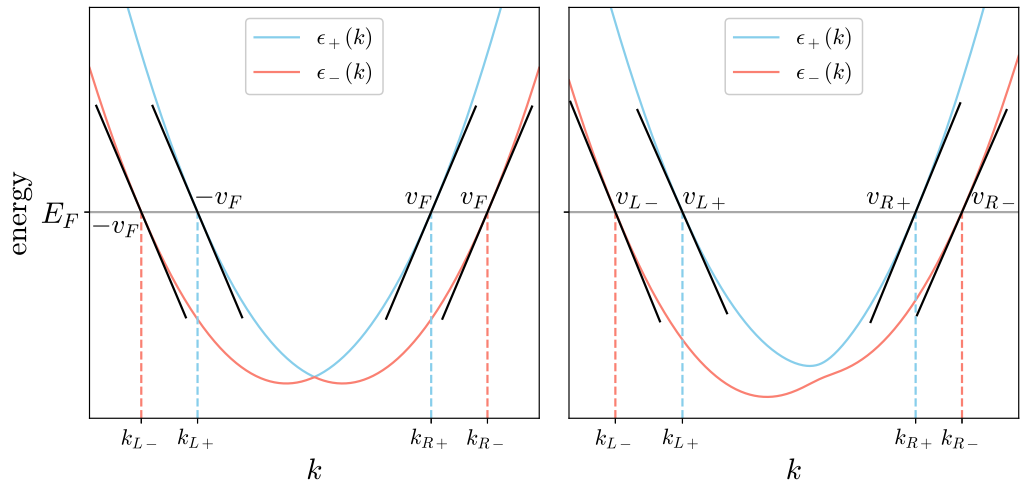

FIGURE 2.3: Linear band dispersion of the TL liquids with only SOC (left) and with both SOC and Zeeman coupling (right). The different Fermi velocities are indicated.

The TL liquid theory focuses on the low-energy properties of 1D electronic systems, and the energy dispersion is linearized around the Fermi energy. In this chapter, we assume that the basics of the TL liquid theory are known by the reader. The Hamiltonian in real space reads

$$\mathcal{H} = -iv_F \sum_\sigma \int_x dx \left(\psi^\dagger_{R,\sigma}\partial_x\psi_{R,\sigma} - \psi^\dagger_{L,\sigma}\partial_x\psi_{L,\sigma}\right) + \mathcal{H}_{\rm SO} + \mathcal{H}_{\rm Z} + \mathcal{H}_{\rm int}, \tag{2.76}$$

where v_F is the original Fermi velocity (i.e., without SOC or magnetic field), $\sigma = \uparrow, \downarrow$ labels the spin of the electron, and $r = R, L$ labels the right and left moving electrons. The SOC Hamiltonian is chosen along the z direction and the magnetic field in the xz plane,

$$\mathcal{H}_{\rm SO} = \alpha \sum_r \int_x dx \psi^\dagger_r \sigma_z \partial_x \psi_r, \tag{2.77}$$

$$\mathcal{H}_{\rm Z} = -\sum_r \int_x dx \psi^\dagger_r (b_\parallel \sigma_z + b_\perp \sigma_x)\psi_r, \tag{2.78}$$

where $\psi^\dagger_r = (\psi^\dagger_{r,\uparrow}, \psi^\dagger_{r,\downarrow})$. The interaction Hamiltonian $\mathcal{H}_{\rm int}$ is SU(2)-symmetric and contains terms quadratic in the charge densities $\rho_r = \sum_\sigma \psi^\dagger_{r,\sigma}\psi_{r,\sigma}$. Without neither $\mathcal{H}_{\rm SO}$ nor $\mathcal{H}_{\rm Z}$, the Hamiltonian is SU(2)-symmetric and there are two doubly degenerate Fermi momenta $\pm k_F$. With SOC, but without magnetic field, the Fermi momenta split into four points: $k_{r,\sigma} = rk_F - \sigma m^*$ [see Eq. (2.72)]. Moreover, the SOC Hamiltonian simply shifts the branches of the original quadratic Hamiltonian left or right depending on the spin, such that the Fermi velocity is left unaffected by SOC, and is $(-)v_F$ at both $k_{R(L),\sigma}$ Fermi momenta. The momentum splitting can be removed by a unitary transformation $T = \exp(i\sigma m k\hat{x})$ which translates k by σm. This transformation cancels the effect of SOC and restores the original SU(2) symmetry of the system. Only once $b_\perp \neq 0$, the SU(2) cannot be restored and a finite spin resonance is possible, as discussed previously. Note that in this discussion, the interaction does not play any role as it is SU(2)-invariant.

With a finite Zeeman splitting, the Fermi momenta split into four as described in Eq. (2.70). To each momentum corresponds a different eigen-spinor direction which defines the + and − bands. For a given $r = R$ or L, we furthermore assume that the difference in the Fermi momenta is small enough so that both eigen-spinors are in the same direction $\hat{\mathbf{n}}_{rk_F}$ defined in Eq. (2.69). The corresponding states are written $\psi^\dagger_{r,+}$ and $\psi^\dagger_{r,-}$.

Additionally, the Fermi velocities $v_{r,\sigma}$ split into four: one for each Fermi momenta (shown in Fig. 2.3),

$$|v_{r,\sigma}| = v_F - \alpha\sigma\left[\sqrt{(1-r\tilde{b}_\parallel)^2+\tilde{b}_\perp^2} - \frac{1-r\tilde{b}_\parallel}{\sqrt{(1-r\tilde{b}_\parallel)^2+\tilde{b}_\perp^2}}\right], \tag{2.79}$$

where $\tilde{b}_\parallel = b_\parallel/(\alpha k_F)$ and $\tilde{b}_\perp = b_\perp/(\alpha k_F)$. We also define $\delta v_r = \left|v_{r,+}\right| - \left|v_{r,-}\right|$. We see here once again that the right and left moving electrons are only symmetric when $b_\parallel = 0$ in which case $v_{R,\sigma} = v_{L,\sigma}$ and $\delta v_R = \delta v_L$. The non-interacting part of the low-energy Hamiltonian around the Fermi momenta is hence concisely written as

$$\mathcal{H}_0 = -i\sum_{r,\sigma} v_{r,\sigma}\int_x dx\left(\psi^\dagger_{r,\sigma}\partial_x\psi_{r,\sigma}\right). \tag{2.80}$$

Before performing the bosonization, let us write the optical conductivity in terms of the fermionic field. Only the SOC current

$$j_{\mathrm{SO}}(x) = \sum_r \alpha\psi^\dagger_r(x)\sigma_z\psi_r(x) \tag{2.81}$$

is responsible for the spin resonance. The time evolution of j_{SO} is akin to the evolution of σ_z and is constant unless $b_\perp \neq 0$. Indeed, all the other Hamiltonians conserve σ_z. It is now convenient to work in the spin basis $(\tilde{\sigma}_x, \tilde{\sigma}_y, \tilde{\sigma}_z)$ which satisfies $\tilde{\sigma}_z = \hat{\mathbf{n}}_{rk_F}\cdot\boldsymbol{\sigma}$ and $\sigma_z = \hat{\mathbf{n}}_{rk_F}\cdot\tilde{\boldsymbol{\sigma}}$, obtained after a π rotation along $\hat{\mathbf{n}}_{rk_F} + \hat{\mathbf{z}}$. The time evolution of j_{SO} is obtained from

$$\begin{aligned}(\hat{\mathbf{n}}_{rk_F}\cdot\tilde{\boldsymbol{\sigma}})(t) =& e^{i\Omega_r\tilde{\sigma}_z t/2}(\hat{\mathbf{n}}_{rk_F}\cdot\tilde{\boldsymbol{\sigma}})e^{-i\Omega_r\tilde{\sigma}_z t/2}\\ =&\hat{\mathbf{n}}_{rk_F}\cdot\tilde{\boldsymbol{\sigma}} + \frac{2b_\perp}{\Omega}\left[(1-\cos\Omega_r t)\tilde{\sigma}_x + \sin\Omega_r t\tilde{\sigma}_y\right]\\ =&\frac{2(\alpha r k_F - b_\parallel)}{\Omega_r}\tilde{\sigma}_z - \frac{2b_\perp}{\Omega_r}[\tilde{\sigma}_+(t) + \tilde{\sigma}_-(t)],\end{aligned} \tag{2.82}$$

where $\Omega_r = 2\Delta(rk_F)$ is the energy gap defined in Eq. (2.68) and $\tilde{\sigma}_\pm(t) = e^{\pm i\Omega_r t}\tilde{\sigma}_\pm$. We clearly identify the second term in the last line of Eq. (2.82) as the origin of the spin resonance. Finally, because we are working with a low-energy effective theory, we need to take into account the differences of Fermi momenta between the + and − branches. This is done using the unitary transformation

$$\psi^\dagger_{r,\sigma} \to e^{-i\delta k_{r,\sigma}x}\psi^\dagger_{r,\sigma} = \exp\left[i\sigma r\frac{m^*\Omega_r}{2k_F}x\right]\psi^\dagger_{r,\sigma} \equiv \exp\left[i\sigma p_r x\right]\psi^\dagger_{r,\sigma}, \tag{2.83}$$

where $p_r = r\frac{m^*\Omega_r}{2k_F}$ and we have used Eq. (2.70) for an expression for $\delta k_{r,\sigma}$. The transformation effectively shifts the Fermi momenta $k_{r,\sigma}$ to rk_F. The optical conductivity

reads

$$\sigma'(\omega) = \frac{\alpha^2}{L\omega}\sum_r \int_0^L dx \int_0^\infty dt e^{i\omega t}\frac{2b_\perp}{\Omega_r}\times \Bigg(\underbrace{\langle[\psi^\dagger_{r,+}(x,t)\psi_{r,-}(x,t),\psi^\dagger_{r,-}(0,0)\psi_{r,+}(0,0)]\rangle}_{I_{+-,-+}} e^{2ip_r x} + \underbrace{\langle[\psi^\dagger_{r,-}(x,t)\psi_{r,+}(x,t),\psi^\dagger_{r,+}(0,0)\psi_{r,-}(0,0)]\rangle}_{I_{-+,+-}} e^{-2ip_r x}\Bigg). \tag{2.84}$$

Using the standard formalism of the TL liquid theory (see, e.g., Ref. [102]), let us introduce a transformation to the bosonic operators $(\theta_c, \phi_c, \theta_s, \phi_s)$, where c stands for 'charge' and s for 'spin', defined by

$$\psi_{r,\sigma} = U_{r,\sigma}\frac{e^{irk_F}}{\sqrt{2\pi a_0}} e^{-i(r\phi_\sigma - \theta_\sigma)}, \tag{2.85}$$

where $\phi_\sigma = (\phi_c + \sigma\phi_s)/\sqrt{2}$, $\theta_\sigma = (\theta_c + \sigma\theta_s)/\sqrt{2}$, a_0 is the ultraviolet cutoff length, and $U_{r,\sigma}$ are the Klein factors which ensure the proper anticommutation relations.

After adding the interaction, the Hamiltonian reads

$$\mathcal{H} = \int \frac{dx}{2\pi}\Big[v_c K_c(\partial_x\theta_c)^2 + \frac{v_c}{K_c}(\partial_x\phi_c)^2 + v_s K_s(\partial_x\theta_s)^2 + \frac{v_s}{K_s}(\partial_x\phi_s)^2\Big] + \delta v_1[\partial_x\phi_c\partial_x\theta_s + \partial_x\phi_s\partial_x\theta_c] + \delta v_2[\partial_x\phi_c\partial_x\phi_s + \partial_x\theta_c\partial_x\theta_s], \tag{2.86}$$

where we have defined $\delta v_1 = \frac{\delta v_L - \delta v_R}{2}$ and $\delta v_2 = \frac{\delta v_L + \delta v_R}{2}$. Here c (s) stands for the charge (spin) channel, and v_c (v_s) is the velocity of plasmons (spins). The different TL liquid parameters v_s, v_c, K_c and K_s explicitly depend on the interactions [102] which we do not specify. In the non-interacting limit $\mathcal{H}_{\rm int} = 0$, they satisfy $v_c = v_s = v_{R,+}$ and $K_c = K_s = 1$. In Eq. (2.86), the terms irrelevant in the low-energy limit (as calculated with the renormalization group) when $K_c < 1$ (repulsive interaction) are neglected. Moreover, we assume that the deviations from the full SU(2) symmetry are small which is true for small SOC ($\alpha \ll v_F$) and magnetic field ($\|\mathbf{b}\|/k_F \ll v_F$). In this limit, the correction to $K_s = 1$ are of the order of $(\alpha/v_F)^2$ and $\mathbf{b}^2/(v_F k_F)^2$ [38, 103] and in the following we set $K_s = 1$.

To express the optical conductivity in terms of the bosonic operators, we define the time-ordered correlation function in imaginary time ($\tau = -it$)

$$I^T_{+-,-+}(x,\tau) = \langle T_\tau \psi^\dagger_{r,+}(x,\tau)\psi_{r,-}(x,\tau)\psi^\dagger_{r,-}(0,0)\psi_{r,+}(0,0)\rangle, \tag{2.87}$$

and a similar definition for $I^T_{-+,+-}(x,\tau)$, which are related to the retarded correlation defined in Eq. (2.84) through $I_{+-,-+}(x,t) = I^T_{+-,-+}(x,t) - [I^T_{-+,+-}(x,t)]^*$ for $t > 0$, where we used $\langle\psi^\dagger_-(0)\psi_+(0)\psi^\dagger_+(t)\psi_-(t)\rangle = [\langle\psi^\dagger_-(t)\psi_+(t)\psi^\dagger_+(0)\psi_-(0)\rangle]^*$.

Defining $Y(x,\tau) = i\sqrt{2}(r\phi_s - \theta_s)$ (hence $e^Y/(2\pi a_0) = \psi^\dagger_{r,+}\psi_{r,-}$ and $e^{-Y}/(2\pi a_0) = \psi^\dagger_{r,-}\psi_{r,+}$), we obtain

$$I^T_{+-,-+}(x,\tau) = \frac{1}{(2\pi a_0)^2}\langle T_\tau e^{Y(x,\tau)}e^{-Y(0,0)}\rangle = \frac{1}{(2\pi a_0)^2}e^{-\frac{1}{2}\langle T_\tau(Y(x,\tau)-Y(0,0))^2\rangle} \equiv \frac{1}{(2\pi a_0)^2}e^{g(x,\tau)}. \tag{2.88}$$

The second equality is true because Y is linear and the Hamiltonian is quadratic in the bosonic fields so that we can use the Wick theorem [102]. After a Fourier transform,

$$g(x,\tau) = \sum_{q,\omega} \Big[e^{i(qx-\omega\tau)} - 1\Big]\langle Y(q,\omega)Y(-q,-\omega)\rangle. \tag{2.89}$$

Similarly, we find $I^T_{+-,-+}(x,\tau) = I^T_{-+,+-}(x,\tau)$ because Y only appears squared.

Finally, the calculation of the average $\langle Y(q,\omega)Y(-q,-\omega)\rangle$ can be done using a path integral. The correlation functions of the bosonic fields are calculated through the generating functional $\mathcal{Z}[\mathbf{J}]$,

$$\begin{aligned}\mathcal{Z}[\mathbf{J}] &= \int \prod_i \mathcal{D}\Phi_i \exp\left[\int d\tau \int dx\left(-\frac{1}{2}\mathbf{\Phi}^\intercal M\mathbf{\Phi} + \mathbf{J}^\intercal\mathbf{\Phi}\right)\right] \\ &= (\det M)^{-\frac{1}{2}} \exp\left[\frac{1}{2}\mathbf{J}^\intercal M^{-1}\mathbf{J}\right],\end{aligned} \tag{2.90}$$

where $\mathbf{\Phi}^\intercal = (\phi_c,\phi_s,\theta_c,\theta_s)$ is the transpose of $\mathbf{\Phi}$, M is a 4×4 matrix which describes Lagrangian of the system, and $\mathbf{J} = (J_1,J_2,J_3,J_4)$ are extra variables. The second line of Eq. (2.90) is obtained after a Gaussian path integral. The bosonic correlation functions are calculated from the action with $\mathbf{J} = 0$,

$$\langle\Phi_i(x,\tau)\Phi_j(0,0)\rangle = \left.\frac{\partial^2 \ln\mathcal{Z}}{\partial J_i(x,\tau)\partial J_j(0,0)}\right|_{\mathbf{J}=0} = \int\frac{d\omega}{2\pi}\int\frac{dq}{2\pi}e^{i(qx-\omega\tau)}M^{-1}_{ij}(q,\omega), \tag{2.91}$$

and thus

$$\langle Y(q,\omega)Y(-q,-\omega)\rangle = -2\Big[M^{-1}_{\phi_s\phi_s} + M^{-1}_{\theta_s\theta_s} - rM^{-1}_{\phi_s\theta_s} - rM^{-1}_{\theta_s\phi_s}\Big], \tag{2.92}$$

where $r = 1(R)$ or $r = -1(L)$. The matrix M is obtained from the Euclidean action

$$S = \int d\tau\left[\int dx\left(\frac{i}{\pi}\partial_x\theta_c\partial_\tau\phi_c + \frac{i}{\pi}\partial_x\theta_s\partial_\tau\phi_s\right) - \mathcal{H}\right] \equiv \int d\tau\int dx\frac{1}{2}\mathbf{\Phi}^\intercal M\mathbf{\Phi}. \tag{2.93}$$

In the $(\phi_c,\phi_s,\theta_c,\theta_s)$ basis, we obtain

$$M(q,\omega) = \begin{pmatrix} \frac{v_c}{\pi K_c}q^2 & \frac{\delta v_2}{2\pi}q^2 & \frac{i}{\pi}q\omega & \frac{\delta v_1}{2\pi}q^2 \\ \frac{\delta v_2}{2\pi}q^2 & \frac{v_s}{\pi K_s}q^2 & \frac{\delta v_1}{2\pi}q^2 & \frac{i}{\pi}q\omega \\ \frac{i}{\pi}q\omega & \frac{\delta v_1}{2\pi}q^2 & \frac{v_cK_c}{\pi}q^2 & \frac{\delta v_2}{2\pi}q^2 \\ \frac{\delta v_1}{2\pi}q^2 & \frac{i}{\pi}q\omega & \frac{\delta v_2}{2\pi}q^2 & \frac{v_sK_s}{\pi}q^2 \end{pmatrix}. \tag{2.94}$$

The inverse of M can then be calculated[1] and expanded in powers of δv_1 and δv_2. Up to quadratic order and setting $K_s = 1$,

$$\begin{aligned} &M^{-1}_{\phi_s\phi_s} + M^{-1}_{\theta_s\theta_s} - rM^{-1}_{\phi_s\theta_s} - rM^{-1}_{\theta_s\phi_s} \\ &\quad= \frac{2\pi i}{q(r\omega+iqv_s)} - (\delta v_r)^2\left[\frac{\pi q}{4K_c}\frac{qv_c(K_c^2+1)+2irK_c\omega}{(\omega^2+q^2v_c^2)+(r\omega+iqv_s)^2}\right].\end{aligned} \tag{2.95}$$

The last step consists of integrating over q and ω to obtain $g(x,\tau)$ in Eq. (2.89). The calculation is very technical. Thus, we mostly skip it, and directly give the final result. The ω integration can be done using the residue theorem for the poles below the real line (because of the $e^{-i\omega\tau}$ factor with $\tau > 0$) which appear at $\omega = \pm iv_sq$ and $\omega = \pm iv_cq$. After performing the q integration and analytical continuation, the

[1] We used Mathematica.

main contributions come from the sum of $\ln(x \pm v_{c,s}t)$ terms with different prefactors which, once exponentiated, result in algebraic terms in $(x \pm v_{c,s}t)$ with different exponents.

Using $I_{+-,-+}(x,t) = I^T_{+-,-+}(x,t) - [I^T_{+-,-+}(x,t)]^*$ the optical conductivity for an infinitely long wire reads

$$\sigma(\omega) = C \int_{-\infty}^{\infty} dx \int_0^{\infty} dt (e^{i(\omega t - 2p_r x)} + e^{i(\omega t + 2p_r x)})[K(t + i\delta) - K(t - i\delta)], \tag{2.96}$$

where C is a constant,

$$K(t) = \frac{1}{(x - rv_c t)^{\lambda}(x + rv_c t)^{\mu}(x - rv_s t)^{\nu}}, \tag{2.97}$$

and

$$\begin{aligned}
\lambda &= (\delta v_r)^2 \frac{(K_c + 1)^2}{8K_c} \frac{1}{(v_c - v_s)^2}, \\
\mu &= (\delta v_r)^2 \frac{(K_c - 1)^2}{8K_c} \frac{1}{(v_c + v_s)^2}, \\
\nu &= 2 - (\delta v_r)^2 \frac{K_c v_c^2 + K_c v_s^2 + (K_c^2 + 1) v_c v_s}{2K_c (v_c - v_s)^2}.
\end{aligned} \tag{2.98}$$

In this form we can see that the poles in $K(t)$ at $x = \pm v_{c/s}t$ result in peaks in $\sigma'(\omega)$ at frequencies $\omega_{\text{res}} = 2|p_r|v_{c/s}$ (keeping only the positive frequencies) corresponding to spin resonance (v_s) and an extra plasmon resonance (v_c). In the non-interacting limit, $v_c = v_s$ and we recover the original resonance frequency $\omega_{\text{res}} = 2|p_r|v_s = 2\Delta(rk_F)$. In this case, the exponents satisfy $\mu = 0$ and $\lambda + \nu = 2$ so that

$$K(t) = \frac{1}{(x - rv_s t)^2}. \tag{2.99}$$

The x integral can be performed using the residue theorem. For positive ω, only the $e^{i(\omega t - 2p_r x)}$ term in $\sigma'(\omega)$ is relevant, and only the poles in the lower (upper) half-plane contribute for $r = R$ (L). In Eq. (2.96), only the $K(t - i\delta)$ term involves the poles in the appropriate half-plane and the equation becomes

$$\sigma(\omega > 0) = 4\pi C|p_r| \int_0^{\infty} e^{i(\omega - 2|p_r|v_s)} = i \frac{4\pi C|p_r|}{\omega - 2|p_r|v_s + i\gamma}, \tag{2.100}$$

where a attenuation factor $\omega \to \omega + i\gamma$ was introduced. The real part is thus a Lorentzian function and in the $\gamma \to 0$ limit,

$$\sigma'(\omega > 0) = 4\pi^2 C|p_r|\delta(\omega - 2|p_r|v_s). \tag{2.101}$$

As expected, we recover the resonance peak at the original spin resonance frequency. By comparing the expression with what we obtained in the non-interacting wire [see Eq. (2.75)] using a $(|p_r|/k_F) \times n/2$ factor (with $n = 2k_F/\pi$) for to the density of electrons in the range of momenta contributing to the spin resonance (in the TL liquid theory, they all contribute to the same $\omega = 2\Delta(rk_F)$)[2], we have

$$C = \frac{\alpha^2 \mathbf{b}_{\perp}^2}{8\pi^2 \Delta(rk_F)^3} \approx \frac{\mathbf{b}_{\perp}^2}{8\pi^2 \alpha^2 k_F}, \tag{2.102}$$

[2] This is simply equivalent to changing $\frac{1}{L}\sum_k \to \frac{1}{2\pi}\int_k dk$ in Eq. (2.75) with $\Delta(k) = \Delta(rk_F) = |p_r|v_s$.

where the approximation in the second equality is valid in the small field limit $\|\mathbf{b}\| \ll \alpha k_F$ in which case $\Delta(rk_F) \approx \alpha k_F$. With interactions, C should also depend on the cut-off length a_0 as $a_0^{\lambda+\mu+\nu-2}$ from dimensional analysis.

A similar calculation can be performed for the plasmon and spin resonances in the interacting case, but the complex integrals are more involved. We refer to Ref. [38] for the calculations. In the limit where the two resonance peaks are sufficiently distinct $|(v_c - v_s)p_r| \ll \gamma$, the spin resonance around $\omega_{\text{res,s}} = 2|p_r|v_s$ is

$$\sigma'(\omega) \approx C \frac{(2|p_r|)^{\nu-1}}{(v_c - v_s)^{\lambda}(v_c + v_s)^{\mu}\Gamma(\nu)} \frac{\gamma}{\left[(\omega - \omega_{\text{res,s}})^2 + \gamma^2\right]^{1-\frac{\lambda+\mu}{2}}}, \tag{2.103}$$

where $\Gamma(\nu)$ is the Gamma function. Hence, a significant deviation from the Lorentzian can be caused by the interactions. The optical conductivity at the plasmon resonance around $\omega_{\text{res,c}} = 2|p_r|v_c$ is

$$\sigma'(\omega) \approx C \frac{2\pi\lambda(2|p_r|)^{\lambda-1}}{(2v_c)^{\mu}(v_c - v_s)^{\nu}(2 - \mu - \nu)} \frac{\gamma}{\left[(\omega - \omega_{\text{res,c}})^2 + \gamma^2\right]^{1-\frac{\mu+\nu}{2}}}, \tag{2.104}$$

with much weaker amplitude than the spin resonance because $\lambda \propto (\delta v_r)^2$. It would thus appear as a small extra peak when $\omega_{\text{res,s}}$ and $\omega_{\text{res,c}}$ are well enough separated.

2.4 1D Hubbard model

As promised, we now consider the Hubbard model. As for the 1DEG, we study the synergetic effects of the magnetic field and the SOC on the dynamical response functions. There are two main distinctions between the Hubbard model and the electron gas. First, the continuous translation symmetry is broken by the lattice. This causes the energy dispersion to be cosine-like. Most importantly, the SOC Hamiltonian is also altered and adopts a periodic shape with the periodicity of the Brillouin zone. Therefore, the SOC current j_{SO}, responsible for the EDSR, strongly depends on the position of the Fermi energy in the band. In the limit of a quadratic dispersion, i.e., for a Fermi energy at the very bottom or very top of the band, the results (without interactions) agree with those for the electron gas. Secondly, the interaction in the Hubbard model cannot be fully understood with a TL liquid approach. In particular at half-filling, the system becomes a Mott insulator [104] for any finite repulsive interaction $U > 0$ (in 1D, there is no phase transition) due to umklapp processes. In the following, we show that the EDSR signal is strongly affected and vanish in the strongly correlated regime at half-filling because of the umklapp scattering.

The Hubbard Hamiltonian is

$$\mathcal{H} = -t \sum_i \left[\mathbf{c}_{i+1}^{\dagger}\mathbf{c}_i + \text{H.c.}\right] + U \sum_i n_{i,\uparrow} n_{i,\downarrow}, \tag{2.105}$$

where t is the transfer integral which quantifies the hopping amplitude. Moreover, the SOC and the magnetic field Hamiltonians are

$$\mathcal{H}_{\text{SO}} = i\lambda \sum_i \left[\mathbf{c}_{i+1}^{\dagger}(\hat{\mathbf{d}} \cdot \boldsymbol{\sigma})\mathbf{c}_i - \text{H.c.}\right], \tag{2.106}$$

$$\mathcal{H}_{\text{Z}} = -\sum_i \mathbf{c}_i^{\dagger}(\mathbf{b} \cdot \boldsymbol{\sigma})\mathbf{c}_i. \tag{2.107}$$

Here, $\mathcal{H}_{SO}$ is the effective SOC Hamiltonian in the lattice caused by the absence of inversion symmetry centered at the middle of the bonds [see the discussion in Sec. 1.4], λ is the SOC strength, and $\hat{\mathbf{d}}$ is the "SOC vector" (it points in the direction of the SOC internal magnetic field) and is assumed uniform throughout the system. In the following we set the lattice spacing to $a = 1$.

Let us first concentrate on the non-interacting part of $\mathcal{H}$. In the formalism of Sec. 2.3.1,

$$\epsilon_0(k) = -2t\cos(k), \tag{2.108}$$

$$\Delta(k) = \|2\lambda\sin(k)\hat{\mathbf{d}} - \mathbf{b}\| = \sqrt{(2\lambda\sin(k) - \mathbf{b}_\parallel)^2 + \mathbf{b}_\perp^2}, \tag{2.109}$$

$$\hat{\mathbf{n}}_k = \frac{2\lambda\sin(k)\hat{\mathbf{d}} - \mathbf{b}}{\Delta(k)}, \tag{2.110}$$

where, as before, the magnetic field is split into $\mathbf{b} = b_\parallel\hat{\mathbf{d}} + \mathbf{b}_\perp$ and $b_\parallel = b\cos\varphi$. As an example, Fig. 2.4 shows the dispersion relation with parameters chosen such that the effects of SOC and Zeeman splitting on the dispersion are clear ($t = 1$, $\lambda = 0.3$, $b = 0.1$, $\varphi = \pi/4$),

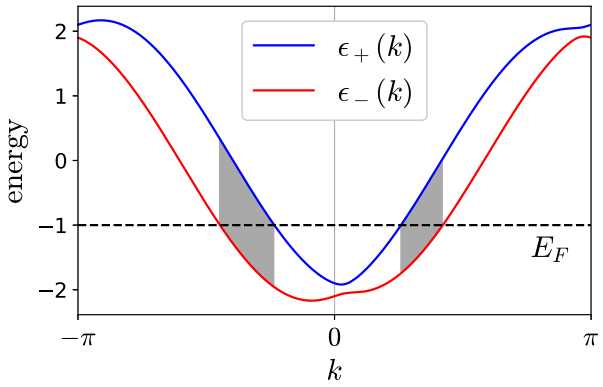

FIGURE 2.4: Dispersion relation in the 1D tight-binding model. The gap between the two lines is $2\Delta(k)$. The shaded regions correspond to momenta contributing to the optical conductivity at $T = 0$ at frequencies $\omega = 2\Delta(k)$. The parameters are $t = 1$, $\lambda = 0.3$, $b = 0.1$ and $\varphi = \pi/4$.

Due to the discrete nature of the system, the proper definition of the current operator is not obvious. Here we introduce the standard definition in the tight-binding model which is consistent with the relation $j(k) = \partial_k\mathcal{H}(k)$. A physically satisfactory definition (see, e.g., Ref. [65]) relies on the discrete lattice polarization operator

$$P = \sum_i x_i n_i, \tag{2.111}$$

where x_i is the position of site i. The current operator is then defined as the time derivative of P

$$j \equiv \dot{P} = -i[P, \mathcal{H}], \tag{2.112}$$

which satisfies a discrete continuity equation $\sum_i \partial_t n_i + \partial_x j = 0$ (some care has to be taken when defining the discrete spatial derivative ∂_x). From Eqs. (2.111) and (2.112)

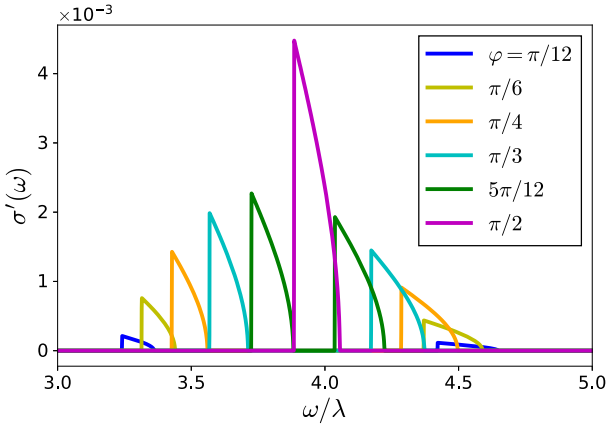

FIGURE 2.5: Optical conductivity of the tight-binding model ($U = 0$) for $t = 1$, $\lambda = 0.3$, and $b = 0.1$ at half-filling ($E_F = 0$), for different angles φ between $\mathbf{b}$ and $\hat{\mathbf{d}}$ at $T = 0$. The optical conductivity is unitless, as explained in the main text.

we get

$$j = \sum_i \left[\mathbf{c}_{i+1}^\dagger (it\sigma_0 + \lambda \hat{\mathbf{d}} \cdot \boldsymbol{\sigma}) \mathbf{c}_i\right] + \text{H.c.}, \tag{2.113}$$

where we have used the identity $[n_\alpha, c_\beta^\dagger c_\gamma] = c_\alpha^\dagger c_\gamma \delta_{\alpha\beta} - c_\beta^\dagger c_\alpha \delta_{\alpha\gamma}$. By analogy with Eq. (2.59),

$$j_K(k) = 2t \sin(k), \quad j_{SO}(k) = 2\lambda \cos(k). \tag{2.114}$$

The SO current thus depends on the crystal quasimomentum due to the periodic potential.

The EDSR, which is the only source of finite optical conductivity at $\omega > 0$ when $U = 0$, originates from j_{SO} and the optical conductivity becomes

$$\sigma'(\omega) = \frac{16\pi\lambda^2 \mathbf{b}_\perp^2}{L\omega^3} \sum_k \cos(k) \left(\langle n_{k-}\rangle - \langle n_{k+}\rangle\right) \delta(\omega - 2\Delta(k)). \tag{2.115}$$

Equation (2.115) is similar to Eq. (2.75) but with an extra $\cos(k)$ term. Figure 2.5 shows the optical conductivity at half-filling ($E_F = 0$) calculated with the same parameters as in Fig. 2.4 ($t = 1$, $\lambda = 0.3$, $b = 0.1$), for different values of φ. There are two peaks for the left and right moving electrons around $\omega_{res} = 2\Delta(\pm k_F)$, where the Fermi wave vector is now defined by $-2t\cos(k_F) = E_F$. When $\varphi = \pi/2$, the two peaks merge together as the $-k \leftrightarrow k$ symmetry is recovered. As for the 1DEG, the EDSR peaks have an intrinsic width which, for small $b \sim \lambda \ll t$, scales as $\delta_w \sim \lambda^2/t$ [see Eq. (2.73)].

A few words about the units of $\sigma'(\omega)$ plotted in Fig. 2.5 are in order. The SI unit of the optical conductivity is the siemens per meter (S/m). However, in a 1D system the current density has units of Ampere and hence the 1D optical conductivity has units of $S \cdot m$. As we set $e = 1$, $a = 1$ and $\hbar = 1$, $\sigma'(\omega)$ as defined in Eq. (2.115) is unitless. In particular, it is invariant under a rescaling of the energy. To recover the SI units, $\sigma'(\omega)$ has to be multiplied by a $e^2 a/\hbar$ factor. The usual optical conductivity (i.e., the physical one measured in three dimensions) is obtained from the 1D optical conductivity using $\sigma_{3D} = \sigma_{1D}/a_\perp^2$, where $a_\perp$ is the lattice spacing perpendicular to the chain direction of the 1D system.

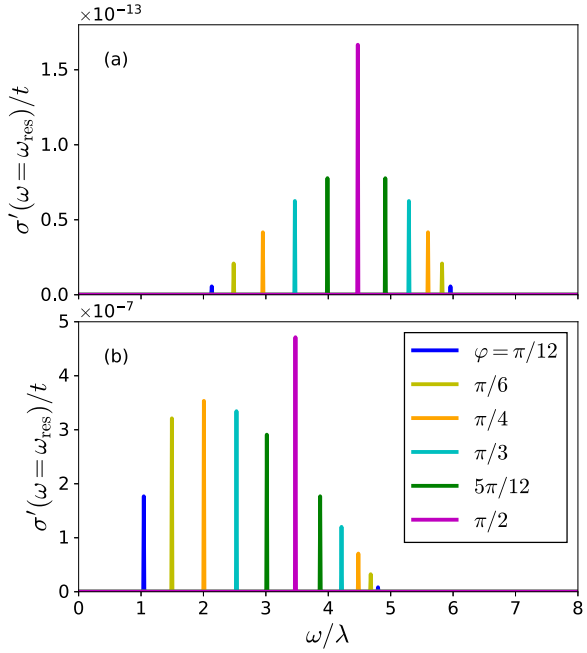

FIGURE 2.6: Optical conductivity of the tight-binding model ($U = 0$) for $\lambda/t = b/t = 10^{-3}$ at (a) half-filling and (b) quarter-filling for different angles φ between $\mathbf{b}$ and $\hat{\mathbf{d}}$ at $T = 0$. The optical conductivityis plotted in units of t since the Dirac delta function has been factored out, as explained in the main text.

We now consider the more physically realistic limit where $t \gg \lambda \sim b$ and we set $\lambda/t = b/t = 10^{-3}$ in our calculations, which corresponds to a magnetic field of ~ 1.7 T when $t = 100$ meV. In Fig. 2.6, $\sigma'(\omega)$ is plotted at half- and quarter-filling. With this set of parameters, the peaks are very narrow because all contributing momenta k roughly correspond to the same frequency $\omega_{\text{res}} = 2\Delta(\pm k_F)$ with a reasonable numerical resolution. Therefore, we factorize $\delta(\omega - \omega_{\text{res}})$ and we only show the multiplying factor, which is plotted in units of t.

The dependence of $\sigma'(\omega)$ on E_F is due to the $\cos(k)$ term in Eq. (2.115). In particular, at $E_F = 0$ (which correspond to one electron per site, or a half-filled system), the momenta contributing to resonance are close to $\pm\pi/2$ and the amplitude of the EDSR is highly suppressed due to the vanishing SO current $j_{\text{SO}}(k) \propto \cos(k)$. Otherwise, the optical conductivity behave similarly than for the continuum model, and is only non-zero when both λ and $b_\perp$ are finite.

As opposed to the free electron model, in the crystal all physical quantities are periodic in k. As a consequence, the SO current must vanish at some momenta in the Brillouin zone. In 1D, those momenta ($k = \pm\pi/2$) coincide with $\pm k_F$ at half-filling but this do not have any profound meaning (i.e., it is just a coincidence). Finally, $j_{\text{SO}}(k) \propto \cos(k)$ is suppressed at half-filling but does not completely vanish, as shown in Figs. 2.5 and 2.6. It originates from the momenta k close but not equal to k_F (between $k_{r,+}$ and $k_{r,-}$) which contribute at zero temperature.

As we show later in this chapter, this is in contrast to the 2D case where an electric-dipole-induced spin resonance is allowed by SOC even when $b = 0$ [73, 105–107]. In addition, we will see that in 2D the $\cos(k)$ term (which becomes $\cos(k_x) +$

$\cos(k_y)$ on a square lattice) has deeper implications regarding the resonance spectrum.

2.4.1 Effect of interactions

We now proceed to add the interaction term $\mathcal{H}_{\text{int}} = U \sum_i n_{i,\uparrow} n_{i,\downarrow}$ in the 1D Hubbard Hamiltonian (2.105).

We calculate the effect of interactions on the resonance using exact diagonalization in finite systems. There are four different states per site (empty, spin up, spin down, and doubly occupied). Because of the lack of SU(2) or U(1) spin symmetry, the calculations quickly become too expensive for large systems. We explicitly consider the system in two situations: (i) half-filling with 7 electrons in 7 sites, (ii) quarter-filling with 4 electrons in 8 sites. The sizes of the corresponding Hilbert spaces are 3432 for (i) and 1820 for (ii). The optical conductivity for $\omega > 0$ in the canonical ensemble is given by

$$\sigma'(\omega) = \frac{\pi}{L} \sum_{\substack{mn \\ E_m \neq E_n}} \frac{e^{-\beta E_m} - e^{-\beta E_n}}{Z} \frac{|\langle \psi_m | j | \psi_n \rangle|^2}{\omega_{mn}} \delta(\omega - \omega_{mn}), \tag{2.116}$$

where $|\psi_m\rangle$ is a many-body eigenstate with energy E_m, $\omega_{mn} = E_n - E_m$, Z is the partition function, and $\beta = 1/k_B T$ is the inverse temperature.

Lieb and Wu [108] first exactly solved the 1D Hubbard model in 1968. They proved that in the 1D Hubbard model, the ground state exhibits no conductor-insulator transition at half-filling. Instead, the system is an insulator for any $U > 0$ with a finite gap Δ_{opt} in the optical absorption. Besides, away from half-filling the system shows no optical gap for all U, and is hence metallic.

In the Hubbard model, a finite U has two effects on $\sigma'(\omega)$. First, new additional optical resonances between the ground state and excited states are allowed. The optical conductivity of the Hubbard model is a long-standing problem and has been studied to a large extent with both analytic and numerical methods at half-filling [75–78] and away from half-filling [70–72, 109, 110]. Those effects are "purely optical" in the sense that neither the SOC nor the Zeeman coupling are needed. While interesting, those effects are not the focus of this thesis. Nevertheless, in Sec. 2.4.2 we briefly consider the synergetic effects of SOC and Zeeman splitting on the high-energy optical transitions in the Mott insulating phase at half-filling. Secondly, in the Hubbard model with SOC and Zeeman splitting, interactions alter the EDSR contribution which we studied at $U = 0$. We concentrate on this effect in the present section.

The size of Δ_{opt}, the optical gap, has been calculated exactly [79] in the "bare" Hubbard model (with $\lambda = b = 0$) and approaches $\Delta_{\text{opt}} \propto \sqrt{U/t} \exp(-2\pi t/U)$ when $U \to 0$. Hence, the gap vanishes exponentially when $U \lesssim 2t$. The addition of SOC in an infinitely large system do not affect this results, as the SU(2) spin symmetry can be recovered with a gauge transformation. For a finite system with periodic boundary conditions, however, corrections are expected [111]. With the magnetic field, the expression for Δ_{opt} is not exact anymore, but is still a good approximation for small b/t.

For the numerical calculations, the parameters are set to $\lambda/t = b/t = 10^{-3}$ and the spin resonance peaks are very narrow when $U = 0$ as shown in Fig. 2.6. For the system sizes we consider, the resonances for left and right moving fermions each

correspond to a transition from the ground state to only one excited state, with amplitude and frequency determined from Eq. (2.116). Therefore, the spin resonance is characterized by its frequency ω_{res} and its peak amplitude, which both varies continuously from their $U = 0$ values.

The results at half-filling are shown in Fig. 2.7 with $\varphi = \pi/2$ (i.e., $b_{\parallel} = 0$ and there is only one peak) together with the exact value of Δ_{opt} calculated from Refs. [79, 108] in the thermodynamic limit. Interestingly, we find that in the region where the optical gap is exponentially suppressed, the amplitude increases as U gets larger. However, as soon as the optical gap reaches $\Delta_{\text{opt}} \sim t$, $\sigma'(\omega_{\text{res}})$ gets progressively smaller and tends to zero as U increases. When the optical gap reaches values similar to the kinetic hopping t, the electrons become more and more frozen in place and we naturally expect localized spins to appear and obstruct the current j_{SO} responsible for the EDSR.

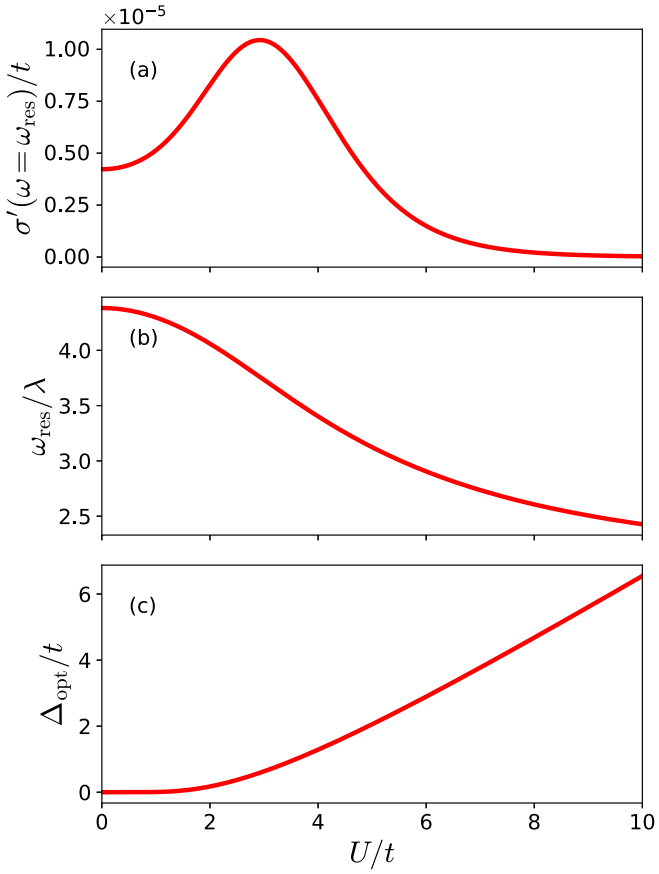

FIGURE 2.7: (a) The optical conductivity at ω_{res}, and (b) ω_{res} plotted as a function of the interaction strength U for $\varphi = \pi/2$ ($b_{\parallel} = 0$) at half-filling (7 electrons in 7 sites) with parameters $\lambda/t = b/t = 10^{-3}$. (c) The exact optical gap in the thermodynamic limit (without magnetic field) as calculated in Refs. [79, 108].

In the non-interacting models, the EDSR and the magnetic-dipole-induced ESR are closely related (and even proportional to each other in the 1D continuum model). At half-filling, their evolutions with respect to the interaction U is completely different as the spin susceptibility does not rely on the ability of the electrons to move. In Fig. 2.8, the dynamical spin susceptibility at ω_{res} is shown as a function of U where

$\phi = \pi/2$ and the direction of the corresponding AC magnetic field $\tilde{\mathbf{B}}(t)$ is chosen perpendicular to the static field $\mathbf{b}$ and either perpendicular or parallel to the SOC vector $\hat{\mathbf{d}}$. The corresponding components of the spin susceptibility are labelled $\chi_\perp(\omega)$ and $\chi_\parallel(\omega)$, respectively.

The direction of the total effective Zeeman field $\Delta(k)\hat{\mathbf{n}}_k$ (from $\mathbf{b}$ and SOC) depends on k but is in the $\mathbf{b}\hat{\mathbf{d}}$ plane. In a SU(2)-symmetric spin system with an extra U(1) symmetric Zeeman coupling, the resonance is unaffected by SU(2)-symmetric interactions [94]. In our system, SOC is defined through a spin-dependent hopping, so that the spin resonance is affected by interactions through SOC. However, when $\tilde{\mathbf{B}} \perp \hat{\mathbf{d}}$, $\hat{\mathbf{n}}_k$ is always perpendicular to $\tilde{\mathbf{B}}$ and the spin resonance is independent of the direction $\hat{\mathbf{n}}_k$ in the plane. In this case, the *amplitude* of the resonance is independent of U as can be seen in Fig. 2.8. For $\tilde{\mathbf{B}} \parallel \hat{\mathbf{d}}$, the angle between $\hat{\mathbf{n}}_k$ and $\tilde{\mathbf{B}}$ is affected by SOC and thus the amplitude of $\chi''_\parallel(\omega_{\text{res}})$ depends on U as shown in Fig. 2.8. The effect of SOC on the spins scales as $1/U$. Indeed, for sufficiently large U, the physics of the system is understood in terms of local spins with effective nearest neighbor spin interaction. In particular, the SOC contribution to the spin interactions scales as $t\lambda/U$ and takes the form of the DM interaction (the large-coupling effective spin Hamiltonian is considered in Sec. 2.4.2). Therefore, for large U, $\chi''_\parallel(\omega_{\text{res}})$ tends to the value it would have without SOC: $\chi''_\perp(\omega_{\text{res}})$. The interplay between SOC, Zeeman splitting, and interactions nevertheless results in a shift in the frequency ω_{res} of the spin resonance, as shown in Fig. 2.7(b).

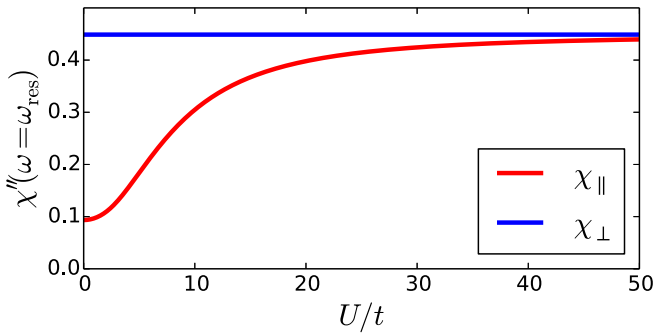

FIGURE 2.8: The magnetic susceptibility at ω_{res} is plotted as a function of the interaction strength U for $\varphi = \pi/2$ ($b_\parallel = 0$) at half-filling (7 electrons in 7 sites) with parameters $\lambda/t = b/t = 10^{-3}$. The ac magnetic field is chosen perpendicular to $\mathbf{b}$ and either parallel ($\chi_\parallel$) or perpendicular ($\chi_\perp$) to $\hat{\mathbf{d}}$.

Finally, the results for the quarter-filling case are shown in Fig. 2.9 for $\varphi = \pi/2$ ($b_\parallel = 0$, only one peak) and $\varphi = 5\pi/12$ (two peaks for left and right moving electrons). At quarter-filling, the system is gapless and the EDSR is observed even in the strongly correlated regime. As for the TL liquid, the interaction renormalizes the amplitude of the resonance. For $\varphi = \pi/2$, already for small U/t, both the amplitude and frequency ω_{res} are significantly modified. They both eventually converge to fixed values for sufficiently large U/t. For $\varphi = 5\pi/12$, the evolution of two peaks is shown in Fig. 2.9(c) and (d). In this case too, U modifies the amplitude and shifts ω_{res}. Interestingly, only one peak survives at large U/t (the one with with the smaller resonant frequency). It is unclear, however, whether this is a finite-size effect.

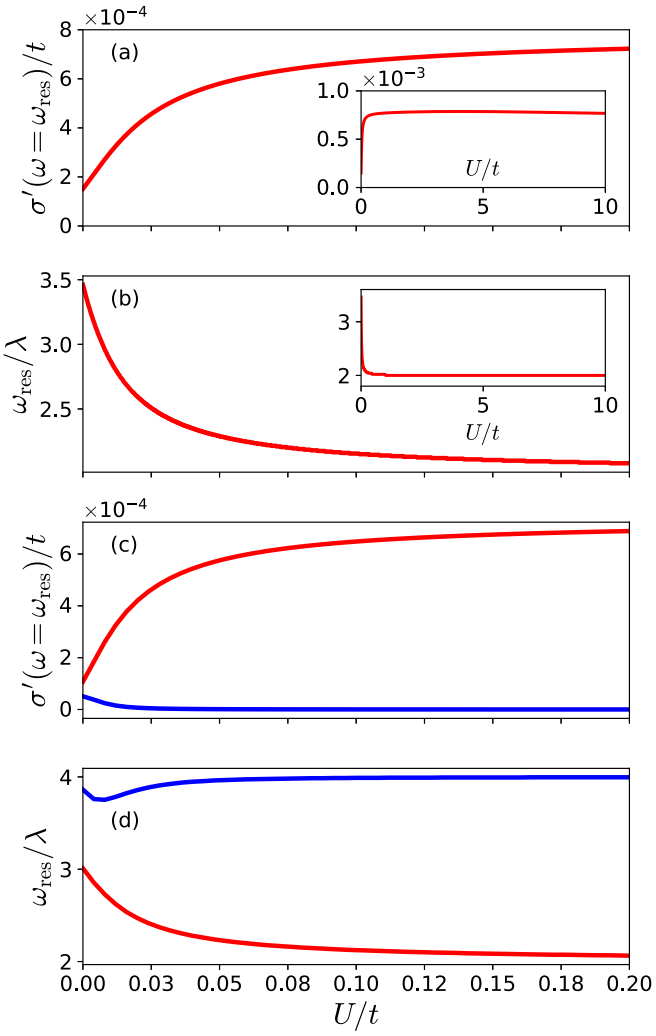

FIGURE 2.9: The optical conductivity at $\omega_{\rm res}$ and $\omega_{\rm res}$ are plotted as a function of the interaction strength U at quarter-filling (4 electrons in 8 sites) for two different values of φ with parameters $\lambda/t = b/t = 10^{-3}$. (a) and (b): The amplitude and the resonance frequency for $\varphi = \pi/2$ ($b_{\parallel} = 0$) are depicted, respectively. The insets represent the same plots in an extended region of U. (c) and (d): The amplitudes and the resonance frequencies for $\varphi = 5\pi/12$ ($b_{\parallel} \neq 0$) are depicted, respectively.

2.4.2 Large coupling limit at half-filling

In the $U/t \to \infty$ limit at half-filling, the system is a Mott insulator and the EDSR signal tends to zero due to freezing of the electrons. We will see in Chapters 3 and 4 that spin resonances at low energies, with amplitude scaling as $(t/U)^n$ for some integer n, are still possible in the Mott insulating phase under some conditions.

However, here we consider the effect of SOC and **b** on the more conventional optical excitations at the energy scale $\omega \sim U$ [75–78]. In the large U limit with $\lambda = b = 0$, the optical gap separates the so-called upper and lower Hubbard bands and is well approximated by $\Delta_{\rm opt} \simeq U - 4t + 8\ln(2)t^2/U$ [79]. The optical conductivity of the bare Hubbard model in this limit at $T = 0$ is finite at frequencies between $\omega \simeq U - 4t$

and $\omega \simeq U + 4t$ [75] corresponding to transitions from the lower band to the upper band. In the $\lambda, b \ll t \ll U$ limit, this behavior is not expected to change.

The effective spin Hamiltonian is obtained from second-order perturbation theory in the hopping (both t and λ) and reads

$$\mathcal{H}_{\text{spin}} = \mathcal{H}_{\text{ex}} - \sum_i \mathbf{b} \cdot \mathbf{S}_i, \tag{2.117}$$

$$\mathcal{H}_{\text{ex}} = \sum_i J\left(S_i^x S_{i+1}^x + S_i^y S_{i+1}^y\right) + J^z S_i^z S_{i+1}^z + \mathbf{D} \cdot (\mathbf{S}_i \times \mathbf{S}_{i+1}), \tag{2.118}$$

where

$$J = \frac{4(t^2 - \lambda^2)}{U}, \quad J^z = \frac{4(t^2 + \lambda^2)}{U}, \quad \mathbf{D} = \frac{8t\lambda}{U}\hat{\mathbf{d}}. \tag{2.119}$$

The spin z direction is defined by $S^z = \hat{\mathbf{d}} \cdot \mathbf{S}$.

The optical conductivity is obtained from the current-current correlation function $\chi_{jj}(\omega)$ using $\sigma'(\omega) = -\chi''_{jj}(\omega)/(\omega L)$. The current-current correlation function reads

$$\begin{aligned} \chi_{jj}(\omega) &= \langle\psi_0| j \frac{1}{E_0 - \mathcal{H} + \omega + i\delta} j |\psi_0\rangle \\ &= \sum_n \frac{|\langle\psi_0|j|\psi_n\rangle|^2}{E_0 - E_n + \omega + i\delta}, \end{aligned} \tag{2.120}$$

where $|\psi_0\rangle$ is the ground state of the full Hubbard Hamiltonian with energy $E_0 = O(t)$, and $|\psi_n\rangle$ are the excited states with energy $E_n = U + O(t)$, to which optical transitions from the ground state are allowed.

In order to qualitatively describe the effect of SOC and $\mathbf{b}$, we neglect corrections of the order of t/U. In this case, $\sigma'(\omega)$ becomes a delta peak at $\omega = U$ and we study its amplitude. Additionally, by neglecting the t/U contribution, the ground state is purely magnetic (there are no doubly occupied sites). Hence, we look for an effective expression of Eq. (2.120) using the spin Hamiltonian (2.117). The contribution of order t/U in E_0 and E_n are neglected and $\sigma'(\omega)$ has only one contribution at $\omega = U$. The ground state of the spin Hamiltonian (2.117) becomes $\left|\psi_0^s\right\rangle \equiv \mathcal{P}_S |\psi_0\rangle$, where $\mathcal{P}_S$ is the projection operator onto the magnetic Hilbert space.

In the $U \gg t$ limit, we then have

$$\chi_{jj}(\omega) = \left\langle\psi_0^s\right| j \frac{1}{O(t) - [U + O(t)] + \omega + i\delta} j \left|\psi_0^s\right\rangle. \tag{2.121}$$

For $U \to \infty$, $\left|\psi_0^s\right\rangle = |\psi_0\rangle$ and Eq. (2.121) holds exactly. Droping the $O(t)$ terms coming from the dispersion of the bands, we can factorize Eq. (2.121) using

$$\frac{1}{U}\mathcal{P}_S j^2 \mathcal{P}_S = -\mathcal{H}_{\text{ex}} + \text{const.}. \tag{2.122}$$

The resonance at $\omega = U$ is therefore given by

$$\sigma'(\omega) = -\pi\left(\frac{1}{L}\langle\mathcal{H}_{\text{ex}}\rangle_S - \frac{J^z}{4}\right)\delta(\omega - U), \tag{2.123}$$

where $\langle\cdot\rangle_S$ is the statistical average with respect to the spin Hamiltonian $\mathcal{H}_{\text{spin}}$ (2.117).

From Eq. (2.123), we calculated $\sigma'(\omega = U)$ for different λ and b as a function of the angle φ between $\mathbf{b}$ and $\hat{\mathbf{d}}$. The calculation was done at zero temperature using exact diagonalization. Because the Hamiltonian has translation symmetry, the Hilbert

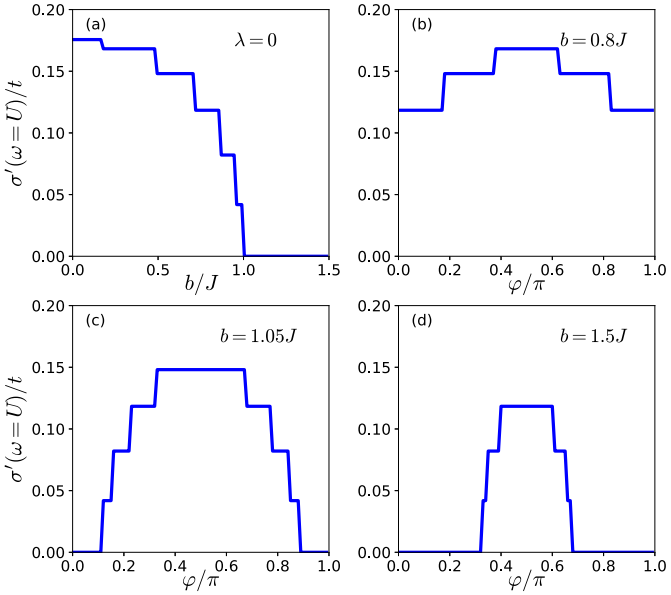

FIGURE 2.10: Optical conductivity of the effective spin model [Eq. (2.123)] for $U/t = 50$ ($J/t = 0.08$) at $\omega = U$. The multiplicative factor in front of the Dirac delta function is plotted. (a): The amplitude is shown as a function of the magnetic field b without SOC. (b), (c) and (d): The amplitude is shown as a function of φ, with SOC ($\lambda/t = 10^{-3}$), for $b = 0.8J$, $1.05J$ and $1.5J$, respectively. The calculations were made in a system of 12 spins at $T = 0$.

space can be split into subspaces characterized by different values of the total momentum, and the Hamiltonian has a block diagonal form. Using this symmetry, the exact diagonalization could be performed in systems of up to 12 sites.

The results for the 12-site system are shown in Fig. 2.10. The step-like behavior is caused by finite-size effects. First, we see that $\sigma'(\omega = U)$ vanishes for large b when $\lambda = 0$. Indeed, when b increases the system progressively becomes magnetically polarized and $\langle \mathcal{H}_{\text{ex}} \rangle_{\text{S}}$ approaches $LJ^z/4$ in Eq. (2.123). This can be understood from the Pauli principle: when all the electrons have their spin along the $\mathbf{b}$, the hopping of the electrons is impossible. Conversely, with SOC, the hopping is accompanied by a spin rotation. Therefore, for a large magnetic field $\mathbf{b}$, the Pauli principle does not completely hinder the hopping and a finite resonance is recovered. The recovery depends on the angle φ and is maximal when $\hat{\mathbf{d}}$ is perpendicular to $\mathbf{b}$. This effect is shown in Fig. 2.10(b), (c) and (d).

2.4.3 Discussion

In the present section, we considered the EDSR due to synergetic effects of SOC and magnetic field in the 1D Hubbard model. In particular, we calculated its dependence on the angle ϕ between the SOC vector $\hat{\mathbf{d}}$ and the magnetic field $\mathbf{b}$.

The system is split into two phases depending on the filling and the interaction U. First, in the metallic phase in a broad sense (i.e., zero or exponentially small Δ_{opt}), the EDSR is always expected and dominates over the magnetic-dipole-induced resonance. The resonance at $U = 0$ and its dependence on E_F, $\mathbf{b}$, and $\hat{\mathbf{d}}$ is well understood from our results. Interestingly, the interplay between SOC and Zeeman splitting has been observed experimentally in quasi-1D magnetic systems. In 1D spin systems,

the low-energy physics can be described in terms of spinons which behave very similarly to electrons in a metallic regime [112,113]. The ESR spectrum (magnetically induced in this case) splits into contributions from left and right movers depending on the angle φ consistent with our results.

Secondly, in the insulating phase at half-filling, the EDSR is progressively suppressed as the optical gap exceeds $\Delta_{\text{opt}} \gtrsim t$, which we observed using exact diagonalization. The suppression of the EDSR is directly linked to the absence of gapless spinful particles that couple to the electric field. The magnetic susceptibility is affected but not suppressed by the optical gap, and the magnetic-dipole-induced ESR does not vanish at large U.

In the strong-coupling limit at half-filling, we also investigated the optical response at $\omega_{\text{res}} \sim U$. In this energy range, the transitions are intrinsically optical but are affected by the spin of the electrons through SOC. They correspond to transitions between the lower and upper Hubbard bands separated by the optical gap. We calculated the synergetic effects of $\mathbf{b}$ and SOC on the current-current response neglecting $O(t/U)$ corrections.

2.5 2D systems

To conclude this chapter, we investigate the spin resonance in 2D systems with SOC in a static magnetic field $\mathbf{b}$. Moreover, we only consider the effects of magnetic field through the Zeeman coupling, which forces us to choose $\mathbf{b}$ in the 2D plane. The general formalism developed in Sec. 2.3.1 is also applicable in two dimensions. However, in 2D systems, the direction $\hat{\mathbf{d}}_{\mathbf{k}}$ of the SOC current explicitly depends on momentum. This has several implications that we consider in the following.

2.5.1 2D electron gas

The impact of a large SOC on the spin resonances are considerably different in 1D and 2D systems. This is understood most easily in the 2DEG. In the 1DEG, $\hat{\mathbf{d}}$ is constant and we decomposed $\mathbf{b}$ into components parallel and orthogonal to $\hat{\mathbf{d}}$. In the 2DEG with Rashba and Dresselhaus SOC, we have both $\hat{\mathbf{d}}_{\mathbf{k}}$ and $\mathbf{b}$ in the 2D plane, but their relative angle depends on $\mathbf{k}$. The SOC Hamiltonian is

$$\mathcal{H}_{\text{SO}}(k) = \mathbf{D}(\mathbf{k}) \cdot \boldsymbol{\sigma}, \qquad \text{with} \qquad \mathbf{D}(\mathbf{k}) = (\alpha_D k_x - \alpha_R k_y, \alpha_R k_x - \alpha_D k_y). \tag{2.124}$$

For a magnetic field $\mathbf{b} = (b_x, b_y)$, the two bands are then characterized by

$$\epsilon_0(\mathbf{k}) = \frac{\mathbf{k}^2}{2m^*}, \tag{2.125}$$

$$\Delta(\mathbf{k}) = \|\mathbf{D}(\mathbf{k}) - \mathbf{b}\| = \sqrt{(\alpha_D k_x - \alpha_R k_y - b_x)^2 + (\alpha_R k_x - \alpha_D k_y - b_y)^2}. \tag{2.126}$$

Figure 2.11 show the Fermi surfaces of the two branches for different Fermi energies E_F and parameters. The energy eigen-spinor direction, $\hat{\mathbf{n}}_{\mathbf{k}}$ is given by

$$\hat{\mathbf{n}}_{\mathbf{k}} = \frac{\mathbf{D}(\mathbf{k}) - \mathbf{b}}{\Delta(\mathbf{k})}. \tag{2.127}$$

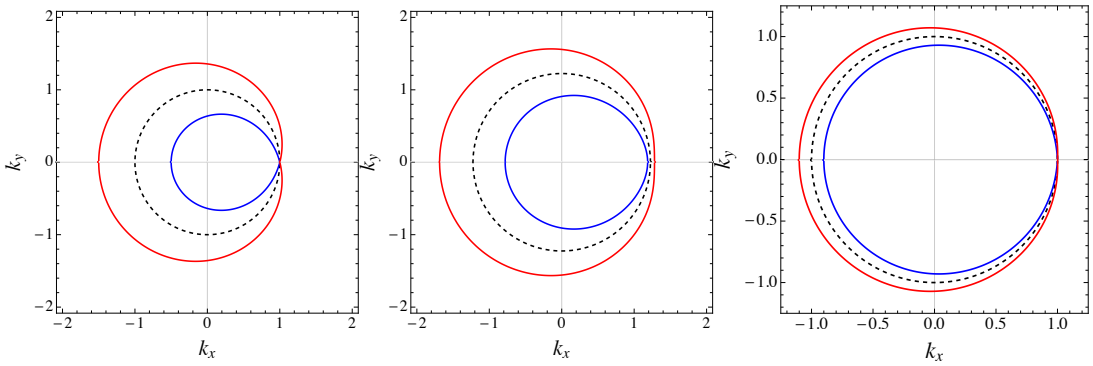

FIGURE 2.11: Fermi surfaces of the 2DEG with energy dispersions $\epsilon_+(\mathbf{k})$ (blue line) and $\epsilon_-(\mathbf{k})$ (red line). The Fermi surface $\mathcal{S}_0$ corresponding to $\epsilon_0(\mathbf{k})$ is also indicated (black dashed line). The different parameters are $\alpha_R = b_y = 1$, $\alpha_D = b_x = 0$ and $E_F = 2$, $m^* = 0.25$ (left), $E_F = 3$, $m^* = 0.25$ (middle), and $E_F = 10$, $m^* = 0.05$ (right).

Moreover, the current defined in Eq. (2.59) is now a vector in the 2D plane,

$$\begin{aligned}\mathbf{j}(\mathbf{k}) =& \boldsymbol{\nabla}_{\mathbf{k}}\epsilon_0(\mathbf{k})\sigma_0 + \boldsymbol{\nabla}_{\mathbf{k}}(\Delta(\mathbf{k})\hat{\mathbf{n}}_{\mathbf{k}})\cdot\boldsymbol{\sigma} \\ \equiv& \mathbf{j}_{\mathrm{K}}(\mathbf{k})\sigma_0 + \underbrace{\sum_{i=x,y}\left[j^i_{\mathrm{SO}}(\mathbf{k})\hat{\mathbf{d}}^i_{\mathbf{k}}\cdot\boldsymbol{\sigma}\right]\hat{\mathbf{e}}_i}_{\mathbf{j}_{\mathrm{SO}}(\mathbf{k})}.\end{aligned} \tag{2.128}$$

For the 2DEG,

$$\hat{\mathbf{d}}^x_{\mathbf{k}} = \frac{(\alpha_D, \alpha_R, 0)}{\sqrt{\alpha_R^2+\alpha_D^2}} \equiv \hat{\mathbf{d}}^x, \qquad \hat{\mathbf{d}}^y_{\mathbf{k}} = \frac{-(\alpha_R, \alpha_D, 0)}{\sqrt{\alpha_R^2+\alpha_D^2}} \equiv \hat{\mathbf{d}}^y, \quad \text{and} \tag{2.129}$$

$$j^x_{\mathrm{SO}}(\mathbf{k}) = j^y_{\mathrm{SO}}(\mathbf{k}) = \sqrt{\alpha_R^2+\alpha_D^2} \tag{2.130}$$

are all independent of $\mathbf{k}$. We note that at this point, the bold notation for vectors can represent both a vector in spin space and a vector in "real" space (i.e., a spatial vector). The context prevents any ambiguity. We also note that when considering the current $\mathbf{j}(\mathbf{k})\cdot\hat{\mathbf{u}}$ in the direction $\hat{\mathbf{u}} = (u_x, u_y)$, in general $\hat{\mathbf{d}}^u_{\mathbf{k}} \neq \hat{\mathbf{u}}\cdot(\hat{\mathbf{d}}^x_{\mathbf{k}}, \hat{\mathbf{d}}^y_{\mathbf{k}}) = u_x\hat{\mathbf{d}}^x_{\mathbf{k}} + u_y\hat{\mathbf{d}}^y_{\mathbf{k}}$. Instead we have

$$j^u_{\mathrm{SO}}(\mathbf{k})\hat{\mathbf{d}}^u_{\mathbf{k}} = \hat{\mathbf{u}}\cdot(j^x_{\mathrm{SO}}(\mathbf{k})\hat{\mathbf{d}}^x_{\mathbf{k}}, j^y_{\mathrm{SO}}(\mathbf{k})\hat{\mathbf{d}}^y_{\mathbf{k}}). \tag{2.131}$$

For the 2DEG, we have $j^x_{\mathrm{SO}} = j^y_{\mathrm{SO}}$ and thus $\hat{\mathbf{d}}^u_{\mathbf{k}}$ and $\hat{\mathbf{u}}\cdot(\hat{\mathbf{d}}^x_{\mathbf{k}}, \hat{\mathbf{d}}^y_{\mathbf{k}})$ are in the same (spin) direction. They are equal only when $\alpha_R = 0$ or $\alpha_D = 0$ so that $\hat{\mathbf{d}}^x_{\mathbf{k}}\cdot\hat{\mathbf{d}}^y_{\mathbf{k}} = 0$.

The SOC direction $\mathbf{D}(\mathbf{k})/\|\mathbf{D}(\mathbf{k})\|$ does *not* correspond to the SOC current direction $\hat{\mathbf{d}}^i_{\mathbf{k}}$ as

$$\hat{\mathbf{d}}^i_{\mathbf{k}} \equiv \frac{\partial_{k_i}\mathbf{D}(\mathbf{k})}{\left\|\partial_{k_i}\mathbf{D}(\mathbf{k})\right\|} \neq \frac{\mathbf{D}(\mathbf{k})}{\|\mathbf{D}(\mathbf{k})\|}. \tag{2.132}$$

Therefore, EDSR is possible even with $\mathbf{b} = 0$ because $\mathbf{D}(\mathbf{k}) = \sqrt{\alpha_R^2+\alpha_D^2}(k_x\hat{\mathbf{d}}^x + k_y\hat{\mathbf{d}}^y)$ so that generally

$$[\mathbf{D}(\mathbf{k})\cdot\boldsymbol{\sigma}, \hat{\mathbf{d}}^i_{\mathbf{k}}\cdot\boldsymbol{\sigma}] \neq 0, \tag{2.133}$$

and $\mathbf{j}_{\mathrm{SO}}$ has a non-trivial time evolution [73, 105–107]. The optical conductivity along a given direction $\hat{\mathbf{u}}$ is then calculated as in the 1D case from the current matrix elements $\left|\langle\mathbf{k}+|\hat{j}^u_{\mathrm{SO}}(\mathbf{k})|\mathbf{k}-\rangle\right|^2 = (j^u_{\mathrm{SO}}(\mathbf{k}))^2\sin^2\phi^u_{\mathbf{k}}$ where $\cos\phi^u_{\mathbf{k}} = \hat{\mathbf{d}}^u_{\mathbf{k}}\cdot\hat{\mathbf{n}}_{\mathbf{k}}$ and we have used

the notation $\hat{j}^u_{\rm SO}(\mathbf{k}) = j^u_{\rm SO}(\mathbf{k})\hat{\mathbf{d}}^u_{\mathbf{k}} \cdot \boldsymbol{\sigma}$. We find

$$|\langle \mathbf{k}+|\hat{j}^x_{\rm SO}(\mathbf{k})|\mathbf{k}-\rangle|^2 = \frac{1}{\Delta(\mathbf{k})^2}\Big[k_y(\alpha_R^2-\alpha_D^2)+\alpha_R b_x-\alpha_D b_y\Big]^2,$$
$$|\langle \mathbf{k}+|\hat{j}^y_{\rm SO}(\mathbf{k})|\mathbf{k}-\rangle|^2 = \frac{1}{\Delta(\mathbf{k})^2}\Big[k_x(\alpha_R^2-\alpha_D^2)+\alpha_D b_x-\alpha_R b_y\Big]^2, \tag{2.134}$$

which reduce to Eq. (2.75) in the 1D limit (e.g., in the x direction so that $k_y = 0$ and $\hat{\mathbf{d}} \propto (\alpha_D, \alpha_R)$). Note that in general, a finite optical Hall conductivity $\sigma'_{xy}(\omega)$ is also expected, originating from

$$\langle \mathbf{k}-|\hat{j}^x_{\rm SO}(\mathbf{k})|\mathbf{k}+\rangle\langle \mathbf{k}+|\hat{j}^y_{\rm SO}(\mathbf{k})|\mathbf{k}-\rangle = \hat{\mathbf{d}}^x_{\mathbf{k}}\cdot\hat{\mathbf{d}}^y_{\mathbf{k}} - (\hat{\mathbf{d}}^x_{\mathbf{k}}\cdot\hat{\mathbf{n}}_{\mathbf{k}})(\hat{\mathbf{d}}^y_{\mathbf{k}}\cdot\hat{\mathbf{n}}_{\mathbf{k}})$$
$$= -\frac{1}{\Delta(\mathbf{k})^2}\Big[k_y(\alpha_R^2-\alpha_D^2)+\alpha_R b_x-\alpha_D b_y\Big]\Big[k_x(\alpha_R^2-\alpha_D^2)+\alpha_D b_x-\alpha_R b_y\Big], \tag{2.135}$$

where the first line is true in general (as long as there is no magnetic field in the $\hat{\mathbf{z}}$ direction) and the second line is specific to the 2DEG. This is a *dissipative* Hall conductivity which is symmetric, $\sigma'_{xy}(\omega) = \sigma'_{yx}(\omega)$, and is solely a result of the anisotropy of the system. The 2DEG is anisotropic when $\mathbf{b} \neq 0$, but also when both $\alpha_R \neq 0$ and $\alpha_D \neq 0$ (even without magnetic field), in which cases the optical Hall conductivity can be finite.

In addition, there is always a proper set of basis vectors $\hat{\mathbf{e}}_1$ and $\hat{\mathbf{e}}_2$ in the xy plane such that $\sigma'_{12}(\omega) = 0$ and the optical conductivity tensor is diagonal. In particular, when either $\alpha_D = 0$ or $\alpha_R = 0$, $\sigma'_{xy}(\omega) = 0$ for a magnetic field $\hat{\mathbf{b}}$ along $\hat{\mathbf{x}}$ or $\hat{\mathbf{y}}$. From now on we consider $\alpha_D = 0$ for simplicity, unless explicitly stated.

In the limit where $\alpha_R \sim b/k_F \ll v_F$, the two Fermi surfaces are very close. In one dimension, this leads to the shrinking of the width of the peaks so that they are eventually well described with Dirac delta functions. In two dimensions, the same approximation can be done, but there remains a 1D momentum integral along the Fermi surface $\mathcal{S}_0 = \{\mathbf{k}\,, \epsilon_0(\mathbf{k}) = E_F\}$ (i.e., the Fermi surface of the system without SOC or magnetic field, see Fig. 2.11). In this approximation, the 2D optical conductivity in, say, the x direction reads,

$$\sigma'_x(\omega) = \frac{\pi}{S\omega}\sum_{\mathbf{k}} \Big|\langle \mathbf{k}+|\hat{j}^x_{\rm SO}|\mathbf{k}-\rangle\Big|^2(\langle n_{\mathbf{k}-}\rangle - \langle n_{\mathbf{k}+}\rangle)\delta(\omega - 2\Delta(\mathbf{k}))$$
$$\approx \frac{\pi}{S\omega}\sum_{\mathbf{k}\in\mathcal{S}_0} f(\mathbf{k})\Big|\langle \mathbf{k}+|\hat{j}^x_{\rm SO}|\mathbf{k}-\rangle\Big|^2\delta(\omega - 2\Delta(\mathbf{k})), \tag{2.136}$$

where S is the surface of the system and $f(\mathbf{k})$ accounts for all the momenta near $\mathbf{k} \in \mathcal{S}_0$ between the actual Fermi surfaces of the two branches which are assumed to contribute to the same frequency $\omega \approx 2\Delta(\mathbf{k})$. From Eq. (2.136), we see that there is a continuum of spin excitations with frequencies corresponding roughly to the gap $2\Delta(\mathbf{k})$ along the Fermi surface $\mathcal{S}_0$, which is simply a circle of radius $k_F = \sqrt{2m^*E_F}$ for the 2DEG. The extrema of $\Delta(\mathbf{k})$ for $\mathbf{k} \in \mathcal{S}_0$ must satisfy $\boldsymbol{\nabla}\Delta(\mathbf{k}) \cdot \hat{\mathbf{u}}_{\mathbf{k}} = 0$ where $\hat{\mathbf{u}}_{\mathbf{k}}$ is the unit vector along the Fermi surface at $\mathbf{k}$. For the 2DEG,

$$\hat{\mathbf{u}}_{\mathbf{k}} = \frac{1}{\sqrt{k_x^2+k_y^2}}\begin{pmatrix} k_y \\ -k_x \end{pmatrix}, \tag{2.137}$$

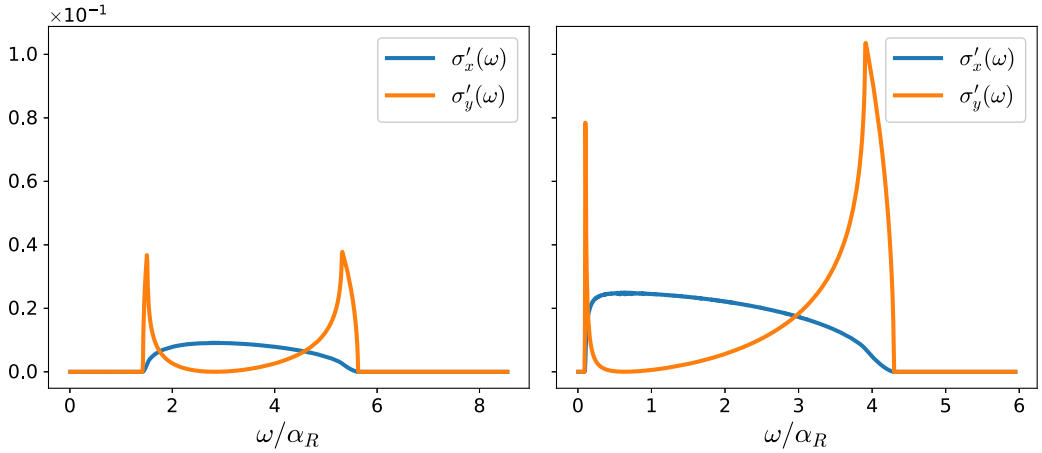

FIGURE 2.12: Optical conductivity in the x and y direction of the 2DEG with parameters $m^* = 0.05$, $\alpha_R = b_y = 1$, $b_x = 0$ and with Fermi energy $E_F = 30$ (right) and $E_F = 11$ (left), close to the compensation point $E_F = 10$ depicted in Fig. 2.11.

and thus the extrema satisfy

$$\boldsymbol{\nabla}\Delta(\mathbf{k}) \cdot \begin{pmatrix} k_y \\ -k_x \end{pmatrix} = 0. \tag{2.138}$$

The solution of Eq. (2.138) (with $\alpha_D = 0$) is the line $b_x k_x = -b_y k_y$, or $k_y = 0$ for a magnetic field along $\hat{\mathbf{y}}$. In this case, the intersections with $\mathcal{S}_0$ are $\mathbf{k} = (\pm k_F, 0)$ so that the continuum ranges between $\omega = 2\Delta((k_F, 0))$ and $\omega = 2\Delta((-k_F, 0))$, connecting the peaks from the right and left moving electrons in the 1DEG. The optical conductivity in the x and y direction is shown in Fig. 2.12.

Furthermore, in the 2DEG there are "compensation points" where $\Delta(\mathbf{k})$ vanishes and the resonance frequency ω can get arbitrarily small for the right Fermi energy [114]. This happens when the Zeeman splitting is compensated by the SOC splitting, $\alpha_R k_F = b$ (independently of the direction of $\mathbf{b}$) [see Fig. 2.11(left) and (right)].[3]

Finally, by performing the integral along $\mathcal{S}_0$ in Eq. (2.136), a "gap density of state" term arises, which can lead to Van Hove-like singularities. Those singularities also occur when $\boldsymbol{\nabla}\Delta(\mathbf{k}) \cdot \hat{\mathbf{u}}_\mathbf{k} = 0$. Therefore, singularities in the optical conductivity are expected at frequencies $\omega = 2\Delta(\mathbf{k})$ such that: (i) $\mathbf{k}$ belongs to the Fermi surface $\mathcal{S}_0$, (ii) $\mathbf{k}$ satsifies Eq. (2.138). Consequently, they show up at the edges of the continuum, as can be seen in Fig. 2.12 for $\sigma'_x(\omega)$. However, the $\hat{j}^{x/y}_{\mathrm{SO}}$ factor in Eq. (2.136) is highly anisotropic. It vanishes at the singularities for a current direction orthogonal to $\mathbf{b}$. For instance for $b_x = 0$, the singularities correspond to momenta with $k_y = 0$ and thus $\hat{j}^x_{\mathrm{SO}}$ vanishes in Eq. (2.134), which is why the singularities do not show up in $\sigma'_x(\omega)$ in Fig. 2.12. In the 2D Hubbard model, the more complex band structure creates additional singularities depending on the position of the Fermi energy in the band, as we discuss in Sec. 2.5.3.

2.5.2 Effect of interactions

Here, we briefly discuss the effect of interactions on the spin resonances in the 2DEG for completeness. We do not make any explicit calculations, but only state results

[3] Note that if the SOC is not rotationally invariant (when both $\alpha_R \neq 0$ and $\alpha_D \neq 0$), the gap can only vanish for a specific amplitude *and* direction of $\mathbf{b}$.

from the literature, mainly Refs. [95, 115]. In the absence of SOC and Zeeman splitting, the excitation spectrum has a well-known collective plasmon mode which, in two dimensions, has a $\sqrt{q}$ dispersion at small momentum q [116]. In a 2D system with SOC, there is an additional continuum of excitations at $q = 0$ which lies above the plasmon mode. As we already discussed, this continuum arises in the non-interacting system and correspond to single-particle excitations. However, the interactions create new collective modes. First, there is an extra optical plasmon mode which lies above the continuum, in addition to the usual $\sqrt{q}$ plasmon. Secondly, new spin collective modes arise [115, 117, 118], which are called "chiral-spin waves" and are solely due to SOC, and are to some extent similar to Silin-Legget modes in partially polarized Fermi liquid [115, 119], with the difference that the external magnetic field is replaced with the internal SOC field. Those collective modes were theoretically investigated by identifying the poles in the susceptibility in the charge (for plasmons) and spin (for chiral-spin waves) sectors, using for instance the RPA theory for the electron-electron interaction [115]. Due to SOC, spin collective modes also appear in the optical conductivity through EDSR.

Besides, the effect of the additional external magnetic field $\mathbf{B}$ on the spin collective modes was also studied recently [95]. As the magnitude $\|\mathbf{B}\| = B$ increases, two of the spin collective modes merge with the continuum of excitations at two critical fields. Then, at a third critical field B_c, the continuum reaches $\omega = 0$ and becomes gapless (as in the non-interacting 2DEG, when $\alpha_R k_F = g\mu_B B/2$) and hence degenerate with the remaining mode. Above B_c, there is only one collective mode with a renormalized Larmor frequency and the conventional ESR regime is reached for $B \to \infty$.

2.5.3 2D tight-binding model

Finally, we consider the non-interacting Hubbard model, or simply tight-binding model, in two dimensions. As in the 1D case, the electronic band structure is similar to the 2DEG only near the top and bottom of the band. Additionally, we now also have a choice in the lattice structure which influences the EDSR spectrum. We consider two lattices: a regular square lattice and a regular triangular lattice. In the following we calculate for each lattice: (i) the Bloch Hamiltonian, (ii) the SO current, (iii) the positions in $\mathbf{k}$-space of the Van Hove-like singularities and finally we plot the optical conductivity for different Fermi energies within the band width.

Square lattice

After a Fourier transform, the Bloch Hamiltonian is

$$\mathcal{H}(\mathbf{k}) = -2t\Big(\cos k_x + \cos k_y\Big) + 2\lambda\Big(\sin k_x \hat{\mathbf{d}}^x + \sin k_y \hat{\mathbf{d}}^y\Big)\cdot\boldsymbol{\sigma} - \mathbf{b}\cdot\boldsymbol{\sigma}, \tag{2.139}$$

where $\hat{\mathbf{d}}^{x/y}$ are defined in Eq. (2.129). We thus have

$$\begin{aligned}
\epsilon_0(\mathbf{k}) &= -2t\Big(\cos k_x + \cos k_y\Big) \\
\Delta(\mathbf{k}) &= \Big\|2\lambda\Big(\sin k_x \hat{\mathbf{d}}^x + \sin k_y \hat{\mathbf{d}}^y\Big) - \mathbf{b}\Big\| \\
\hat{\mathbf{n}}_{\mathbf{k}} &= \frac{2\lambda\Big(\sin k_x \hat{\mathbf{d}}^x + \sin k_y \hat{\mathbf{d}}^y\Big) - \mathbf{b}}{\Delta(\mathbf{k})}.
\end{aligned} \tag{2.140}$$

For the current operators, we find

$$\mathbf{j}(\mathbf{k}) = \mathbf{j}_{\mathrm{K}}(\mathbf{k}) + \Big(\underbrace{2\lambda \cos k_x \hat{\mathbf{d}}^x \cdot \boldsymbol{\sigma}}_{\hat{j}^x_{\mathrm{SO}}(\mathbf{k})}, \underbrace{2\lambda \cos k_y \hat{\mathbf{d}}^y \cdot \boldsymbol{\sigma}}_{\hat{j}^y_{\mathrm{SO}}(\mathbf{k})} \Big), \tag{2.141}$$

so that

$$\begin{aligned} \left| \langle \mathbf{k}+ | \hat{j}^x_{\mathrm{SO}}(\mathbf{k}) | \mathbf{k}- \rangle \right|^2 &= \frac{4\lambda^2}{\Delta(\mathbf{k})^2} \cos^2 k_x \Big[2\lambda \sin k_y (\bar{\alpha}_R^2 - \bar{\alpha}_D^2) + \bar{\alpha}_R b_x - \bar{\alpha}_D b_y \Big]^2, \\ \left| \langle \mathbf{k}+ | \hat{j}^y_{\mathrm{SO}}(\mathbf{k}) | \mathbf{k}- \rangle \right|^2 &= \frac{4\lambda^2}{\Delta(\mathbf{k})^2} \cos^2 k_y \Big[2\lambda \sin k_x (\bar{\alpha}_R^2 - \bar{\alpha}_D^2) + \bar{\alpha}_D b_x - \bar{\alpha}_R b_y \Big]^2, \end{aligned} \tag{2.142}$$

where $\bar{\alpha}_R = \alpha_R(\alpha_R^2 + \alpha_D^2)^{-1/2}$ and $\bar{\alpha}_D = \alpha_D(\alpha_D^2 + \alpha_D^2)^{-1/2}$ so that $\bar{\alpha}_R^2 + \bar{\alpha}_D^2 = 1$. For simplicity, we once again fix $\alpha_D = 0$ so that $\bar{\alpha}_R = 1$. Also, as for the 2DEG, a finite optical Hall conductivity is generally expected, but it vanishes when $\alpha_D = 0$ and $\mathbf{b}$ is along $\hat{\mathbf{x}}$ and $\hat{\mathbf{y}}$. Hence we do not consider it.

The most interesting point about the tight-binding model, is that because of the non-constant curvature of $\epsilon_0(\mathbf{k})$, the equation for the Van Hove-like singularities, $\boldsymbol{\nabla}\Delta(\mathbf{k}) \cdot \hat{\mathbf{u}}_{\mathbf{k}} = 0$, becomes

$$\boldsymbol{\nabla}\Delta(\mathbf{k}) \cdot \begin{pmatrix} \sin k_y \\ -\sin k_x \end{pmatrix} = 0. \tag{2.143}$$

As for the 2DEG, the line $k_y = 0$ is a solution when $b_x = 0$, but other solutions exist and additional sharp peaks are expected in the optical conductivity. For $b_x = 0$, the solutions of Eq. (2.143) are

$$\sin(k_y) = 0 \qquad \text{and} \qquad \cos(k_y) = \cos(k_x) - \frac{b_y}{2\lambda \tan(k_x)}. \tag{2.144}$$

The optical conductivity is calculated in the physical $\lambda, b \ll t$ limit (we set $t = 1000$, $\lambda = 1$, $b_x = 0$, $b_y = 1$). In the right of Fig. 2.13, we show the optical conductivity in the x and y directions for several values of $E_F \in [-W, W]$ where $W = 4t$ is half the band width. In the left of Fig. 2.13, we show a colormap of $\Delta(\mathbf{k})$ in momentum space with the Fermi surface $\mathcal{S}_0$ indicated for the corresponding E_F. Additionally, the dashed lines indicate the solutions Eq. (2.144) for the singularities. The points $\mathbf{k} = \mathbf{k}_i$ at which those lines cross $\mathcal{S}_0$ are shown as black dots, and the singularities are correctly found at $\omega = 2\Delta(\mathbf{k}_i)$, when not suppressed by the SO current factor. The corresponding peaks in $\sigma'(\omega)$ and points $\mathbf{k}_i$ are labelled accordingly. In the 1D system, the SO current factor systematically suppressed the optical conductivity at half-filling. We see in Fig. (2.143) for $E_F = 0$ that, while the singularities at $\mathbf{k}_i = (\pm\pi/2, \pm\pi/2)$ [s' and s'' in Fig. 2.13] are suppressed by the cosine term in $\hat{j}^{x/y}_{\mathrm{SO}}$, other singularities survive.

For $E_F = -0.99W$ and $-0.93W$, the Fermi energy is near the bottom of the bands and we recover the results of the 2DEG. By symmetry, this is also true at the top of the bands for $E_F \gtrless W$. In contrast to the 2DEG, there are additional compensations points for intermediate Fermi energies, e.g., at $E_F = -0.07W$. The singularities s_1 and s_2 at half-filling ($E_F = 0$) correspond to the same momentum on $\mathcal{S}_0$ but still show two close but distinct peaks in $\sigma'_y(\omega)$ due to the finite distance between the two Fermi surfaces of the actual ϵ_+ and ϵ_- bands. We thus have demonstrated that the shape of the band structure heavily influences the EDSR.

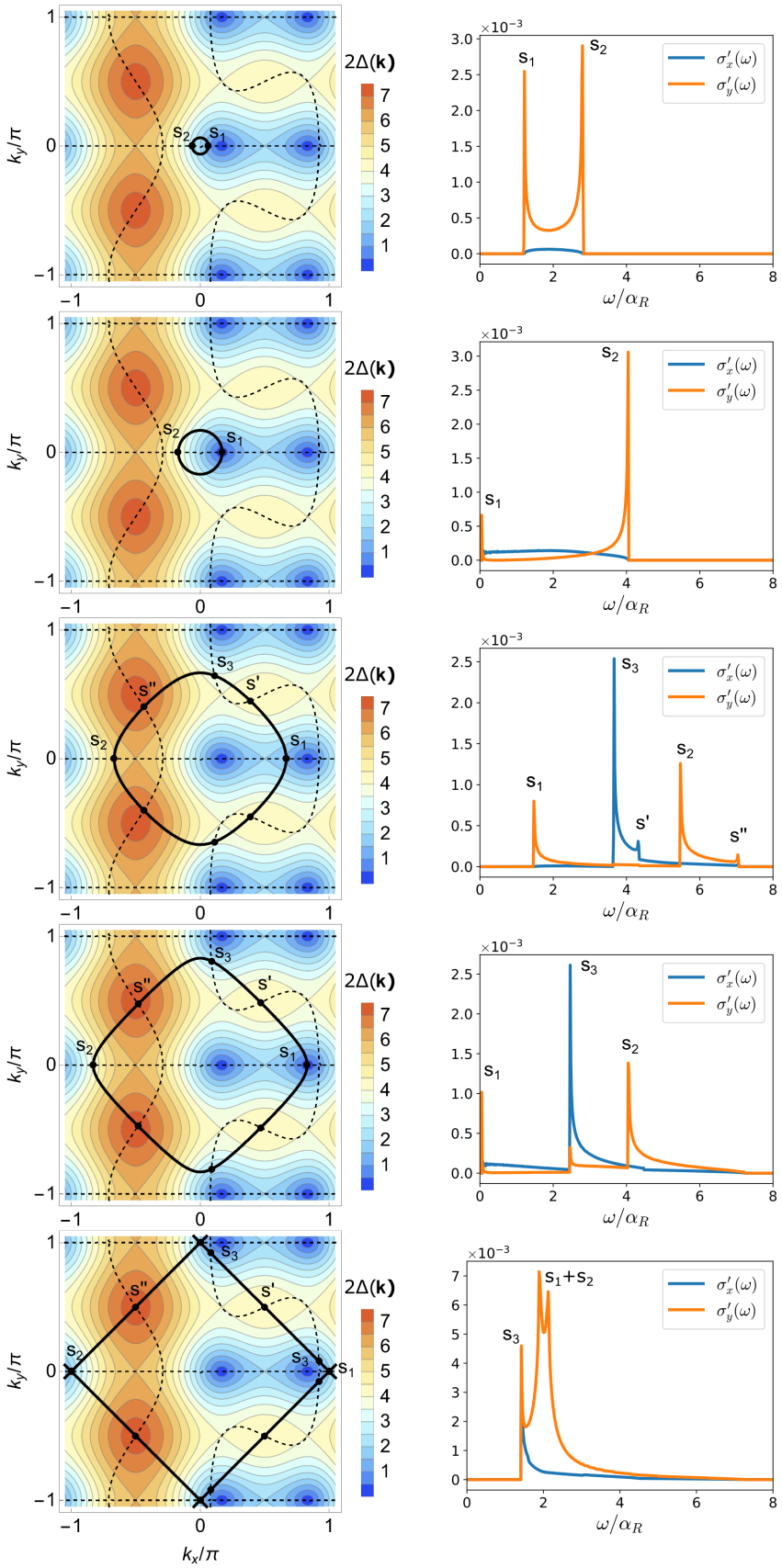

FIGURE 2.13: Left: colormap of $2\Delta(\mathbf{k})$ in the square lattice as a function of $\mathbf{k}$, Fermi surface $\mathcal{S}_0$ (black line) and solution of Eq. (2.143) (dashed line) with $t = 1000$, $\lambda = b_y = 1$, and $b_x = 0$. Right: corresponding optical conductivity in the x and y directions. Top to bottom: $E_F/W = -0.99, -0.93, -0.25, -0.07, 0$.

Triangular lattice

In the following, we finally consider the same calculations in the triangular lattice to emphasize that the spectrum depends on the band structure. The Bloch Hamiltonian in the triangular lattice is concisely written as

$$\mathcal{H}(\mathbf{k}) = -2t\sum_{i=1}^{3}\cos(\hat{\mathbf{a}}_i\cdot\mathbf{k}) + 2\lambda\sum_{i=1}^{3}\Big[\sin(\hat{\mathbf{a}}_i\cdot\mathbf{k})(\hat{\mathbf{d}}_i\cdot\boldsymbol{\sigma})\Big] - \mathbf{b}\cdot\boldsymbol{\sigma} \tag{2.145}$$

where $\hat{\mathbf{a}}_i$ are unit vectors separating nearest neighbors on the triangular lattice, the $\hat{\mathbf{d}}_i$ unit vectors correspond to the Rashba SOC and are in the 2D plane, and $\hat{\mathbf{a}}_i\cdot\hat{\mathbf{d}}_i = 0$,

$$\begin{aligned}
&\hat{\mathbf{a}}_1 = (1,0), \qquad \hat{\mathbf{a}}_2 = (\frac{1}{2},\frac{\sqrt{3}}{2}), \qquad \hat{\mathbf{a}}_3 = (\frac{1}{2},-\frac{\sqrt{3}}{2}),\\
&\hat{\mathbf{d}}_1 = (0,1), \qquad \hat{\mathbf{d}}_2 = (-\frac{\sqrt{3}}{2},\frac{1}{2}), \qquad \hat{\mathbf{d}}_3 = (\frac{\sqrt{3}}{2},\frac{1}{2}).
\end{aligned} \tag{2.146}$$

The SO current operator is

$$\mathbf{j}_{\mathrm{SO}}(\mathbf{k}) = 2\lambda\sum_{i=1}^{3}\Big[\cos(\hat{\mathbf{a}}_i\cdot\mathbf{k})(\hat{\mathbf{d}}_i\cdot\boldsymbol{\sigma})\Big]\hat{\mathbf{a}}_i. \tag{2.147}$$

The optical conductivity is calculated from the matrix elements of $\mathbf{j}_{\mathrm{SO}}(\mathbf{k})$ as previously. The results are plotted in Fig. 2.14 for $E_F = -5t$ with $\mathbf{b}$ along $\hat{\mathbf{y}}$ (top), for $E_F = 1.5t$ with $\mathbf{b}$ along $\hat{\mathbf{y}}$ (center) and along $\hat{\mathbf{x}}$ (bottom). Due to the triangular lattice structure, the spectra for a magnetic field in the $\hat{\mathbf{x}}$ and $\hat{\mathbf{y}}$ directions are not equivalent.

The singularities are once again found at momenta which solve $\boldsymbol{\nabla}\Delta(\mathbf{k})\cdot\hat{\mathbf{u}}_{\mathbf{k}} = 0$ where $\hat{\mathbf{u}}_{\mathbf{k}}$ is along the Fermi surface $\mathcal{S}_0$ so that the equation becomes

$$\boldsymbol{\nabla}\Delta(\mathbf{k})\cdot\begin{pmatrix} -\sqrt{3}\cos(k_x/2)\sin\big(\sqrt{3}k_y/2\big)\\ \sin(k_x)+\sin(k_x/2)\cos\big(\sqrt{3}k_y/2\big)\end{pmatrix} = 0. \tag{2.148}$$

The solutions to Eq. (2.148) (found numerically) are plotted in Fig. 2.14 together with the Fermi surface $\mathcal{S}_0$ and their intersections, which correspond to the Van Hove-like singularities. The different peaks in $\sigma'(\omega)$ are labelled correspondingly.

Once again, at the bottom of the band ($E_F = -5t$), the optical conductivity is similar to that of the 2DEG. For E_F in the middle of the band, here $E_F = 1.5t$, we observe multiple peaks in $\sigma'(\omega)$ whose positions depend on the direction of the magnetic field relative to the lattice. We thus conclude that the EDSR spectrum in the 2D tight-binding model is made of a continuum with singularities whose number and positions highly depend on, of course, SOC and the magnetic field, but also on the lattice structure and the Fermi energy.

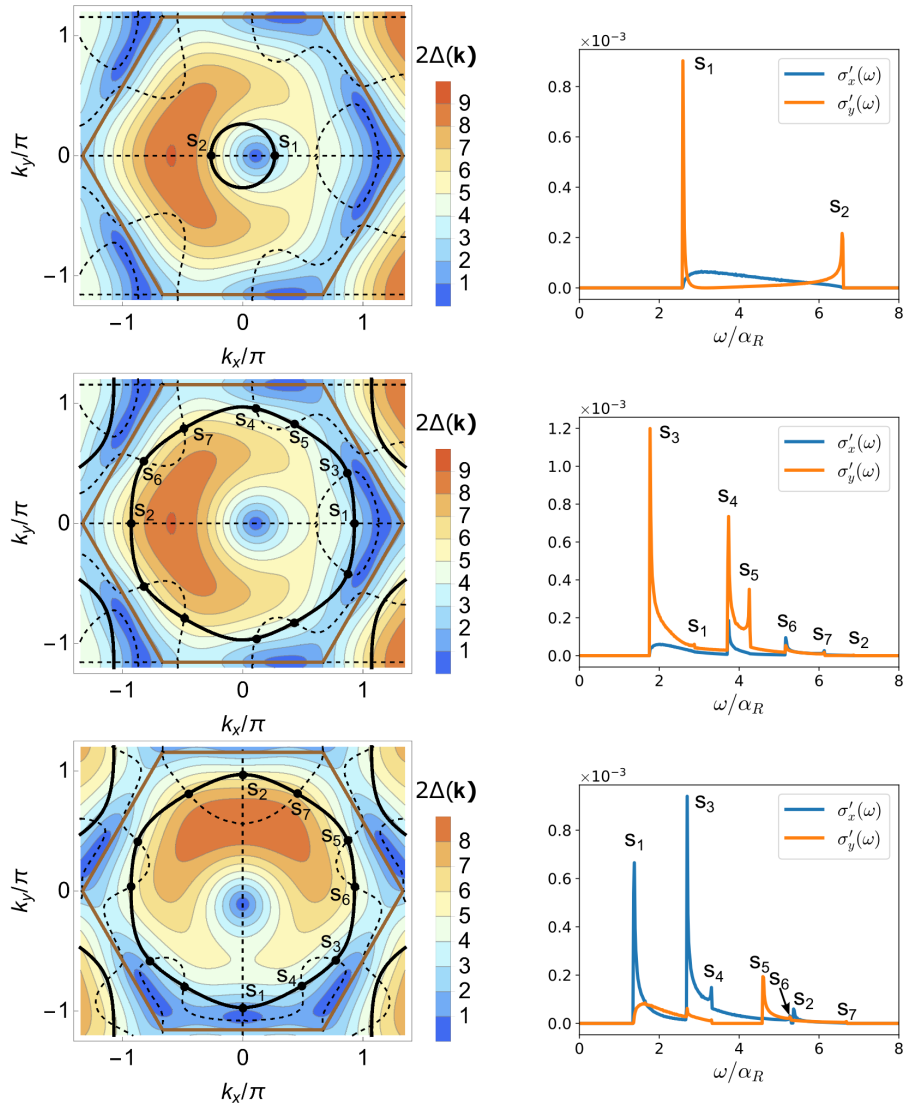

FIGURE 2.14: Left: colormap of $2\Delta(\mathbf{k})$ in the triangular lattice as a function of $\mathbf{k}$, Fermi surface $\mathcal{S}_0$ (black line), solutions of Eq. (2.148) (dashed line), and edges of the Brillouin zone (brown line). Right: corresponding optical conductivity in the x and y directions. The parameters are $t = 1000$, $\lambda = b = 1$ and top: $E_F = -5t$, $\mathbf{b} = b\hat{\mathbf{y}}$; middle: $E_F = 1.5t$, $\mathbf{b} = b\hat{\mathbf{y}}$; bottom: $E_F = 1.5t$, $\mathbf{b} = b\hat{\mathbf{x}}$.

2.6 Discussion

In this chapter, various results were presented, all concerning EDSR in 1D and 2D systems. In this final section, we emphasize what we think are the most important results.

In Secs. 2.2 and 2.3, we mostly reviewed known results as an introduction to the chapter. Nevertheless, the formalism that we introduced in Sec. 2.3 is more general that what is found in the literature. This is, in particular, because neither the magnetic field **b** nor the SOC are assumed to be small, and **b** can point in any directions. The most important results are thus found in Secs. 2.4 and 2.5 of the chapter.

In Sec. 2.4, we showed our results for the EDSR in the 1D single-band Hubbard model. First we highlighted the effects of the lattice in the non-interacting case. We showed that the EDSR spectrum strongly depends on the shape of the band structure, and on the position of the Fermi level.

We also discussed the effect of the Hubbard interaction on the EDSR. In particular, we showed using exact diagonalization that, at half-filling, when the optical gap is larger than the kinetic hopping, the umklapp scattering suppresses the EDSR.

Finally, in Sec. 2.5, we considered 2D systems with strong SOC and magnetic field. We showed that the continuous spectrum has unexpected Van Hove-like singularities, arising from the interplay between SOC and Zeeman splitting. Moreover, we showed that the optical conductivity is highly anisotropic, and that the number of singularities and their positions depend on the electronic band structure, the Fermi level, and the lattice shape.

Chapter 3

Virtual hopping effects in the Mott insulating phase

In this chapter and the following ones, we focus on the Mott insulating phase of the Hubbard model.

In band theory, the basic distinction between metals and insulators revolves around the position of the Fermi level and the corresponding filling of the electronic states. However, in 1937, transition-metal oxides with partially filled d-orbital bands were discovered, which could not be explained with band theory [120]. It was then understood that the origin of the insulating phase is the strong Coulomb repulsion. In an important work, N. F. Mott subsequently provided the theoretical foundation of how the insulating phase emerges from the electron-electron interaction [121]. The resulting insulating state is now known as the Mott insulator. Understanding of the effects of interaction in Mott insulators and the metal-insulator transition has been theoretically achieved through the Hubbard model which is now widely used to describe Mott insulators. As mentioned in Sec. 2.4.2, in the Mott insulating phase of the Hubbard model, the original electronic band (in the non-interacting limit) is split into two bands, the upper and lower Hubbard bands, separated by an energy gap of the order of the on-site Coulomb repulsion [122].

Therefore, in the strong-coupling limit, the electrons are frozen and localized at each site of the lattice. While excitations between the lower and upper Hubbard bands are optically possible (above the optical gap), the low-energy properties are described in terms of the remaining spin and orbital degrees of freedom. Thereupon, we will refer to the low-energy band as the "low-energy subspace" of the Hilbert space. For the single-band Hubbard model, in this subspace all the states have one electron per site on average. The optical response is hence expected to be featureless below the optical gap of order $\omega \sim U$. In Sec. 2.4.2, we indeed showed that the EDSR, a spin resonance in the lower band, was suppressed in the $U \to \infty$ limit because of the optical gap.

However, small charge fluctuations cannot be completely neglected due to virtual hopping of the electrons. They are, on the contrary, very important as they are the origin of the effective spin-spin interactions in magnetic Mott insulators.

Let us consider the single-band Hubbard model for electrons at half-filling (one electron per site),

$$\mathcal{H} = \mathcal{H}_{\text{hop}} + \mathcal{H}_{\text{int}} = -t \sum_{\langle i,j \rangle} \sum_{\sigma=\uparrow,\downarrow} c^{\dagger}_{i,\sigma} c_{i,\sigma} + U \sum_{i} n_{i,\uparrow} n_{i,\downarrow}. \tag{3.1}$$

Multi-orbital systems are considered in the following chapters. When $t/U = 0$ exactly, the low-energy subspace contains 2^N states $|\phi_m\rangle$, where N is the number of

sites, with exactly one electron per site which can be written as

$$|\phi_m\rangle = |\sigma_1\rangle \otimes |\sigma_2\rangle \otimes |\sigma_3\rangle \otimes \cdots \otimes |\sigma_N\rangle\,, \tag{3.2}$$

where $|\sigma_i\rangle = c^\dagger_{i,\sigma_i}|0_i\rangle$ represents a single-site state at site i with one electron with spin σ_i. Each $|\sigma_i\rangle$ state lives in a Hilbert space of dimension two and all operators acting on this Hilbert space can be written in terms of SU(2) operators: the identity operator σ_0, and the Pauli matrices σ_x, σ_y, and σ_z. All operators acting on the subspace spanned by $\{|\phi_m\rangle\}_{m=1}^{m=2^N}$ can naturally be written in terms of the spin 1/2 operators

$$\mathbf{S}_i = \frac{1}{2}\sum_{s,s'} c^\dagger_{i,s}\boldsymbol{\sigma}_{s,s'}c_{i,s'}. \tag{3.3}$$

We call the subspace spanned by the $|\phi_m\rangle$ states the "magnetic subspace". Now, the Hamiltonian (3.1) is trivial in this subspace, $\langle\phi_m|\mathcal{H}|\phi_n\rangle = 0$ for all m and n. The low-energy subspace (spanned by the exact energy eigenstates) is exactly the magnetic subspace when $t/U = 0$, and we infer that the non-trivial physics arises when we allow $t/U \gtrapprox 0$, i.e., from virtual hopping of the electron.

As t/U increases, there are 2^N eigenstates adiabatically connected to the magnetic states $|\phi_m\rangle$, which are denoted by $|\psi_m\rangle$. In the limit of small t/U each magnetic state $|\phi_m\rangle$ is indeed adiabatically transformed into a new state $|\psi_m\rangle$ which is mostly made of the pure magnetic state $|\phi_m\rangle$, but still contains a small part of states with doubly occupied sites (or "polar states"). In this limit, we thus have a one-to-one correspondence between the original magnetic states at $t = 0$ and the exact low-energy states at $t > 0$, which defines the unitary transformation $\mathbb{U}$,

$$|\phi_m\rangle \to \alpha\,|\phi_m\rangle + \beta\,|\pi_m\rangle \equiv |\psi_m\rangle = \mathbb{U}^\dagger\,|\phi_m\rangle\,, \tag{3.4}$$

where $\alpha \gg \beta$ are coefficients and $|\pi_m\rangle$ represents the polar states contained in $|\psi_m\rangle$[1]. Practically, $\mathbb{U}^\dagger$ is usually calculated up to a certain order in t/U which we treat as a perturbation. For instance, from degenerate perturbation theory at second order in t/U we have

$$\begin{aligned}|\psi_m\rangle = |\phi_m\rangle &+ \sum_\pi |\pi\rangle\,\frac{\langle\pi|\mathcal{H}_{\text{hop}}|\phi_m\rangle}{-E_\pi} + \sum_{\pi,\pi'}|\pi\rangle\,\frac{\langle\pi|\mathcal{H}_{\text{hop}}|\pi'\rangle\,\langle\pi'|\mathcal{H}_{\text{hop}}|\phi_m\rangle}{E_{\pi'}E_\pi}\\ &- \frac{1}{2}\,|\phi_m\rangle\sum_\pi\frac{\langle\phi_m|\mathcal{H}_{\text{hop}}|\pi\rangle\,\langle\pi|\mathcal{H}_{\text{hop}}|\phi_m\rangle}{E_\pi^2} + O(\frac{t^3}{U^3}),\end{aligned} \tag{3.5}$$

where $|\pi\rangle$ are polar eigenstates of $\mathcal{H}_{\text{int}}$ with energy $E_\pi = nU$ ($n > 0$), and the magnetic states $|\phi_m\rangle$ must be chosen as eigenstates of $\mathcal{H}^2_{\text{hop}}$ in the magnetic subspace. Here we have used the fact that $\langle\phi_m|\mathcal{H}_{\text{hop}}|\phi_n\rangle = 0$.

Because the magnetic states exist in a much smaller Hilbert space than the exact eigenstates $|\psi_m\rangle$, but most of the weight of the exact eigenstates belongs to the magnetic subspace, we can generally define effective operators which solely act on the

[1] Note that to be precise, Eq. (3.4) is only exact at arbitrarily high order in t/U when considering a proper basis for the magnetic subspace. Otherwise different magnetic states $|\phi_n\rangle$ might appear in $|\psi_m\rangle$ with $n \neq m$.

magnetic subspace. The resulting effective low-energy theory of the model is defined through the bijective mapping between the magnetic states and the real eigenstates. Any operator O has a unique expression in terms of spin operators, namely

$$\begin{aligned} O \to O_{\text{eff}} &= \sum_{m,n} |\phi_m\rangle\langle\psi_m| O |\psi_n\rangle\langle\phi_n| \\ &= P_0\left(\mathbb{U} O \mathbb{U}^\dagger\right) P_0, \end{aligned} \tag{3.6}$$

where P_0 is the projection operator onto the magnetic subspace. In order words, the effective operator O_{eff} is defined by identifying the matrix elements

$$\langle\phi_m|O_{\text{eff}}|\phi_n\rangle \equiv \langle\psi_m|O|\psi_n\rangle\,. \tag{3.7}$$

The most natural operator to consider is the Hamiltonian which yields the antiferromagnetic Heisenberg spin Hamiltonian at second order in $\mathcal{H}_{\text{hop}}$,

$$\mathcal{H}_{\text{eff}} = P_0 \frac{\mathcal{H}_{\text{hop}}^2}{-U} P_0 = \frac{4t^2}{U} \sum_{\langle i,j\rangle} \left(\mathbf{S}_i \cdot \mathbf{S}_j - \frac{1}{4}\right). \tag{3.8}$$

Treating the hopping Hamiltonian as a perturbation and keeping terms in O_{eff} up to order n is equivalent to study the effect of virtual hopping on loops of length up to n sites. During virtual processes, the electrons move around and can be in high-energy states until returning to a low-energy state. It is therefore natural to wonder if such virtual hopping can be the cause of electric-dipole-induced transitions within the low-energy subspace. Such processes exist if there are finite matrix elements of the electric dipole moment in the low-energy subspace. In the non-interacting models considered in Chapter 2, we considered the electric dipole moment through the current operator. This was a logical choice as both the non-interacting Hamiltonian and the current operator are diagonal when written in momentum space in terms of single-particle wave functions. This is evidently not true anymore in the strongly correlated regime. On the contrary, when treating the hopping as a perturbation, all the considered states are eigenvectors of $\mathcal{H}_{\text{int}}$ and hence eigenvectors of the number operators $n_{i,\sigma}$. As a result, it is more convenient to consider the electric dipole through the polarization operator $\sum_{i,} n_i \mathbf{r}_i$, where $\mathbf{r}_i$ is the position of site i and $n_i = n_{i,\uparrow} + n_{i,\downarrow}$. The electric polarization and current are related by a time derivative and the optical conductivity at $\omega > 0$ can be written in terms the auto-correlation function of either of those operators, as explained in Sec. 1.3.1 of Chapter 1.

That said, a word of caution is in order when dealing with a many-body system. The operator $\sum_i n_i \mathbf{r}_i$ only takes into account the charge of the electrons and thus depends on the origin used for the spatial vectors because $\sum_i n_i \neq 0$. Of course, the real system is charge neutral due to the charge of the nuclei. At half-filling, the total charge is zero when there is exactly N electrons in a system of N sites, which is always true because $\mathcal{H}$ conserves the total number of electrons. In other words, the actual total charge is $\sum_i \delta n_i = 0$ where $\delta n_i = n_i - 1$. The origin-independent polarization operator is therefore

$$\mathbf{P} = \sum_i \delta n_i \mathbf{r}_i. \tag{3.9}$$

If this operator has finite matrix elements in the low-energy subspace $\langle\psi_m|\mathbf{P}|\psi_n\rangle \neq 0$, it implies that electric-dipole-induced magnetic transitions are possible.

This problem in the single-band Hubbard model was first considered in Refs. [40, 123]. They showed that the operator $\mathbf{P}_{\text{eff}}$ is indeed non-trivial in systems on a lattice

with loops of odd number of sites, such as triangular loops for which the operator was calculated explicitly. In general, we can write

$$\mathbf{P}_{\text{eff}} = P_0\Big(\mathbb{U}O\mathbb{U}^\dagger\Big)P_0 = \sum_{n>2}(\frac{t}{U})^n\mathbf{P}^{(n)}, \tag{3.10}$$

where $\mathbf{P}^{(n)}$ is an operator acting in the magnetic space, i.e., written in terms of spin operators. The original Hubbard model (3.1) at half-filling can be equivalently written in an electron-hole symmetric way by replacing the interaction Hamiltonian with $U\sum_i n_{i,\uparrow}n_{i,\downarrow} \to (U/2)\sum_i(n_i-1)^2$, which is possible because $\sum_i \delta n_i = 0$ at half-filling. To prove that only loops with an odd number of sites, which correspond to terms with n odd in Eq. (3.10), result in non-trivial contributions to $\mathbf{P}_{\text{eff}}$, we consider the following particle-hole transformation:

$$\begin{aligned} c^\dagger_{i,\uparrow} &\to c_{i,\downarrow}, \qquad & c^\dagger_{i,\downarrow} &\to -c_{i,\uparrow}, \\ c_{i,\uparrow} &\to c^\dagger_{i,\downarrow}, \qquad & c_{i,\downarrow} &\to -c^\dagger_{i,\uparrow}. \end{aligned} \tag{3.11}$$

Under this transformation, the different operators transform in the following way,

$$\begin{aligned} \mathbf{P} &\to -\mathbf{P} \\ \mathbf{S} &\to \mathbf{S} \\ \mathcal{H}_{\text{hop}} &\to -\mathcal{H}_{\text{hop}} \\ \mathcal{H}_{\text{int}} &\to \mathcal{H}_{\text{int}}. \end{aligned} \tag{3.12}$$

In other words, the transformation maps $t \to -t$ and $U \to U$ while changing the sign of $\mathbf{P}_{\text{eff}}$ and does not affect the $\mathbf{P}^{(n)}$ operator (because their are related to spin operators). We can immediately conclude that $\mathbf{P}^{(n)} = 0$ when n is even so that the first contribution corresponds to $n = 3$.

3.1 Three-site polarization

Let us consider a system of three sites $i = 1, 2$, and 3 forming a triangle. The effective polarization in this system was derived in Ref. [40]. Because the derivation is instructive, we show here a fast way to find $\mathbf{P}_{\text{eff}}$ with perturbation theory. First of all, symmetry considerations are in order. The effective polarization operator must be written in terms of $\mathbf{S}_1$, $\mathbf{S}_2$, and $\mathbf{S}_3$. Because $\mathbf{P}_{\text{eff}}$ is even under time reversal while the spin operators are odd, only the terms $\mathbf{S}_1\cdot\mathbf{S}_2$, $\mathbf{S}_2\cdot\mathbf{S}_3$, and $\mathbf{S}_3\cdot\mathbf{S}_1$ are allowed. The polarization is a vector and it should act like one when considering the C_3 rotations and mirror symmetries of the triangle, which, in terms of spins, correspond to different permutations of $\mathbf{S}_1$, $\mathbf{S}_2$, and $\mathbf{S}_3$. It is straigthforward to show that, for the $\hat{\mathbf{x}}$ and $\hat{\mathbf{y}}$ axes fixed as shown in Fig. 3.1, the effective polarization reads

$$\mathbf{P}_{\text{eff}} = \begin{pmatrix} P_x \\ P_y \end{pmatrix} = aC\begin{pmatrix} \mathbf{S}_1\cdot(\mathbf{S}_2+\mathbf{S}_3) - 2\mathbf{S}_2\cdot\mathbf{S}_3 \\ \sqrt{3}\mathbf{S}_1\cdot(\mathbf{S}_2-\mathbf{S}_3) \end{pmatrix}, \tag{3.13}$$

where a is the distance between sites and C is a constant that we calculate shortly. Henceforth we set $a = 1$.

For three spins 1/2, the total spin is either $S_{\text{tot}} = 1/2$ or $S_{\text{tot}} = 3/2$. In the latter case, the state is C_3 symmetric and we must have $\mathbf{P}_{\text{eff}} = 0$, which is satisfied by Eq. (3.13) because we have $\mathbf{S}_1\cdot\mathbf{S}_2 = \mathbf{S}_2\cdot\mathbf{S}_3 = \mathbf{S}_3\cdot\mathbf{S}_1$. The $S_{\text{tot}} = 1/2$ subspace contains,

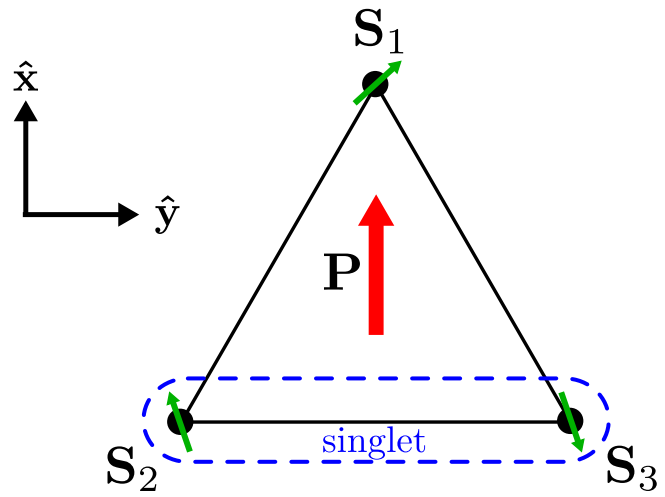

FIGURE 3.1: Triangle-shaped three-site system in a low-energy $S_{\text{tot}} = 1/2$ state with non-zero polarization $\mathbf{P}$ due to the finite hopping between the sites. The spin operators $\mathbf{S}_i$ ($i \in \{1, 2, 3\}$) refer to the purely magnetic state (a ground state when $t = 0$) adiabatically connected to the actual energy eigenstate when $t \neq 0$.

for instance, states with a singlet one bond and an unentangled spin 1/2 on the remaining site. Such states have a net polarization in the direction perpendicular to the singlet bond, as shown in Fig. 3.1.

Let us now calculate the constant C. In the triangle, $\mathbf{P} = \delta n_1 \mathbf{r}_1 + \delta n_2 \mathbf{r}_2 + \delta n_3 \mathbf{r}_3$, where $\mathbf{r}_i$'s are the positions of the three sites, such that $\mathbf{P}_{\text{eff}} = \delta n_{1,\text{eff}} \mathbf{r}_1 + \delta n_{1,\text{eff}} \mathbf{r}_2 + \delta n_{1,\text{eff}} \mathbf{r}_3$ where, from the symmetry considerations,

$$\delta n_{1,\text{eff}} = \frac{2C}{\sqrt{3}} (\mathbf{S}_1 \cdot (\mathbf{S}_2 + \mathbf{S}_3) - 2\mathbf{S}_2 \cdot \mathbf{S}_3), \tag{3.14}$$

and the expressions for $\delta n_{2,\text{eff}}$ and $\delta n_{3,\text{eff}}$ are obtained using cyclic permutations. The magnetic state depicted in Fig. 3.1 has a spin singlet on the 2-3 bond and is thus *symmetric* under the permutation of sites 2 and 3, so that it overall satisfies the Fermionic statistics[2]. The corresponding state with $\sigma = \uparrow$ at site 1 is given by

$$|\phi\rangle = \frac{1}{\sqrt{2}} \left(c^\dagger_{1,\uparrow} c^\dagger_{2,\uparrow} c^\dagger_{3,\downarrow} - c^\dagger_{1,\uparrow} c^\dagger_{2,\downarrow} c^\dagger_{3,\uparrow} \right) |0\rangle \,, \tag{3.15}$$

which is an exact eigenstate when $t = 0$. For finite t, we need to calculate the exact eigenstate $|\psi\rangle$ keeping terms up to third order in t/U in Eq. (3.5), which is quite cumbersome. However, the symmetries of the Hamiltonian can be used to simplify the calculation. Only exited states with two $\uparrow$ spins and one $\downarrow$ spin, which are also symmetric under the permutation of sites 2 and 3, are contained in $|\psi\rangle$:

$$|\psi\rangle = \alpha_0 |\phi\rangle + \sum_{i=1}^{3} \alpha_i |\pi_i\rangle \,, \tag{3.16}$$

[2]For some reason, in Ref. [40] they state that this state is antisymmetric under exchange. The final result is, however, the same.

where $\sum_{i=0}^{3}\alpha_i^2 = 1$ and[3]

$$
\begin{aligned}
|\pi_1\rangle &= \frac{1}{\sqrt{2}}\left(c^\dagger_{1,\uparrow}c^\dagger_{2,\uparrow}c^\dagger_{2,\downarrow} + c^\dagger_{1,\uparrow}c^\dagger_{3,\uparrow}c^\dagger_{3,\downarrow}\right)|0\rangle\,,\\
|\pi_2\rangle &= \frac{1}{\sqrt{2}}\left(c^\dagger_{1,\uparrow}c^\dagger_{1,\downarrow}c^\dagger_{2,\uparrow} + c^\dagger_{1,\uparrow}c^\dagger_{1,\downarrow}c^\dagger_{3,\uparrow}\right)|0\rangle\,,\\
|\pi_3\rangle &= \frac{1}{\sqrt{2}}\left(c^\dagger_{2,\uparrow}c^\dagger_{3,\uparrow}c^\dagger_{3,\downarrow} + c^\dagger_{2,\uparrow}c^\dagger_{2,\downarrow}c^\dagger_{3,\uparrow}\right)|0\rangle\,,
\end{aligned}
\tag{3.17}
$$

so that $\langle\psi|\delta n_1|\psi\rangle = \alpha_2^2 - \alpha_3^2$. The coefficients α_{0-3} are expanded as

$$
\begin{aligned}
\alpha_0 &= 1 + \sum_{n=1}^{\infty} a_n(\frac{t}{U})^n, \qquad & \alpha_1 &= \sum_{n=1}^{\infty} b_n(\frac{t}{U})^n,\\
\alpha_2 &= \sum_{n=1}^{\infty} c_n(\frac{t}{U})^n, & \alpha_3 &= \sum_{n=1}^{\infty} d_n(\frac{t}{U})^n
\end{aligned}
\tag{3.18}
$$

and the coefficients can be determined up to arbitrarily high order in (t/U) by calculating the eigenstates of the Hamiltonian in the subspace spanned by $\{|\phi\rangle, |\pi_1\rangle, |\pi_2\rangle, |\pi_3\rangle\}$:

$$
\mathcal{H} = \begin{pmatrix} 0 & -2t & t & t\\ -2t & U & t & -t\\ t & t & U-t & 0\\ t & -t & 0 & U+t \end{pmatrix}.
\tag{3.19}
$$

By solving $\mathcal{H}\mathbf{v} = \epsilon\mathbf{v}$ where $\mathbf{v} = (\alpha_0, \alpha_1, \alpha_2, \alpha_3)$ together with $\|\mathbf{v}\| = 1$ up to second order in t/U, we find

$$
\begin{aligned}
\alpha_0 &= 1 - 3\frac{t^2}{U^2} + O\left(\frac{t^3}{U^3}\right), \qquad & \alpha_1 &= 2\frac{t}{U} + O\left(\frac{t^3}{U^3}\right),\\
\alpha_2 &= -\frac{t}{U} - 3\frac{t^2}{U^2} + O\left(\frac{t^3}{U^3}\right), & \alpha_3 &= -\frac{t}{U} + 3\frac{t^2}{U^2} + O\left(\frac{t^3}{U^3}\right),\\
\epsilon &= -6\frac{t^2}{U^2} + O\left(\frac{t^3}{U^3}\right).
\end{aligned}
\tag{3.20}
$$

Finally, using Eq. (3.14) and the fact that $(\mathbf{S}_1\cdot(\mathbf{S}_2+\mathbf{S}_3) - 2\mathbf{S}_2\cdot\mathbf{S}_3)\,|\phi\rangle = 3/2\,|\phi\rangle$, we have

$$
\sqrt{3}C = \langle\phi|\delta n_{1,\text{eff}}|\phi\rangle = \langle\psi|\delta n_1|\psi\rangle = \alpha_2^2 - \alpha_3^2 = 12\frac{t^3}{U^3} + O\left(\frac{t^5}{U^5}\right),
\tag{3.21}
$$

and the constant in Eq. (3.13) is $C = 4\sqrt{3}t^3/U^3 + O\left(t^5/U^5\right)$.

How does this relation between spins and electric polarization affect the spin resonance? In the different systems investigated in Chapter 2, the single-particle SO current operator, which is responsible for the spin resonance, is directly proportional to the spin operator of each electron. As a result, the frequencies of the resonance is the same for both the electric-dipole-induced spin resonance and the standard magnetic-dipole-induced ESR.

This is the most important difference between the results of Chapter 2, intrinsically originating from the physics of non-interactions electrons, and the phenomenon

[3] In the Appendix of Ref. [40], they use the antisymmetric states with a − sign but eventually obtain the same expressions.

considered in the present chapter. The many-body effects dictate the effective magnetic theory, within which the electric dipole moment can also have finite matrix elements, as shown by Eq. (3.13). In the low-energy subspace, the electric polarization, originally a single-particle operator, becomes a multi-spin operator. Therefore, it enables new magnetic transitions (i.e., transitions within the low-energy subspace) through the fluctuating electric dipole moment of the electrons. In other words, the spin resonance induced by electric dipoles and magnetic dipoles can have different frequencies.

This is most simply seen in the three-site system discussed above. For the antiferromagnetic Heisenberg model, the four degenerate ground states have $S_{\text{tot}} = 1/2$. The quartet is described with an $S^z = \pm 1/2$ quantum number and an additional pseudospin variable. The states are labelled $|S^z, \tau^z\rangle$ where τ^z is commonly chosen to be the spin chirality operator

$$\tau^z = \frac{2}{\sqrt{3}}(\mathbf{S}_1 \times \mathbf{S}_2) \cdot \mathbf{S}_3, \tag{3.22}$$

which has eigenvalues $\pm 1/2$ in the $S_{\text{tot}} = 1/2$ manifold. Moreover, it closes an SU(2) algebra with

$$\begin{aligned} \tau^x &= \frac{1}{3}[2\mathbf{S}_2 \cdot \mathbf{S}_3 - \mathbf{S}_1 \cdot (\mathbf{S}_2 + \mathbf{S}_3)] \propto P_x \\ \tau^y &= \frac{1}{3}\Big[\sqrt{3}\mathbf{S}_1 \cdot (\mathbf{S}_2 - \mathbf{S}_3)\Big] \propto P_y. \end{aligned} \tag{3.23}$$

Therefore, magnetic dipole transitions are possible between $|\downarrow, \tau^z\rangle$ and $|\uparrow, \tau^z\rangle$ and electric dipole transitions are possible between $|S^z, -\rangle$ and $|S^z, +\rangle$, where we have labelled $S^z = \uparrow, \downarrow$ and $\tau^z = \pm$. In some real systems, such as the molecular magnet V_{15} [124], the degeneracy of the quartet is lifted by, for instance, the symmetry-allowed DM interaction between the spins: $\sum_{i,j} D_z(\mathbf{S}_i \times \mathbf{S}_j)_z$. In this case, the $S_{\text{tot}} = 1/2$ manifold is split into two doublets, $\{|\uparrow, +\rangle, |\downarrow, -\rangle\}$ and $\{|\uparrow, -\rangle, |\downarrow, +\rangle\}$, with an energy gap $\Delta = \sqrt{3}D_z$ [40]. As a consequence, transitions caused by both and AC electric field and an AC magnetic field have the same absorption frequency $\omega = \Delta$. However, with the addition of a static magnetic field $\mathbf{B} = B_z\hat{\mathbf{z}}$ perpendicular to the triangle, all four states have different energies and the magnetic-dipole-induced (MD-induced) and electric-dipole-induced (ED-induced) spin resonance correspond to different frequencies, as pictured in Fig. 3.2

We should nonetheless add that this simple analysis of the phenomenon lacks the following consideration. The polarization operator is an effective operator and any changes in the Hamiltonian will also modify $\mathbf{P}_{\text{eff}}$, such as the DM interaction and the magnetic field mentioned above. For instance, it was shown in Refs. [125, 126] that with the addition of the spin-dependent hopping due to SOC, (which leads to the DM term in the spin Hamiltonian), the effective polarization on the triangle itself has extra terms including spin-antisymmetric $\mathbf{S}_i \times \mathbf{S}_j$ terms. The above analysis of the electric-dipole-induced resonance frequency is thus only sound when the extra terms causing the splitting are small.

An important remark is that the effective polarization was derived from an inversion-symmetric Hamiltonian, which might be counter intuitive. Indeed, the polarization, as a vector, should vanish in a system with inversion symmetry. There are two scenarios to consider in order to understand the role of $\mathbf{P}_{\text{eff}}$. First, in a system with unbroken inversion symmetry, all states are either even or odd with respect to the

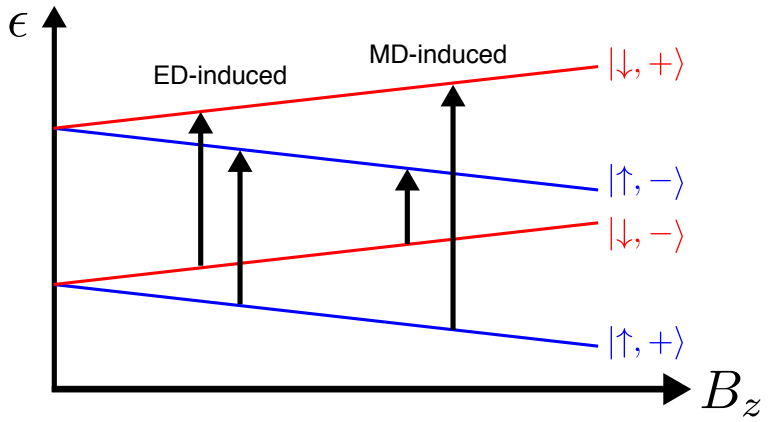

FIGURE 3.2: Energy levels of the four states in the $S_{\text{tot}} = 1/2$ ground state manifold of a three-spin triangle system with finite DM interaction as a function of an applied static magnetic field in the z direction. The allowed ED-induced and MD-induced resonances are indicated with black arrows. Figure adapted from Ref. [40].

symmetry. In such a system, the expectation value of **P**, and all the diagonal elements $\langle\psi_i|\mathbf{P}|\psi_i\rangle$, where $|\psi_i\rangle$ is an energy eigenstate, vanish. However, the polarization as a quantum operator has off-diagonal matrix elements between states of different parity. Its importance hence lies in the dynamical properties of the system, and it affects the response functions. Secondly, in some systems the inversion symmetry is spontaneously broken, for instance by a specific magnetic order, and the expectation value of **P** can be finite even in the ground state.

The latter case is a well-known phenomenon in multiferroics, materials exhibiting both ferromagnetism and ferroelectricity. The magnetoelectric (ME) coupling, i.e., coupling between the spins and the electric polarization, described by Eq. (3.13) has been studied intensively in systems with triangular spin trimers. The emergence of a finite electric polarization was predicted in different systems such as trimerized Mott insulators [127] and spin ice [128], and the electric-dipole-induced spin dynamics was studied in molecular magnets [129, 130]. Through the low-energy magnetic excitations of the system, the optical conductivity has a contribution below its optical gap in the Mott insulating phase. This so-called subgap conductivity was furthermore investigated in different systems including the Mott insulator on the kagome lattice in a valence bond solid phase [125, 131], and different quantum spin liquids on the triangular [26] and kagome lattices [27] (which both contain triangular loops). The case of quantum spin liquids, characterized by a lack of magnetic ordering, is particularity interesting because the lack of order is accompanied by a continuum of spin excitations [132], which can then be reached from the ground state through an AC electric field. Quantum spin liquids are generally expected in systems with triangular loops due to the intrinsic geometrical frustration accompanying the lattices [133]. The subgap optical conductivity is thus continuous in such quantum spin liquids. It was observed experimentally in κ-(BEDT-TTF)$_2$Cu$_2$(CN)$_3$ [28, 134] and Herbertsmithite [29] which confirmed the theoretical predictions.

3.2 Two-site polarization

Up to now, the effective polarization in the insulating phase of the Hubbard model was restricted to three-site (or more) subsystems, because of the presence of a particle-hole symmetry. It is natural to wonder whether the Hubbard model can be tweaked in order to accommodate a finite effective polarization at *second order* in t/U, i.e., on each bond of the lattice, instead of trimers. One way to achieve this is to consider a multi-orbital Hubbard model, for which the Mott insulating phase is achieved without necessarily having a particle-hole symmetry. This is the focus of the next two chapters.

In this section, we derive a formalism for the two-site polarization of a more general Hubbard model with one spinful particle per site but with any number of bands. This situation can be, for instance, a single-band Hubbard model (i.e., hydrogen s^1 atoms), but also p^1 and (more physically relevant) d^1 systems, which corresponds to certain transition metal oxides. It could also be a d^9 system where holes are the particles, or a d^5 system with large cubic crystal field (CF) splitting the t_{2g} and e_g orbitals so that a single-hole Hubbard model is used. This last situation is exactly what we consider in Chapter 4. For now, we keep the N-band model general, so that there are $2N$ single-particle states on each site. The two-site model, for sites i and j is written as

$$\mathcal{H} = \sum_{\gamma,\gamma'=1}^{2N} \left[c^\dagger_{i,\gamma} T^{\gamma\gamma'}_{ij} c_{j,\gamma'} + \text{H.c.} \right] + \mathcal{H}_{\text{ion}} + \mathcal{H}_{\text{int}}, \tag{3.24}$$

where $\gamma = 1, \ldots, 2N$ labels the single-particle states. In addition to the interaction Hamiltonian $\mathcal{H}_{\text{int}}$, a single-particle on-site Hamiltonian $\mathcal{H}_{\text{ion}}$ which splits the $2N$ states is allowed (e.g., CF or SOC). We choose our single-particle state $c^\dagger_\gamma |0\rangle$ such that they diagonalize $\mathcal{H}_{\text{ion}}$. Furthermore, we assume that $\gamma = 1, 2$ is the Kramers doublet forming the ground state (split from the other states) which we label $\sigma = \uparrow, \downarrow$, respectively, with on-site energy $E_0^{(1)}$. The hopping matrix $T^{\gamma\gamma'}_{ij}$ generally describes the hopping amplitudes between the $\gamma, \gamma' = 1, \ldots, 2N$ eigenstates on neighboring sites.

First, we construct the $M = 2N(2N-1)/2$ two-particle states on a given site i,

$$|J, \mu, i\rangle = \sum_{\gamma_1\gamma_2}^{2N} m^\mu_{\gamma_1\gamma_2} c^\dagger_{i,\gamma_1} c^\dagger_{i,\gamma_2} |0_i\rangle , \tag{3.25}$$

where $\mu = 1, \ldots, M$ labels the states and $m^\mu_{\gamma_1\gamma_2}$ simply maps all the (γ_1, γ_2) pairs to the label μ. For a given μ, $m^\mu_{\gamma_1\gamma_2}$ is non-zero for only one given pair (γ_1, γ_2), for which it is equal to one. For instance, we can choose, $m^1_{12} = 1$, $m^2_{13} = 1$, etc.. The diagonalization of the full on-site Hamiltonian with two particles and their interaction gives the eigenstates

$$|D, \xi, i\rangle = \sum_{\mu=1}^{M} a_{\xi\mu} |J, \mu, i\rangle , \tag{3.26}$$

and their respective energies $E^{(2)}_\xi$.

Applying a second-order perturbation expansion in the hopping parameters, the two-site effective Hamiltonian is

$$\mathcal{H}_{\text{eff}} = \sum_\xi \frac{1}{-\epsilon_\xi} P_0 \mathcal{H}^{ij}_{\text{hop}} |D, \xi, j\rangle \langle D, \xi, j| \mathcal{H}^{ji}_{\text{hop}} P_0 + (i \leftrightarrow j), \tag{3.27}$$

where P_0 is the projection operator onto states with a single-particle ground state on each site ($\gamma = 1, 2$). The energies of the intermediate states relative to the ground state are given by $\epsilon_\xi = E^{(2)}_\xi + E^{(0)} - 2E^{(1)}_0$, where $E^{(0)}$ is the on-site energy of the state with no particles.

Similarly, the second-order perturbation expansion for the polarization operator (3.9), calculated from the polar states in Eq. (3.5) at first order in $\mathcal{H}_{\text{hop}}$, is

$$\mathbf{P}_{\text{eff}} = a\hat{\mathbf{e}}_{ij}\left[\sum_\xi \frac{1}{\epsilon^2_\xi} P_0 \mathcal{H}^{ij}_{\text{hop}} \left|D, \xi, j\right\rangle \left\langle D, \xi, j\right| \mathcal{H}^{ji}_{\text{hop}} P_0 - (i \leftrightarrow j)\right], \tag{3.28}$$

where $\hat{\mathbf{e}}_{ij}$ is the unit vector pointing from site i to site j and a is the distance between the sites. We have used the fact that the polar states with two particles on site j have $\mathbf{P} = a\hat{\mathbf{e}}_{ij}$ and the ones with two particles on site i have $\mathbf{P} = -a\hat{\mathbf{e}}_{ij}$. Henceforth we set $a = 1$. One can then calculate (see, e.g., Ref. [135])

$$P_0 \mathcal{H}^{ij}_{\text{hop}} \left|D, \xi, j\right\rangle = \sum_{\sigma,\sigma'=\pm} A^\xi_{\sigma,\sigma'} c^\dagger_{i,\sigma} c^\dagger_{j,\sigma'} \left|0\right\rangle, \tag{3.29}$$

with

$$A^\xi_{ij,\sigma\sigma'} = \sum_{\gamma=1}^{2N} \sum_{\mu=1}^{M} T^{\sigma\gamma}_{ij} a_{\xi\mu} (m^\mu_{\gamma\sigma'} - m^\mu_{\sigma'\gamma}). \tag{3.30}$$

Finally, the effective polarization operator is along the $\hat{\mathbf{e}}_{ij}$ direction and its amplitude reads

$$P_{\text{eff}} = \sum_{\sigma\sigma'} \sum_{\sigma_1\sigma'_1} \left[\sum_{\xi=1}^{M} \frac{1}{\epsilon^2_\xi} \left(A^\xi_{ij,\sigma\sigma'} (A^\xi_{ij,\sigma_1\sigma'_1})^* - A^\xi_{ji,\sigma'\sigma} (A^\xi_{ji,\sigma'_1\sigma_1})^* \right)\right] B_{i,\sigma\sigma_1} B_{j,\sigma'\sigma'_1}, \tag{3.31}$$

where $B_{i,\sigma\sigma'} = c^\dagger_{i,\sigma} c_{i,\sigma'}$, such that

$$\begin{aligned} B_{i,\uparrow\uparrow} &= S^z_i + I/2, \\ B_{i,\downarrow\downarrow} &= -S^z_i + I/2, \\ B_{i,\uparrow\downarrow} &= S^+_i, \\ B_{i,\downarrow\uparrow} &= S^-_i, \end{aligned} \tag{3.32}$$

where I is the identity operator. Similarly, the Hamiltonian is

$$\mathcal{H}_{\text{eff}} = -\sum_{\sigma\sigma'} \sum_{\sigma_1\sigma'_1} \left[\sum_{\xi=1}^{M} \frac{1}{\epsilon_\xi} \left(A^\xi_{ij,\sigma\sigma'} (A^\xi_{ij,\sigma_1\sigma'_1})^* + A^\xi_{ji,\sigma'\sigma} (A^\xi_{ji,\sigma'_1\sigma_1})^* \right)\right] B_{i,\sigma\sigma_1} B_{j,\sigma'\sigma'_1}. \tag{3.33}$$

In Ref. [135] it is noted that $(A^\xi_{ji,\sigma'\sigma}) = (A^\xi_{ij,\sigma\sigma'})^*$. However, we argue that this is not true and that in general A^ξ_{ji} and A^ξ_{ij} are not simply related[4]. Equation (3.31) is especially useful for a numerical evaluation of the perturbation theory, for instance when the numerical exact diagonalization is too heavy.

[4] Even for the single-band model with diagonal hopping $T = t\sigma_0$, it is straightforward (there is only one polar state per site) to show that $(A^\xi_{ji,\sigma'\sigma}) \neq (A^\xi_{ij,\sigma\sigma'})^*$ but $A_{ji,\sigma'\sigma} = -A_{ij,\sigma\sigma'}$ instead.

To conclude this chapter, we investigate the two-site effective polarization in the single-band Hubbard model,

$$\mathcal{H} = \sum_{\alpha,\beta=\pm} \left[c^\dagger_{i\alpha} T_{\alpha\beta} c_{j\beta} + \text{H.c.}\right] + \frac{U}{2}\left[(n_i - 1)^2 + (n_j - 1)^2\right], \tag{3.34}$$

with the most general 2×2 hopping matrix defined by eight independent real parameters

$$T = t\sigma_0 + \mathbf{d} \cdot \boldsymbol{\sigma} \equiv (t_1 + it_2)\sigma_0 + (\mathbf{d}_1 + i\mathbf{d}_2) \cdot \boldsymbol{\sigma}, \tag{3.35}$$

where t_1, t_2, d_1^i, d_2^i for $i \in \{x, y, z\}$ are all real. Physically, t_1 is the usual hopping, the complex t_2 hopping comes, e.g., from the Peierls substitution [136] induced by a magnetic flux through the Aharonov-Bohm effect [137], and the d_2^i's correspond to the Aharonov-Casher phase [86] originating from SOC, as shown in Chapter 2. The d_1^i terms are less usual. This spin-anisotropic real hopping has been proposed as a way to realize the Kitaev honeycomb spin model [35], with bond-dependent Ising interaction, on optical lattices [138]. The model with only t_1 and $\mathbf{d}_1$ is often called the Kitaev-Hubbard model [139, 140]. The t_1 and $\mathbf{d}_2$ hoppings preserve time reversal symmetry while the t_2 and $\mathbf{d}_1$ terms are odd under time reversal.

As discussed previously, the particle-hole transformation (3.11) hinders any finite effective polarization at second order in $\mathcal{H}_{\text{hop}}$ when only $t_1 \neq 0$. The generalized hopping can be separated in $\mathcal{H}^-_{\text{hop}}$, containing the $t_1\sigma_0 + i\mathbf{d}_2 \cdot \boldsymbol{\sigma}$ terms, and $\mathcal{H}^+_{\text{hop}}$, containing the $it_2\sigma_0 + \mathbf{d}_1 \cdot \boldsymbol{\sigma}$ terms, which are odd and even with respect to the particle-hole transformation, respectively. Thus, in the expression of P_{eff} at second order in $\mathcal{H}_{\text{hop}}$, the contribution from $(\mathcal{H}^\pm_{\text{hop}})^2$ vanishes and only $\mathcal{H}^\pm_{\text{hop}}\mathcal{H}^\mp_{\text{hop}}$ terms remain. As they are also odd under time reversal, the effective polarization only contains single-spin operator. Using Eq. (3.31), we find

$$P_{\text{eff}} = \frac{4}{U^2}\left[(t_1\mathbf{d}_1 + t_2\mathbf{d}_2) \cdot \left(\mathbf{S}_i - \mathbf{S}_j\right) + (\mathbf{d}_1 \times \mathbf{d}_2) \cdot \left(\mathbf{S}_i + \mathbf{S}_j\right)\right]. \tag{3.36}$$

Finally, a finite polarization is also observed when there is a difference between the chemical potential at the two sites. This is maybe more intuitive because the inversion symmetry is explicitly broken, and the electrons are more likely to be on one site than the other, unless they form a spin triplet because of the Pauli exclusion principle (in the case of spin-independent hopping). The Hamiltonian

$$\mathcal{H} = -t \sum_{i\alpha} \left[c^\dagger_{i+1,\alpha} c_{i\alpha} + \text{H.c.}\right] + \sum_i (-1)^i \frac{\Delta}{2} n_i + \frac{U}{2} \sum_i (n_i - 1)^2, \tag{3.37}$$

was studied in Ref. [141]. It corresponds to a chain made of donor and acceptor molecules stacked alternatingly, and Δ is the difference between the energy levels of the donor and acceptor molecules. For $U > \Delta$, the ground state of this model is the ionic Mott insulator with one electron on each site. For $U < \Delta$, the ground state is neutral with all the odd sites fully occupied while the even ones are empty. In the ionic Mott insulator, the effective polarization can be calculated at second order in the hopping, but Eq. (3.31) has to be modified to account for the different on-site potential. As there is only one band, the calculation is straightforward and the polarization is found to be

$$P_{\text{eff}} = \frac{8t^2 U\Delta}{(U^2 - \Delta^2)^2} \sum_i (-1)^i \left(\frac{1}{4} - \mathbf{S}_i \cdot \mathbf{S}_{i+1}\right), \tag{3.38}$$

which is consistent with the expression in Ref. [141] up to a constant (which we should not neglect for the polarization). As anticipated, a finite polarization is observed on a pair of sites only for the singlet state. In real materials, a spin-Peierls transition occurs below a critical temperature T_{SP} due to the coupling between the molecular displacement and the spins. Below T_{SP}, the system is made of singlet dimers which lead to a uniform ferroelectric moment as derived in Eq. (3.38). The optical response due to Eq. (3.38) in the ionic Hubbard model was calculated in Ref. [141].

We have now exhausted all the possibilities to design a single-band Hubbard model that leads to a finite polarization operator at second order in the hopping. The single-band model, however, lacks a crucial ingredient that is essential in various materials: the orbital degree of freedom. When the Hubbard model is used to study *d*-orbital transition metal compounds, the orbital degree of freedom cannot be neglected, and a multi-band Hubbard model should be adopted. This is the focus of the next chapter.

Chapter 4

Magnetoelectric coupling in the multi-band Hubbard model

The ME effect generally refers to the cross-coupling of the magnetic and electric properties of a material. Multiferroics exhibit the static ME effect, i.e., the cross-control of electric polarization and magnetisation by a magnetic and electric field, respectively [12, 18–24]. Multiferroics are attracting a lot of attention in particular due to the potential applications in novel multifunctional devices [25]. As mentioned in the Introduction, magnetic multiferroics (or type-II multiferroics [23]) such as $TbMnO_3$, for which the ferroelectricity only emerges in the magnetically ordered phase, are especially interesting due to the profound physics behind their properties.

There exist three types of mechanisms for the local ME coupling between the spins $\mathbf{S}_i$ and $\mathbf{S}_j$ at neighboring sites i and j and the local two-site electric polarization $\mathbf{P}_{ij}$: (i) the exchange-striction mechanism originating from the symmetric spin exchange interaction $\mathbf{S}_i \cdot \mathbf{S}_j$ [142], (ii) the spin dependent *p-d* hybridization mechanism causing single spin anisotropy [143–145], and (iii) the spin current mechanism (or inverse Dzyaloshinskii-Moriya interaction) originating from SOC, which causes a spin antisymmetric $\mathbf{P}_{ij}$ that is expressed as a function of $\mathbf{S}_i \times \mathbf{S}_j$ [146–148].

Based on symmetry considerations, the mechanism (iii) is the most general as the electric polarization depending on $\mathbf{S}_i \times \mathbf{S}_j$ can appear regardless of the local symmetry of the *i*-*j* bond [149] (the "highest symmetry" case correspond to $\mathbf{P}_{ij} \propto \hat{\mathbf{e}}_{ij} \times (\mathbf{S}_i \times \mathbf{S}_j)$, where $\hat{\mathbf{e}}_{ij}$ is the unit vector parallel to the bond). In particular, it is allowed in a system with inversion symmetry while the lack of inversion symmetry centered at the middle of the bonds and spin sites is necessary for the mechanisms (i) and (ii), respectively.

The ME effect can also be dynamical. For multiferroics, a striking feature of the ME effect is the collective motion of the spins that can be driven by an AC electric field: the so-called electromagnons [150–156]. They are the Goldstone modes associated with the ferroelectricity and the hybridization of spin waves with the electric polarization.

However, the ME effect is not limited to multiferroics. It can appear in magnetic Mott insulators even without long-range ordering, and thus without the static ME effect and the accompanying reduction of the symmetry. The ME coupling influences the charge dynamics of the electrons in the magnetic energy scale, far below the optical gap. Consequently, the magnetic excitations can be probed with an AC electric field, e.g., by measuring the terahertz (THz) dielectric response.

For instance, electric-dipole-induced spin resonances are in principle possible in a quantum spin gapped system, with a ground state made of nonmagnetic spin singlet and no long-range order [157]. In fact, transitions between the spin singlet and spin triplet states, which are forbidden for magnetic dipole transitions, have been observed in various spin gapped systems in ESR experiments [158–162]. While

potential singlet-triplet mixing due to, e.g., the DM interaction makes the transition possible [163, 164], it has also been suggested that the ME effect is the origin of the observed resonance [165, 166]. In Ref. [157], they recently showed the singlet-triplet transitions in the spin-1/2 $KCuCl_3$ compound are driven by the AC electric field. Indeed, through the mechanism (iii) (which is generally allowed by symmetry), the polarization is written in terms of $\mathbf{S}_i \times \mathbf{S}_j$ and thus has finite matrix elements between singlet and triplet states.

In the previous chapter, we considered the effective polarization emerging from virtual hopping of the electrons. This is yet another mechanism for the ME coupling. In multiferroics, the mechanisms behind the electric polarization typically rely on the electroelastic effects involving the displacement of the ions forming the lattice. By contrast, the polarization emerging from virtual hopping is purely 'electronic', in the sense that it only involes the charge of the electrons carrying the spins. By focussing on the Hubbard model, in this chapter we consider the electronic ME coupling in the multi-band Hubbard model.

As mentioned in the previous chapter, the subgap optical conductivity due to ME coupling was observed in some gapless spin liquids [26–29], and explained by the electronic ME mechanism based on ring exchange interaction on triangular and kagome lattices [26, 27].

More recently, a continuous subgap optical conductivity was observed in a different type of quantum spin liquid, which cannot be explained with the ME mechanism on triangular loops. In a series of THz spectroscopy measurements, the response of α-$RuCl_3$ was measured [30–34], and it was shown that it had a strong electric-dipole-induced contribution [31]. The subgap optical conductivity is calculated in Chapter 5, and the experimental results are shown in Fig. 5.3. α-$RuCl_3$ is a Kitaev material, a d-orbital Mott insulator in close proximity to the Kitaev honeycomb model [35]. The Kitaev honeycomb model is exactly solvable and has a quantum spin liquid ground state. It was proposed to be realizable in real materials through the Jackeli-Khaliullin mechanism [49], and has attracted much attention in recent years. The Kitaev model can be analytically solved in terms of Majorana Fermion, and is the focus of Chapter 6 where it is thoroughly described.

Potential Kitaev materials, such as 'Kitaev Iridates' A_2IrO_3 with A=Na, Li [50–52, 167–169] and α-$RuCl_3$ [53–55, 58, 170–172], nevertheless all eventually become antiferromagnetic below a critical temperature T_N ($\approx 8K$ for α-$RuCl_3$), which indicates that the Kitaev spin model does not reflect all the physics of the materials. Nonetheless, a residual continuum of excitations have been consistently observed above and below T_N which suggests some remnants of the Majorana physics of the Kitaev model [31, 56, 58, 59]. In order to calculate the optical conductivity in such systems, we first need to understand the underlying ME coupling, which is the focus of the present chapter.

Motivated by the THz spectroscopy observation of the subgap optical conductivity, we aim to understand and derive the mechanisms behind the ME coupling in α-$RuCl_3$. The magnetic moments in the Kitaev materials come from the electrons around the TM ions, ruthenium or iridium, in the $4d^5$ and $5d^5$ electronic configuration, respectively. The orbitals in $4d$ and $5d$ TM compounds are relatively widespread and thus close to an itinerant regime [173] or a molecular orbital crystal [174]. In addition, SOC is very strong in $4d$ and $5d$ compounds [87–89] and, combined with the electron correlation, heavily influences the electronic and magnetic structure [87–89]. It is therefore natural to expect consequent charge fluctuations of the localized particles through virtual hopping to neighboring ions, and a significant electronic ME coupling.

Starting from the three-band Hubbard model, we proceed to derive the effective polarization operator in the low-energy manifold, in terms of pseudospin 1/2 variables on each TM site. Because of time reversal symmetry, there are no single-spin terms and we only consider two-spin terms from nearest-neighbors. We identify two microscopic mechanisms. To put it briefly, there are two types of matrix elements for the position operator $\mathbf{r}$: (i) the matrix elements $\langle i,\alpha|\mathbf{r}|j,\beta\rangle$, for ions $i \neq j$ with orbitals α and β, originally used in the spin-current model [146], and (ii) the matrix elements $\langle i,\alpha|\mathbf{r}|i,\beta\rangle = \mathbf{r}_i\delta_{\alpha,\beta}$ which involve only one site. For the mechanism (i), we express the ME coupling in d^5 Mott insulators such as Kitaev materials as a function of the different $\langle i,\alpha|\mathbf{r}|j,\beta\rangle$ integrals. Hence, with additional first-principle calculations to evaluate the integrals, the ME effect in Kitaev materials and other d^5 Mott insulators can be evaluated from the results of this chapter.

In addition to the honeycomb lattice of the Kitaev materials, we also consider the electric polarization in the more simple perovskite lattice structure for the same d^5 Hubbard model but with a different geometry for the superexchange mechanism.

The present chapter is structured as follows. In Sec. 4.1, we first introduce the Hamiltonians. In Sec. 4.2, the allowed ME coupling between $\mathbf{P}_{ij}$ and $\mathbf{S}_i\times\mathbf{S}_j$ is derived from symmetry. Next, we emphasize the importance of SOC in Sec. 4.3. In Sec. 4.4, the two different electronic mechanisms for the polarization are discussed starting from the usual LCAO (linear combination of atomic orbitals) approximation of the tight-binding model. In Sec. 4.5, we explicitly calculate the polarization from the mechanisms considered for the two different lattice structures. Finally, the results are discussed in Sec. 4.6.

4.1 Model

We consider the Hamiltonian of a d^5 Mott insulator in a strong octahedral crystal field (CF) environment. The CF originates from the octahedral cage made of ligands (oxygen or chloride) surrounding each TM ion. Because of the cubic symmetry, the d orbitals are split into t_{2g} and e_g orbitals. The lower energy manifold is thus described with one hole occupying the t_{2g} orbitals and is six-fold degenerate.

That being said, we note that in 4d and 5d compounds, the complete neglect of the e_g orbitals is not always well justified [175]. Because of the large spatial extent of the electronic states, the CF splitting Δ_{cubic} is increased while the interactions are reduced. Typically, $\Delta_{\text{cubic}} = 1-5$ eV, the Coulomb repulsion $U = 0.5-3$ eV, and Hund's coupling $J_H = 0.5-0.7$ eV. However, heavier elements have larger SOC, typically $\lambda = 0.1-1$ eV [175]. We are thus in a situation where Hund's first rule (of maximal spin) is violated and low-spin t_{2g}-orbital configurations are preferred, but significant e_g-t_{2g} mixing is not excluded due to the strong SOC. We nevertheless neglect e_g-t_{2g} mixing for simplicity and work in the t_{2g}-orbital subspace as is very often done.

For Kitaev materials, this model has been largely discussed in the literature [176–184]. The 2D Kitaev materials form a honeycomb lattice shown in Fig. 4.2 and two ligands are shared on each TM-TM bond. This is the edge-sharing geometry shown in Fig. 4.1(b). The model on a perovskite lattice corresponds to the corner-sharing geometry shown in Fig. 4.1(a) and has been discussed in the context of iridates or rhodates compounds such as the nearly 2D materials Sr_2IrO_4 and $Sr_2Ir_{1-x}Rh_xO_4$ [135].

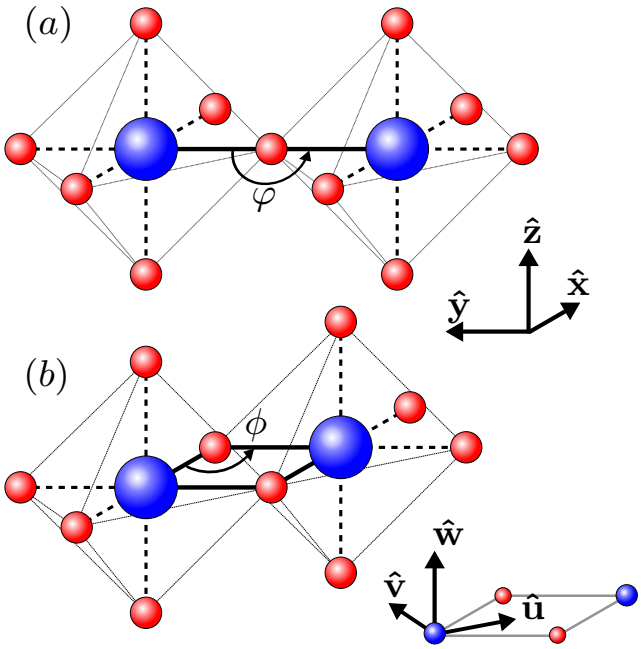

FIGURE 4.1: A pair of TM ions and their neighboring ligands in the (a) corner-sharing and (b) edge-sharing geometries where $\hat{\mathbf{u}} = (\hat{\mathbf{x}} - \hat{\mathbf{y}})/\sqrt{2}$ (a z-bond). The blue spheres are the TM ions and the red spheres the ligands. In the ideal geometries, $\phi = 90°$ and $\varphi = 180°$.

Accordingly, we consider the three-band Hubbard model for the holes with a filling of one hole per site,

$$\mathcal{H} = \mathcal{H}_{\text{hop}} + \mathcal{H}_{\text{ion}} + \mathcal{H}_{\text{int}}, \tag{4.1}$$

which consists of a hopping, non-interacting on-site and interaction Hamiltonian, respectively. The hole fermion operators are concisely written as

$$\mathbf{c}_i^\dagger = (c_{i,yz,\uparrow}^\dagger, c_{i,yz,\downarrow}^\dagger, c_{i,xz,\uparrow}^\dagger, c_{i,xz,\downarrow}^\dagger, c_{i,xy,\uparrow}^\dagger, c_{i,xy,\downarrow}^\dagger). \tag{4.2}$$

The interaction is well described by the Kanamori Hamiltonian [185, 186], which consists of Hund's coupling J_H, intra orbital repulsion U, and inter orbital repulsion $U' = U - 2J_H$ (a good approximation for most materials [186]),

$$\begin{aligned}\mathcal{H}_{\text{int}} =& U \sum_{i,a} n_{i,a,\uparrow} n_{i,a,\downarrow} + (U' - J_H) \sum_{i,a<b,\sigma} n_{i,a,\sigma} n_{i,b,\sigma} + U'_{i,a\neq b} n_{i,a,\uparrow} n_{i,b,\downarrow} \\ & - J_H \sum_{i,a\neq b} c_{i,a,\uparrow}^\dagger c_{i,a,\downarrow} c_{i,b,\downarrow}^\dagger c_{i,b,\uparrow} + J_H \sum_{i,a\neq b} c_{i,a,\uparrow}^\dagger c_{i,a,\downarrow}^\dagger c_{i,b,\downarrow} c_{i,b,\uparrow}.\end{aligned} \tag{4.3}$$

The hopping Hamiltonian is found by calculating the effective hopping between neighboring TM ions in terms of the usual Slater-Koster integrals [187]. It consists of both the superexchange through the ligand(s) between the TM ions and the direct TM-TM hopping. For the superexchange, each hole can jump to the ligands with filled p^6 orbitals at a cost Δ_{pd}, the charge-transfer energy. The physics of the system depends on the relation between Δ_{pd} and U. For the Mott insulators that we consider, the first charge-excited states have polar states with double t_{2g} hole occupancy on a TM ion with energy gap $\sim U$. By contrast, for the charge-excited states of charge-transfer insulators, the hole occupies the p orbitals of a ligand at a cost Δ_{pd}.

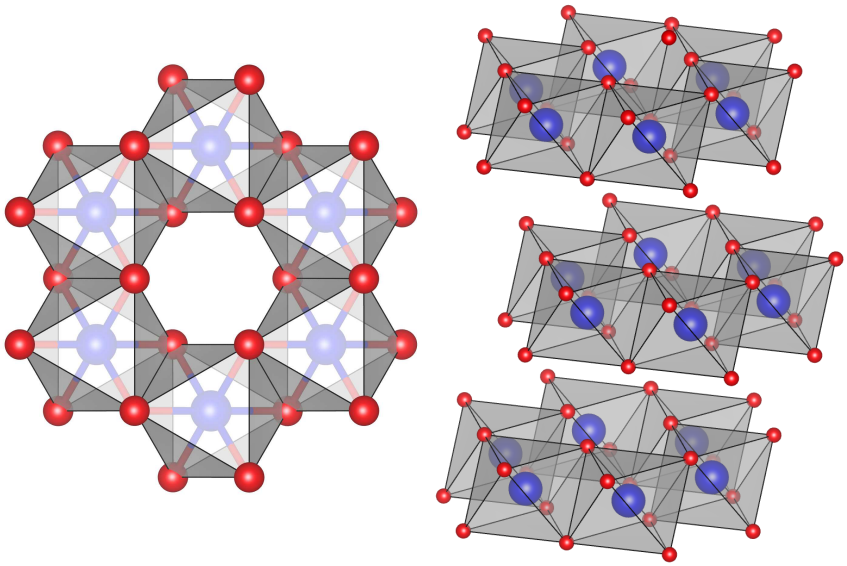

FIGURE 4.2: Honeycomb crystal structure of Kitaev materials. The blue spheres represent the magnetic TM ions and the red spheres the ligand. Each TM-TM bond is in the edge-sharing geometry and the 2D plane is perpendicular to the [111] direction.

We hence consider the limit $\Delta_{pd} \gg U$ for which we can integrate out the states with unfilled p in order to obtain the effective Hubbard Hamiltonian (4.1) involving only TM sites. Furthermore, the intermediate states with two or more holes occupying the p-orbitals of the ligands are neglected and the superexchange effective hopping simply consists of the different TM-L-TM processes through each ligand (L) separately.

Summing up the contributions of the different ligands,

$$\mathcal{H}_{\text{hop}} = -\sum_{\langle ij \rangle} \mathbf{c}_i^\dagger (\hat{T}_{ij} \otimes \mathbb{I}_{2\times 2}) \mathbf{c}_j, \tag{4.4}$$

where $\hat{T}_{ij}$ is the hopping matrix between TM sites i and j,

$$\hat{T}_{ij}^{\alpha\beta} = t_{ij}^{\alpha\beta} + \sum_p \sum_{\gamma=x,y,z} \frac{t_{ip}^{\alpha\gamma} t_{jp}^{\beta\gamma}}{\Delta_{pd}}. \tag{4.5}$$

Here $t_{ij}^{\alpha\beta}$ is the direct hopping between the TM ions at sites i and j with respective orbitals α and β found from the Slater-Koster integrals [187]. The second part is the superexchange mechanism through the ligands labelled by p with orbitals γ in terms of the $t_{ip}^{\alpha\gamma}$ TM-L hoping integrals. In the edge-sharing geometry, there are two ligands ($p = 1, 2$), and there is only one in the corner-sharing geometry ($p = 1$) [see Fig. 4.1]. The exact hopping matrix for both the edge- and corner-sharing geometries are given based on symmetry considerations in the following section.

The on-site six-fold degenerate Hilbert space is lifted by $\mathcal{H}_{\text{ion}}$ which consists of both SOC and an additional CF splitting between the t_{2g} orbitals. The holes originally have an $L = 2$ orbital angular momentum. However, the projected $L = 2$ angular momentum operators $\mathbf{L}$ onto the yz, xz, and xy orbitals is related to the $L = 1$ angular momentum operator $\mathbf{L}(p)$ of a single hole in the p orbitals in the $\{x, y, z\}$ basis by $\mathbf{L}(t_{2g}) = -\mathbf{L}(p)$. Therefore, the orbital angular momentum in t_{2g} orbitals is partially

quenched from $L = 2$ to 1. In other words, the holes have an effective $L = 1$ orbital angular moment in addition to their intrinsic $S = 1/2$ spin angular momentum.

The SOC Hamiltonian is

$$\mathcal{H}_{\mathrm{SO}} = \lambda/2 \sum_{i,a} \mathbf{c}_i^\dagger (L^a \otimes \sigma^a) \mathbf{c}_i, \tag{4.6}$$

where $\lambda > 0$ (for holes), σ^a are the Pauli matrices, and $(L^a)_{bc} = -i\epsilon_{abc}$ (ϵ is the three-dimensional Levi-Civita tensor). In additional to the cubic CF, a lower-symmetry CF distortion

$$\mathcal{H}_{\mathrm{CF}} = \Delta \sum_i \mathbf{c}_i^\dagger [(\mathbf{L} \cdot \hat{\mathbf{n}}_{\mathrm{CF}})^2 \otimes \mathbb{I}_{2\times 2}] \mathbf{c}_i, \tag{4.7}$$

is usually expected, so that $\mathcal{H}_{\mathrm{ion}} = \mathcal{H}_{\mathrm{SO}} + \mathcal{H}_{\mathrm{CF}}$. The unit vector $\hat{\mathbf{n}}_{\mathrm{CF}}$ is the direction of the extra CF elongation ($\Delta < 0$) or compression ($\Delta > 0$) [183]. We only explicitly consider the effects of a distortion perpendicular to the 2D systems considered: a trigonal distortion ($\hat{\mathbf{n}}_{\mathrm{CF}} = [111]$) in the edge-sharing geometry, and a tetragonal ($\hat{\mathbf{n}}_{\mathrm{CF}} = [001]$) distortion in the corner-sharing geometry. Explicitly (up to a constant),

$$\mathbf{L}^2_{[111]} = -\frac{1}{3}\begin{pmatrix} 0 & 1 & 1 \\ 1 & 0 & 1 \\ 1 & 1 & 0 \end{pmatrix} \qquad \text{and} \qquad \mathbf{L}^2_{[001]} = \begin{pmatrix} 1 & 0 & 0 \\ 0 & 1 & 0 \\ 0 & 0 & 0 \end{pmatrix}. \tag{4.8}$$

With only SOC ($\Delta = 0$), the t_{2g} orbitals are split into the states with $J = 1/2$ and $J = 3/2$ total effective angular momentum with energy $-\lambda$ and $\lambda/2$, respectively. The $|J, J^z\rangle$ states are given by

$$\begin{aligned}
\left|\frac{1}{2}, \frac{1}{2}\right\rangle &= \frac{1}{\sqrt{3}}(-|X,\downarrow\rangle - i\,|Y,\downarrow\rangle - |Z,\uparrow\rangle) \\
\left|\frac{1}{2}, -\frac{1}{2}\right\rangle &= \frac{1}{\sqrt{3}}(-|X,\uparrow\rangle + i\,|Y,\uparrow\rangle + |Z,\downarrow\rangle) \\
\left|\frac{3}{2}, \frac{3}{2}\right\rangle &= \frac{1}{\sqrt{2}}(-|X,\uparrow\rangle - i\,|Y,\uparrow\rangle) \\
\left|\frac{3}{2}, \frac{1}{2}\right\rangle &= \frac{1}{\sqrt{6}}(-|X,\downarrow\rangle - i\,|Y,\downarrow\rangle + 2\,|Z,\uparrow\rangle) \\
\left|\frac{3}{2}, -\frac{1}{2}\right\rangle &= \frac{1}{\sqrt{6}}(|X,\uparrow\rangle - i\,|Y,\uparrow\rangle + 2\,|Z,\downarrow\rangle) \\
\left|\frac{3}{2}, -\frac{3}{2}\right\rangle &= \frac{1}{\sqrt{2}}(|X,\downarrow\rangle - i\,|Y,\downarrow\rangle),
\end{aligned} \tag{4.9}$$

where $X = yz$, $Y = xz$, and $Z = xy$.

The CF also splits the t_{2g} states by itself into a b_{2g} state and an e_g pair of states. In general, with both SOC and CF the states are split into three Kramers doublets.

Because $\lambda > 0$, the ground state is always a Kramers doublet which defines a pseudospin 1/2 variable on each site. Moreover, it is assumed that the gap to the other four excited states is larger than the magnetic scale of the effective pseudospin-pseudospin interactions, which is roughly t_{eff}^2/U where t_{eff} generally refers to the amplitude of the TM-TM hopping integrals.

In Sec. 4.5, we use perturbation theory in $\mathcal{H}_{\mathrm{hop}}$ to calculate the polarization operator in the low-energy manifold. In order to perform analytical calculations, $\mathcal{H}_{\mathrm{CF}}$ is also often neglected. Here we mostly consider it as a perturbation. Indeed, while the

additional CF distortion lower the symmetry, its amplitude is typically small compared to SOC. This situation is particularly relevant for late TM ions such as Ir, Os, Rh, and Ru [49]. Nevertheless, we also perform numerical calculations exact in Δ for comparison.

4.2 Symmetry considerations

The finite elements in a tensor relating two physical quantities can be determined from symmetry. This is in particular true for the spin-polarization coupling [149, 188, 189]. We explicitly consider the two edge- and corner-sharing geometries with and without $\mathcal{H}_{\mathrm{CF}}$.

In the low-energy Hilbert space, because of the time-reversal and inversion symmetry, the general form of the ME coupling for the bond $\langle ij \rangle$ is $\mathbf{P} = \hat{m}\big(\mathbf{S}_i \times \mathbf{S}_j\big)$, or

$$\begin{pmatrix} P_x \\ P_y \\ P_z \end{pmatrix} = \begin{pmatrix} m_{xx} & m_{xy} & m_{xz} \\ m_{yx} & m_{yy} & m_{yz} \\ m_{zx} & m_{zy} & m_{zz} \end{pmatrix} \begin{pmatrix} \big(\mathbf{S}_i \times \mathbf{S}_j\big)_x \\ \big(\mathbf{S}_i \times \mathbf{S}_j\big)_y \\ \big(\mathbf{S}_i \times \mathbf{S}_j\big)_z \end{pmatrix}. \tag{4.10}$$

Here the operators $\mathbf{S}_i$ refer to the pseudospin 1/2 variables defined in the low-energy Hilbert space. From now on, we refer to them as "spins".

In the original spin-current model proposed by H. Katsura, N. Nagaosa, and A. V. Balatsky [146], $\mathbf{P}_{ij} \propto \hat{\mathbf{e}}_{ij} \times (\mathbf{S}_i \times \mathbf{S}_j)$, where $\hat{\mathbf{e}}_{ij}$ is the unit vector parallel to the bond, which we henceforth call the Katsura-Nagaosa-Balatsky (KNB) coupling. For a bond in the x direction, it corresponds to $m_{yz} = -m_{zy}$ and all other components equal to zero in Eq. (4.10). However, for a sufficiently low symmetry, there are other allowed matrix elements in $\hat{m}$ determined from the symmetry of the $\langle ij \rangle$ bond.

4.2.1 Edge-sharing geometry

First, we consider the edge-sharing geometry with $\phi = 90°$ TM-L-TM bonds as shown in Fig. 4.1(b).

Full octahedral symmetry

Six ligands form an octahedral cage around each TM ion which defines the $\hat{\mathbf{x}}$, $\hat{\mathbf{y}}$ and $\hat{\mathbf{z}}$ directions. Without any further distortion, the point group is O_h.

In the Kitaev materials of Fig. 4.2, there are three different bond directions: $(\hat{\mathbf{y}} - \hat{\mathbf{z}})/\sqrt{2}$ (an x-bond), $(\hat{\mathbf{z}} - \hat{\mathbf{x}})/\sqrt{2}$ (a y-bond), and $(\hat{\mathbf{x}} - \hat{\mathbf{y}})/\sqrt{2}$ (a z-bond). Henceforth, we only consider the $(\hat{\mathbf{x}} - \hat{\mathbf{y}})/\sqrt{2}$ direction (as shown in Fig. 4.1) and the other two bonds are simply related by cyclic permutations thanks to the C_3 symmetry.

There are three twofold axes (with C_2 symmetry) along $\hat{\mathbf{u}} = (\hat{\mathbf{x}} - \hat{\mathbf{y}})/\sqrt{2}$, $\hat{\mathbf{v}} = (\hat{\mathbf{x}} + \hat{\mathbf{y}})/\sqrt{2}$, and $\hat{\mathbf{w}} = \hat{\mathbf{z}}$ [see Fig. 4.1]. The corresponding bond symmetry group, i.e., containing only elements that leave the bond unmoved, is D_{2h}. From the character table of the group shown in Table 4.1, we can directly read the allowed coupling between different functions; only quantities transforming under the same irreducible representation can be coupled to each other [190].

For the t_{2g} orbitals, the T_2 irreducible representation of O splits into three different irreducible representations of D_{2h}: $T_2 \to B_1 \oplus B_2 \oplus B_3$, for the d_{ab} orbitals where a and b correspond to the $\hat{\mathbf{u}}$, $\hat{\mathbf{v}}$ and $\hat{\mathbf{w}}$ directions.

TABLE 4.1: Character table of D_{2h} with twofold axis in the a, b and c directions. $C_{2,\alpha}$ is a C_2 rotation along the corresponding axis, $\sigma_{\alpha\beta}$ is a reflection across the $\alpha\beta$ plane, and the $\langle ij\rangle$ bond is in the a direction.

D_{2h}	E	$C_{2,a}$	$C_{2,b}$	$C_{2,c}$	I	σ_{bc}	σ_{ac}	σ_{ab}	functions
A_g	1	1	1	1	1	1	1	1	-
$B_{1,g}$	1	1	−1	−1	1	1	−1	−1	S^a
$B_{2,g}$	1	−1	1	−1	1	−1	1	−1	S^b
$B_{3,g}$	1	−1	−1	1	1	−1	−1	1	S^c
A_u	1	1	1	1	−1	−1	−1	−1	$\left(\mathbf{S}_i \times \mathbf{S}_j\right)_a$
$B_{1,u}$	1	1	−1	−1	−1	−1	1	1	a, i-j antisym.
$B_{2,u}$	1	−1	1	−1	−1	1	−1	1	b, $\left(\mathbf{S}_i \times \mathbf{S}_j\right)_b$
$B_{3,u}$	1	−1	−1	1	−1	1	1	−1	c, $\left(\mathbf{S}_i \times \mathbf{S}_j\right)_c$

Therefore, the hopping matrices (4.5) between two sites with t_{2g} orbitals must be

$$\hat{T}_Z(D_{2h}) = \begin{pmatrix} t_{11} & 0 & 0 \\ 0 & t_{22} & 0 \\ 0 & 0 & t_{33} \end{pmatrix}_{\mathcal{B}',\mathcal{B}'} = \begin{pmatrix} t_1 & t_2 & 0 \\ t_2 & t_1 & 0 \\ 0 & 0 & t_3 \end{pmatrix}_{\mathcal{B},\mathcal{B}}, \tag{4.11}$$

where $\mathcal{B} = \{\hat{\mathbf{x}}, \hat{\mathbf{y}}, \hat{\mathbf{z}}\}$ and $\mathcal{B}' = \{\hat{\mathbf{u}}, \hat{\mathbf{v}}, \hat{\mathbf{w}}\}$ are two different bases.

Explicitly, the hopping parameters are [180]

$$\begin{aligned} t_1 &= \frac{t_{dd\pi} + t_{dd\delta}}{2}, \\ t_2 &= \frac{-t_{dd\pi} + t_{dd\delta}}{2} + \frac{t_{pd\pi}^2}{\Delta_{pd}}, \\ t_3 &= \frac{3t_{dd\sigma} + t_{dd\delta}}{4}, \end{aligned} \tag{4.12}$$

where $t_{pd\sigma}, t_{pd\pi}, t_{dd\sigma}, t_{dd\pi}$, and $t_{dd\delta}$ are Slater-Koster integrals [187].

The allowed spin-polarization couplings are found by comparing how the spin operators and the polarization operators transform under the elements of the bond symmetry group. The spin along the axes of $\mathcal{B}$, S^u, S^v, and S^w transform as $B_{1,g}$, $B_{2,g}$, and $B_{3,g}$, respectively, and the cross product in $\mathbf{S}_i \times \mathbf{S}_j$ introduces an extra $B_{1,u}$, odd under inversion. The polarization is a vector and hence P^α transforms as $B_{\alpha,u}$. Following Table 4.1, there are only two allowed independent coupling constants,

$$\hat{m}(D_{2h}) = \begin{pmatrix} 0 & 0 & 0 \\ 0 & 0 & m_4 \\ 0 & m_5 & 0 \end{pmatrix}_{\mathcal{B}',\mathcal{B}'}. \tag{4.13}$$

Note that the matrix $\hat{m}$ does not have to be symmetric or antisymmetric, unlike the hopping matrix which is symmetric. Hence, even with the highest symmetry possible for the edge-sharing geometry, the ME effect is more general than the KNB formula $\mathbf{P} \propto \hat{\mathbf{e}}_{ij} \times (\mathbf{S}_i \times \mathbf{S}_j)$, which would correspond to $m_4 = -m_5$.

Trigonal distortion

It is usual for materials to have a CF distortion deviating from the purely octahedral CF. Let us consider a distortion perpendicular to the 2D plane. This distortion

preserves the C_3 symmetry and is typical for Kitaev materials. It corresponds to an elongation or compression in the $(\hat{\mathbf{x}}+\hat{\mathbf{y}}+\hat{\mathbf{z}})/\sqrt{3}$ direction. The corresponding point group is D_{3d} and the symmetry group of a bond is reduced to $D_{2h} \to C_{2h}$. Its character table is shown in Table 4.2.

TABLE 4.2: Character table of C_{2h} with twofold axis in the a direction. $C_{2,a}$ is the C_2 rotation around $\hat{\mathbf{a}}$, σ_{bc} is the reflection across the plane perpendicular to $\hat{\mathbf{a}}$, and the $\langle ij\rangle$ bond is along the a direction.

C_{2h}	E	$C_{2,a}$	I	σ_{bc}	functions
A_g	1	1	1	1	S^a
B_g	1	−1	1	−1	S^b, S^c
A_u	1	1	−1	−1	$a, \left(\mathbf{S}_i \times \mathbf{S}_j\right)_a$, i-j antisym.
B_u	1	−1	−1	1	$b, \left(\mathbf{S}_i \times \mathbf{S}_j\right)_b$ $c, \left(\mathbf{S}_i \times \mathbf{S}_j\right)_c$

The hopping matrix has one additional t_{23} allowed matrix element,

$$\hat{T}_Z(C_{2h}) = \begin{pmatrix} t_{11} & 0 & 0 \\ 0 & t_{22} & t_{23} \\ 0 & t_{23} & t_{33} \end{pmatrix}_{\mathcal{B}',\mathcal{B}'} = \begin{pmatrix} t_1 & t_2 & t_4 \\ t_2 & t_1 & t_4 \\ t_4 & t_4 & t_3 \end{pmatrix}_{\mathcal{B},\mathcal{B}}, \tag{4.14}$$

and the ME coupling matrix has three additional allowed matrix elements (diagonal in the $\mathcal{B}'$ basis),

$$\hat{m}(C_{2h}) = \begin{pmatrix} m_1 & 0 & 0 \\ 0 & m_2 & m_4 \\ 0 & m_5 & m_3 \end{pmatrix}_{\mathcal{B}',\mathcal{B}'}. \tag{4.15}$$

Additional distortions

While the trigonal distortion is the most commonly considered CF, small C_3-symmetry breaking monoclinic distortion are also sometimes reported. In this case, the only symmetry of the bond is the inversion symmetry relative to its center, and its symmetry group is reduced C_i. Therefore, the only constrain is the inversion symmetry so that T has six independent matrix elements and $\hat{m}$ has nine. In the following, we only consider system with the C_3 symmetry preserved.

There is, however, a special distortion which is worth mentioning. If the two ligands on a given bonds are displaced along $\pm\hat{\mathbf{v}}$, perpendicularly to the bond, the local D_{2h} symmetry of the system made of two ligands and two TM sites is left unbroken (even though the bond symmetry should be lowered to C_{2h}). This is because $\hat{\mathbf{v}}$ is one of the C_2 axes. Hence, the local microscopic processes produce a matrix $\hat{m}$ consistent with Eq. (4.15). Such a distortion is a convenient way to study the effect of a $\phi \neq 90°$ angle in the TM-L-TM bond geometry and is considered in Appendix B.

4.2.2 Corner-sharing geometry

Let us now consider the corner-sharing geometry shown in Fig. 4.1 with $\varphi = 180°$. If $\varphi \neq 180°$, the inversion symmetry centered at the middle of the bond is broken and couplings in addition to those of Eq. (4.10) are allowed. This case is considered in Appendix B.2.

Full octahedral symmetry

The two-octahedra structure has a C_4 axis along $\hat{\mathbf{x}}$ and four C_2 axes. It corresponds to the group D_{4h}, whose character table is shown in Table 4.3.

TABLE 4.3: Character table of D_{4h} with $\hat{\mathbf{a}}$ as the C_4 axis. The $2C_2'$ rotations are around $\hat{\mathbf{b}}$ and $\hat{\mathbf{c}}$, the $2C_2''$ ones around $\hat{\mathbf{b}} \pm \hat{\mathbf{c}}$, and $2\sigma_{v,d}$ are the corresponding reflections. The $\langle ij \rangle$ bond is along $\hat{\mathbf{a}}$.

D_{4h}	E	$2C_{4,a}$	$C_{2,a}$	$2C_2'$	$2C_2''$	I	$2S_4$	σ_{bc}	$2\sigma_v$	$2\sigma_d$	functions
$A_{1,g}$	1	1	1	1	1	1	1	1	1	1	-
$A_{2,g}$	1	1	1	−1	−1	1	1	1	−1	−1	S^a
$B_{1,g}$	1	−1	1	1	−1	1	−1	1	1	−1	-
$B_{2,g}$	1	−1	1	−1	1	1	−1	1	−1	1	bc
E_g	2	0	−2	0	0	2	0	−2	0	0	(S^b, S^c), (ac, ab)
$A_{1,u}$	1	1	1	1	1	−1	−1	−1	−1	−1	-
$A_{2,u}$	1	1	1	−1	−1	−1	−1	−1	1	1	a, i-j antisym.
$B_{1,u}$	1	−1	1	1	−1	−1	1	−1	−1	1	$(\mathbf{S}_i \times \mathbf{S}_j)_a$
$B_{2,u}$	1	−1	1	−1	1	−1	1	−1	1	−1	-
E_u	2	0	−2	0	0	−2	0	2	0	0	(b, c), $\left((\mathbf{S}_i \times \mathbf{S}_j)_b, (\mathbf{S}_i \times \mathbf{S}_j)_c\right)$

For D_{4h}, $T_2 \to B_2 \oplus E$ for the three t_{2g} orbitals. Here, the d_{yz} orbital transforms as B_{2g}, while (d_{xy}, d_{xz}) transforms as E_g. The hopping matrix between the t_{2g} orbitals is thus

$$\hat{T}_x(D_{4h}) = \begin{pmatrix} t_1 & 0 & 0 \\ 0 & t_2 & 0 \\ 0 & 0 & t_2 \end{pmatrix}_{\mathcal{B},\mathcal{B}} . \tag{4.16}$$

Furthermore, we do not consider the direct TM-TM hopping in the corner-sharing geometry. Thus, we find $t_1 = 0$ and $t_2 = -\frac{t_{pd\pi}^2}{\Delta_{pd}} \equiv t$.

Similarly, the ME coupling is found to be

$$\hat{m}_x(D_{4h}) = \begin{pmatrix} 0 & 0 & 0 \\ 0 & 0 & m_1 \\ 0 & -m_1 & 0 \end{pmatrix}_{\mathcal{B},\mathcal{B}} . \tag{4.17}$$

which corresponds to the KNB formula due to the high symmetry of the system (unlike for the edge-sharing geometry).

Tetragonal distortion

The tetragonal distortion is a displacement of the ligands along $\pm\hat{\mathbf{z}}$ from the TM ions and the D_{4h} symmetry is reduced to D_{2h}. The D_{2h} group was already encountered in the edge-sharing geometry and thus the ME coupling is similar to Eq. (4.13). Hence, a deviation from the KNB form is allowed and

$$\hat{m}_x(D_{2h}) = \begin{pmatrix} 0 & 0 & 0 \\ 0 & 0 & m_1 \\ 0 & m_2 & 0 \end{pmatrix}_{\mathcal{B},\mathcal{B}} . \tag{4.18}$$

Note that the explicit hopping matrix is not affected by the distortion because the ligand relevant to the hopping is not affected.

4.3 Importance of spin-orbit coupling

In general, the coupling between the spin and electric polarization operators can emerge from two different sources. The intrinsic Pauli exclusion principle prevents two electrons with the same magnetic state to be on the same site. This is in particular the origin of the ME effect derived Chapter 3. Alternatively, SOC explicitly couples the motion of an electron with its spin. In this section we discuss the role of SOC and show why it is necessary in order to observe a finite coupling involving two-spin operators in systems with inversion symmetry.

Because of inversion symmetry, $\mathbf{P} = \hat{m}(\mathbf{S}_i \times \mathbf{S}_j)$ only has finite matrix elements between the spin singlet state and the spin triplet states. Without SOC, the pseudospins 1/2 forming the ground state manifold are the original spins of the holes. Now, the microscopic operator $\mathbf{P}$ is, by definition, independent of the spin of the electrons. Thus, because the hopping is also spin-independent, the effective polarization operator vanishes in the ground state manifold without SOC. Of course, this argument is only valid when the inversion symmetry is respected. ME effects not relying on SOC, such as the exchange-striction mechanism [142], exist in systems without inversion symmetry.

For a more in-depth understanding of the role of SOC, let us consider a bond $\langle ij \rangle$ and two single-hole wave functions, one on each site, in the on-site ground state manifold. They both transform as a representation, say Γ, of the bond symmetry group. With SOC, Γ is a 2D representation of the spin double group. Without SOC, Γ is just a 1D representation with an extra spin degeneracy.

When building the two-site wave functions, we have an extra degree of freedom coming from the site index: either symmetric or anti-symmetric. The corresponding 1D representations of the bond symmetry group are $\Gamma_{\text{sym}} = 1$, the trivial representation, or Γ_{antisym}, whose identification depends on the group but is odd under inversion symmetry. It is indicated as "i-j antisym." in Tables 4.1, 4.2, and 4.3. Nevertheless, the fermionic statistic imposes the two-hole state to be overall odd under exchange.

Without SOC, $\Gamma \otimes \Gamma = 1$ but both spin singlet and triplet states are available which hence transform as Γ_{sym} and Γ_{antisym}, respectively. Because $\mathbf{P}$ is odd under inversion, only matrix elements between singlet and triplet states are possible which, as already mentioned, must vanish.

With SOC though, each irreducible representation Γ_k in $\Gamma \otimes \Gamma = \sum_k \Gamma_k$ must be paired with either Γ_{sym} or Γ_{antsym} depending on its parity under exchange. Nevertheless, the apparent dichotomy does not correspond to triplet and singlet anymore, so that $\mathbf{P}$ can in principle have finite matrix elements between states of different parity.

4.4 Electric polarization

In order to calculate the effective polarization operator $\mathbf{P}$ in the ground state manifold (i.e., in terms of spin operators) we first need an expression in second quantized notation. In a "pure" lattice model, this was defined intuitively in Eq. (3.9). However, we are now interested in a more complex model with extra ligand sites (which we eventually integrate out). Moreover, we consider actual d-orbital wave functions

with different charge distributions around the TM ions, from which can emerge a finite ME effect (as was first derived in the spin current model [146]). The microscopic **P** is evidently spin-independent and we thus omit the spin degree of freedom in the notation.

It is instructive to take a step back from the tight-binding formulation and to start form the Bloch wave functions

$$\psi_m(\mathbf{k},\mathbf{r}) = \frac{1}{N}\sum_n a_m(\mathbf{R}_n, r)e^{i\mathbf{k}\cdot\mathbf{r}}, \tag{4.19}$$

where $\mathbf{R}_n$ are lattice vectors, N is the number of unit cells and $a_m(\mathbf{R}_n, r)$ is a Wannier function for the unit cells at $\mathbf{R}_n$. The tight-binding model is obtained from the LCAO approximation, which consists of replacing the Wannier function by isolated atomic orbitals, or a linear combinations of them (for unit cells with multiple ions).

For a single bond with two TM ions at positions $\mathbf{r}_1^{\mathrm{TM}}$ and $\mathbf{r}_2^{\mathrm{TM}}$, and M ligands at positions $\mathbf{r}_p^{\mathrm{L}}$ ($p = 1,\ldots,M$), the possible atomic orbitals are

$$\psi_{\mathrm{at}}(\mathbf{r}) = \begin{cases} \psi_\alpha(\mathbf{r}-\mathbf{r}_1^{\mathrm{TM}}), \quad \psi_\alpha(\mathbf{r}-\mathbf{r}_2^{\mathrm{TM}}) \quad (d \text{ orbitals}) \\ \psi_\gamma(\mathbf{r}-\mathbf{r}_p^{\mathrm{L}}) \quad p = 1,\ldots,M \quad (p \text{ orbitals}) \end{cases}, \tag{4.20}$$

where $\alpha \in \{yz, xz, xy, x^2-y^2, 3z^2-r^2\}$, and $\gamma \in \{x, y, z\}$ denotes the d and p orbitals, respectively. Moreover, the orthogonality of the different atomic orbitals is assumed for simplicity. The above atomic orbitals are labelled $|\mathbf{R},\alpha\rangle$ for an ion at position $\mathbf{R}$ with orbital α.

In the following, we argue that in this formalism there are two kinds of contributions to the polarization, defined by the number of sites involved in the matrix elements $\langle\mathbf{R},\alpha|\mathbf{P}|\mathbf{R}',\beta\rangle$. These are grouped into the single-site terms (with $\mathbf{R} = \mathbf{R}'$) and the two-site terms (with $\mathbf{R} \neq \mathbf{R}'$), which we label "lattice polarization" and "hopping polarization", respectively.

4.4.1 Lattice polarization

Because the product of two p or two d orbitals is even under inversion, we have

$$\langle\mathbf{R},\alpha|\mathbf{r}|\mathbf{R},\beta\rangle = \mathbf{R}\delta_{\alpha\beta} + \langle\mathbf{0},\alpha|\mathbf{r}|\mathbf{0},\beta\rangle = \mathbf{R}\delta_{\alpha\beta}. \tag{4.21}$$

The lattice polarization is thus $\sum_i \mathbf{r}_i n_i$, which is intrinsic to any lattice model and corresponds to the operator used in Chapter 3. Here $n_i = \sum_\alpha n_{i,\alpha} = \sum_\alpha c_{i,\alpha}^\dagger c_{i,\alpha}$ and the $\mathbf{r}_i$ vectors are the positions of both ligands and TM ions. As discussed in Chapter 3, the Mott insulator is charge neutral, so that the lattice polarization reads

$$\mathbf{P}_{\mathrm{lat}} = \sum_{i\in\mathrm{TM}} \mathbf{r}_i^{\mathrm{TM}}\delta n_i + \sum_{p\in\mathrm{L}} \mathbf{r}_p^{\mathrm{L}}\delta n_p, \tag{4.22}$$

where $\delta n_i = n_i - n_{\mathrm{TM}}$ for TM ions and $\delta n_p = n_p - n_{\mathrm{L}}$ for ligands. Here n_{TM} and n_{L} are the numbers of electrons (or holes) in the ground state manifold on TM and ligand sites, respectively. In our concrete model we have $n_{\mathrm{TM}} = 1$ and $n_{\mathrm{L}} = 0$ for the holes. The lattice polarization defined here is equivalent (up to a time derivative) to the lattice current (also called the Hubbard current) used in Chapter 2. Hence, the coupling of an electric field to the lattice polarization is equivalent to the coupling arising from the Peierls substitution in the hopping integrals.

The virtual hopping mechanism behind $\mathbf{P}_{\text{lat}}$ was already discussed in Chapter 3. We now have several hopping amplitudes and we henceforth refer to the general effective TM-TM hopping amplitude as t_{eff}. For a finite t_{eff}/U, the ground states contain a small fraction of polar states and we calculate the resulting $\mathbf{P}_{\text{lat}}$ using perturbation theory in powers of t_{eff}/U. In the present model, however, there is another step which consists of integrating out the intermediate states with one hole on a ligand. In the end, there are two types of contributions to $\mathbf{P}_{\text{lat}}$ coming from the TM ions at $\mathbf{r}_i^{\text{TM}}$ and from the ligands at $\mathbf{r}_p^{\text{L}}$ in Eq. (4.22). The contribution from the TM ions at second order in the TM-TM hopping is obtained by using the effecting hopping (4.5) in Eq. (3.28), so that

$$\mathbf{P}^{(\text{TM})}_{\text{lat},\langle ij\rangle,\text{eff}} = \mathbb{P}\Big[\mathcal{H}^{ij}_{\text{hop}}\frac{\mathbb{Q}_j}{(E_0-\mathcal{H}_0)^2}\mathcal{H}^{ji}_{\text{hop}} - \mathcal{H}^{ji}_{\text{hop}}\frac{\mathbb{Q}_i}{(E_0-\mathcal{H}_0)^2}\mathcal{H}^{ij}_{\text{hop}}\Big]\mathbb{P}\mathbf{a}_{ij}, \tag{4.23}$$

where $\mathcal{H}_0$ is the local Hamiltonian $\mathcal{H} = \mathcal{H}_{\text{ion}} + \mathcal{H}_{\text{int}}$, $\mathcal{H}^{ji}_{\text{hop}}$ is the hopping from site i to j defined in Eq. (4.4), and $\mathbb{P}$ and $\mathbb{Q}_k$ are the projection operators on the ground state manifold of $\mathcal{H}_0$ (with energy E_0) and polar states with two holes at the TM site k, respectively. Additionally, $\mathbf{a}_{ij}$ is the vector separating the TM ions i and j whose norm is a, the lattice spacing. Thus, $\mathbf{P}^{(\text{TM})}_{\text{lat},\langle ij\rangle}$ scales as t^2_{eff}/U^2 or $t^4_{pd}/(\Delta^2_{pd}U^2)$ where t_{pd} generally denotes the TM-L hopping integrals.

The second contribution arises when applying $\mathbf{P}_{\text{lat}}$ on a state with one hole on a ligand. After integrating out the intermediate states, it reads

$$\mathbf{P}^{(\text{L})}_{\text{lat},\langle ij\rangle} = \sum_p \sum_{\gamma=x,y,z} \frac{t^{\alpha\gamma}_{ip}t^{\beta\gamma}_{jp}}{\Delta^2_{pd}}\mathbf{r}^{\text{L}}_p\Big(c^\dagger_{i,\alpha}c_{j,\beta} + c^\dagger_{j,\beta}c_{i,\alpha}\Big), \tag{4.24}$$

where the p runs over all ligands at positions $\mathbf{r}^{\text{L}}_p$ between the TM sites i and j and γ labels their p orbitals. The operator $\mathbf{P}^{(\text{L})}_{\text{lat},\langle ij\rangle}$ scales as t^2_{pd}/Δ^2_{pd}, and its projection to the ground state manifold is obtained at first order in $\mathcal{H}_{\text{hop}}$,

$$\mathbf{P}^{(\text{L})}_{\text{lat},\langle ij\rangle,\text{eff}} = \mathbb{P}\Big[\mathbf{P}^{(\text{L})}_{\text{lat},ij}\frac{\mathbb{Q}_j}{E_0-\mathcal{H}_0}\mathcal{H}^{ji}_{\text{hop}} + \mathbf{P}^{(\text{L})}_{\text{lat},ji}\frac{\mathbb{Q}_i}{E_0-\mathcal{H}_0}\mathcal{H}^{ij}_{\text{hop}}\Big]\mathbb{P} + \text{H.c.}, \tag{4.25}$$

which scales as $t^2_{pd}t_{\text{eff}}/(\Delta^2_{pd}U)$ or $t^4_{pd}/(\Delta^3_{pd}U)$. Therefore, it is smaller than the contribution from the TM ions by a $U/\Delta_{pd} \ll 1$ factor. Note that this result is not valid for a charge-transfer insulator.

4.4.2 Hopping polarization

Let us now consider the matrix elements

$$\langle \mathbf{R},\alpha\big|\mathbf{r}\big|\mathbf{R}',\beta\rangle = \langle \mathbf{R},\alpha\big|\mathbf{r}-\mathbf{r}_0\big|\mathbf{R}',\beta\rangle = \left\langle -\frac{\mathbf{d}}{2},\alpha\middle|\mathbf{r}\middle|\frac{\mathbf{d}}{2},\beta\right\rangle \tag{4.26}$$

with $\mathbf{R} \neq \mathbf{R}'$. Here $\mathbf{r}_0 = (\mathbf{R}+\mathbf{R}')/2$ and $\mathbf{d} = \mathbf{R}'-\mathbf{R}$ is the vector separating the two ions: either TM-TM (in which case $\|\mathbf{d}\| = a$) or TM-L. We thus have two types of integrals: *p-d* and *d-d* integrals. The *p-d* integrals satisfy $\langle \mathbf{R},\alpha|\mathbf{r}|\mathbf{R}',\gamma\rangle = \langle \mathbf{R},\gamma|\mathbf{r}|\mathbf{R}',\alpha\rangle$ and the *d-d* integrals satisfy $\langle \mathbf{R},\alpha|\mathbf{r}|\mathbf{R}',\beta\rangle = -\langle \mathbf{R},\beta|\mathbf{r}|\mathbf{R}',\alpha\rangle$. In second quantized notation, it becomes

$$\mathbf{P}_{\text{hop}} = \sum_{\langle i,j\rangle}\sum_{\alpha,\beta}\mathbf{p}_{ij}(\alpha,\beta)\Big(c^\dagger_{i,\alpha}c_{j,\beta} + c^\dagger_{j,\beta}c_{i,\alpha}\Big), \tag{4.27}$$

where $\mathbf{p}_{ij}(\alpha,\beta)$ is the "effective hopping polarization integral" (the equivalent of the hopping matrix $\hat{T}_{ij}$) between the TM ions at site i and j with orbitals α and β, respectively. Because it behaves as a hopping operator, the projection to the ground state manifold is similarly obtained from Eq. (4.25).

As for the hopping matrix (4.5), $\mathbf{p}_{ij}(\alpha,\beta)$ has a direct TM-TM hopping contribution from the *d*-*d* integrals and a TM-L-TM superexchange-like contribution form the *p*-*d* integrals:

$$\mathbf{p}_{ij}(\alpha,\beta) = \left\langle \mathbf{r}_i^{\mathrm{TM}}, \alpha \middle| \mathbf{r} \middle| \mathbf{r}_j^{\mathrm{TM}}, \beta \right\rangle + \sum_p \sum_{\gamma=x,y,z} \frac{\left\langle \mathbf{r}_i^{\mathrm{TM}}, \alpha \middle| \mathbf{r} \middle| \mathbf{r}_p^{\mathrm{L}}, \gamma \right\rangle t_{jp}^{\beta\gamma} + t_{ip}^{\alpha\gamma} \left\langle \mathbf{r}_p^{\mathrm{L}}, \gamma \middle| \mathbf{r} \middle| \mathbf{r}_j^{\mathrm{TM}}, \beta \right\rangle}{\Delta_{pd}}, \quad (4.28)$$

where p and γ label the ligands between the two TM ions and their orbitals.

In the original KNB article about the spin current model [146], similar *p*-*d* integrals were used to derive the ME coupling. However, the integrals were roughly evaluated by neglecting the atomic spacing (i.e., by setting $d = \|\mathbf{d}\| = 0$). Following this approximation, all the finite *p*-t_{2g} integrals, $\left\langle p_z \middle| y \middle| d_{yz} \right\rangle$ and its six permutations, are equal to each other.

However, this approximation is not clearly justified and in the following we discuss the different *p*-*d* and *d*-*d* integrals for a general vector $\mathbf{d}$ separating the two ions. The method used is reminiscent of the original work of Slater and Koster, in which the hopping integrals of the Hamiltonian are evaluated [187]. We find five distinct *p*-*d* polarization integrals and two distinct *d*-*d* polarization integrals allowed by symmetry.

To recapitulate, we have identified two different mechanisms. First, the lattice polarization itself has a contribution from the TM ions which scales as $a \cdot t_{pd}^4/(\Delta_{pd}^2 U^2)$ and a contribution from the ligands which scales as $a \cdot t_{pd}^4/(\Delta_{pd}^3 U)$ (which is systematically smaller). Secondly, the effective hopping polarization in the ground state manifold is obtained at first order in $\mathcal{H}_{\mathrm{hop}}$ and thus scales as $p_{\mathrm{eff}} t_{\mathrm{eff}}/U$, where p_{eff} represents the amplitude of the hopping polarization between two TM sites defined by Eq. (4.28). In terms of *p*-*d* integrals, the scaling reads $p_{pd} t_{pd}^3/(\Delta_{pd}^2 U)$. Thus, we can determine the dominant contribution by comparing p_{eff} and $a \cdot t_{\mathrm{eff}}/U$, or by directly comparing p_{pd} and $a \cdot t_{pd}/U$.

4.4.3 Polarization integrals

The $\left\langle -\frac{\mathbf{d}}{2}, \alpha \middle| \mathbf{r} \middle| \frac{\mathbf{d}}{2}, \beta \right\rangle$ integrals can be classified with respect to the angular momentum along $\mathbf{d}$ of the different spherical harmonics centered at $-\mathbf{d}/2$ and $\mathbf{d}/2$ (for the orbitals), and at the origin (for $\mathbf{r}$). The p orbitals are linear combinations of $p\sigma$, and $p\pi_\pm$ and the d orbitals are linear combinations of $d\sigma$, $d\pi_\pm$ and $d\delta_\pm$ functions, where σ, $\pi_\pm$, and $\delta_\pm$ refer to the functions with $m = 0$, $m = \pm 1$ and $m = \pm 2$ angular momentum along $\mathbf{d}$, respectively. As shown in Table 4.4, they coincide with the cubic harmonics. In the following, the positions of the two ions are implicitly set to $-\mathbf{d}/2$ and $\mathbf{d}/2$ and the integrals are written $\langle \alpha | \mathbf{r} | \beta \rangle$.

TABLE 4.4: Cubic harmonics of p and d orbitals expressed with respect to their component of angular momentum along the $\hat{\mathbf{z}}$ axis.

x	y	z	yz	xz	xy	$\frac{x^2-y^2}{2}$	$\frac{3z^2-r^2}{2\sqrt{3}}$
π_+	π_-	σ	π_-	π_+	δ_+	δ_-	σ

First, there are five independent p-d integrals. In other words, there are five symmetry channels allowed. The σ component of $\mathbf{r}$ is along $\mathbf{d}$ (longitudinal) and the $\pi_\pm$ components are orthogonal to it (transverse). The two longitudinal integrals are

$$P^{\parallel}_{pd\sigma} = \langle p_\sigma|\sigma|d_\sigma\rangle \tag{4.29}$$
$$P^{\parallel}_{pd\pi} = \langle p_{\pi_\pm}|\sigma|d_{\pi_\pm}\rangle \tag{4.30}$$

and the three transverse integrals are

$$P^{\perp}_{p\pi d\sigma} = \langle p_{\pi_\pm}|\pi_\pm|d_\sigma\rangle\,, \tag{4.31}$$
$$P^{\perp}_{p\sigma d\pi} = \langle p_\sigma|\pi_\pm|d_{\pi_\pm}\rangle\,, \tag{4.32}$$
$$P^{\perp}_{p\pi d\delta} = \langle p_{\pi_\pm}|\pi_\mp|d_{\delta_+}\rangle = \pm\langle p_{\pi_\pm}|\pi_\pm|d_{\delta_-}\rangle\,. \tag{4.33}$$

In this notation σ and $\pi_\pm$ directly labels the projections of $\mathbf{r}$ on the σ and $\pi_\pm$ axes.

There are two finite transverse d-d integrals,

$$P^{\perp}_{d\sigma d\pi} = \langle d_\sigma|\pi_\pm|d_{\pi_\pm}\rangle = -\langle d_{\pi_\pm}|\pi_\pm|d_\sigma\rangle\,, \tag{4.34}$$
$$P^{\perp}_{d\pi d\delta} = \langle d_{\pi_\pm}|\pi_\mp|d_{\delta_+}\rangle = \pm\langle d_{\pi_\pm}|\pi_\pm|d_{\delta_-}\rangle = -\langle d_{\delta_+}|\pi_\mp|d_{\pi_\pm}\rangle = \mp\langle d_{\delta_-}|\pi_\pm|d_{\pi_\pm}\rangle\,, \tag{4.35}$$

and the longitudinal integrals vanish.

From symmetry considerations, it is possible to calculate all $\left\langle -\frac{\mathbf{d}}{2},\alpha\middle|\mathbf{r}\middle|\frac{\mathbf{d}}{2},\beta\right\rangle$ p-d and d-d integrals for any vector $\mathbf{d}$. We follow the notation of Slater and Koster [187] and use (l,m,n) for the direction cosines of $\mathbf{d}$. For instance we find

$$\begin{aligned}\left\langle p_x\middle|x\middle|d_{xy}\right\rangle = {}& \sqrt{3}l^3mP^{\parallel}_{pd\sigma} + lm\left(1-2l^2\right)P^{\parallel}_{pd\pi}\\ &+ \sqrt{3}lm\left(1-l^2\right)P^{\perp}_{p\pi d\sigma} + lm\left(1-2l^2\right)P^{\perp}_{p\sigma d\pi}\\ &- lm\left(1-l^2\right)P^{\perp}_{p\pi d\delta}.\end{aligned} \tag{4.36}$$

Expressions for all the other p-t_{2g} and t_{2g}-t_{2g} integrals are given in Appendix A. In particular, for $\mathbf{d}$ along the $\hat{\mathbf{z}}$ axis, the six mentioned p-t_{2g} integrals split into three,

$$\begin{aligned}\langle p_x|z|d_{xz}\rangle &= \langle p_y|z|d_{yz}\rangle = P^{\parallel}_{pd\pi},\\ \langle p_z|y|d_{yz}\rangle &= \langle p_z|x|d_{xz}\rangle = P^{\perp}_{p\sigma d\pi},\\ \langle p_x|y|d_{xy}\rangle &= \langle p_y|x|d_{xy}\rangle = P^{\perp}_{p\pi d\delta}.\end{aligned} \tag{4.37}$$

In the limit where $d = \|\mathbf{d}\| \to 0$, the d-d integrals vanish and the integrals of Eq. (4.37) are equal. This can be seen in Fig. 4.3,

The polarization integrals in Eqs. (4.29), (4.29), and (4.29) are evaluated numerically as a function of d using the hydrogen-like atomic obritals defined by

$$\begin{aligned}\psi_{nlm}(\mathbf{r}) &= R_{nl}(r)Y_{lm}(\theta,\phi)\\ R_{nl}(r) &= \sqrt{\left(\frac{2Z}{na_0}\right)^3\frac{(n-l-1)!}{2n[(n+l)!]}}e^{-Zr/na_0}\left(\frac{2Zr}{na_0}\right)^l L^{2l+1}_{n-l-1}\left(\frac{2Zr}{na_0}\right),\end{aligned} \tag{4.38}$$

where $Y_{lm}(\theta,\phi)$ are spherical harmonics, Z is the atomic number, r is the distance from the nucleus, a_0 is the Bohr radius, and L^{2l+1}_{n-l-1} are generalized Laguerre polynomials. Figure 4.3 shows the results for chromium ($Z = 24$, $3d$ orbitals) and oxygen ($Z = 8$, $2p$ orbitals) on the left, and for ruthenium ($Z = 44$, $4d$ orbitals) and chloride ($Z = 17$, $3p$ orbitals) on the right. We note that for a typical inter-atomic distance 2Å $\sim 3.8a_0$,

the integrals are smaller than their zeroth order approximations (at $d = 0$) by a factor of $\sim 10^{4-6}$.

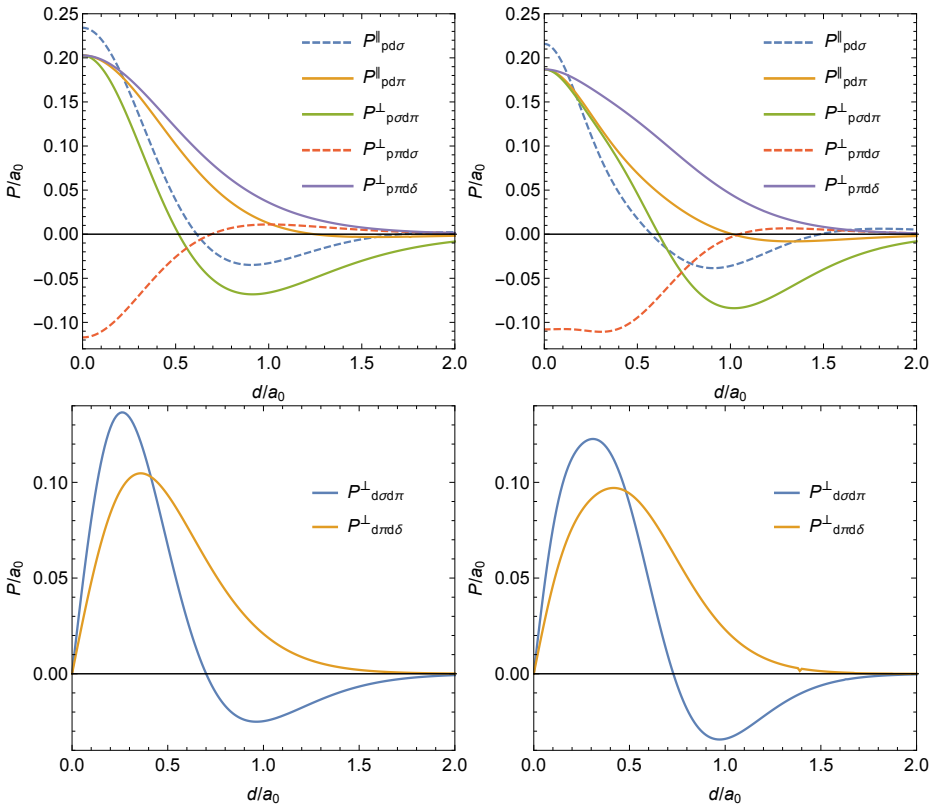

FIGURE 4.3: The different p-d (top) and d-d (bottom) polarization integrals as a function of the atomic spacing d, in units of a_0, the Bohr radius. The cases of chromium and oxygen atoms (left) and ruthenium and chloride atoms (right) are plotted using hydrogen-like atomic orbitals.

Nevertheless, it is important to realize that the hydrogen-like atom model is generally not a very good approximation. This is especially true for $4d$ and $5d$ TM compounds because of the large spatial extent of the actual electronic orbitals. In such a case, the polarization integrals would be enhanced (as for the kinetic hopping integrals) reflecting the higher itinerancy of the system. While first-principle calculations are necessary for a better evaluation of the integrals, the symmetry classification presented here is still valid.

4.5 Microscopic mechanisms

We are now ready to calculate the effective polarization operators originating from the microscopic operators defined in Sec. 4.4. Our goal is to explicitly calculate the allowed coupling constants m_{1-5} in Eq. (4.15) for the edge-sharing geometry, and m_{1-2} in Eq. (4.18) for the corner-sharing geometry. The contributions coming from $\mathbf{P}_{\text{lat}}$ and $\mathbf{P}_{\text{hop}}$ are split as

$$m_i = a\mathbb{A}_i + \mathbb{B}_i, \tag{4.39}$$

where $\mathbb{A}_i$ and $\mathbb{B}_i$ originate from the lattice and hopping polarization operator, respectively. Here the contributions $\mathbb{A}_i$ are unitless while the contributions $\mathbb{B}_i$ have units

of distance coming from the polarization integrals. In the following, we present the calculations in detail and the final results are summarized in Tables 4.5 and 4.6.

4.5.1 Edge-sharing geometry

Lattice polarization

Let us consider the ideal edge-sharing geometry with two TM ions at sites i and j separated by the vector $a\hat{\mathbf{u}}$, and two ligands also separated by a distance a when $\phi = 90°$ as shown in Fig. 4.1. In Appendix B, the calculations are extended to include the $\phi \neq 90°$ case. Choosing the origin for $\mathbf{P}$ at the middle of the bond, the contribution $\mathbf{P}_{\text{lat}}$ from the TM ions is always along $\hat{\mathbf{u}}$ and the contribution from the ligands is perpendicular to it. Without any distortion, it is in the $\hat{\mathbf{v}}$ direction.

Without trigonal distortion, we see in Eq. (4.13) that from symmetry considerations, $m_1 = 0$. Hence, the contribution to $\mathbf{P}_{\text{lat}}$ along the bond coming from the TM ions vanishes due to the high D_{2h} symmetry of the bond. More intuitively, this can be understood from the original microscopic Hamiltonian (4.1). With the trigonal CF $\Delta = 0$, the on-site Hamiltonian is $O(3)$ rotationally invariant because we neglect the e_g orbitals. The bond symmetry is encoded in the hopping matrix which has three eigenvectors corresponding to the three C_2 axes of the D_{2h} group: $\hat{\mathbf{u}}$, $\hat{\mathbf{v}}$, and $\hat{\mathbf{w}}$. The on-site energy eigenstates are grouped into three Kramers pairs (or three states with a pseudospin variable). Because SOC is rotationally invariant, the hopping is completely diagonal with respect to the pseudospins. As the polarization only connect states with different parities, the contribution from $\mathbf{P}_{\text{lat}}^{(\text{TM})}$ along the bond must vanish. When $\Delta \neq 0$, the hopping is no longer diagonal with respect to the pseudospins and a finite contribution is possible.

In fact, when the CF Hamiltonian and the hopping can be simultaneously diagonalized (i.e., when $(\hat{\mathbf{x}} + \hat{\mathbf{y}} + \hat{\mathbf{z}})/\sqrt{3}$ is an eigenvector of the hopping matrix $\hat{T}(C_{2h})$), there is an accidental symmetry and the D_{2h} symmetry is recovered. In this case too, m_1 must vanish. We find that this happens when $t_1 + t_2 - t_3 - t_4 = 0$.

Using perturbation theory at second order in $\mathcal{H}_{\text{hop}}$, we find a contribution to m_1,

$$\mathbf{P}_{\text{lat, eff}}^{(\text{TM})} = \mathbb{A}_1\left[\hat{\mathbf{u}} \cdot \left(\mathbf{S}_i \times \mathbf{S}_j\right)\right] a\hat{\mathbf{u}}. \tag{4.40}$$

From Eq. (4.23),

$$\mathbb{A}_1\left[\hat{\mathbf{u}} \cdot \left(\mathbf{S}_i \times \mathbf{S}_j\right)\right] = P_{ij} - P_{ji}, \tag{4.41}$$

where

$$P_{ij} = \mathbb{P}\mathcal{H}_{\text{hop}}^{ij} \frac{\mathbb{Q}_j}{(E_0 - \mathcal{H}_0)^2} \mathcal{H}_{\text{hop}}^{ji} \mathbb{P}. \tag{4.42}$$

Here, $\mathcal{H}_0 = \mathcal{H}_{\text{SOC}} + \mathcal{H}_{\text{CF}} + \mathcal{H}_{\text{int}}$. However, the calculation is too cumbersome to be performed analytical with the introduction of the trigonal CF. The analytical calculation is made possible by treating both $\mathcal{H}_{\text{hop}}$ and $\mathcal{H}_{\text{CF}}$ as perturbations. At the lowest order (second order in the hopping and first order in Δ),

$$P_{ij} = \left[-\frac{2}{3\lambda} \mathbb{P}_{\frac{1}{2}} \mathcal{H}_{\text{hop}}^{ij} \frac{\mathbb{Q}_j}{(E_0 - \mathcal{H}_0')^2} \mathcal{H}_{\text{hop}}^{ji} \mathbb{P}_{\frac{3}{2}} \mathcal{H}_{\text{CF}} \mathbb{P}_{\frac{1}{2}} + \mathbb{P}_{\frac{1}{2}} \mathcal{H}_{\text{hop}}^{ij} \frac{\mathbb{Q}_j}{(E_0 - \mathcal{H}_0')^2} \mathcal{H}_{\text{CF}} \frac{\mathbb{Q}_j}{E_0 - \mathcal{H}_0'} \mathcal{H}_{\text{hop}}^{ji} \mathbb{P}_{\frac{1}{2}} \right] + \text{H.c.}, \tag{4.43}$$

where $\mathcal{H}_0' = \mathcal{H}_{\text{SOC}} + \mathcal{H}_{\text{int}}$, and $\mathbb{P}_{\frac{1}{2}}$ and $\mathbb{P}_{\frac{3}{2}}$ are the projection operators on the $J = 1/2$ states and the $J = 3/2$ states [defined in Eq. (4.9)], respectively. The full expression

of $\mathbb{A}_1$ is too large to be printed in its entirety, but it can be written as

$$\begin{aligned}\mathbb{A}_1 =&\Delta(t_1+t_2-t_3-t_4)\frac{J_H}{\lambda}\times\frac{\sum_{a+b+c=9} f_{abc}(t_1,t_2,t_3,t_4)U^a J_H^b \lambda^c}{\sum_{a+b+c=12} n_{abc} U^a J_H^b \lambda^c}\\ &\xrightarrow[U\gg J_H,\lambda]{} \sqrt{2}\frac{64}{81}\Delta(t_1+t_2-t_3-t_4)(t_1+t_2+t_3)\frac{J_H}{\lambda U^3},\end{aligned} \tag{4.44}$$

where the functions f_{abc} are linear in t_{1-4} and the quantities n_{abc} are scalars. Note that while Eq. (4.44) vanishes when $J_H = 0$, we find that this is not the case when using exact diagonalization on the two-site cluster. Hence we conclude that some higher order terms remain when $J_H = 0$ in the perturbation theory.

The calculation of $\mathbb{A}_1$ was also performed using perturbation exact in Δ and using exact diagonalization on a two-site system. The perturbation exact in Δ was performed from Eq. (3.31) using a basis in which the interaction Hamiltonian is block-diagonal to accelerate the calculations [62,135]. In Fig. 4.4, we plot $\mathbb{A}_1$ calculated with the three methods: exact diagonalization, perturbation theory (quadratic in the hopping) and from Eq. (4.44) (quadratic in the hopping and linear in the CF distortion). The physical parameters were set to $U = 2310$ meV, $J_H = 320$ meV, $\lambda = 140$ meV, which correspond to typical values for α-$RuCl_3$ [180, 182]. In Fig. 4.4(a), (b), and (c), we set $t_1 = t_3 = 0$ and calculate $\mathbb{A}_1$ as a function of t_2 and Δ. For α-$RuCl_3$, the trigonal CF distortion Δ is typically somewhere between -15 meV and -70 meV (not so small compared to λ), and $t_2 \approx 150$ meV. In Fig. 4.4(d), we also consider finite values for t_1 and t_3 and plot exact diagonalization results for different sets of realistic values. We find that for typical values of the hopping amplitudes, the perturbation theory calculations very well reproduces the exact diagonalization calculations. Moreover, the perturbation theory linear in Δ is, in most cases, a surprisingly good approximation up to relatively large values of Δ as along as $\Delta < \lambda$ (which is usually the case in $4d$ and $5d$ materials due to strong SOC). Interestingly, the behavior depends considerably on the hopping integrals and their relative amplitudes. In particular, the sign of $\mathbb{A}_1$ changes as $|t_3/t_2|$ increases. Finally, we properly observe in Fig. 4.4(c) and (d) the fact that both SOC and the trigonal CF are required in order have a finite $\mathbf{P}$ along the bond. Indeed, $\mathbb{A}_1 \to 0$ for $\Delta \to \pm\infty$, which is equivalent to $\lambda \to 0$.

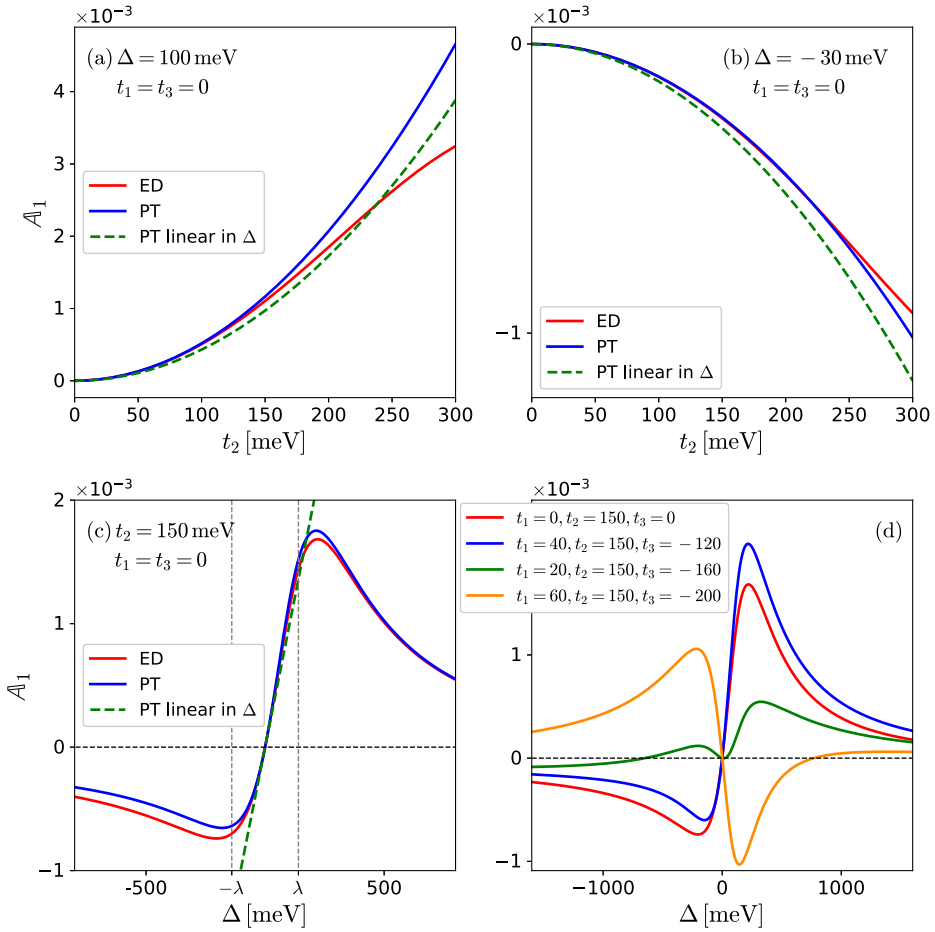

FIGURE 4.4: Numerical evaluation of $\mathbb{A}_1$ in Eq. (4.40). Results using exact diagonalization (ED) (red line), perturbation theory (PT) exact in Δ (blue line), and perturbation theory linear in Δ (green dashed line) are plotted in (a), (b), and (c), for typical values of the physical parameters: $U = 2310$ meV, $J_H = 320$ meV, $\lambda = 140$ meV, and we set $t_1 = t_3 = 0$. It is plotted (a) as a function of t_2 with $\Delta = 100$ meV, (b) as a function of t_2 with $\Delta = -30$ meV, and (c) as a function of Δ with $t_2 = 150$ meV. (d) shows ED calculation of $\mathbb{A}_1$ as a function of Δ for different sets of values t_{1-3} taken from the literature [180, 182]. The values are indicated in meV units.

The second contribution to $\mathbf{P}_{\text{lat}}$ is given in Eq. (4.24). It comes from the intermediate states with holes on the ligands. After integrating out the intermediate states, it is closely related to the terms in the hopping matrix $\hat{T}$ arising from the TM-L-TM processes. However, the two different ligands are in opposite directions from the middle of the bond so that the corresponding matrix is antisymmetric. For simplicity, in the following we neglect the displacement of the ligands caused by the trigonal CF (i.e., we assume that the two ligands are in the $\pm\mathbf{v}$ directions). Hence, we only consider the effect of Δ through $\mathcal{H}_{\text{CF}}$. In this case,

$$\mathbf{P}_{\text{lat}}^{(\text{L})} = \frac{t_{pd\pi}^2}{\Delta_{pd}^2}\left[\mathbf{c}_i^\dagger \begin{pmatrix} 0 & -1 & 0 \\ 1 & 0 & 0 \\ 0 & 0 & 0 \end{pmatrix} \mathbf{c}_j + \text{H.c.}\right]\frac{a}{2}\hat{\mathbf{v}}. \tag{4.45}$$

With $\Delta \neq 0$, we now from symmetry [see Eq. (4.15)] that in general $\mathbb{A}_{2-5}$ are finite.

Neglecting the displacement of the ligands along the **w** axis is equivalent to neglecting $\mathbb{A}_3$ and $\mathbb{A}_5$ so that

$$\mathbf{P}^{(\mathrm{L})}_{\mathrm{lat,\,eff}} = \Big[\mathbb{A}_2\hat{\mathbf{v}}\cdot\big(\mathbf{S}_i\times\mathbf{S}_j\big) + \mathbb{A}_4\hat{\mathbf{w}}\cdot\big(\mathbf{S}_i\times\mathbf{S}_j\big)\Big]a\hat{\mathbf{v}}. \tag{4.46}$$

Moreover, without trigonal CF, only $\mathbb{A}_4$ is finite and $\mathbb{A}_2 = 0$. We already mentioned that an extra U/Δ_{pd} factor is expected in $\mathbb{A}_2$ and $\mathbb{A}_4$ relatively to the contribution $\mathbb{A}_1$ from the TM ions. Hence, the $\mathbb{A}_1$ component should be dominant in the $U \ll \Delta_{pd}$ limit, as long as Δ is not too small (in which case $\mathbb{A}_4$ may be larger).

The results for $\mathbb{A}_2$ and $\mathbb{A}_4$ are given in Table 4.5. The calculation is similar to that of the hopping polarization given in the following.

Hopping polarization

Let us now calculate the coupling constants $\mathbb{B}_{1-5}$ arising from $\mathbf{P}_{\mathrm{hop}}$. In the C_{2h} bond symmetry, the operator (given in Eq. (4.27)) can always be decomposed as

$$\mathbf{P}_{\mathrm{hop}} = \Big[b_1\hat{M}_u\Big]\hat{\mathbf{u}} + \Big[b_2\hat{M}_v + b_4\hat{M}_w\Big]\hat{\mathbf{v}} + \Big[b_5\hat{M}_v + b_3\hat{M}_w\Big]\hat{\mathbf{w}}, \tag{4.47}$$

where the hopping operators $\hat{M}_n$ (with $n \in \{u, v, w\}$) are defined by

$$\begin{aligned}
\hat{M}_u &= \frac{1}{\sqrt{2}}\mathbf{c}_i^\dagger\begin{pmatrix}0&0&1\\0&0&1\\-1&-1&0\end{pmatrix}\mathbf{c}_j + \mathrm{H.c.},\\
\hat{M}_v &= \frac{1}{\sqrt{2}}\mathbf{c}_i^\dagger\begin{pmatrix}0&0&-1\\0&0&1\\1&-1&0\end{pmatrix}\mathbf{c}_j + \mathrm{H.c.},\\
\hat{M}_w &= \mathbf{c}_i^\dagger\begin{pmatrix}0&1&0\\-1&0&0\\0&0&0\end{pmatrix}\mathbf{c}_j + \mathrm{H.c.}.
\end{aligned} \tag{4.48}$$

The hopping operators are defined such that $\hat{M}_n$ transforms as $\big(\mathbf{S}_i\times\mathbf{S}_j\big)_n$ in the higher symmetry D_{2h} group.

Without trigonal distortion, $\hat{M}_n$ is proportional to $\big(\mathbf{S}_i\times\mathbf{S}_j\big)_n$ when projected in the ground state manifold because of the D_{2h} symmetry, and only b_4 and b_5 are non-zero in Eq. (4.47) (which contributes to $\mathbb{B}_4$ and $\mathbb{B}_5$, respectively). With the addition of $\mathcal{H}_{\mathrm{CF}}$, $\big(\mathbf{S}_i\times\mathbf{S}_j\big)_v$ and $\big(\mathbf{S}_i\times\mathbf{S}_j\big)_w$ both transform as the irreducible representation B_u of C_{2h}. Hence, the b_2 and b_4 terms mix and contribute to both $\mathbb{B}_2$ and $\mathbb{B}_4$, and similarly the b_5 and b_3 contribute to both $\mathbb{B}_5$ and $\mathbb{B}_3$. From Eq. (4.25), at first order in $\mathcal{H}_{\mathrm{hop}}$ the effective operators are concisely written as

$$\hat{M}_{n,\mathrm{eff}} = \mathbb{P}\hat{M}_n\frac{\mathbb{Q}}{E_0-\mathcal{H}_0}\mathcal{H}_{\mathrm{hop}}\mathbb{P} + \mathrm{H.c.}, \tag{4.49}$$

where $\mathbb{Q} = \mathbb{Q}_i + \mathbb{Q}_j$ is the projector on polar states. When $\Delta \neq 0$, we also treat $\mathcal{H}_{\mathrm{CF}}$ as a perturbation, as in Eq. (4.43), and at first order in both Δ and the hopping we obtain

$$\begin{aligned}
\hat{M}_{n,\mathrm{eff}} = \Bigg[&-\frac{2}{3\lambda}\mathbb{P}_{\frac{1}{2}}\hat{M}_n\frac{\mathbb{Q}}{E_0-\mathcal{H}_0'}\mathcal{H}_{\mathrm{hop}}\mathbb{P}_{\frac{3}{2}}\mathcal{H}_{\mathrm{CF}}\mathbb{P}_{\frac{1}{2}} - \frac{2}{3\lambda}\mathbb{P}_{\frac{1}{2}}\mathcal{H}_{\mathrm{hop}}\frac{\mathbb{Q}}{E_0-\mathcal{H}_0'}\hat{M}_n\mathbb{P}_{\frac{3}{2}}\mathcal{H}_{\mathrm{CF}}\mathbb{P}_{\frac{1}{2}}\\
&+\mathbb{P}_{\frac{1}{2}}\hat{M}_n\frac{\mathbb{Q}}{E_0-\mathcal{H}_0'}\mathcal{H}_{\mathrm{CF}}\frac{\mathbb{Q}}{E_0-\mathcal{H}_0'}\mathcal{H}_{\mathrm{hop}}\mathbb{P}_{\frac{1}{2}}\Bigg] + \mathrm{H.c.}.
\end{aligned} \tag{4.50}$$

When $\Delta = 0$, we can write $\hat{M}_{n,\text{eff}} = \mathbb{M}_n\big(\mathbf{S}_i \times \mathbf{S}_j\big)\cdot\hat{\mathbf{n}}$ so that $\mathbb{B}_4 = b_4\mathbb{M}_w$ and $\mathbb{B}_5 = b_5\mathbb{M}_v$. From Eq. (4.49) we explicitly calculate

$$\mathbb{M}_n = \frac{\sum_{a+b+c=4} g^n_{abc}(t_1,t_2,t_3)U^a J_H^b \lambda^c}{\sum_{a+b+c=5} m_{abc} U^a J_H^b \lambda^c} \xrightarrow[U\gg J_H]{} -\frac{16}{9}\frac{2t_1+t_3}{U} \equiv \mathbb{M}, \tag{4.51}$$

where the functions g^n_{abc} are linear in t_{1-3} and the quantities m_{abc} are scalars. Here (unlike for Eq. (4.44)), $U \gg \lambda$ is not assumed. We see that Hund's coupling is responsible for the anisotropy as $\mathbb{M}_u = \mathbb{M}_v = \mathbb{M}_w \equiv \mathbb{M}$ when $J_H/U = 0$. This is reminiscent of the effective Hamiltonian which only exhibits the anisotropic Kitaev magnetic interaction when $J_H \neq 0$ [180].

When $\Delta \neq 0$ and in the $U \gg J_H$ limit, we calculate

$$\begin{aligned}
\hat{M}_{u,\text{eff}} &\xrightarrow[U\gg J_H]{} \left[\mathbb{M} - \frac{32}{81}\Delta\frac{2t_1+4t_2+t_3+8t_4}{\lambda U}\right]\big(\mathbf{S}_i\times\mathbf{S}_j\big)\cdot\hat{\mathbf{u}} \\
\hat{M}_{v,\text{eff}} &\xrightarrow[U\gg J_H]{} \left[\mathbb{M} + \frac{32}{81}\Delta\frac{2t_1-4t_2+t_3-8t_4}{\lambda U}\right]\big(\mathbf{S}_i\times\mathbf{S}_j\big)\cdot\hat{\mathbf{v}} + \left[\sqrt{2}\frac{32}{81}\Delta\frac{2t_1+t_3}{\lambda U}\right]\big(\mathbf{S}_i\times\mathbf{S}_j\big)\cdot\hat{\mathbf{w}} \\
\hat{M}_{w,\text{eff}} &\xrightarrow[U\gg J_H]{} \left[\mathbb{M} - \frac{128}{81}\Delta\frac{t_2+2t_4}{\lambda U}\right]\big(\mathbf{S}_i\times\mathbf{S}_j\big)\cdot\hat{\mathbf{w}} + \left[\sqrt{2}\frac{32}{81}\Delta\frac{2t_1+t_3}{\lambda U}\right]\big(\mathbf{S}_i\times\mathbf{S}_j\big)\cdot\hat{\mathbf{v}}.
\end{aligned} \tag{4.52}$$

From Eqs. (4.52) and (4.47), we can relate the contributions $\mathbb{B}_{1-5}$ in Eq. (4.39) to the coefficients b_{1-5}, which we still need to calculate. We note that while the expressions in Eq. (4.52) are only valid in a certain limit, they can be obtained without approximation numerically.

The coefficients b_{1-5} are expressed in terms of the polarization integrals introduced in Sec. 4.4 using Eq. (4.28). Because we neglect their displacement, the two ligands are at a $d = a/\sqrt{2}$ distance in the $\hat{\mathbf{x}}$ and $-\hat{\mathbf{y}}$ directions from site i, and only b_4 and b_5 are finite. We calculate

$$\begin{aligned}
b_4 &= -P^{\perp}_{d\pi d\delta} - \sqrt{2}\frac{P^{\parallel}_{pd\pi}t_{pd\pi}}{\Delta_{pd}}, \\
b_5 &= \frac{1}{4}\Big(\sqrt{6}P^{\perp}_{d\sigma d\pi} - \sqrt{2}P^{\perp}_{d\pi d\delta}\Big) + \sqrt{2}\frac{P^{\perp}_{p\sigma d\pi}t_{pd\pi}}{\Delta_{pd}}.
\end{aligned} \tag{4.53}$$

Therefore, even when $\Delta = 0$, the KNB formula $\mathbf{P} \propto \hat{\mathbf{u}}\times\big(\mathbf{S}_i\times\mathbf{S}_j\big)$ (which corresponds to $b_4 = -b_5$) is only recovered when $a = 0$. Indeed, in this case the d-d integrals vanish and $P^{\parallel}_{pd\pi} = P^{\perp}_{p\sigma d\pi}$. The final expressions for $\mathbb{B}_{1-5}$ are given in Table 4.5.

The expressions taking into account the displacement of the ligands towards the bond ($\phi \neq 90°$ but still along the $\mathbf{v}$ axis) is given in Appendix B.1.

4.5.2 Corner-sharing geometry

Here we repeat the same calculation for the corner-sharing geometry with $\varphi = 180°$ depicted in Fig. 4.1(a) for a bond in the $\hat{\mathbf{x}}$ direction. The more general $\varphi \neq 180°$ case, which lacks inversion symmetry, is considered in Appendix B.2.

Lattice polarization

We show that for the corner-sharing geometry, the lattice polarization vanishes in the ground state manifold. From Eqs. (4.17) and (4.18), we infer that there is no polarization along the bond and $\mathbf{P}^{(TM)}_{\text{lat,eff}} = 0$ even with the tetragonal distortion (which

TABLE 4.5: Coupling coefficients defined in Eqs. (4.15) and (4.39) for the edge-sharing geometry in the $J_H/U \to 0$ limit (and $\lambda/U \to 0$ for $\mathbb{A}_1$). The CF is included through $\mathcal{H}_{\text{CF}}$ but the displacement of the ligands is neglected.

$\mathbb{A}_1$	=	$\sqrt{2}\frac{64}{81}\Delta(t_1+t_2-t_3-t_4)(t_1+t_2+t_3)\frac{J_H}{\lambda U^3}$
$\mathbb{A}_2$	=	$-\frac{t_{pd\pi}^2}{\Delta_{pd}^2}\sqrt{2}\frac{16}{81}\Delta\frac{2t_1+t_3}{\lambda U}$
$\mathbb{A}_3$	=	0
$\mathbb{A}_4$	=	$\frac{t_{pd\pi}^2}{\Delta_{pd}^2}\left[\frac{8}{9}\frac{2t_1+t_3}{U}+\frac{64}{81}\Delta\frac{t_2+2t_4}{\lambda U}\right]$
$\mathbb{A}_5$	=	0
$\mathbb{B}_1$	=	0
$\mathbb{B}_2$	=	$-[P^{\perp}_{d\pi d\delta}+\sqrt{2}\frac{P^{\parallel}_{pd\pi}t_{pd\pi}}{\Delta_{pd}}]\sqrt{2}\frac{32}{81}\Delta\frac{2t_1+t_3}{\lambda U}$
$\mathbb{B}_3$	=	$[\frac{1}{4}\left(\sqrt{6}P^{\perp}_{d\sigma d\pi}-\sqrt{2}P^{\perp}_{d\pi d\delta}\right)+\sqrt{2}\frac{P^{\perp}_{p\sigma d\pi}t_{pd\pi}}{\Delta_{pd}}]\sqrt{2}\frac{32}{81}\Delta\frac{2t_1+t_3}{\lambda U}$
$\mathbb{B}_4$	=	$[P^{\perp}_{d\pi d\delta}+\sqrt{2}\frac{P^{\parallel}_{pd\pi}t_{pd\pi}}{\Delta_{pd}}]\left[\frac{16}{9}\frac{2t_1+t_3}{U}+\frac{128}{81}\Delta\frac{t_2+2t_4}{\lambda U}\right]$
$\mathbb{B}_5$	=	$[\frac{1}{4}\left(\sqrt{6}P^{\perp}_{d\sigma d\pi}-\sqrt{2}P^{\perp}_{d\pi d\delta}\right)+\sqrt{2}\frac{P^{\perp}_{p\sigma d\pi}t_{pd\pi}}{\Delta_{pd}}]\left[-\frac{16}{9}\frac{2t_1+t_3}{U}+\frac{32}{81}\Delta\frac{2t_1-4t_2+t_3-8t_4}{\lambda U}\right]$

we verified using perturbation theory). Moreover, the ligand is located exactly at the middle of the bond so that $\mathbf{P}^{(\text{L})}_{\text{lat}} = 0$ by definition. Therefore, there is no ME effect from the lattice polarization.

Hopping polarization

In the corner-sharing geometry, we directly decompose the microscopic operator $\mathbf{P}_{\text{hop}}$ (given in Eq. (4.27)) into

$$\mathbf{P}_{\text{hop}} = \left[-t_{pd\pi}P^{\perp}_{p\pi d\sigma}\hat{N}_z\right]\hat{\mathbf{y}} + \left[t_{pd\pi}P^{\perp}_{p\pi d\sigma}\hat{N}_y\right]\hat{\mathbf{z}}, \tag{4.54}$$

where $\hat{N}_a = [\mathbf{c}_i^{\dagger}\hat{\mathcal{A}}_a\mathbf{c}_j + \text{H.c.}]$, and $(\hat{\mathcal{A}}_a)_{bc} = \epsilon_{abc}$ for $a = x, y$, and z.

In the $U \gg J_H$ limit, we obtain

$$\begin{aligned}\hat{N}_{z,\text{eff}} &\xrightarrow[U\gg J_H]{} \left[\frac{32}{9}\frac{t}{U}-\frac{64}{81}\Delta\frac{t(U+6\lambda)}{U^2\lambda}\right]\left(\mathbf{S}_i\times\mathbf{S}_j\right)_z \\ \hat{N}_{y,\text{eff}} &\xrightarrow[U\gg J_H]{} \left[\frac{32}{9}\frac{t}{U}+\frac{128}{81}\Delta\frac{t(U-3\lambda)}{U^2\lambda}\right]\left(\mathbf{S}_i\times\mathbf{S}_j\right)_y.\end{aligned} \tag{4.55}$$

In this case too, J_H is responsible for the anisotropy when $\Delta = 0$. The final expressions for the m_1 and m_2 coupling constants of Eq. (4.18) are given in Table 4.6. In this geometry, the KNB formula is respected when $\Delta = 0$ and the deviation emereging from the tetragonal CF roughly scales as Δ/λ relatively to the $\Delta = 0$ contribution. We emphasize that this scaling is only accurate in the $\lambda \gg \Delta$ limit.

TABLE 4.6: Coupling coefficients defined in Eqs. (4.18) and (4.39) for the corner-sharing geometry in the $J_H/U \to 0$ limit. The CF is included through $\mathcal{H}_{\text{CF}}$ but the displacement of the ligands is neglected

$\mathbb{A}_1$	=	0
$\mathbb{A}_2$	=	0
$\mathbb{B}_1$	=	$-t_{pd\pi}P^{\perp}_{p\pi d\sigma}\left[\frac{32}{9}\frac{t}{U} - \frac{64}{81}\Delta\frac{t(U+6\lambda)}{U^2\lambda}\right]$
$\mathbb{B}_2$	=	$t_{pd\pi}P^{\perp}_{p\pi d\sigma}\left[\frac{32}{9}\frac{t}{U} + \frac{128}{81}\Delta\frac{t(U-3\lambda)}{U^2\lambda}\right]$

4.6 Discussion

In this chapter, a theory for the electric polarization in d^5 Mott insulators from electronic mechanisms was developed. In particular, we reconciled two approaches used to explain ME behaviors.

The "hopping polarization" relies on matrix elements such as $\langle d_{xy}|y|p_y\rangle$ and is related to the formalism originally used in the spin-current model [146] and in other extensions [188]. From symmetry considerations, the theory was expanded by classifying the different two-center integrals (without neglecting the ion-ion distance). This classification is reminiscent of the one used by Slater and Koster for the hopping integrals [187].

Secondly, the "lattice polarization", intrinsic to any lattice model and already discussed in Chapter 3, is defined by the positions of the particles on the lattice. ME effects arising from the lattice polarization were first mentioned in Ref. [40] in lattices with triangular loops. Such ME effects were shown to lead to a subgap optical conductivity in some quantum spin liquids in the triangular and kagome lattice. In this chapter, we proved that in multi-orbital systems with strong SOC, the same mechanism based on virtual hopping of the electrons lead to a finite ME effects on single bonds, at *second* order in the hopping Hamiltonian. From our results, we conclude that (i) in the $\Delta_{pd} \gg U$ limit, the $\mathbf{P}^{(\text{L})}_{\text{lat}}$ contribution is suppressed by a factor of U/Δ_{pd} compared to $\mathbf{P}^{(\text{TM})}_{\text{lat}}$, and (ii) the edge-sharing geometry is crucial to observe a finite $\mathbf{P}_{\text{eff}}$ along the TM-TM bond. Indeed, in the corner-sharing geometry, even when $\varphi \neq 180°$ (as shown in Appendix B.2), the effective polarization along the bond vanishes.

We thus stress that, while in the corner-sharing geometry, the polarization is basically $\mathbf{P}_{ij} \propto \hat{\mathbf{e}}_{ij} \times \mathbf{S}_i \times \mathbf{S}_j$ with corrections arising from the CF distortion, in the intrinsically more involved edge-sharing geometry, the spin-polarization coupling always deviates from the KNB formula.

The contributions from the two mechanisms considered, $\mathbf{P}_{\text{hop,eff}}$ and $\mathbf{P}_{\text{lat,eff}}$, are set side by side by comparing the relevant kinetic and polarization integrals. Specifically, if $p_{pd} \gg a \cdot t_{pd}/U$, the $\mathbf{P}_{\text{hop,eff}}$ dominates, and if $p_{pd} \ll a \cdot t_{pd}/U$, $\mathbf{P}_{\text{lat,eff}}$ does. Actually, it is slightly more complex as can be seen in Table 4.5. The leading contribution of $\mathbf{P}_{\text{lat,eff}}$ comes from $\mathbb{A}_1$ and the one of $\mathbf{P}_{\text{hop,eff}}$ from $\mathbb{B}_4$ and $\mathbb{B}_5$. Hence, the lattice polarization as an extra $J_H\Delta/(\lambda U)$ factor relatively to the hopping polarization. In other words, in the limit where $\Delta_{pd}/U \to \infty$, the leading contribution in $\|\mathbf{P}_{\text{lat,eff}}\|/\|\mathbf{P}_{\text{hop,eff}}\|$ scales as $J_H\Delta/(\lambda U) \times a t_{pd}/(p_{pd}U)$. However, because in $4d$ and $5d$ TM compounds the different energy scales are not so distinct ($\Delta \lesssim t_{1-4} \lesssim \lambda \lesssim J_H \lesssim U$), this result might not always be accurate. We also note that the different ME coupling constants m_{1-5} in Eq. (4.39) can be evaluated more accurately by performing the perturbation theory calculations numerically or by using exact diagonalization on finite-size clusters. Nevertheless, complementary first-principle methods are needed to evaluate

the different physical parameters, in particular the polarization integrals which is a new concept and has thus not been calculated yet. The ME effects in d^5 Mott insulators can then be calculated from our results.

The original motivation for the calculations performed in this chapter is the THz optical conductivity observed in α-$RuCl_3$ [30–34]. We thus proposed a potential microscopic origin for the subgap optical conductivity in terms of the charge fluctuation of the electrons. In the following chapter, we calculate the dynamical response of $\mathbf{P}_{\text{eff}}$ and the resulting optical conductivity in the magnetic ground state manifold described with the 'pure Kitaev model'.

Chapter 5

Optical conductivity of ideal Kitaev materials

In this final chapter, motivated by recent experiments of THz spectroscopy of α-$RuCl_3$ [30–34] (some of them shown in Fig. 5.3), we consider the subgap optical conductivity of Kitaev materials using the results for the ME coupling derived in Chapter 4. In particular, the authors of Ref. [31] showed that the continuous absorption spectrum has a large contribution which originates from electric-dipole-induced transitions. That being said, we consider the limit where the low-energy physics is governed by the "pure" Kitaev model which we discuss in detail in Sec. 5.1.

The dynamics of Kitaev materials in the magnetic energy scale is determined from the low-energy effective spin Hamiltonian emerging from the original microscopic Hamiltonian (4.1). Including the trigonal distortion, it generally reads

$$\mathcal{H}_{\text{eff}} = \sum_{\alpha\neq\beta\neq\gamma} \sum_{\langle ij\rangle_\gamma} \left[K S_i^\gamma S_j^\gamma + J \mathbf{S}_i \cdot \mathbf{S}_j + \Gamma S_i^\alpha S_j^\beta + \Gamma'(S_i^\gamma S_j^\alpha + S_i^\alpha S_j^\gamma) \right], \tag{5.1}$$

where $\gamma \in \{x, y, z\}$ and $\langle ij\rangle_\gamma$ denotes the $\langle ij\rangle$ nearest-neighbor bonds in the $\hat{\mathbf{u}}_\gamma$ direction, as depicted in Fig. 5.1. This Hamiltonian is called the KHΓΓ′ model because it contains the Kitaev interaction (the first term), the Heisenberg interaction (the second term), and the anisotropic Γ and Γ′ terms.

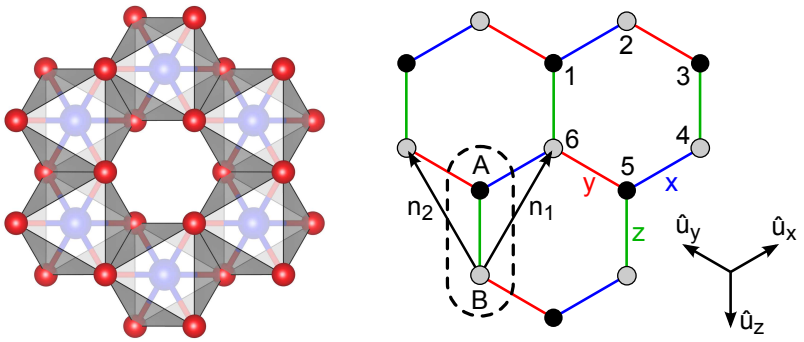

FIGURE 5.1: (Left) Honeycomb crystal structure of Kitaev materials. (Right) Three hexagonal plaquettes of the honeycomb lattice. The different bond types ($\gamma = x, y, z$) are along the unit vectors $\hat{\mathbf{u}}_x$, $\hat{\mathbf{u}}_y$, and $\hat{\mathbf{u}}_z$, respectively. The A and B sublattices are colored in black and grey, respectively. The region encircled by a dashed line represents a unit cell and $\mathbf{n}_1$ and $\mathbf{n}_2$ are vectors connecting neighboring unit cells.

Historically, the Kitaev honeycomb model (the first term in Eq. (5.1)) was introduced in 2006 by A. Kitaev [35]. This model is a rare instance of an exactly solvable 2D interacting quantum model. Moreover, its ground state is a quantum spin liquid, an elusive state of matter fist predicted by Anderson in 1973 [191] but still not conclusively observed experimentally. The Kitaev model is solved in terms of Majorana quasiparticles

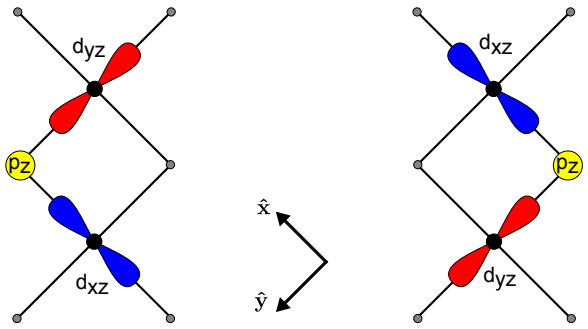

FIGURE 5.2: Orbitals active in the TM-L-TM hopping processes (for a z bond) leading to the Jackeli-Khaliullin mechanism. The black and grey disks represent the TM ions and the ligands, respectively.

and provides an ideal playground to study a whole class of spin liquids thanks to its analyticity [47].

In addition, its potential realization in actual materials was suggested by Jackeli and Khaliullin [49] and the model has attracted a lot of attention in the last decade. The Jackeli-Khaliullin mechanism originates from the TM-L-TM hopping processes with angle $\phi = 90°$ shown in Fig. 5.2. Neglecting the direct hopping, the hopping is described by Eq. (4.12) with $t_2 = \frac{t_{pd\pi}^2}{\Delta_{pd}}$, so that the hopping matrix for the $\gamma = x$, y, and z bonds are

$$T_x = \begin{pmatrix} 0 & 0 & 0 \\ 0 & 0 & t_2 \\ 0 & t_2 & 0 \end{pmatrix}, \qquad T_y = \begin{pmatrix} 0 & 0 & t_2 \\ 0 & 0 & 0 \\ t_2 & 0 & 0 \end{pmatrix}, \qquad T_z = \begin{pmatrix} 0 & t_2 & 0 \\ t_2 & 0 & 0 \\ 0 & 0 & 0 \end{pmatrix}. \tag{5.2}$$

In this case, the effective Hamiltonian is exactly the Kitaev model and only $K \neq 0$ in Eq. (5.1).

That being said, the different potential Kitaev materials mentioned in Chapter 4 all eventually reach a magnetically ordered state below T_N [50–55]. There are thus deviations from the pure Kitaev model [192].

Nevertheless, for α-$RuCl_3$, various experimental results suggest a close proximity to the Kitaev model. These include Raman scattering [56, 57], inelastic neutron scattering [58, 59], THz spectroscopy [30–34], where an unusual broad magnetic excitation was observed, and thermal transport experiments [60, 61], where a finite thermal Hall effect was observed. The observations made in these experiments have been attributed to the fractionalized spin excitations of the Kitaev model.

However, the interpretation of the observations in terms of Majorana quasiparticles is still controversial [173, 193], and the question of the origin of the unorthodox experimental results is not yet settled.

In this chapter, we show that the continuous subgap optical conductivity can be explained in terms Majorana fermions. We combine the results of Chapter 4 for the effective electric polarization operator with the known exact results of the Kitaev model in order to calculate the optical conductivity originating from the Majorana fermions in the 'pure Kitaev limit'. We show that even in this pristine limit, there is a non-trivial contribution to the optical conductivity which matches the experimental results surprisingly well. This suggests that the continuous part of the spectrum of the real material mostly originates from Majorana quasiparticles, even with the addition of the integrability-breaking terms in the Hamiltonian (5.1).

In Fig. 5.3(a), (b), and (c), we show three different THz spectroscopy measurements of α-$RuCl_3$ from Refs. [31], [33], and [32], respectively. The observed subgap optical conductivity is the main motivation for the calculations done in this chapter.

The absorption spectra are shown for different temperatures, and are plotted in terms of different related physical quantities (the real part of optical conductivity in Fig. 5.3(a), the imaginary part of the dielectric constant in Fig. 5.3(b), and the absorption coefficient in Fig. 5.3(c)). In Fig. 5.3(c), the $T = 60$ K spectrum is taken as a reference. In Fig. 5.3(a) and (b), a double-peak structure can be seen with a first peak at around 1.5 meV, and a second broader peak above 4 meV. Moreover, there is a gap below 1 meV. The second peak can also be seen in Fig. 5.3(c) (the frequencies below 2 meV are not shown so that the first peak cannot be seen). In addition, there is a magnon peak at around 2.5 meV in Fig. 5.3(a) and (c) below 6 K, which is due to the magnetic ordering. Note that we do not predict this peak in our calculations because we only consider the spin liquid state.

We also show our final results for the optical conductivity in Fig. 5.3(d) for comparison. A similar figure is also shown in Fig. 5.11 at the end of this chapter. In the rest of the chapter, in particular in Sec. 5.2, we explain how we calculated this plot. The plot shows the subgap optical conductivity calculated in the pure Kitaev model for two different ME mechanisms corresponding to σ'^A and σ'^B (more details are given in Sec. 5.2). The overall two-peak structure with a low-energy gap is also found from our calculations (for α-$RuCl_3$, $J_K \approx 1.5$ meV).

In Sec. 5.1, we first introduce the Kitaev model and its exact solution in terms of Majorana fermions. Then, in Sec. 5.2, we calculate the subgap optical conductivity by combining analytical and numerical methods.

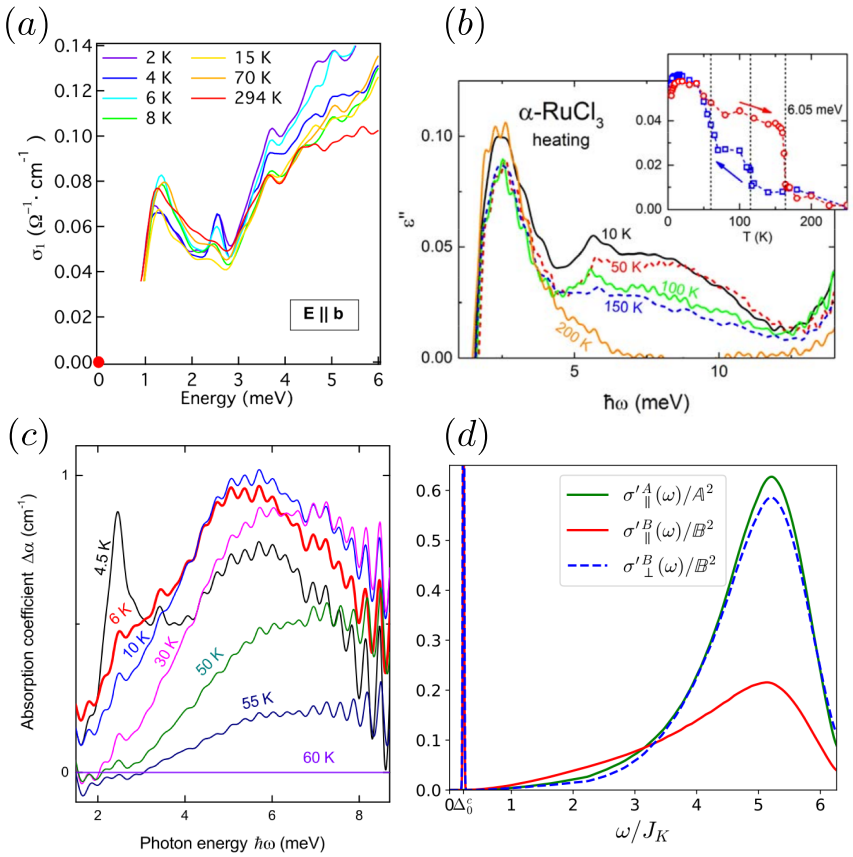

FIGURE 5.3: (a), (b), and (c): THz spectroscopy measurements of α-$RuCl_3$. (d): subgap optical conductivity calculated in the pure Kitaev model. Reprinted figures with permission from Refs. [31] and [32] Copyright (2017) by the American Physical Society, and from Ref. [33].

5.1 The Kitaev honeycomb model

Exact analytical results for the dynamics of the Kitaev model [42] have been used to predict the signatures of Majorana quasiparticles in Raman [43, 47, 57], inelastic neutron [44–47], and resonant x-ray scatterings [48]. Here we present a short derivation of the main analytical properties of the model that we will use to calculate the optical conductivity.

We use the following notation for the Kitaev model,

$$\mathcal{H}_K = -\sum_{a=x,y,z}\sum_{\langle ij\rangle_a} J_K^a \sigma_i^a \sigma_j^a, \tag{5.3}$$

where the Pauli matrices $\boldsymbol{\sigma}_i = 2\mathbf{S}_i$. Later, we will set $J_K^x = J_K^y = J_K^z = J_K$ $(= -K/4)$, but for now we keep the Hamiltonian general. The Hamiltonian (5.3) is solvable due to its macroscopic number of conserved quantities. The most important observation is that on each hexagon of the honeycomb lattice, there is a specific product of Pauli matrices $W_p = \sigma_1^y\sigma_2^z\sigma_3^x\sigma_4^y\sigma_5^z\sigma_6^x$ [refer to Fig. 5.1 for site labels] which satisfies $[W_p, \mathcal{H}_K] = 0$, and for any pair of hexagons $[W_p, W_{p'}] = 0$. Hence, on each plaquette there is a $\mathbb{Z}_2$ conserved quantity $w_p = \pm 1$ (the eigenvalue of W_p). Those operators are usually called $\mathbb{Z}_2$ flux operators and the plaquette p is said to be flux-free for $w_p = 1$ and to have a flux when $w_p = -1$, by analogy with a magnetic flux. For a system with N unit cells and periodic boundary conditions, the full Hilbert space can thus be separated in different flux sectors for different sets of $\{w_1, \ldots, w_N\}$. As there are $2N$ spins for N plaquettes, the total dimension is 2^{2N} and each of the 2^N flux sectors still has a large size of 2^N.

In his seminal paper, Kitaev introduced on each site four Majorana fermions $\hat{c}_i$, $\hat{b}_i^x$, $\hat{b}_i^y$, and $\hat{b}_i^z$ which satisfy usual Majorana fermion anti-commutation relations

$$\{\hat{b}_i^a, \hat{b}_j^b\} = 2\delta_{ij}\delta_{ab}, \qquad \{\hat{b}_i^a, \hat{c}_j\} = 0, \qquad \{\hat{c}_i, \hat{c}_j\} = 2\delta_{ij}, \tag{5.4}$$

where $a, b \in \{x, y, z\}$. They are called Majorana fermions because they anticommute with each other, they are their own complex conjugate $\hat{c}_i^\dagger = \hat{c}_i$, and their square is $\hat{c}_i^2 = 1$. Majorana fermions can be thought of as the "real" and "imaginary" parts of usual "complex" fermions, in the sense that any complex fermion can be decomposed into two Majorana fermions, and inversely, a complex fermion can always be built out of two Majorana fermions. The dimension of the on-site Hilbert space spanned by the four Majorana fermions is 4, and the operators written with a "hat" symbol act in this Hilbert space. For now this is just an arbitrary definition, but a special mapping between the spin on each site and the four Majorana fermions is introduced,

$$\hat{\sigma}_i^a = i\hat{c}_i\hat{b}_i^a \quad \Rightarrow \quad \{\hat{\sigma}_i^a, \hat{\sigma}_i^b\} = 2\delta_{ab}, \quad [\hat{\sigma}_i^a, \hat{\sigma}_j^b] = 0 \quad \text{for } i \neq j, \tag{5.5}$$

and the Hamiltonian becomes

$$\hat{\mathcal{H}}_K = i\sum_a \sum_{\langle ij\rangle_a} J_K^a \hat{u}_{\langle ij\rangle_a}\hat{c}_i\hat{c}_j, \qquad \hat{u}_{\langle ij\rangle_a} = i\hat{b}_i^a\hat{b}_j^a. \tag{5.6}$$

Note that bond operators $\hat{u}_{\langle ij\rangle_a} = -\hat{u}_{\langle ij\rangle_a}$ and we use the convention $i \in A$ sublattice and $j \in B$ sublattice from now on. The variables $\hat{u}_{\langle ij\rangle_a}$ are constants of motion with, again, eigenvalues ± 1. They fix the $\mathbb{Z}_2$ fluxes as we have

$$\hat{W}_p = \hat{u}_{12}\hat{u}_{32}\hat{u}_{34}\hat{u}_{54}\hat{u}_{56}\hat{u}_{16}, \tag{5.7}$$

for the hexagon of Fig. 5.1. Therefore, the Hamiltonian is block diagonal in sectors with different sets of values $\{u_{\langle ij\rangle_a}\}$ ($u_{\langle ij\rangle_a}$, without the hat, refers to the eigenvalue of $\hat{u}_{\langle ij\rangle_a}$) and the problem is reduced to a problem of free fermions in each sector. The Hamiltonian (5.6) is indeed quadratic in the c fermions once the bond variables are fixed. For this reason, the b Majorana fermions are called *flux* fermions and the c Majorana femrions are called *matter* or *itinerant* fermions. A matter fermions moving around a hexagon picks up a phase equal to 0 or π depending on the value $w_p = \pm 1$, hence the analogy with the magnetic flux.

Because the original "physical" Hilbert space of the $2N$ spins is of size 2^{2N}, the new Hilbert space, of size 4^{2N}, is artificially enlarged and a projection to the physical Hilbert space is required for the mapping between spins and Majorana to be reliable. This mapping is uniquely defined by requiring the correct SU(2) spin algebra $[\hat{\sigma}^a, \hat{\sigma}^b] = 2i\epsilon_{abc}\hat{\sigma}^c$, which translates to imposing

$$\hat{D}_j \equiv \hat{c}_j \hat{b}_j^x \hat{b}_j^y \hat{b}_j^z = 1. \tag{5.8}$$

The operators $\hat{D}_j$ commute with all the spin operators and with $\hat{\mathcal{H}}_K$ in the enlarged Hilbert space (but not with the $\hat{u}_{ij}$'s). In other words, a state in the enlarged Hilbert space is physical if it satisfies $\hat{D}_j |\Psi\rangle_{\text{phys}} = |\Psi\rangle_{\text{phys}}$ for all sites j. Because $\hat{D}_j$ has eigenvalues ± 1, the projector P onto the physical Hilbert space is

$$P = \prod_i \frac{1 + \hat{D}_i}{2} \tag{5.9}$$

Note that several choices for the sets $\{u_{\langle ij\rangle_a}\}$ can give the same set of fluxes $\{w_p\}$. This is due to the extra dimensions of the enlarged Hilbert space, which can be understood as an extra gauge choice [47]. At each site, we can introduce the gauge transformation $\hat{c}_i \to \theta_i \hat{c}_i$ and $\hat{u}_{ij} \to \theta_i \hat{u}_{ij} \theta_j$, where $\theta_i \pm 1$. It does not change the flux in each plaquette and thus the energy spectrum for a given set $\{w_p\}$ is also invariant. This gives 2^{2N} different choices for the gauge variable and thus the 2^{4N} states of the enlarged Hilbert space are 2^{2N}-fold degenerate.

Furthermore, we introduce the complex *bond fermions* on each bond $\langle ij\rangle_a$ ($i \in A$, $j \in B$) defined by

$$\hat{\chi}_{\langle ij\rangle_a} = \frac{1}{2}(\hat{b}_i^a + i\hat{b}_j^a), \qquad a = x, y, z. \tag{5.10}$$

In terms of the bond fermions,

$$\begin{aligned} \hat{\sigma}_i^a &= i\hat{c}_i\left(\hat{\chi}_{\langle ij\rangle_a} + \hat{\chi}^\dagger_{\langle ij\rangle_a}\right) \quad (i \in A) \\ \hat{\sigma}_j^a &= c_j\left(\hat{\chi}_{\langle ij\rangle_a} - \hat{\chi}^\dagger_{\langle ij\rangle_a}\right) \quad (j \in B) \\ \hat{u}_{\langle ij\rangle_a} &= 2\hat{\chi}^\dagger_{\langle ij\rangle_a}\hat{\chi}_{\langle ij\rangle_a} - 1 \end{aligned} \tag{5.11}$$

Therefore, when working with states $|\Psi\rangle$ for which the bond fermion numbers $\hat{\chi}^\dagger_{\langle ij\rangle_a}\hat{\chi}_{\langle ij\rangle_a}$ (and thus $\hat{u}_{\langle ij\rangle}$) are good quantum numbers, any states can can be written as a direct product

$$|\Psi\rangle = |F\rangle \otimes |M\rangle\,, \tag{5.12}$$

where $\hat{\chi}^\dagger_{ij}\hat{\chi}_{ij}|F\rangle = \frac{u_{ij}+1}{2}|F\rangle$ (F stands for *flux* and M for *matter*). The spin operator $\hat{\sigma}_i^a$ has two effects: it adds a Majorana matter fermion at site i and it changes the bond fermion number of the bond $\langle ij\rangle_a$, which is equivalent to changing $u_{\langle ij\rangle_a} \to$

$-u_{\langle ij\rangle_a}$. Therefore, the operator $\hat{\sigma}_i^a$ adds a π flux to the two hexagons sharing the bond $\langle ij\rangle_a$. This is depicted in Fig. 5.4 for a $a = x$ bond. Moreover, because the $u_{\langle ij\rangle_a}$'s are constants of motion, this property is also true at finite time for $\hat{\sigma}_i^a(t)$ (in the Heisenberg picture).

5.1.1 Diagonalization and Bogoliubov transformation

In a given flux sector and choice for the set $\{u_{ij} = \pm 1\}$, the Hamiltonian is conveniently written in matrix notation as

$$\hat{\mathcal{H}}_K = \frac{i}{2}\begin{pmatrix} c_A & c_B \end{pmatrix}\begin{pmatrix} 0 & M \\ -M^\intercal & 0 \end{pmatrix}\begin{pmatrix} c_A \\ c_B \end{pmatrix}, \tag{5.13}$$

where c_A (c_B) is an array of the N matter Majorana fermions on the A (B) sublattice. The real matrix M is defined by the relation $M_{ij} = J_K^a u_{\langle ij\rangle_a}$ (for a a-bond) and we have used the relation $u_{ij} = -u_{ji}$. Note that in this notation, the indices $i \in A$ and $j \in B$ are mutually exclusive. The eigenmodes are obtained from a canonical transformation of the above matrix [194]. In order to do so we use the singular value decomposition of the matrix M (possible for any real matrix) into $M = USV^\intercal$ where U and V are $N\times N$ orthogonal matrices, $S = \mathrm{diag}(\epsilon_1, \ldots \epsilon_N)$ is an $N \times N$ diagonal matrix, and $\epsilon_{1-N} \geq 0$ are the singular values of M. We define the new Majorana fermions

$$\begin{aligned} (\hat{d}'_1, \ldots, \hat{d}'_N) &= c_A U, \\ (\hat{d}''_1, \ldots, \hat{d}''_N) &= c_B V, \end{aligned} \tag{5.14}$$

and the Hamiltonian becomes $\mathcal{H}_K = i\sum_{m=1}^N \epsilon_m \hat{d}'_n \hat{d}''_n$. In terms of the complex fermions

$$\hat{a}_m = \frac{1}{2}\left(\hat{d}'_m + i\hat{d}''_m\right) \qquad \hat{a}_m^\dagger = \frac{1}{2}\left(\hat{d}'_m - i\hat{d}''_m\right), \tag{5.15}$$

the Hamiltonian takes the canonical form

$$\mathcal{H}_K = \sum_m \omega_m\left(\hat{a}_m^\dagger \hat{a}_m - \frac{1}{2}\right), \tag{5.16}$$

where $\omega_m = 2\epsilon_m$. This diagonalization procedure can be done with systems of $2N \sim 10000$ spins in less than a minute (we used systems of size up to 80×80 unit cells, or 12800 spins).

The eigenmodes of two different flux sectors corresponding to the Hamiltonians

$$\hat{\mathcal{H}}_a = \sum_m \omega_m^a\left(\hat{a}_m^\dagger \hat{a}_m - \frac{1}{2}\right) \qquad \text{and} \qquad \hat{\mathcal{H}}_b = \sum_m \omega_m^b\left(\hat{b}_m^\dagger \hat{b}_m - \frac{1}{2}\right) \tag{5.17}$$

are related by the Bogoliubov transformation $\hat{b}_m^\dagger = \sum_n \left(\mathcal{X}_{mn}\hat{a}_n^\dagger + \mathcal{Y}_{mn}\hat{a}_n\right)$, or

$$\begin{pmatrix} \mathcal{X}^* & \mathcal{Y}^* \\ \mathcal{Y} & \mathcal{X} \end{pmatrix}\begin{pmatrix} a \\ a^\dagger \end{pmatrix} = \begin{pmatrix} b \\ b^\dagger \end{pmatrix}, \tag{5.18}$$

where $a = (\hat{a}_1, \ldots, \hat{a}_N)$ and $b = (\hat{b}_1, \ldots, \hat{b}_N)$. The transformation matrices obey the conditions

$$\begin{aligned} \mathcal{X}\mathcal{X}^\dagger + \mathcal{Y}\mathcal{Y}^\dagger &= 1, \qquad & \mathcal{X}\mathcal{Y}^\intercal + \mathcal{Y}\mathcal{X}^\intercal &= 0, \\ \mathcal{X}^\dagger\mathcal{X} + \mathcal{Y}^\intercal\mathcal{Y}^* &= 1, \qquad & \mathcal{X}^\intercal\mathcal{Y}^* + \mathcal{Y}^\dagger\mathcal{X} &= 0, \end{aligned} \tag{5.19}$$

and are related to the orthogonal matrices U_a, V_a, and U_b, V_b (of the two singular value decompositions) by

$$\begin{aligned}\mathcal{X} &= \frac{1}{2}\Big[U_b^\intercal U_a + V_b^\intercal V_a\Big],\\ \mathcal{Y} &= \frac{1}{2}\Big[U_b^\intercal U_a - V_b^\intercal V_a\Big].\end{aligned} \tag{5.20}$$

Note that Eq. (5.18) exists for any pair of sets of complex fermions. However, in our construction, $\mathcal{X}^* = \mathcal{X}$ and $\mathcal{Y}^* = \mathcal{Y}$ as the matrices are actually always real.

Finally, the Hamiltonians $\hat{\mathcal{H}}_a$ and $\hat{\mathcal{H}}_b$ define two ground states $\left|M_0^a\right\rangle$ and $\left|M_0^b\right\rangle$ with energies $E_0^a = -\sum_m \omega_m^a/2$ and $E_0^b = -\sum_m \omega_m^b/2$, respectively. The states exist in the "matter" Hilbert space and are generally related by the expression [195]

$$\left|M_0^b\right\rangle = \left[\det\left(\mathcal{X}^\dagger\mathcal{X}\right)\right]^{1/4} e^{-\frac{1}{2}\sum_{mn}\mathcal{F}_{mn}\hat{a}_m^\dagger\hat{a}_n^\dagger}\left|M_0^a\right\rangle, \tag{5.21}$$

where

$$\mathcal{F} = [\mathcal{X}^*]^{-1}\mathcal{Y}^*. \tag{5.22}$$

In our case, we also have $\left[\det\left(\mathcal{X}^\dagger\mathcal{X}\right)\right]^{1/4} = \sqrt{|\det(\mathcal{X})|}$ and thus

$$\left\langle M_0^b\middle|M_0^a\right\rangle = \sqrt{|\det(\mathcal{X})|}. \tag{5.23}$$

Note that the relation (5.21) only makes sense when the two ground states have the same *matter fermion parity*. In general, Hamiltonians quadratic in Majorana fermions do not conserve the total fermion number, but conserve the total fermion parity, defined by the parity of the total number of complex fermions in any basis. Indeed, Bogoliubov transformations between different bases conserve the parity [see Eq. (5.18)]. If the ground states $\left|M_0^a\right\rangle$ and $\left|M_0^b\right\rangle$ have different parities, we have $\left\langle M_0^b\middle|M_0^a\right\rangle = 0$ and $\det(\mathcal{X}) = 0$, and thus $\mathcal{F}$ is ill-defined.

5.1.2 Ground state flux sector

To find the overall ground state of $\hat{\mathcal{H}}_K$, one must, in principle, compare the ground state energies for all possible flux sectors. Fortunately, Lieb showed that in such translationally invariant system, the ground state is in the flux free sector [196] (except for small system sizes [197]). We still have a gauge choice and simply choose $u_{ij} = 1$ on all bonds.

In the flux-free sector, the Hamiltonian is easily solved after a Fourier transform to momentum space. In order to do so, we first introduce complex fermions on each z-bond (green bonds in Fig. 5.1) $\langle ij\rangle_z$ at position $\mathbf{r}$ (which denotes the position of the unit cells of the $\langle ij\rangle_z$ bond),

$$\hat{f}_{\mathbf{r}} = \frac{1}{2}(\hat{c}_{A\mathbf{r}} + i\hat{c}_{B\mathbf{r}}), \qquad \text{and} \qquad \hat{f}_{\mathbf{r}}^\dagger = \frac{1}{2}(\hat{c}_{A\mathbf{r}} - \hat{c}_{B\mathbf{r}}). \tag{5.24}$$

In vector notation, this is equivalent to $c_A = f^\dagger + f$ and $c_B = i(f^\dagger - f)$, and the Hamiltonian reads [47]

$$\hat{\mathcal{H}}_0 = \frac{1}{2}\begin{pmatrix} f^\dagger & f\end{pmatrix}\begin{pmatrix} h & \Delta \\ \Delta^\dagger & -h\end{pmatrix}\begin{pmatrix} f \\ f^\dagger\end{pmatrix}, \tag{5.25}$$

where

$$h = M + M^\intercal = h^\intercal,$$
$$\Delta = M^\intercal - M = -\Delta^\intercal. \tag{5.26}$$

After the Fourier transform

$$\hat{f}_{\mathbf{q}} = \frac{1}{\sqrt{N}} \sum_{\mathbf{r}} e^{i\mathbf{q}\cdot r} \hat{f}_{\mathbf{r}}, \qquad \hat{f}^\dagger_{\mathbf{q}} = \frac{1}{\sqrt{N}} \sum_{\mathbf{r}} e^{-i\mathbf{q}\cdot r} \hat{f}^\dagger_{\mathbf{r}} = (\hat{f}_{\mathbf{q}})^\dagger,$$
$$\Delta_{\mathbf{q}} = \sum_{\mathbf{r}-\mathbf{r}'} e^{i\mathbf{q}\cdot(\mathbf{r}-\mathbf{r}')} \Delta_{\mathbf{r}-\mathbf{r}'}, \qquad h_{\mathbf{q}} = \sum_{\mathbf{r}-\mathbf{r}'} e^{i\mathbf{q}\cdot(\mathbf{r}-\mathbf{r}')} h_{\mathbf{r}-\mathbf{r}'}, \tag{5.27}$$

we obtain

$$\hat{\mathcal{H}}_0 = \frac{1}{2} \sum_{\mathbf{q}} \begin{pmatrix} \hat{f}^\dagger_{\mathbf{q}} & \hat{f}_{-\mathbf{q}} \end{pmatrix} \begin{pmatrix} h_{\mathbf{q}} & \Delta_{\mathbf{q}} \\ -\Delta_{\mathbf{q}} & -h_{\mathbf{q}} \end{pmatrix} \begin{pmatrix} \hat{f}_{\mathbf{q}} \\ \hat{f}^\dagger_{-\mathbf{q}} \end{pmatrix}. \tag{5.28}$$

The Hamiltonian is just like a Bogoliubov-de Gennes Hamiltonian for superconductors. Finally, we notice that $\Delta_{\mathbf{q}} = -2i\,\mathrm{Im}(M_{\mathbf{q}})$ and $h_{\mathbf{q}} = 2\,\mathrm{Re}(M_{\mathbf{q}})$, where

$$M_{\mathbf{q}} = \sum_{\mathbf{r}-\mathbf{r}'} e^{i\mathbf{q}\cdot(\mathbf{r}-\mathbf{r}')} M_{\mathbf{r}-\mathbf{r}'} = \sum_{a=x,y,z} J^a_K e^{i\mathbf{q}\cdot\mathbf{n}_a}. \tag{5.29}$$

Here $\mathbf{n}_x = \mathbf{n}_1 = (1/2, \sqrt{3}/2)$, $\mathbf{n}_y = \mathbf{n}_2 = (-1/2, \sqrt{3}/2)$ and $\mathbf{n}_z = (0,0)$ [see Fig. 5.1]. Because $\Delta_{\mathbf{q}}$ is imaginary, the Hamiltonian is made diagonal by a simple Bogoliubov transformation [35],

$$\begin{pmatrix} \hat{a}_{\mathbf{q}} \\ \hat{a}^\dagger_{-\mathbf{q}} \end{pmatrix} = \begin{pmatrix} \cos\theta_{\mathbf{q}} & -i\sin\theta_{\mathbf{q}} \\ -i\sin\theta_{\mathbf{q}} & \cos\theta_{\mathbf{q}} \end{pmatrix} \begin{pmatrix} \hat{f}_{\mathbf{q}} \\ \hat{f}^\dagger_{-\mathbf{q}} \end{pmatrix}, \tag{5.30}$$

where $\tan 2\theta_{\mathbf{q}} = \mathrm{Im}(M_{\mathbf{q}})/\,\mathrm{Re}(M_{\mathbf{q}})$. The final Hamiltonian is given by

$$\mathcal{H}_0 = \sum_{\mathbf{q}} 2\left|M_{\mathbf{q}}\right| \left(\hat{a}^\dagger_{\mathbf{q}} \hat{a}_{\mathbf{q}} - \frac{1}{2} \right). \tag{5.31}$$

Therefore, the ground state $|M_0\rangle$ (such that $\hat{a}_{\mathbf{q}}|M_0\rangle = 0$) is a spin liquid with two types of excitations: static localized flux excitations (i.e., with a π flux in some plaquettes), and itinerant matter Majorana fermions. The flux excitations are gapped while the matter excited states $\hat{a}^\dagger_{\mathbf{q}}|M_0\rangle$ have an energy spectrum $\omega_{\mathbf{q}} = 2\left|J^x_K e^{i\mathbf{q}\cdot\mathbf{n}_1} + J^y_K e^{i\mathbf{q}\cdot\mathbf{n}_1} + J^z_K\right|$ which is gapless if $\left|J^z_K\right| < \left|J^x_K\right| + \left|J^y_K\right|$ (or any of the other two permutations), and otherwise gapped. In particular, at the isotropic point $J^x_K = J^x_K = J^z_K \equiv J_K$ that we consider thereupon, the dispersion is gapless and very similar to that of graphene with a linear dispersion at the two Dirac points.

5.1.3 Projection operator

Finally, we state some properties of the projection operator P in Eq. (5.9), which will prove useful to calculate the correlation functions. By expanding the product,

$$P = \frac{1}{2^{2N}} \left(1 + \sum_{i=1}^{2N} \hat{D}_i + \sum_{i_1<i_2}^{2N} \hat{D}_{i_1}\hat{D}_{i_2} + \cdots + \prod_i \hat{D}_i \right) = \frac{1}{2^{2N}} \sum_{\{i\}} \prod_{i\in\{i\}} \hat{D}_i, \tag{5.32}$$

where in the last summation, $\{i\}$ runs over all possible subsets of distinct indices in $\Lambda = \{1, \ldots, 2N\}$. We also define $\hat{D} = \prod_{i\in\Lambda} \hat{D}_i$. Because $\hat{D}_i^2 = 1$, the products $\prod_{i\in S} \hat{D}_i$ for two complementary sets $S = \{i\}$ and $S = \Lambda\backslash\{i\}$ only differ by a factor $\hat{D}$ so that P

can be factorized [198, 199],

$$P = \left(\frac{1}{2^{2N-1}} \sum_{\{i\}}{}' \prod_{i \in \{i\}} \hat{D}_i \right) \left(\frac{1 + \hat{D}}{2} \right) \equiv P' P_0, \tag{5.33}$$

where the primed sum only runs on half the possible subsets so that if $\{i\}$ is included, $\Lambda \backslash \{i\}$ is not. Therefore, the value of $D = \pm 1$ (a product of all $8N$ Majorana fermions), splits the Hilbert space in two: if $D = -1$ the system is unphysical and the projection vanishes, and if $D = 1$, the projection P' results in a superposition of all states with nonequivalent bond fermion numbers $\hat{\chi}^\dagger_{\langle ij \rangle_a} \hat{\chi}_{\langle ij \rangle_a}$ but with the same w_p fluxes in all plaquettes (i.e., a superposition of all gauge choices $\{\theta_i\}$). Because the operators $\hat{D}_i$ commute with all the spin operators, for any operators $\hat{O}$ written in terms of spins and any unprojected state $|\Psi\rangle$ in the $D = 1$ sector,

$$\langle \Psi | P \hat{O} P | \Psi \rangle = \langle \Psi | \hat{O} P' | \Psi \rangle \,. \tag{5.34}$$

Furthermore, we note that in P', except for the identity, there are only terms that changes the bond fermions numbers on one or several bonds. Thus, if $\hat{O}$ does not change any bond fermion numbers,

$$\frac{\langle \Psi | P \hat{O} P | \Psi \rangle}{|\langle \Psi | P | \Psi \rangle|^2} = \langle \Psi | \hat{O} | \Psi \rangle \,, \tag{5.35}$$

and the projection into the physical Hilbert space is unnecessary [47, 198]. In the calculations of the following section, only a few operators will require the projection P', which, by imposing the conservation of the bond fermions numbers, boils down to simply keeping one of the terms in P' (typically a pair $\hat{D}_i \hat{D}_j$).

The value $D = \pm 1$ is very closely related to the total fermion parity of the system, $(-1)^{N_\chi + N_f}$, where $N_\chi = \sum_{\langle ij \rangle} \hat{\chi}^\dagger_{ij} \hat{\chi}_{ij}$ is the total flux fermion number, and $N_f = \sum_{\mathbf{r}} \hat{f}^\dagger_{\mathbf{r}} f_{\mathbf{r}}$ the total matter fermion number. However, in Ref. [199], the authors showed that the actual relation between D and the fermion parities in a system with periodic conditions is not trivial and has an extra factor

$$D = (-1)^\theta (-1)^{N_\chi + N_f}, \tag{5.36}$$

where θ depends on the shape of the system, its size, and the choice of boundary conditions. In fact, their results show that the calculations of physical quantities in other works were performed without the extra θ factor and thus in the unphysical sector. Indeed, the authors of Ref. [194] made clear that the ground state in the flux-free sector $|0\rangle = |F_0\rangle \otimes |M_0\rangle$ is actually always unphysical for systems with periodic boundary conditions.

Nevertheless, in Ref. [194], the authors showed that in the thermodynamics limit $N \to \infty$, dynamical quantities such as the spin structure factor converge to the same values in the physical and unphysical sectors so that the distinction is not important. For this reason, in the following section we use $|0\rangle$ as if it were a physical state.

5.2 Dynamical correlation functions

The main objective of this chapter is to calculate the subgap optical conductivity of idealized Kitaev materials using the pure Kitaev model. It is instructive to first calculate the more "simple" dynamical spin susceptibility.

5.2.1 Spin susceptibility

The dynamical spin susceptibility is directly related to the spin structure factor which has been calculated analytically in the Kitaev model [42, 44, 45, 47] and is typically measured with inelastic neutron scattering. For THz spectroscopy and ESR measurements, the actual measured quantity is the imaginary part of the dynamical spin susceptibility $\chi''(\omega)$, which is related to the spin structure factor $S(\omega)$ via the fluctuation-dissipation theorem $\chi''(\omega) = (1 - e^{-\beta\omega})S(\omega)/2$, where β is the inverse temperature. We only consider the $T = 0$ situation at the Γ point $\mathbf{q} = (0, 0)$. Using the Kubo formula (see Eq. (1.13)) we have

$$\chi_{ab}(\omega) = \frac{i}{4S} \sum_{ij} \int_0^\infty dt e^{i\omega t} \langle 0|\sigma_i^a(t)\sigma_j^b(0)|0\rangle , \tag{5.37}$$

where S is the total surface[1]. Here i and j both run over all lattice sites, and $|0\rangle = |F_0\rangle|M_0\rangle$ is the ground state of the Kitaev model. The ground state is flux-free and we work with the gauge where $u_{ij} = 1$ on all bonds. It follows that $\hat{\chi}_{ij}^\dagger|F_0\rangle = 0$ and $\langle F_0|\hat{\chi}_{ij} = 0$. Using Eq. (5.11) to express the spin operators in terms of Majorana fermions, we obtain

$$\begin{aligned}
\langle 0|\hat{\sigma}_i^a(t)\hat{\sigma}_j^b(0)|0\rangle &= -\langle M_0|\langle F_0| e^{i\mathcal{H}t}\hat{c}_i\hat{\chi}^\dagger_{\langle ik\rangle_a} e^{-i\mathcal{H}t}\hat{c}_j\hat{\chi}_{\langle jl\rangle_b}|F_0\rangle|M_0\rangle , && \text{if} \quad i \in A, j \in A,\\
&= \ \ i\langle M_0|\langle F_0| e^{i\mathcal{H}t}\hat{c}_i\hat{\chi}^\dagger_{\langle ik\rangle_a} e^{-i\mathcal{H}t}\hat{c}_j\hat{\chi}_{\langle lj\rangle_b}|F_0\rangle|M_0\rangle , && \text{if} \quad i \in A, j \in B,\\
&= -i\langle M_0|\langle F_0| e^{i\mathcal{H}t}\hat{c}_i\hat{\chi}^\dagger_{\langle ki\rangle_a} e^{-i\mathcal{H}t}\hat{c}_j\hat{\chi}_{\langle jl\rangle_b}|F_0\rangle|M_0\rangle , && \text{if} \quad i \in B, j \in A,\\
&= -\langle M_0|\langle F_0| e^{i\mathcal{H}t}\hat{c}_i\hat{\chi}^\dagger_{\langle ki\rangle_a} e^{-i\mathcal{H}t}\hat{c}_j\hat{\chi}_{\langle lj\rangle_b}|F_0\rangle|M_0\rangle , && \text{if} \quad i \in B, j \in B,
\end{aligned} \tag{5.38}$$

where k is the nearest-neighbor connected to i by an a-bond and l is the nearest-neighbor connected to j by a b-bond. We now want to integrate out the flux degree of freedom. As already mentioned, a single spin operator reverses the fluxes of the two plaquettes on each side of the bond it affects. Because we take the expectation value in the flux-free sector, the two pairs of plaquettes affected by $\hat{\sigma}_i^a$ and $\hat{\sigma}_j^b$ must be the same so that the product $\hat{\sigma}_i^a\hat{\sigma}_j^b$ does not change the flux in any hexagon. This is due to the orthogonality of the sectors with different flux patterns. Therefore, only terms with $a = b$ and either $\langle ij\rangle_a$ forming a nearest-neighbor pair or $i = j$ give finite contributions, as can be seen in Fig. 5.4. This was first shown in Ref. [42] using the selection rules of the flux sectors that we just described.

To show this concretely, we use the important relation

$$\chi^\dagger_{\langle ij\rangle_\gamma} e^{-i\mathcal{H}t} = e^{-i(\mathcal{H}+V_{ij})t}\chi^\dagger_{\langle ij\rangle_\gamma}, \tag{5.39}$$

where $V_{ij} = -2iJ_K\hat{c}_i\hat{c}_j$. Let $\mathcal{H}_0$ be the matter Hamiltonian in the flux-free sector with $u = 1$ on all bonds. Then, Eq. (5.39) implies that $\mathcal{H}_0 + V_{ij}$ is the Hamiltonian with all bond variables $u = 1$ except on the bond $\langle ij\rangle_\gamma$ where $u_{\langle ij\rangle_\gamma} = -1$.

[1] In order to obtain a physical quantity, one must replace $S \to a_\perp S$ where $a_\perp$ is the inter-layer distance

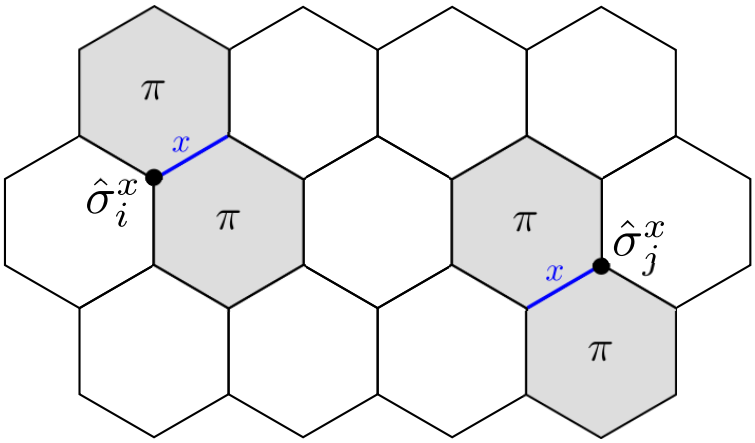

FIGURE 5.4: Effects of $\hat{\sigma}^a_i$ and $\hat{\sigma}^b_j$ with $a = b = x$ when applied on the flux-free sector. Both operators create two adjacent π fluxes, indicated in grey, which share the x bond connected to site i or j (indicated in blue), respectively. The two pairs of fluxes only cancel if $a = b$ and if i and j are nearest neighbors separated by a a-bond (or if $i = j$).

In the final step, we use $\langle F_0|\hat{\chi}^\dagger_{\langle ik\rangle_a}\hat{\chi}_{\langle lj\rangle_b}|F_0\rangle = \delta_{il}\delta_{jk}$ (and thus $a = b$). For each bond, say the a-bond $\langle ij\rangle_a$ with $i \in A$ and $j \in B$, we have four terms

$$\begin{aligned}
\langle 0|\hat{\sigma}^a_{Ai}(t)\hat{\sigma}^a_{Ai}(0)|0\rangle &= \quad \langle M_0|\, e^{i\mathcal{H}_0 t}\hat{c}_{Ai}e^{-i(\mathcal{H}_0+V_{ij})t}\hat{c}_{Ai}\,|M_0\rangle\,,\\
\langle 0|\hat{\sigma}^a_{Ai}(t)\hat{\sigma}^a_{Bj}(0)|0\rangle &= -i\,\langle M_0|\, e^{i\mathcal{H}_0 t}\hat{c}_{Ai}e^{-i(\mathcal{H}_0+V_{ij})t}\hat{c}_{Bj}\,|M_0\rangle\,,\\
\langle 0|\hat{\sigma}^a_{Bj}(t)\hat{\sigma}^a_{Ai}(0)|0\rangle &= \quad i\,\langle M_0|\, e^{i\mathcal{H}_0 t}\hat{c}_{Bj}e^{-i(\mathcal{H}_0+V_{ij})t}\hat{c}_{Ai}\,|M_0\rangle\,,\\
\langle 0|\hat{\sigma}^a_{Bj}(t)\hat{\sigma}^a_{Bj}(0)|0\rangle &= \quad \langle M_0|\, e^{i\mathcal{H}_0 t}\hat{c}_{Bj}e^{-i(\mathcal{H}_0+V_{ij})t}\hat{c}_{Bj}\,|M_0\rangle\,.
\end{aligned} \tag{5.40}$$

The spin correlation is thus ultra-short ranged. All correlations beyond nearest-neighbor pairs vanish completely. Moreover, only pairs of spins along the same direction (corresponding to the bond direction) give a finite contribution. Hence $\chi''_{ab} = 0$ for $a \neq b$ and χ'' is isotropic because of the C_3 symmetry ($\chi_{xx} = \chi_{yy} = \chi_{zz} \equiv \chi$). This flux selection rule, which originates in the static nature of the fluxes, is easily understood by graphically identifying the fluxes affected by a given operator as shown in Fig. 5.4. This will be useful when dealing with the optical conductivity as we will have four-spin operators.

For the spin structure factor, there exist different methods of calculating the matrix elements (5.40), such as a mapping to the exact X-ray edge problem [44, 47]. Here, we use the so-called "few-particle response" approach as it is also applicable for the electric-dipole-induced response. In the following, we show how to use this approach in order to calculate the optical conductivity.

We have two matter Hamiltonians: the flux-free Hamiltonian $\mathcal{H}_0 \equiv \mathcal{H}_a$ (all $u_{\langle ij\rangle}$'s = 1) and the two-flux Hamiltonian $\mathcal{H}_0 + V_{ij} \equiv \mathcal{H}_b$ (all $u_{\langle ij\rangle}$'s = 1 except for $u_{\langle ij\rangle} = -1$), and we use the notations introduced in Sec. 5.1.1. In the Lehmann representation,

$$\left\langle M^a_0\right| e^{i\mathcal{H}_a t}\hat{c}_i e^{-i\mathcal{H}_b t}\hat{c}_j\left|M^a_0\right\rangle = \sum_\lambda e^{-i\Delta_\lambda t}\left\langle M^a_0\right|\hat{c}_i\left|\lambda\right\rangle\left\langle\lambda\right|\hat{c}_j\left|M^a_0\right\rangle, \tag{5.41}$$

where $\Delta_\lambda = E^b_\lambda - E^a_0$, $\mathcal{H}_a\left|M^a_0\right\rangle = E^a_0\left|M^a_0\right\rangle$, and $|\lambda\rangle$ are the eigenstates of $\mathcal{H}_b$ with energies E^b_λ, so that $\sum_\lambda |\lambda\rangle\langle\lambda| = 1$. After a Fourier transform and keeping only the imaginary

part in Eq. (5.37), we obtain

$$\chi''(\omega) = \frac{1}{6\sqrt{3}}\Big(\Pi_{Ai,Ai} - i\Pi_{Ai,Bj} + i\Pi_{Bj,Ai} + \Pi_{Bj,Bj}\Big), \tag{5.42}$$

where

$$\Pi_{kl}(\omega) = \pi \sum_{\lambda} \langle M_0^a|\hat{c}_k|\lambda\rangle\langle\lambda|\hat{c}_l|M_0^a\rangle \delta(\omega - \Delta_\lambda). \tag{5.43}$$

In Eq. (5.42), we used the fact that there are N bonds of any type (x, y, or z) so that we can just multiply by N the contribution of a single bond, in this case an arbitrary $\langle ij\rangle$ bond. Furthermore, the total surface is $S = Ns_h$ where $s_h = (3\sqrt{3}/2)a^2$ is the area of a single hexagon and a is the length of the bonds (which we set to unity). We also used the fact that Π_{kl} is real when k and l are on the same sublattice and purely imaginary when on different sublattices, as we show shortly. Interestingly, even though the system is gapless, the spin susceptibility must vanish below a so-called flux gap $\Delta_0^b = E_0^b - E_0^a \approx 0.263 J_K$ because only transitions from the flux-free sector to the two-flux sectors are allowed.

In the few-particle response approach, we write the states $|\lambda\rangle$ with M excited fermions as

$$|\lambda\rangle = \hat{b}^\dagger_{\lambda_1}\hat{b}^\dagger_{\lambda_2}\ldots\hat{b}^\dagger_{\lambda_M}\left|M_0^b\right\rangle, \tag{5.44}$$

with energy $E_\lambda = \sum_{m=1}^{M}\omega^b_{\lambda_m} + E_0^b$.

We verify numerically that the ground states $\left|M_0^a\right\rangle = |M_0\rangle$ and $\left|M_0^b\right\rangle$ have the same fermion parity[2]. Hence, only states with odd M contribute. In fact, it was shown in Refs. [43, 47] that the contribution to the total weight of the response quickly decreases for increasing M, and that single-particle excitations ($M = 1$) capture 98% of the total weight. In the following, we derive a way to systematically calculate the response for any M and explicitly consider the excited states with $M = 1$ and $M = 3$.

All that is left to do is to calculate the different matrix elements $\left\langle M_0^a\middle|\hat{c}_k\middle|\lambda\right\rangle$. This is done explicitly by using the Bogoliubov transformation (5.18) and the relation between the ground states $\left|M_0^a\right\rangle$ and $\left|M_0^b\right\rangle$ in Eq. (5.21). For the single-particle states we find

$$\begin{aligned}\left\langle M_0^a\middle|\hat{c}_{Ai}\hat{b}^\dagger_\lambda\middle|M_0^b\right\rangle &= \sqrt{|\det(\mathcal{X})|}\left(U_a\mathcal{X}^{*-1}\right)_{i\lambda}\\ \left\langle M_0^a\middle|\hat{c}_{Bj}\hat{b}^\dagger_\lambda\middle|M_0^b\right\rangle &= -i\sqrt{|\det(\mathcal{X})|}\left(V_a\mathcal{X}^{*-1}\right)_{j\lambda},\end{aligned} \tag{5.45}$$

where we used different identities in Eq. (5.19) to simplify the equations. In addition, because in our specific construction we showed that $\mathcal{X}$ is real, we see that the single-particle contribution to Π_{kl} is real (imaginary) for sites on the same sublattice (different sublattices). The three-particle matrix elements are found to be (after a

[2] This is not always true in the anisotropic case $J_K^x \neq J_K^y \neq J_K^z$.

number of simplifications)

$$\begin{aligned}
\left\langle M_0^a \middle| \hat{c}_{Ai} \hat{b}^\dagger_{\lambda_1} \hat{b}^\dagger_{\lambda_2} \hat{b}^\dagger_{\lambda_3} \middle| M_0^b \right\rangle = \quad & \sqrt{|\det(\mathcal{X})|} \Big[\left(U_a \mathcal{X}^{*-1}\right)_{i\lambda_1} \left(\mathcal{Y} \mathcal{X}^{*-1}\right)_{\lambda_2\lambda_3} \\
& + \left(U_a \mathcal{X}^{*-1}\right)_{i\lambda_2} \left(\mathcal{Y} \mathcal{X}^{*-1}\right)_{\lambda_3\lambda_1} \\
& + \left(U_a \mathcal{X}^{*-1}\right)_{i\lambda_3} \left(\mathcal{Y} \mathcal{X}^{*-1}\right)_{\lambda_1\lambda_2} \Big], \\
\left\langle M_0^a \middle| \hat{c}_{Bj} \hat{b}^\dagger_{\lambda_1} \hat{b}^\dagger_{\lambda_2} \hat{b}^\dagger_{\lambda_3} \middle| M_0^b \right\rangle = -i & \sqrt{|\det(\mathcal{X})|} \Big[\left(V_a \mathcal{X}^{*-1}\right)_{j\lambda_1} \left(\mathcal{Y} \mathcal{X}^{*-1}\right)_{\lambda_2\lambda_3} \\
& + \left(V_a \mathcal{X}^{*-1}\right)_{j\lambda_2} \left(\mathcal{Y} \mathcal{X}^{*-1}\right)_{\lambda_3\lambda_1} \\
& + \left(V_a \mathcal{X}^{*-1}\right)_{j\lambda_3} \left(\mathcal{Y} \mathcal{X}^{*-1}\right)_{\lambda_1\lambda_2} \Big].
\end{aligned} \tag{5.46}$$

In general, we have a sort of modified Wick's theorem, which is already apparent in Eq. (5.46). It is consistent with some matrix elements calculated in other works, but yields significantly simplified expressions. It is written as

$$\left\langle M_0^a \middle| x_1 \dots x_{2n} \middle| M_0^b \right\rangle = \left(\sqrt{|\det(\mathcal{X})|} \right)^{1-n} \sum (-1)^P \left\langle M_0^a \middle| x_{i_1} x_{j_1} \middle| M_0^b \right\rangle \dots \left\langle M_0^a \middle| x_{i_n} x_{j_n} \middle| M_0^b \right\rangle, \tag{5.47}$$

where the sum is over all partitions of $1, \dots, 2n$ into pairs $\{(i_1, j_1), \dots, (i_n, j_n)\}$ with $i_m < j_m$, and P is the permutation that takes $1, \dots, 2n$ to $i_1, j_1, \dots, i_n, j_n$. Furthermore, the operators x_i can be any linear combination of matter fermions, both complex and Majorana (i.e., any linear combination of $\hat{c}_i$, $\hat{b}_\lambda$, $\hat{b}^\dagger_\lambda$, $\hat{a}_m$, and $\hat{a}^\dagger_m$). In particular, we have

$$\left\langle M_0^a \middle| \hat{b}^\dagger_{\lambda_1} \hat{b}^\dagger_{\lambda_2} \middle| M_0^b \right\rangle = \sqrt{|\det(\mathcal{X})|} \left(\mathcal{Y} \mathcal{X}^{*-1}\right)_{\lambda_1\lambda_2}, \tag{5.48}$$

which, when combined with Eqs. (5.45) and (5.47) reproduces Eq. (5.46). For states with $M > 3$, we thus just have to keep adding extra $\left\langle M_0^a \middle| \hat{b}^\dagger_\lambda \hat{b}^\dagger_{\lambda'} \middle| M_0^b \right\rangle$ terms. This shows that indeed Π_{kl} is always real (imaginary) for sites on the same sublattice (different sublattices).

The spin susceptibility from single-particle excitations and three-particle excitations is plotted in Fig. 5.5, and is consistent with the results of Ref. [44].

5.2.2 Optical conductivity

In order to calculate the optical response of the Kitaev materials from the effective low-energy polarization operator $\mathbf{P}_{\text{eff}}$, we need to know its dynamical evolution in the low-energy manifold. The low-energy optical conductivity is thus

$$\sigma^\alpha(\omega) = \frac{\omega}{V} \int_0^\infty dt e^{i\omega t} \langle 0 | P^\alpha_{\text{eff}}(t) P^\alpha_{\text{eff}}(0) | 0 \rangle, \tag{5.49}$$

where $\mathbf{P}_{\text{eff}} = \sum_{\langle ij \rangle} \mathbf{P}_{ij}$ and, in the C_{2h} bond symmetry group [see Eq. (4.15)],

$$\mathbf{P}_{ij} = \begin{pmatrix} m_1 & 0 & 0 \\ 0 & m_2 & m_4 \\ 0 & m_5 & m_3 \end{pmatrix}_{\mathcal{B}'_\gamma \mathcal{B}'_\gamma} (\mathbf{S}_i \times \mathbf{S}_j), \tag{5.50}$$

where the matrix $\hat{m}$ is explicitly written in the $\mathcal{B}'_\gamma = \{\hat{\mathbf{u}}_\gamma, \hat{\mathbf{v}}_\gamma, \hat{\mathbf{w}}_\gamma\}$ basis attached to the bond $\langle ij \rangle_\gamma$ (see Fig. 4.1), and $\hat{\mathbf{u}}_\gamma$ is along the bond and corresponds to the vectors in Fig. 5.1. Note that $\hat{\mathbf{v}}_\gamma$ and $\hat{\mathbf{w}}_\gamma$ are not simply in-plane and out-of-plane vectors as is seen in Fig. 4.2. Specifically, in terms of the $\mathcal{B} = \{\hat{\mathbf{x}}, \hat{\mathbf{y}}, \hat{\mathbf{z}}\}$ basis fixed by the octahedral

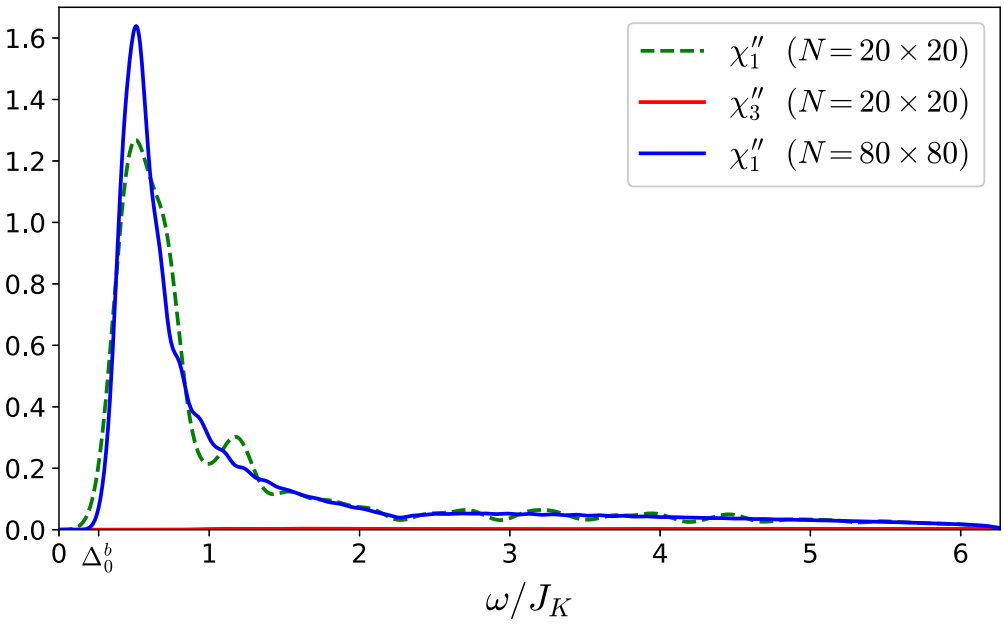

FIGURE 5.5: Dynamical spin susceptibility from single-particle excitations $\chi_1''(\omega)$ and three-particle excitations $\chi_3''(\omega)$ in units of $1/J_K$. The computations were performed in a system of $N = 20 \times 20$ unit cells (with Gaussian broadening $\delta = 0.1J_K$) and of $N = 80 \times 80$ unit cells (with $\delta = 0.05J_K$) only for χ_1''. Only frequencies up to $\omega = \Delta_0^b + \omega_N^b$ are shown for χ_3''.

CF shown in Fig. 5.6 (see also Fig. 4.1),

$$\begin{aligned}
\hat{\mathbf{u}}_x &= \frac{1}{\sqrt{2}}(\hat{\mathbf{y}} - \hat{\mathbf{z}}) & \hat{\mathbf{u}}_y &= \frac{1}{\sqrt{2}}(\hat{\mathbf{z}} - \hat{\mathbf{x}}) & \hat{\mathbf{u}}_z &= \frac{1}{\sqrt{2}}(\hat{\mathbf{x}} - \hat{\mathbf{y}}) \\
\hat{\mathbf{v}}_x &= \frac{1}{\sqrt{2}}(\hat{\mathbf{y}} + \hat{\mathbf{z}}) & \hat{\mathbf{v}}_y &= \frac{1}{\sqrt{2}}(\hat{\mathbf{z}} + \hat{\mathbf{x}}) & \hat{\mathbf{v}}_z &= \frac{1}{\sqrt{2}}(\hat{\mathbf{x}} + \hat{\mathbf{y}}) \\
\hat{\mathbf{w}}_x &= \hat{\mathbf{x}} & \hat{\mathbf{w}}_y &= \hat{\mathbf{y}} & \hat{\mathbf{w}}_z &= \hat{\mathbf{z}}
\end{aligned} \tag{5.51}$$

The matrix elements m_{1-5} are given in Table 4.5.

Two remarks are in order. First, we have to remember that we consider the pure Kitaev limit. That is, only the hopping $t_2 \neq 0$ and $\Delta = 0$ in the original Hubbard model. The matrix elements of $\hat{m}$ should therefore reflect this limit. Concretely, from Table 4.5, we thus only have two finite parameters: $m_4 = \mathbb{B}_4$ and $m_5 = \mathbb{B}_5$. Moreover, $\mathbb{B}_4 \approx -\mathbb{B}_5$ for small atomic spacing. However, if the lattice polarization mechanism is dominant, $p_{\text{eff}} \ll a\, t_{\text{eff}}/U$ and $\Delta \neq 0$, then the polarization is along the bond and it also makes sense to consider a finite $m_1 = \mathbb{A}_1 \propto \Delta$ at first order in the trigonal distortion Δ. Secondly, the matrix $\hat{m}$ is the same for every bond when written in a bond-dependent basis $\mathcal{B}'_\gamma$. We thus need to rewrite the coupling in a bond-independent basis in order to calculate the optical conductivity. For Kitaev materials, the Ising axes in the $\sum_{\langle ij \rangle} S_i^\gamma S_j^\gamma$ Hamiltonian are the axes of the $\mathcal{B} = \{\hat{\mathbf{x}}, \hat{\mathbf{y}}, \hat{\mathbf{z}}\}$ basis fixed by the octahedral CF. It is convenient to choose a basis $\tilde{\mathcal{B}} = \{\mathbf{X}, \mathbf{Y}, \mathbf{Z}\}$ for the polarization where $\mathbf{X}$ and $\mathbf{Y}$ are in the plane and $\mathbf{Z}$ is out-of-plane. For concreteness, let us choose the vectors as indicated in Fig. 5.6. (In the end, $\sigma_\alpha(\omega)$ turns out to

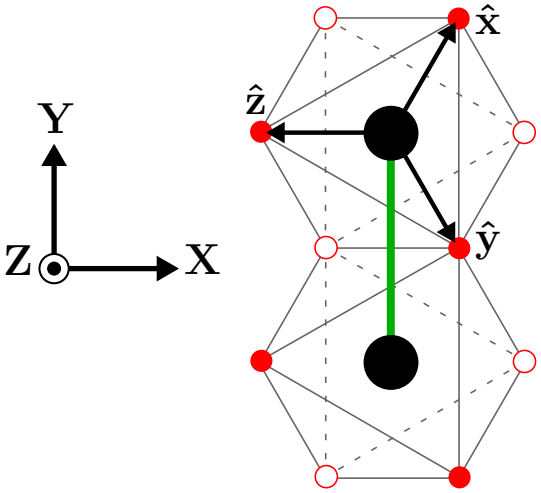

FIGURE 5.6: Single z-bond of a Kitaev material with two magnetic sites (large black circles) and the surrounding ligands (red circles). The bases $\mathcal{B} = \{\hat{\mathbf{x}}, \hat{\mathbf{y}}, \hat{\mathbf{z}}\}$ and $\tilde{\mathcal{B}} = \{\mathbf{X}, \mathbf{Y}, \mathbf{Z}\}$ are shown. The filled (empty) red circles are the ligands above (below) the magnetic sites, in the Z direction.

be isotropic in the 2D plane, so that the orientation of the basis in the plane is not important.) The bases $\tilde{\mathcal{B}}$ for $\mathbf{P}_{ij}$ and $\mathcal{B}$ for $\mathbf{S}_i \times \mathbf{S}_j$ are thus independent of the bond type and the coupling matrix becomes

$$\begin{pmatrix} P^X_{ij} \\ P^Y_{ij} \\ P^Z_{ij} \end{pmatrix}_{\tilde{\mathcal{B}}} = \hat{m}^\gamma \begin{pmatrix} (\mathbf{S}_i \times \mathbf{S}_j)_x \\ (\mathbf{S}_i \times \mathbf{S}_j)_y \\ (\mathbf{S}_i \times \mathbf{S}_j)_z \end{pmatrix}_{\mathcal{B}}, \tag{5.52}$$

where

$$\hat{m}^\gamma \equiv \mathcal{R}_{\mathcal{B}'_\gamma \to \tilde{\mathcal{B}}} \begin{pmatrix} m_1 & 0 & 0 \\ 0 & m_2 & m_4 \\ 0 & m_5 & m_3 \end{pmatrix} \mathcal{R}_{\mathcal{B} \to \mathcal{B}'_\gamma}. \tag{5.53}$$

Here, $\mathcal{R}_{\mathcal{B}_1 \to \mathcal{B}_2}$ stands for the change of basis from basis $\mathcal{B}_1$ to $\mathcal{B}_2$. Using Einstein notation, Eq. (5.52) is written as

$$P^\alpha_{\langle ij \rangle_\gamma} = \frac{1}{4} \hat{m}^\gamma_{\alpha\beta} \epsilon_{\beta ab} \sigma^a_i \sigma^b_j. \tag{5.54}$$

We are now in a position to calculate the matrix elements $\langle 0 | P^\alpha_{ij}(t) P^\alpha_{kl}(0) | 0 \rangle$. From the flux selection rule, we can considerably reduce the number of relevant terms. Without loss of generality, let us consider a z-bond. Because $a \neq b$ in Eq. (5.54), the operator $\sigma^a_i \sigma^b_j$ always creates a pair of π fluxes: both σ^a_i and σ^b_j create two π fluxes but there is always one hexagon where two π fluxes add and cancel. The six corresponding operators are shown in Fig. 5.7. For the first two operators $O_1 \equiv \sigma^x_i \sigma^y_j$ and $O_2 \equiv \sigma^y_i \sigma^x_j$, no other operators in $\mathbf{P} = \sum_{ij} \mathbf{P}_{ij}$ create the same flux pattern. Hence, the correlation functions $\langle O_1(t) O_1(0) \rangle$, $\langle O_1(t) O_2(0) \rangle$, $\langle O_2(t) O_1(0) \rangle$, and $\langle O_2(t) O_2(0) \rangle$ appear in $\langle P^\alpha(t) P^\alpha(0) \rangle$. Using the mirror symmetry $(\mathbf{X}, \mathbf{Y}, \mathbf{Z}) \to (-\mathbf{X}, \mathbf{Y}, \mathbf{Z})$ of the Kitaev spin Hamiltonian, one can show that there are only two independent correlation

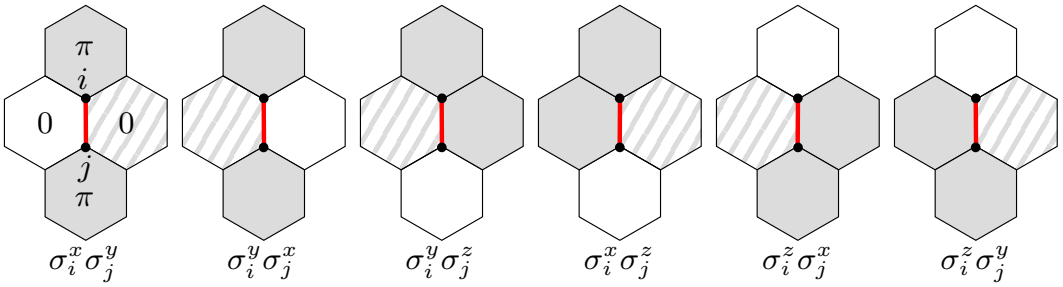

FIGURE 5.7: Different spin operators appearing in $\mathbf{P}_{ij}$ for a z-bond $\langle ij\rangle_z$ and their respective flux configurations. The grey plaquettes indicate where the π fluxes are created and the striped plaquettes indicate were two π fluxes cancel each other.

functions,

$$C_1(t) \equiv \langle O_1(t)O_1(0)\rangle = \langle O_2(t)O_2(0)\rangle, \qquad C_2(t) \equiv \langle O_1(t)O_2(0)\rangle = \langle O_2(t)O_1(0)\rangle, \tag{5.55}$$

which are the same for any bonds (due to C_3 and translation symmetry). For the other four operators, it is not so simple because the same flux patterns are possible for bonds *other* than $\langle ij\rangle_\gamma$. All operators in $\mathbf{P} = \sum_{ij}\mathbf{P}_{ij}$ creating the same pair of fluxes as the third operator in Fig. 5.7 ($\sigma_i^y\sigma_j^z$) are shown in Fig. 5.8 and labelled O_{3-6}. Moreover, we explicitly labelled from 1 to 6 the six sites which are relevant for the operators. From these operators, we have a maximum of 16 new correlation func-

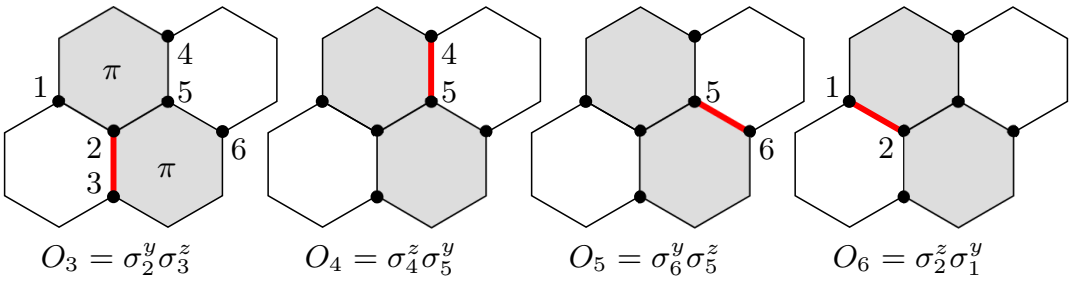

FIGURE 5.8: All the spin operators appearing in $\sum_{kl}\mathbf{P}_{kl}$ which create the same pair of flux as $O_3 = \sigma_i^y\sigma_j^z$. The bond corresponding to the operators are indicated in red. The grey plaquettes show where the π fluxes are created and the six relevant sites are labelled from 1 to 6.

tions $\langle O_m(t)O_n(0)\rangle$, with $m, n = 3, \ldots 6$. However, as before, most of them are related by mirror symmetry and there are only four independent correlation functions,

$$\begin{aligned} C_3(t) &\equiv \langle O_3(t)O_3(0)\rangle, & C_4(t) &\equiv \langle O_3(t)O_4(0)\rangle, \\ C_5(t) &\equiv \langle O_3(t)O_5(0)\rangle, & C_6(t) &\equiv \langle O_3(t)O_6(0)\rangle. \end{aligned} \tag{5.56}$$

Finally, the last three flux configurations for the $\langle ij\rangle_z$ bond in Fig. 5.7 are also simply related by mirror symmetries and the corresponding correlation functions involve the same $C_{3-6}(t)$.

Let us now explicitly write $\langle P^{\alpha}_{ij}(t) \sum_{kl} P^{\alpha}_{kl}(0)\rangle$ as a function of $C_{1-6}(t)$ using Eq. (5.54). In order to do so, we split P^{α}_{ij} into the six operators of Fig. 5.7 and obtain

$$\begin{aligned}\sum_{kl}\langle P^{\alpha}_{\langle ij\rangle_z}(t)P^{\alpha}_{kl}(0)\rangle = \quad & \frac{1}{16}\Big[(m^z_{\alpha z})^2(C_1(t)-C_2(t)) \\ & + (m^z_{\alpha z})^2(C_1(t)-C_2(t)) \\ & + (m^z_{\alpha x})^2(C_3(t)-C_4(t)) + m^z_{\alpha x}m^y_{\alpha x}(C_5(t)-C_6(t)) \\ & + (m^z_{\alpha y})^2(C_3(t)-C_4(t)) + m^z_{\alpha y}m^x_{\alpha y}(C_5(t)-C_6(t)) \\ & + (m^z_{\alpha y})^2(C_3(t)-C_4(t)) + m^z_{\alpha y}m^x_{\alpha y}(C_5(t)-C_6(t)) \\ & + (m^z_{\alpha x})^2(C_3(t)-C_4(t)) + m^z_{\alpha x}m^y_{\alpha x}(C_5(t)-C_6(t))\Big], \end{aligned} \tag{5.57}$$

where each line comes from one of the operators in Fig. 5.7 (in the same order). Summing over all the $\langle ij\rangle$ bonds, we get

$$\begin{aligned}\langle P^{\alpha}(t)P^{\alpha}(0)\rangle = & \frac{N}{8}\sum_{\gamma}\Big[(m^{\gamma}_{\alpha\gamma})^2(C_1(t)-C_2(t))\Big] \\ & + \frac{N}{8}\sum_{\gamma\neq\nu\neq\mu}\Big[(m^{\gamma}_{\alpha\mu})^2(C_3(t)-C_4(t)) + m^{\gamma}_{\alpha\mu}m^{\nu}_{\alpha\mu}(C_5(t)-C_6(t))\Big]. \end{aligned} \tag{5.58}$$

Using Eq. (5.52) it becomes

$$\begin{aligned}\langle P^X(t)P^X(0)\rangle =& \frac{N}{16}(\sqrt{2}m_3-m_4)^2(C_1(t)-C_2(t)) + \frac{N}{16}\Big[3m_1^2+(m_2-\sqrt{2}m_5)^2\Big](C_3(t)-C_4(t)) \\ & + \frac{N}{32}\Big[3m_1(m_1+2m_2-2\sqrt{2}m_5)-(m_2-\sqrt{2}m_5)^2\Big](C_5(t)-C_6(t)), \\ \langle P^Y(t)P^Y(0)\rangle =& \langle P^X(t)P^X(0)\rangle, \\ \langle P^Z(t)P^Z(0)\rangle =& \frac{N}{8}\Big[(m_3+\sqrt{2}m_4)^2(C_1(t)-C_2(t)) \\ & + (\sqrt{2}m_2+m_5)^2(C_3(t)-C_4(t)+C_5(t)-C_6(t))\Big], \end{aligned} \tag{5.59}$$

which shows that the optical conductivity is isotropic in the plane. We also verify $\langle P^{\alpha}(t)P^{\beta}(0)\rangle = 0$ for $\alpha \neq \beta$.

The final step consists of calculating the correlation functions $C_{1-6}(t)$ and their Fourier transforms using the Majorana formalism. There are three different flux sectors to consider: the flux-free sector, the two-flux sector with adjacent π fluxes, and the two-flux sector with π fluxes separated by a bond. To simplify the notation, we write all the operator in the same four-hexagon cluster centered around the $\langle 25\rangle$ x-bond, i.e., we use the $\langle ij\rangle = \langle 25\rangle_x$ bond for the C_1 and C_2 correlation function, as shown in Fig. 5.9. We need to calculate the expectation values of the four-spin

operators (we drop the hat symbol to lighten the notation)

$$\begin{aligned}
C_1(t) &= \langle M_0|\langle F_0|\sigma_2^x(t)\sigma_5^y(t)\sigma_2^x(0)\sigma_5^y(0)|F_0\rangle|M_0\rangle\\
C_2(t) &= \langle M_0|\langle F_0|\sigma_2^x(t)\sigma_5^y(t)\sigma_2^y(0)\sigma_5^x(0)P'|F_0\rangle|M_0\rangle\\
C_3(t) &= \langle M_0|\langle F_0|\sigma_2^y(t)\sigma_3^z(t)\sigma_2^y(0)\sigma_3^z(0)|F_0\rangle|M_0\rangle\\
C_4(t) &= \langle M_0|\langle F_0|\sigma_2^y(t)\sigma_3^z(t)\sigma_4^z(0)\sigma_5^y(0)|F_0\rangle|M_0\rangle\\
C_5(t) &= \langle M_0|\langle F_0|\sigma_2^y(t)\sigma_3^z(t)\sigma_6^y(0)\sigma_5^z(0)P'|F_0\rangle|M_0\rangle\\
C_6(t) &= \langle M_0|\langle F_0|\sigma_2^y(t)\sigma_3^z(t)\sigma_2^z(0)\sigma_1^y(0)P'|F_0\rangle|M_0\rangle\,.
\end{aligned} \tag{5.60}$$

Note that for $C_2(t)$, $C_5(t)$, and $C_6(t)$, while the flux in each hexagon is left unchanged by the four-spin operators, the bond fermion numbers are changed on some bonds. Hence, Eq. (5.35) cannot be used and the projector P' onto the physical Hilbert space is necessary. Here, it amounts to replacing P' with D_2D_5, which reads

$$D_2D_5 = -iu_{\langle 25\rangle_x}c_2c_5(\chi^\dagger_{\langle 2\cdot\rangle_y}+\chi_{\langle 2\cdot\rangle_y})(\chi^\dagger_{\langle 2\cdot\rangle_z}+\chi_{\langle 2\cdot\rangle_z})(\chi^\dagger_{\langle\cdot 5\rangle_y}-\chi_{\langle\cdot 5\rangle_y})(\chi^\dagger_{\langle\cdot 5\rangle_z}-\chi_{\langle\cdot 5\rangle_z}), \tag{5.61}$$

where $\langle i\cdot\rangle_\gamma$ refers to the γ-bond that includes the site i (e.g., $\langle 2\cdot\rangle_z = \langle 23\rangle$).

We do not show the detailed calculation but simply state the main steps. As before, we first integrate out the flux sector. Then, we are left with an expression with either four or six matter fermions. For instance,

$$C_3(t) = -\langle M_0|e^{i\mathcal{H}_0 t}c_2c_3e^{-i(\mathcal{H}_0+V_{21}+V_{23})t}c_2c_3|M_0\rangle\,. \tag{5.62}$$

For the matter Hamiltonian $\mathcal{H}(\{u\})$ in a general flux sector in the gauge defined by $\{u_{\langle ij\rangle_\gamma}\}$, we have

$$c_i\mathcal{H}(\{u\})c_i = \mathcal{H}(\{\tilde{u}\}), \qquad \text{where} \quad \tilde{u}_{\langle mn\rangle} = \begin{cases} -u_{\langle mn\rangle} & \text{if } i=m \text{ or } n\\ u_{\langle mn\rangle} & \text{else}\end{cases}. \tag{5.63}$$

Then, from the relation $c_ie^Oc_i = e^{c_iOc_i}$, which is equivalent to a change of gauge, we obtain

$$C_3(t) = \langle M_0|e^{i\mathcal{H}_0 t}c_3e^{-i(\mathcal{H}_0+V_{25})t}c_3|M_0\rangle\,. \tag{5.64}$$

This is exactly the kind of expressions that we obtained for the spin susceptibility as it involves the same matter Hamiltonians (with the same pairs of adjacent π fluxes). Let us similarly label $\mathcal{H}_a \equiv \mathcal{H}_0$ and $\mathcal{H}_b \equiv \mathcal{H}_0 + V_{25}$.[3]

The correlation functions C_{3-6} can be written using the same matter Hamiltonian $\mathcal{H}_b$. However, for C_1 and C_2, we define the Hamiltonian $\mathcal{H}_c \equiv \mathcal{H}_0 + V_{23} + V_{65}$, depicted in Fig. 5.9, whose ground state $|M_0^c\rangle$ also has the same matter fermion parity as $|M_0^a\rangle$ and $|M_0^b\rangle$. After the Fourier transform, the final expressions for $\tilde{C}_i(\omega) = \mathrm{Re}\{\int_0^\infty dt e^{i\omega t}C_i(t)\}$ are

$$\tilde{C}_3 = \Pi_{33}(\omega), \quad \tilde{C}_4(\omega) = i\Pi_{34}(\omega), \quad \tilde{C}_5(\omega) = -i\Pi_{36}(\omega), \quad \tilde{C}_6(\omega) = -\Pi_{31}(\omega), \tag{5.65}$$

[3]Note that we could further simplify $c_3e^{-i\mathcal{H}_bt}c_3 = e^{-i(\mathcal{H}_b+V_{\langle\cdot 3\rangle_x}+V_{\langle\cdot 3\rangle_y}+V_{\langle\cdot 3\rangle_z})}$, and eliminate the c_3 operator. However, in this new gauge the ground state must have the opposite matter fermion parity than that of $|M_0^b\rangle$ (because three bond fermions are added while the total parity cannot be changed by the gauge transformation). For this reason, we work with $\mathcal{H}_a$ and $\mathcal{H}_b$ (whose ground states have the same matter fermion parity) and the relation (5.21) between $|M_0^a\rangle$ and $|M_0^b\rangle$ holds.

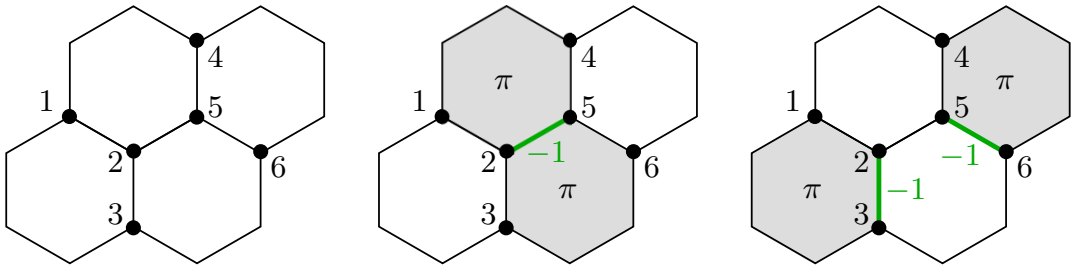

FIGURE 5.9: Three Hamiltonians defined in the matter Hilbert space and in different flux sectors. The gauge used to defined them is indicated by the green bonds for which $u = -1$, and $u = 1$ on all the other bonds.

where $\Pi_{kl}(\omega)$ is the operator that was defined for the spin susceptibility in Eq. (5.43),

$$\Pi_{kl}(\omega) = \pi \sum_{\lambda_b} \langle M_0^a | c_k | \lambda_b \rangle \langle \lambda_b | c_l | M_0^a \rangle \delta(\omega - \Delta_{\lambda_b}). \tag{5.66}$$

Here we explicitly write λ_b to indicate that the $|\lambda_b\rangle$'s are eigenstates of $\mathcal{H}_b$, and $\Delta_{\lambda_b} = E^b_{\lambda_b} - E^a_0$. For the correlation functions C_1 and C_2 we find

$$\begin{aligned} \tilde{C}_1(\omega) &= \pi \sum_{\lambda_c} |\langle M_0^a | \lambda_c \rangle|^2 \delta(\omega - \Delta_{\lambda_c}) \\ \tilde{C}_2(\omega) &= -i\pi \sum_{\lambda_c} \langle M_0^a | c_2 c_5 | \lambda_c \rangle \langle \lambda_c | M_0^a \rangle \delta(\omega - \Delta_{\lambda_c}), \end{aligned} \tag{5.67}$$

where $|\lambda_c\rangle$ are the eigenstates of $\mathcal{H}_c$ and $\Delta_{\lambda_c} = E^c_{\lambda_c} - E^a_0$. For $\mathcal{H}_c$, the flux gap is slightly different: $\Delta^0_c = E^c_0 - E^a_0 \approx 0.226 J_K$ ($\Delta^0_b \approx 0.263 J_K$).

The correlations functions can be calculated with the few-particle response approach. The matrix elements in the correlation functions $\tilde{C}_{3-6}$ are given by Eqs. (5.45) and (5.46) for the single-particle and three-particle contributions, respectively. The matrix elements in $\tilde{C}_{1-2}$ are remarkably different. Because they contain zero or two matter fermions, an even number, only the states $|\lambda_c\rangle$ with an even number of excitations contributes. Most importantly, the ground state $|\lambda_c\rangle = \left|M^c_0\right\rangle$ also contributes to the response which results in a peaked response at the energy $\omega = \Delta^c_0 = E^c_0 - E^a_0$. The zero-particle matrix elements are,

$$\begin{aligned} \left\langle M_0^a \middle| M_0^c \right\rangle &= \sqrt{|\det(\mathcal{X})|}, \\ \left\langle M_0^a \middle| \hat{c}_{Ai} \hat{c}_{Bj} \middle| M_0^c \right\rangle &= i \sqrt{|\det(\mathcal{X})|} \left(U_a V_a^\dagger - U_a \mathcal{F} V_a^\intercal \right)_{ij}, \end{aligned} \tag{5.68}$$

where the matrices $\mathcal{X}$ and $\mathcal{F}$ are defined in Sec. 5.1.1 for the Bogoliubov transformation between the canonical complex fermions of $\mathcal{H}_a$ and $\mathcal{H}_c$. To avoid confusion with

the matter Majorana fermions, we use the notation $\mathcal{H}_c = \sum_\lambda \omega^c_\lambda \hat{\mathbb{c}}^\dagger_\lambda \hat{\mathbb{c}}_\lambda + E^c_0$. The two-particle matrix elements $\left\langle M^a_0 \middle| \hat{\mathbb{c}}^\dagger_{\lambda_1} \hat{\mathbb{c}}^\dagger_{\lambda_2} \middle| M^c_0 \right\rangle = \sqrt{|\det(\mathcal{X})|}\left(\mathcal{Y}\mathcal{X}^{*-1}\right)_{\lambda_1\lambda_2}$ were already calculated in Eq. (5.48) and from the pseudo-Wick's theorem (5.47) and Eq. (5.45) we find

$$\begin{aligned}\left\langle M^a_0 \middle| \hat{c}_{Ai}\hat{c}_{Bj}\hat{\mathbb{c}}^\dagger_{\lambda_1}\hat{\mathbb{c}}^\dagger_{\lambda_2} \middle| M^c_0 \right\rangle = i\sqrt{|\det(\mathcal{X})|}\Big[&\left(U_a V_a^\dagger - U_a \mathcal{F} V_a^\intercal\right)_{ij}\left(\mathcal{Y}\mathcal{X}^{*-1}\right)_{\lambda_1\lambda_2} \\ &+ \left(U_a \mathcal{X}^{*-1}\right)_{i\lambda_1}\left(V_a \mathcal{X}^{*-1}\right)_{j\lambda_2} \\ &- \left(U_a \mathcal{X}^{*-1}\right)_{i\lambda_2}\left(V_a \mathcal{X}^{*-1}\right)_{j\lambda_1}\Big]. \end{aligned} \tag{5.69}$$

In Eq. (5.58), only the differences $\tilde{C}_i - \tilde{C}_{i+1}$ for $i = 1, 3$, and 5 appear. In Fig. 5.10, the single- and three-particle contributions to $\tilde{C}_3 - \tilde{C}_4$ and $\tilde{C}_5 - \tilde{C}_6$ and the zero- and two-particle contributions to $\tilde{C}_1 - \tilde{C}_2$ are plotted.

Finally, we can calculate the optical conductivity from Eq. (5.59). We already saw that there can be up to five independent parameters m_{1-5} for the ME coupling in a system with C_3 symmetry. As mentioned earlier, if the lattice polarization mechanism is dominant, the ME coupling is well described with only $m_1 = \mathbb{A}_1 \equiv \mathbb{A}$ ($\mathbf{P}_{ij} \parallel \hat{\mathbf{u}}_\gamma$, where $\hat{\mathbf{u}}_\gamma$ is along the $\langle ij\rangle_\gamma$ bond), and if the hopping polarization mechanism is dominant, the ME coupling is well described with only $m_4 = \mathbb{B}_4$ and $m_5 = \mathbb{B}_5$. Moreover, we assume the deviation from the KNB coupling to be small (i.e., $m_4 \approx -m_5$ and $\mathbf{P}_{ij} \propto \hat{\mathbf{u}}_\gamma \times \mathbf{S}_i \times \mathbf{S}_j$) and set $-\mathbb{B}_4 = \mathbb{B}_5 \equiv \mathbb{B}$.

In the following, we consider the optical conductivity $\sigma'(\omega)$ for the two scenarios:

$$\begin{aligned}\mathbf{P}_{\langle ij\rangle_\gamma} &= \mathbb{A}\Big[\hat{\mathbf{u}}_\gamma \cdot \left(\mathbf{S}_i \times \mathbf{S}_j\right)\Big] \cdot \hat{\mathbf{u}}_\gamma \Rightarrow \sigma'^A(\omega), \\ \mathbf{P}_{\langle ij\rangle_\gamma} &= \mathbb{B}\Big[\hat{\mathbf{u}}_\gamma \times \left(\mathbf{S}_i \times \mathbf{S}_j\right)\Big] \quad \Rightarrow \sigma'^B(\omega).\end{aligned}$$

The in-plane $\sigma_\parallel$ and out-of-plane $\sigma_\perp$ components of the optical conductivity are found from Eqs. (5.49) and (5.59) and are related to the correlation functions by

$$\begin{aligned}\sigma'^A_\parallel(\omega) &= \frac{\omega}{24\sqrt{3}}\mathbb{A}^2\left[3(\tilde{C}_3(\omega) - \tilde{C}_4(\omega)) + \frac{3}{2}(\tilde{C}_5(\omega) - \tilde{C}_6(\omega))\right], \\ \sigma'^A_\perp(\omega) &= 0, \\ \sigma'^B_\parallel(\omega) &= \frac{\omega}{24\sqrt{3}}\mathbb{B}^2\Big[(\tilde{C}_1(\omega) - \tilde{C}_2(\omega)) + 2(\tilde{C}_3(\omega) - \tilde{C}_4(\omega)) - (\tilde{C}_5(\omega) - \tilde{C}_6(\omega))\Big], \\ \sigma'^B_\perp(\omega) &= \frac{\omega}{24\sqrt{3}}\mathbb{B}^2\Big[4(\tilde{C}_1(\omega) - \tilde{C}_2(\omega)) + 2(\tilde{C}_3(\omega) - \tilde{C}_4(\omega)) + 2(\tilde{C}_5(\omega) - \tilde{C}_6(\omega))\Big],\end{aligned} \tag{5.70}$$

where we have used $S = N(3\sqrt{3}/2)$ for the total surface. In Fig. 5.11, $\sigma'^A_\parallel/\mathbb{A}^2$, $\sigma'^B_\parallel/\mathbb{B}^2$, and $\sigma'^B_\perp/\mathbb{B}^2$ are plotted. Those are unitless quantities. To recover the proper units, $\sigma'^A/\mathbb{A}^2$ and $\sigma'^B/\mathbb{B}^2$ have to be multiplied by $e^2\mathbb{A}^2/(\hbar a_\perp)$ and $e^2\mathbb{B}^2/(\hbar a^2 a_\perp)$, respectively. The magnetic dipole contribution $\omega\chi''(\omega)$ is also shown for comparison. The electric-dipole-induced and magnetic-dipole-induced absorption rates from the same electromagnetic wave scale as $\sigma'(\omega)$ and $(g\mu_B/c)^2\omega\chi''(\omega)$, respectively [see Eq. (2.1)], so that the unitless quantity $\omega\chi''(\omega)$ has to be multiplied by $(g\mu_B)^2/(\hbar c^2 a^2 a_\perp)$ in order to be compared with the optical conductivity. The optical conductivity $\sigma'^A(\omega)$ corresponds to what we calculated in Ref. [62].

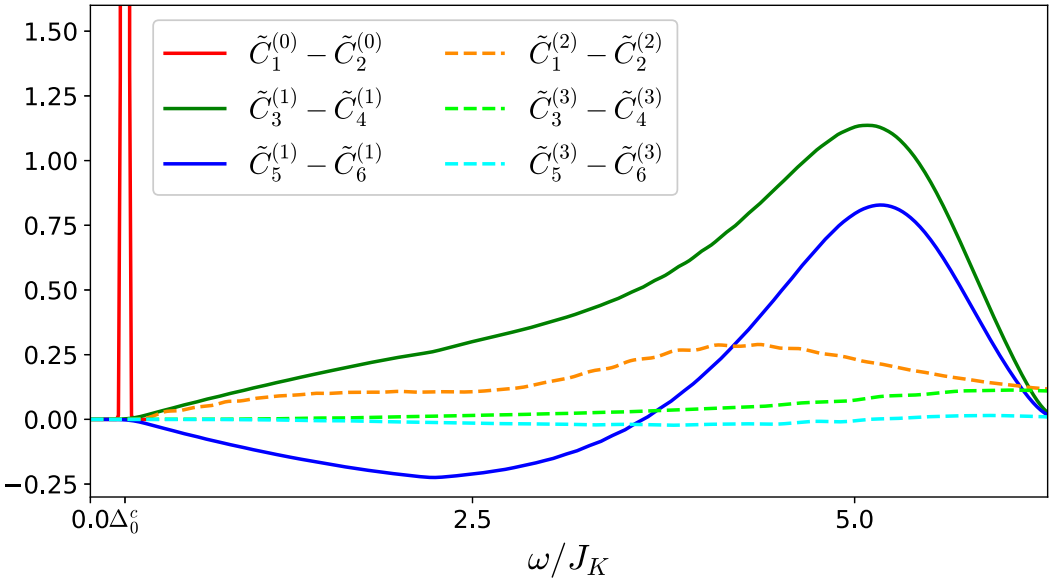

FIGURE 5.10: Relevant correlations functions $C_i^{(n)} - C_{i+1}^{(n)}$ from zero-, single-, two-, and three-particle excitations ($n = 0$, 1, 2, and 3, respectively). The computations were performed in a system of $N = 20 \times 20$ unit cells (with Gaussian broadening $\delta = 0.1 J_K$) for $n = 3$, $N = 40 \times 40$ unit cells (with $\delta = 0.07 J_K$) for $n = 2$, and $N = 80 \times 80$ unit cells (with $\delta = 0.07 J_K$) for $n = 1$ and 0. Only frequencies up to $\omega = \Delta_0^b + \omega_N^b$ are shown.

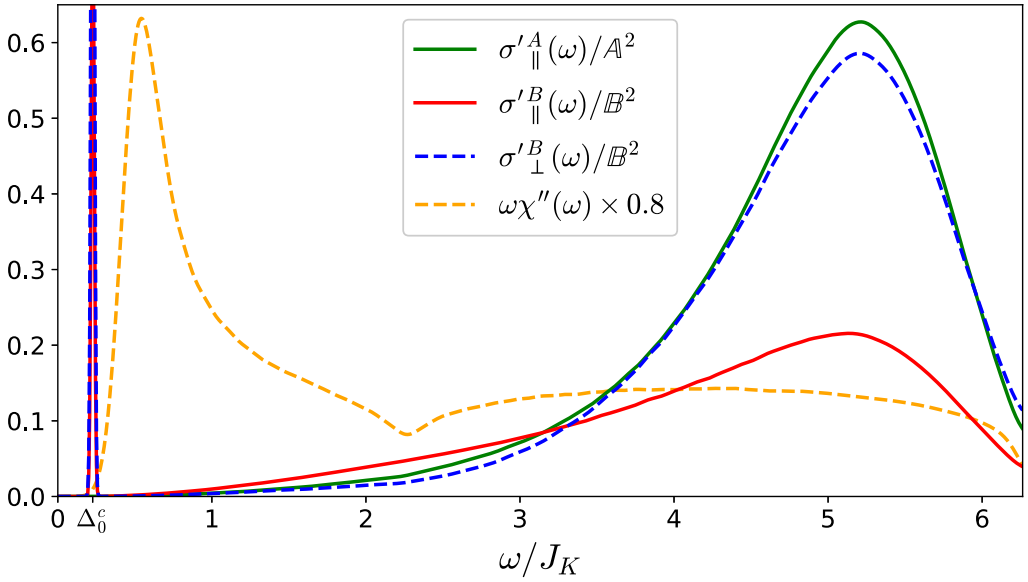

FIGURE 5.11: Optical conductivity defined in Eq. (6.70) originating from up to three-particle excitations. The magnetic dipole contribution $\omega\chi''(\omega)$ (with a 0.8 factor) is also shown for comparison. Only frequencies up to $\omega = \Delta_0^b + \omega_N^b$ are shown.

5.3 Discussion

The optical response of the pure Kitaev model has been derived using the analyticity of the model and a generally allowed coupling between electric polarization and spin operators discussed in Chaper 4, arising from virtual hopping of the electrons between the magnetic sites via the ligands.

In the many THz spectroscopy experiments performed for the Kitaev material α-$RuCl_3$ [30–34], the absorption originates from both magnetic-dipole-induced and electric-dipole-induced transitions. However, the material being a Mott insulator, often only the magnetic-dipole-induced transitions are discussed.

Nevertheless, it was shown in Ref. [31] that the absorption continuum of α-$RuCl_3$ is too strong to be attributed to direct coupling to magnetic dipole moments, and that there is a dominant contribution from electric-dipole-induced transitions. Because, even in the Mott insulating phase, the orbitals of $4d$ ruthenium are slightly delocalized, fluctuations of the electronic charge are expected. Thus, we proposed a mechanism for the optical conductivity through virtual hopping of the electrons in Chapter 4.

In the present chapter, we showed that even in the pure Kitaev limit, a finite subgap optical conductivity arises from the finite ME coupling. It has both similarities and differences from the purely magnetic response. On the one hand, the electric-dipole-induced transitions from the ground states are only allowed between the flux-free sector and a two-flux sector. For an effective polarization operator on a γ-bond involving $(\mathbf{S}_i \times \mathbf{S}_j) \cdot \hat{\mathbf{u}}_\gamma$ and $(\mathbf{S}_i \times \mathbf{S}_j) \cdot \hat{\mathbf{v}}_\gamma$, the two π fluxes are in adjacent hexagons, as shown in Fig. 5.7, because they always contain either a σ_i^γ or σ_j^γ term. In this case, the relevant matter Hamiltonian is $\mathcal{H}_b$. Interestingly, the same Hamiltonian is required for the calculation of the simpler spin dynamical correlation function, which implies that the transitions take place between the same flux sectors. However, whereas the spin susceptibility has a peak around $\omega \approx 0.5 J_K$, the optical conductivity peaks around $\omega \approx 5 J_K$.

On the other hand, for an effective polarization operator involving $(\mathbf{S}_i \times \mathbf{S}_j) \cdot \hat{\mathbf{w}}_\gamma$, the two fluxes are in hexagons separated by the $\langle ij \rangle_\gamma$ bond, as shown in Fig. 5.7, because in this case there is no σ^γ term. Hence, another matter Hamiltonian $\mathcal{H}_c$ is needed. Those transitions have different parity properties which result in a strong delta peak contribution right at the flux gap $\omega = \Delta_0^c$ in Fig. 5.11.

We considered the optical conductivity for two different scenarios concerning the ME coupling. For $\mathbf{P}_{ij} = \mathbb{A}\left[\hat{\mathbf{u}}_\gamma \cdot \left(\mathbf{S}_i \times \mathbf{S}_j\right)\right] \cdot \hat{\mathbf{u}}_\gamma$, only the two-flux sector with adjacent π fluxes is relevant and there are no delta peak at $\omega = \Delta_0^c$. Moreover the out-of-plane optical conductivity vanishes. For the KNB mechanism, however, both in-plane and out-of-plane optical conductivities are finite and show a sharp peak at $\omega = \Delta_0^c$. Hence, the optical conductivity has a two-peak structure.

One must be cautious when comparing our findings with the THz experiments. Obviously, experiments are performed at finite temperatures and our results are only valid at $T = 0$. Moreover, in real Kitaev materials, additional integrability breaking terms are indispensable to explain the antiferromagnetic order below T_N.

In this case, even the calculation of the spin susceptibility becomes a challenge. In recent articles, it was shown that the spin structure factor evolves smoothly from the results of the pure Kitaev model using numerical [193,200,201] and parton mean-field methods [202] close to the Kitaev spin liquid regime of the pure Kitaev model. We thus expect that our results are meaningful physically in the putative proximate Kitaev spin liquid. It is indeed believed that, for α-$RuCl_3$, even away from the pure Kitaev limit, there are still remnants of the Majorana physics and the continuum

observed in the response can be understood in terms of fractionalized spin excitations [56, 58–60]. In addition, it was shown that even below T_N an in-plane magnetic field of 8 T suppresses the magnetic order and the system is in a field-induced quantum spin liquid state [203].

Because we do not know the values of $\mathbb{A}$ and $\mathbb{B}$, it is hard to evaluate the different contributions we calculated in terms of a physical THz response. However, if we compare the magnetic dipole contribution $\omega\chi''(\omega) \times (g\mu_B)^2/(\hbar c^2 a^2 a_\perp)$ (with $g = 2$) with the results in Ref. [31], it only accounts for around 7% of the measured signal just above the sharp gap at $\omega \approx 1$ meV ($\omega \approx 0.7 J_K$ for a typical value of $J_K \approx 1.5$ meV). We thus conclude that the main weight of the spectrum originates from electric-dipole-induced transitions.

Furthermore, the spectrum we calculated bears striking similarities with the loss spectrum obtained in some of the THz spectroscopy measurements (see Fig. 5.3). A double-peak spectrum with peaks at energies $\omega \approx 2$ meV and $\omega \approx 7$ meV and a gap-like feature below $\omega \approx 1$ meV is typically observed (see, e.g., Refs. [31, 33]). Those peaks cannot be attributed to the phonon mode, which is located at around $\omega \approx 15$ meV.

Chapter 6

Summary and outlook

In the present thesis, electric-dipole-induced magnetic transitions were investigated in different systems. The study of electron spin dynamics and how it can be affected by the motional degree of freedom of the electrons is related to various areas of physics. In the context of semiconductors physics, access to electric-field-mediated spin control has applications in spintronics. In the context of multiferroics, electromagnons, spin waves which can be exited by an AC electric field, have been extensively studied, motivated by both the potential real-world applications and the fundamentally interesting physics at play. Moreover, in the contexts of quantum spin liquids, optical measurements have been shown to be insightful probes of the fractionalized spin excitations of some systems. With this background in mind, we chose to focus on a simple and universal model, the Hubbard model, and extensively investigated the different origins of electric-dipole-induced magnetic transitions.

The Hubbard model is a deceptively simple model which has evolved from a toy model to an experimentally relevant model for strongly correlated electron systems. The model can describe both metals and insulators and we correspondingly used two approaches. The thesis was therefore effectively split in two parts.

First, the weak coupling limit was studied in Chapter 2. The synergetic effect of SOC and Zeeman coupling on the spin resonance has non-trivial effects even when neglecting interactions. We reviewed the original results of combined resonances (cyclotron and spin flip) in the Landau levels of a 2DEG in the Zeeman limit, and also discussed already known results of EDSR in the Tomonaga-Luttinger liquid that we generalized. Then, we presented our original results concerning EDSR in a lattice model. We showed how the lattice potential affects the optical spectrum and observed characteristic dependencies on the relative direction of the magnetic field and the SOC vector, and on the Fermi energy. In the 2D model in particular, we showed that the resonance spectrum, which is a single peak at the Zeeman energy for vanishing SOC, has a finite width even at $T = 0$. In addition, the spectrum shows multiple Van Hove-like singularities whose characteristics depend on the band structure.

We also described the evolution of the resonance for finite U in small systems using exact diagonalization. We showed that at quarter-filling, the Hubbard interaction modifies the amplitude and frequency of the resonance. In the half-filled case, the system becomes a Mott insulator and the resonance observed at $U = 0$ is enhanced for small U but vanishes when the optical gap becomes larger than the kinetic hopping amplitude t. This shows that the SOC-induced EDSR in metallic systems, introduced as a fundamentally single-particle phenomenon, relies on the spinful particles to be optically gapless.

Also in Chapter 2, the same half-filled 1D Hubbard model was investigated from the strong-coupling limit, $U/t \to \infty$. In this limit, we showed how the interplay

of SOC and Zeeman coupling affects the optical transitions between the upper and lower Hubbard bands at $\omega \sim U \pm 4t$.

As a future prospect, it would be interesting to apply our results to actual materials and predict their magnetic-dipole-induced and electric-dipole-induced absorption spectrum. ESR is above all an experimental method for studying materials and it is thus important to consider experimentally relevant scenarios. Our results rely on the presence of a periodic potential, which justify the discrete model on the lattice, and on strong SOC. Metallic iridates, and other heavy $5d$ or $4d$ TM compounds, would thus be prime candidates. Indeed, $4d$ and $5d$ orbitals are characterized by their delocalization (they are less localized than, e.g., $3d$, $4f$, and $5f$ orbitals). They are thus well described by the Hubbard model with large hoping amplitudes which tends to reduce the electronic repulsion U and the correlation effects. In addition, the heavy TM ions have especially strong SOC. Of course, actual materials have more complicated physics than the pristine models we used, and additional considerations are in order (such as more complex realistic lattices or the additional orbital degree of freedom).

Secondly, in the strong-coupling limit, other mechanisms relying on the strong electronic correlation were considered. To this end, a different formalism was introduced where the hopping Hamiltonian is regarded as a perturbation.

In Chapters 3, 4, and 5, we investigated low-energy optical transitions in the Mott insulating phase of the Hubbard model, i.e., below the optical gap. Our main original results consist of (i) the derivation of the two-spin ME coupling arising from the valence electron charge fluctuation in single-band and d^5 Mott insulators, and of (ii) the calculation of the resulting subgap optical conductivity in the pure Kitaev model.

By carefully considering the different matrix elements of the electronic polarization operator in the tight-binding formulation, we identified two distinct microscopic origins for the electronic ME coupling. From the point-like behavior of the charged particles on the lattice, a finite effective polarization emerges from states with doubly occupied sites via virtual hopping. This phenomenon generally occurs on any lattice model, but the resulting ME effect only systematically arises on closed loops of odd number of sites. However, we showed that for the involved geometry of the Kitaev materials, TM ions with edge-sharing octahedral ligand structures, the ME effect arises even on single bonds. The geometry is indeed important as we showed that the corresponding ME effect is generally absent in the corner-sharing geometry of the perovskite structure.

Additionally, the polarization also has finite matrix elements caused by the charge distribution of the electrons around each ions, i.e., not taken into account by the purely point-like description of the Hubbard model. This lead us to introduce the concept of 'polarization hopping integrals' which are the equivalent of the usual kinetic hopping integrals of the tight-binding model, but for the electric polarization operator instead of the Hamiltonian. The original spin current model made use of such (simplified) integrals to derive the $\mathbf{P}_{ij} \propto \hat{\mathbf{e}}_{ij} \times (\mathbf{S}_i \times \mathbf{S}_j)$ ME coupling. However, by carefully classifying the integrals with respect to different symmetry channels, we derived a more general ME coupling in d^5 Mott insulators. All things considered, we reconciled two approaches to the electronic ME effect in the Hubbard model. We revisited them, and exhaustively derived the resulting ME coupling in a specific class of Mott-insulating TM compounds.

Finally, the limiting case of the pure Kitaev model was studied. Combining an

analytical formulation of the Hamiltonian in terms of Majorana fermions in an enlarged Hilbert space, Bogoliubov transformations, and exact diagonalization, we calculated and compared the subgap optical conductivity emerging from different two-spin ME coupling. In the Kitaev model, the physics is formulated in terms of $\mathbb{Z}_2$ fluxes and itinerant Majorana fermions. Thanks to the macroscopic number of conserved quantities, the dynamical response functions could be handily evaluated at $T = 0$ in large systems of more than 10^4 spins. Because of the quantum spin liquid ground state and the fractionalized magnetic excitations, the subgap optical conductivity is continuous.

The dielectric loss spectrum of the Kitaev materials α-$RuCl_3$ measured with THz spectroscopy has been reported by a number of sources [30–34]. A recurring feature is indeed the continuous low-frequency response which is attributed to remnants of the Kitaev physics. Although a magnetic-dipole-induced response is of course also contributing, it has been argued that the main contribution is electric-dipole-induced. We believe that our results, even though calculated in pristine conditions, shed light on the origin of the electric-dipole-induced transitions. In particular, the calculated spectrum bears striking similarities with the experimentally measured absorption spectrum: a two-peak structure with a sharp gap below $\hbar\omega \approx 1$ meV (see, e.g., [33]).

As a further perspective, it would be interesting to study the optical response of Kitaev materials away from the pure Kitaev model (with the addition of analyticity-breaking terms), and at finite temperatures. While our results explain the origin behind the spectroscopy results, additional considerations are required in order to directly compare our results with the experimental ones. In particular, the following two questions are still unanswered: (1) Why does the THz response exhibits such an anomalous temperature dependence? (2) What is the origin of the gap observed below 1 meV up to room temperature? A full understanding of the relation between the dynamical responses and the different magnetic interactions is still lacking. It would therefore be interesting to study the electric-dipole-induced spin resonance (or other dynamical response functions) in the full KH$\Gamma\Gamma'$ using appropriate methods. Exact analytical method cannot be used but other numerical and approximative analytical methods are relevant to the problem [200, 202, 204].

Finally, in this thesis we chose to focus on d^5 TM compounds with a specific lattice structure because we were motivated by experimental results. Nevertheless, the theory of the ME effect in the Hubbard model is evidently not limited to d^5 materials and thus a generalization to any other microscopic structure is possible.

Appendix A

Polarization integrals

In Table A.1 we list the polarization integrals calculated in Sec. 4.4 for a general bond direction **d** with direction cosines (l, m, n). The entries not written in the table are found by cyclically permuting the coordinates and direction cosines.

$\langle p_x \vert x \vert d_{yz} \rangle$	=	$\sqrt{3}l^2mnP^{\parallel}_{pd\sigma} - 2l^2mnP^{\parallel}_{pd\pi} + \sqrt{3}mn\left(1-l^2\right)P^{\perp}_{p\pi d\sigma} - 2l^2mnP^{\perp}_{p\sigma d\pi} + mn\left(1+l^2\right)P^{\perp}_{p\pi d\delta}$
$\langle p_x \vert y \vert d_{yz} \rangle$	=	$\sqrt{3}lm^2nP^{\parallel}_{pd\sigma} - 2lm^2nP^{\parallel}_{pd\pi} - \sqrt{3}lm^2nP^{\perp}_{p\pi d\sigma} + ln\left(1-2m^2\right)P^{\perp}_{p\sigma d\pi} - ln\left(1-m^2\right)P^{\perp}_{p\pi d\delta}$
$\langle p_x \vert z \vert d_{xy} \rangle$	=	$\sqrt{3}lmn^2P^{\parallel}_{pd\sigma} - 2lmn^2P^{\parallel}_{pd\pi} - \sqrt{3}lmn^2P^{\perp}_{p\pi d\sigma} + lm\left(1-2n^2\right)P^{\perp}_{p\sigma d\pi} - lm\left(1-n^2\right)P^{\perp}_{p\pi d\delta}$
$\langle p_x \vert x \vert d_{xz} \rangle$	=	$\sqrt{3}l^3nP^{\parallel}_{pd\sigma} + ln\left(1-2l^2\right)P^{\parallel}_{pd\pi} + \sqrt{3}ln\left(1-l^2\right)P^{\perp}_{p\pi d\sigma} + ln\left(1-2l^2\right)P^{\perp}_{p\sigma d\pi} - ln\left(1-l^2\right)P^{\perp}_{p\pi d\delta}$
$\langle p_x \vert y \vert d_{xz} \rangle$	=	$\sqrt{3}l^2mnP^{\parallel}_{pd\sigma} + mn\left(1-2l^2\right)P^{\parallel}_{pd\pi} - \sqrt{3}l^2mnP^{\perp}_{p\pi d\sigma} - 2l^2mnP^{\perp}_{p\sigma d\pi} - mn\left(1-l^2\right)P^{\perp}_{p\pi d\delta}$
$\langle p_x \vert z \vert d_{xz} \rangle$	=	$\sqrt{3}l^2n^2P^{\parallel}_{pd\sigma} + n^2\left(1-2l^2\right)P^{\parallel}_{pd\pi} - \sqrt{3}l^2n^2P^{\perp}_{p\pi d\sigma} + l^2\left(1-2n^2\right)P^{\perp}_{p\sigma d\pi} + \left(1-l^2\right)\left(1-n^2\right)P^{\perp}_{p\pi d\delta}$
$\langle p_x \vert x \vert d_{xy} \rangle$	=	$\sqrt{3}l^3mP^{\parallel}_{pd\sigma} + lm\left(1-2l^2\right)P^{\parallel}_{pd\pi} + \sqrt{3}lm\left(1-l^2\right)P^{\perp}_{p\pi d\sigma} + lm\left(1-2l^2\right)P^{\perp}_{p\sigma d\pi} - lm\left(1-l^2\right)P^{\perp}_{p\pi d\delta}$
$\langle p_x \vert y \vert d_{xy} \rangle$	=	$\sqrt{3}l^2m^2P^{\parallel}_{pd\sigma} + m^2\left(1-2l^2\right)P^{\parallel}_{pd\pi} - \sqrt{3}l^2m^2P^{\perp}_{p\pi d\sigma} + l^2\left(1-2m^2\right)P^{\perp}_{p\sigma d\pi} + \left(1-l^2\right)\left(1-m^2\right)P^{\perp}_{p\pi d\delta}$
$\langle p_x \vert z \vert d_{xy} \rangle$	=	$\sqrt{3}l^2mnP^{\parallel}_{pd\sigma} + mn\left(1-2l^2\right)P^{\parallel}_{pd\pi} - \sqrt{3}l^2mnP^{\perp}_{p\pi d\sigma} - l^2mnP^{\perp}_{p\sigma d\pi} - mn\left(1-l^2\right)P^{\perp}_{p\pi d\delta}$
$\langle d_{yz} \vert x \vert d_{yz} \rangle$	=	0
$\langle d_{yz} \vert y \vert d_{yz} \rangle$	=	0
$\langle d_{yz} \vert z \vert d_{yz} \rangle$	=	0
$\langle d_{yz} \vert x \vert d_{xz} \rangle$	=	$\sqrt{3}mn^2P^{\perp}_{d\sigma d\pi} + m\left(1-3n^2\right)P^{\perp}_{d\pi d\delta}$
$\langle d_{yz} \vert y \vert d_{xz} \rangle$	=	$-\sqrt{3}ln^2P^{\perp}_{d\sigma d\pi} - l\left(1-3n^2\right)P^{\perp}_{d\pi d\delta}$
$\langle d_{yz} \vert z \vert d_{xz} \rangle$	=	0
$\langle d_{yz} \vert x \vert d_{xy} \rangle$	=	$\sqrt{3}m^2nP^{\perp}_{d\sigma d\pi} + n\left(1-3m^2\right)P^{\perp}_{d\pi d\delta}$
$\langle d_{yz} \vert y \vert d_{xy} \rangle$	=	0
$\langle d_{yz} \vert z \vert d_{xy} \rangle$	=	$-\sqrt{3}lm^2P^{\perp}_{d\sigma d\pi} - l\left(1-3m^2\right)P^{\perp}_{d\pi d\delta}$

TABLE A.1: Polarization integrals for two ions separated by a vector $\mathbf{d} = |\mathbf{d}|(l, m, n)$. Only the p-t_{2g} and t_{2g}-t_{2g} integrals are considered.

Appendix B

Magnetoelectric coupling with $\phi \neq 90°$ and $\varphi \neq 180°$

B.1 Edge-sharing geometry with $\phi \neq 90°$

In this Appendix, we first consider the displacement of the two ligands toward the middle of the bond along $\pm\hat{\mathbf{v}}$ in the edge-sharing geometry. As discussed in Sec. 4.5.1, $\hat{\mathbf{v}}$ is one of the C_2 axis so that the results will be consistent with the original D_{2h} symmetry group of the bond. Therefore, we can study the angle dependence away from the ideal $\phi = 90°$ bond geometry without introducing additional coupling constant.

The hopping integrals are found to be

$$\begin{aligned} t_1 &= \frac{t_{dd\pi} + t_{dd\delta}}{2} + \frac{t_{pd\pi}^2}{\Delta_{pd}} \cos(\phi), \\ t_2 &= \frac{-t_{dd\pi} + t_{dd\delta}}{2} + \frac{t_{pd\pi}^2}{\Delta_{pd}}, \\ t_3 &= \frac{3t_{dd\sigma} + t_{dd\delta}}{4} + \frac{3}{2}\frac{t_{pd\sigma}^2}{\Delta_{pd}} \cos^3(\phi) + \frac{\left(\sqrt{3}t_{pd\sigma} - t_{pd\pi}\right)t_{pd\pi}}{\Delta_{pd}} \sin(\phi)\sin(2\phi). \end{aligned} \tag{B.1}$$

We note that the integrals themselves also depend on ϕ because of the change in the TM-L distance and/or the TM-TM distance. We do not consider this dependence.[1]

B.1.1 Mechanism

Lattice polarization

The two ligands are separated by a distance $\tilde{a} = a\cot(\phi/2)$ in the $\hat{\mathbf{v}}$ direction where a is still the TM-TM distance. Then $\mathbf{P}_{\text{lat}}^{(\text{L})}$ (given by Eq. (4.45) when $\phi = 90°$) becomes

$$\mathbf{P}_{\text{lat}}^{(\text{L})} = \frac{t_{pd\pi}^2}{\Delta_{pd}^2} \sin(\phi) \left[\mathbf{c}_i^\dagger \begin{pmatrix} 0 & -1 & 0 \\ 1 & 0 & 0 \\ 0 & 0 & 0 \end{pmatrix} \mathbf{c}_j + \text{H.c.} \right] \frac{\tilde{a}}{2} \hat{\mathbf{v}}. \tag{B.2}$$

Note that the $t_{pd\pi}$ integral also depends on ϕ if the TM-L distance $d = a/(2\cos(\phi/2))$ is not kept constant.

[1] Our results are similar to Ref. [180] except for t_3, which might be caused by a different microscopic definition of ϕ.

Lattice polarization

Because there are still no displacement along $\hat{\mathbf{w}}$, only b_4 and b_5 are non-zero. We find,

$$\begin{aligned} b_4 &= -P^{\perp}_{d\pi d\delta} - 2\sin(\phi/2)\frac{t_{pd\pi}}{\Delta_{pd}}\left(P^{\parallel}_{pd\pi} + \cos(\phi)(P^{\parallel}_{pd\pi} - P^{\perp}_{p\pi d\delta})\right) \\ b_5 &= \frac{1}{4}\left(\sqrt{6}P^{\perp}_{d\sigma d\pi} - \sqrt{2}P^{\perp}_{d\pi d\delta}\right) + \frac{\sin(\phi/2)}{2}\frac{1}{\Delta_{pd}}\times \\ &\Big[\cos(\phi)\left(2\sqrt{3}P^{\perp}_{p\pi d\sigma}t_{pd\pi} + P^{\perp}_{p\pi d\delta}(-2\sqrt{3}t_{pd\sigma} + 6t_{pd\pi})\right) \\ &+ \cos(2\phi)(P^{\perp}_{p\sigma d\pi} - P^{\perp}_{p\pi d\delta})(\sqrt{3}t_{pd\sigma} - 2t_{pd\pi}) \\ &+ P^{\perp}_{p\sigma d\pi}(\sqrt{3}t_{pd\sigma} + 2t_{pd\pi}) + P^{\perp}_{p\pi d\delta}(-\sqrt{3}t_{pd\sigma} + 2t_{pd\pi})\Big]. \end{aligned} \tag{B.3}$$

If we actually consider the displacement along [111] corresponding to the trigonal distortion (displacement of the ligands perpendicular to the plane), all b_{1-5} are finite but the calculation is too cumbersome to be done analytically. It can however be done numerically.

B.2 Corner-sharing geometry with $\varphi \neq 180°$

We now consider the more general corner-shared geometry where a displacement of the ligand perpendicular to the bond is allowed. If the ligand displacement is staggered along the square lattice (such as for Sr_2IrO_4), it correspond to a relative rotation of neighboring octahedral structures along the $\hat{\mathbf{z}}$ axis such that $\varphi \neq 180$ [see Fig. 4.1(a)]. The inversion symmetry centered at the middle of the bonds is obviously broken in this case. After the rotation, the cubic orbitals are defined relatively to two different bases, $\mathcal{B}_A = \{\hat{\mathbf{x}}_A, \hat{\mathbf{y}}_A, \hat{\mathbf{z}}\}$ and $\mathcal{B}_B = \{\hat{\mathbf{x}}_B, \hat{\mathbf{y}}_B, \hat{\mathbf{z}}\}$, separated by a $2\alpha = \pi - \varphi$ rotation along the $\hat{\mathbf{z}}$ axis. We furthermore consider a uniform tetragonal distortion $\Delta_A = \Delta_B = \Delta$. A staggered tetragonal distortion (corresponding to $\Delta_A = -\Delta_B$) is also possible (and even expected in some systems [205]), but we do not consider it explicitly. For a bond in the $\hat{\mathbf{x}}$ direction, we define $\alpha > 0$ for a displacement of the ligand in the $+\hat{\mathbf{y}}$ direction.

Full octahedral symmetry with $\alpha \neq 0$

The symmetry group of the bond is reduced to C_{2v}. The corresponding character table is shown in Table B.1.

TABLE B.1: Character table of C_{2v}. The $\langle ij \rangle$ bond is along the $\hat{\mathbf{x}}$ axis.

C_{2v}	E	$C_{2,y}$	σ_{xy}	σ_{yz}	functions
A_1	1	1	1	1	y, $\left(\mathbf{S}_i \times \mathbf{S}_j\right)_z$
A_2	1	1	−1	−1	xz, S^y, $\left(\mathbf{S}_i \times \mathbf{S}_j\right)_x$
B_1	1	−1	1	−1	x, xy, S^y, i-j antisym.
B_2	1	−1	−1	1	z, yz, S^y, $\left(\mathbf{S}_i \times \mathbf{S}_j\right)_y$

Because of the lack of inversion symmetry, the hopping can be antisymmetric and the effective polarization can couple to symmetric two-spin operators. Then, ME coupling contains at most thirty independent coefficients, instead of nine.

The hopping matrices between for x-bonds and y-bonds are

$$\hat{T}_x(C_{2v}) = \begin{pmatrix} t_1 & t_4 & 0 \\ -t_4 & t_2 & 0 \\ 0 & 0 & t_3 \end{pmatrix}_{\mathcal{B},\mathcal{B}} \quad \text{and} \quad \hat{T}_y(C_{2v}) = \begin{pmatrix} t_2 & t_4 & 0 \\ -t_4 & t_1 & 0 \\ 0 & 0 & t_3 \end{pmatrix}_{\mathcal{B},\mathcal{B}} . \tag{B.4}$$

Neglecting the direct *d*-*d* hopping, we have (written in the $\mathcal{B}_A$ and $\mathcal{B}_B$ bases)

$$\hat{T}_x = \begin{pmatrix} 0 & 0 & 0 \\ 0 & t & 0 \\ 0 & 0 & t\cos(2\alpha) \end{pmatrix}_{\mathcal{B}_A,\mathcal{B}_B} \quad \text{and} \quad \hat{T}_y = \begin{pmatrix} t & 0 & 0 \\ 0 & 0 & 0 \\ 0 & 0 & t\cos(2\alpha) \end{pmatrix}_{\mathcal{B}_A,\mathcal{B}_B} . \tag{B.5}$$

In the C_{2v} group, the ME coupling (for an *x*-bond) is

$$\mathbf{P} = \begin{pmatrix} 0 & 0 & 0 \\ 0 & 0 & m_1^A \\ 0 & m_2^A & 0 \end{pmatrix} \left(\mathbf{S}_i \times \mathbf{S}_j\right) + \begin{pmatrix} 0 & 0 & 0 & 0 \\ m_0^D & m_1^D & m_2^D & m_3^D \\ 0 & 0 & 0 & 0 \end{pmatrix} \begin{pmatrix} \mathbb{I} \\ S_i^x S_j^x \\ S_i^y S_j^y \\ S_i^z S_j^z \end{pmatrix} + \begin{pmatrix} 0 & 0 & m_1^\Gamma \\ 0 & 0 & 0 \\ m_2^\Gamma & 0 & 0 \end{pmatrix} \begin{pmatrix} S_i^y S_j^z + S_i^z S_j^y \\ S_i^x S_j^z + S_i^z S_j^x \\ S_i^x S_j^y + S_i^y S_j^x \end{pmatrix}. \tag{B.6}$$

The change of basis from $\mathcal{B}$ to $\mathcal{B}_{A(B)}$ for the spin operators corresponds to the transformation $\mathbf{S}_i \to e^{i\alpha S^z}\mathbf{S}_i e^{-i\alpha S^z}$ ($\mathbf{S}_j \to e^{-i\alpha S^z}\mathbf{S}_j e^{i\alpha S^z}$). For two-spin operators, the change of bases $(\mathcal{B},\mathcal{B}) \to (\mathcal{B}_A,\mathcal{B}_B)$ does not change the irreducible representation of the two-spin operators, so that Eq. (B.6) is left unchanged by the change of bases (the values of the coupling coefficients would nevertheless be altered). Henceforth, we use the $\mathcal{B}$ basis for $\mathbf{P}$ and in the $\mathcal{B}_A$ and $\mathcal{B}_B$ bases for $\mathbf{S}_i$ and $\mathbf{S}_j$, respectively.

Tetragonal distortion

The uniform tetragonal distortion does not affect the C_{2v} symmetry group or the form of $\hat{m}$.

B.2.1 Mechanism

Lattice polarization

In Eq. (B.6), only the m_1^Γ coupling constant lead to a polarization along the bond. However, because the 3×3 matrices defining the tetragonal CF and the hopping commute, the hopping is diagonal in terms of the pseudospin variables, and $\mathbf{P}_{\text{lat}}^{(\text{TM})}$ vanishes.

The contribution from the ligand is given by

$$\mathbf{P}_{\text{lat},x}^{(\text{L})} = \tan(\alpha)\left[\mathbf{c}_i^\dagger \hat{T}_x \mathbf{c}_j + \text{H.c.}\right]\frac{a}{2}\hat{\mathbf{y}} \tag{B.7}$$

$$\mathbf{P}_{\text{lat},y}^{(\text{L})} = -\tan(\alpha)\left[\mathbf{c}_i^\dagger \hat{T}_y \mathbf{c}_j + \text{H.c.}\right]\frac{a}{2}\hat{\mathbf{x}}, \tag{B.8}$$

for *x*-bonds and *y*-bonds, respectively. As shown in the next subsection, the corresponding effective operators only lead to a ME coupling involving diagonal two-spin operators $S_i^\alpha S_j^\alpha$.

Hopping polarization

For a x-bond, we have

$$\mathbf{P}_{\text{hop}} = \left[\hat{N}_S^x + \hat{N}_A^x\right]\hat{\mathbf{x}} + \left[\hat{N}_S^y + \hat{N}_A^y\right]\hat{\mathbf{y}} + \left[\hat{N}_S^z + \hat{N}_A^z\right]\hat{\mathbf{z}}, \tag{B.9}$$

where

$$\hat{N}_{S/A}^a = \mathbf{c}_i^\dagger \hat{\mathcal{N}}_{S/A}^a \mathbf{c}_j + \text{H.c.}. \tag{B.10}$$

Here, S and A stand for symmetric and antisymmetric. By defining $(\hat{\mathcal{A}}_a)_{bc} = \epsilon_{abc}$ and $(\hat{\mathcal{S}}_a)_{bc} = |\epsilon_{abc}|$ (ϵ is the Levi-Civita tensor), we find

$$\begin{aligned}
\hat{\mathcal{N}}_S^x &= \sin(\alpha) t_{pd\pi} P^\perp_{p\pi d\sigma} \hat{\mathcal{S}}_z, & \hat{\mathcal{N}}_A^x &= 0, \\
\hat{\mathcal{N}}_S^y &= -2\sin(\alpha) t_{pd\pi} \begin{pmatrix} 0 & & \\ 0 & P^{\parallel}_{pd\pi} & \\ 0 & 0 & P^\perp_{p\sigma d\pi} + (P^{\parallel}_{pd\pi} + P^\perp_{p\sigma d\pi})\cos(2\alpha) \end{pmatrix}, \\
\hat{\mathcal{N}}_A^y &= -\cos(\alpha) t_{pd\pi} P^\perp_{p\pi d\sigma} \hat{\mathcal{A}}_z, \\
\hat{\mathcal{N}}_S^z &= -\sin(2\alpha) t_{pd\pi} P^\perp_{p\sigma d\pi} \hat{\mathcal{S}}_x, & \hat{\mathcal{N}}_A^z &= \cos(2\alpha) t_{pd\pi} P^\perp_{p\pi d\sigma} \hat{\mathcal{A}}_y.
\end{aligned} \tag{B.11}$$

For a y-bond, the corresponding expressions are obtained after a $\pi/2$ rotation around $\hat{\mathbf{z}}$.

From the C_{2v} symmetry, we infer that $\hat{\mathcal{A}}_{a,\text{eff}} = \mathfrak{a}_a\left(\mathbf{S}_i \times \mathbf{S}_j\right)_a$ and $\hat{\mathcal{S}}_{a,\text{eff}} = \mathfrak{s}_a |\epsilon_{abc}| S_i^b S_j^c$, respectively. In the limit of $U \gg J_H$, the antisymmetric operators are

$$\begin{aligned}
\mathfrak{a}_z &= \frac{32}{9} t \left[\frac{\cos^2(\alpha)}{U} + \Delta \frac{2}{9} \frac{-2U - 3\lambda + (U - 3\lambda)\cos(2\alpha)}{U^2 \lambda} \right] \\
\mathfrak{a}_y &= \frac{32}{9} t \left[\frac{\cos^2(\alpha)}{U} + \Delta \frac{1}{9} \frac{-U - 6\lambda + (5U - 6\lambda)\cos(2\alpha)}{U^2 \lambda} \right].
\end{aligned} \tag{B.12}$$

Once again, J_H is responsible for the anisotropy when $\Delta = 0$. For the symmetric operators, the off-diagonal matrices result in a contribution proportional to J_H. In the limit of $U \gg J_H$,

$$\begin{aligned}
\mathfrak{s}_z &= t J_H \frac{32}{9} \left[\frac{1 - 2\cos(2\alpha)}{(2U + 3\lambda)^2} - \Delta \frac{4}{9} \frac{(2U - 9\lambda)(-1 + 2\cos(2\alpha))}{\lambda(2U + 3\lambda)^2} \right] \\
\mathfrak{s}_x &= t J_H \frac{64}{9} \left[\frac{\cos^2(\alpha)}{(2U + 3\lambda)^2} - \Delta \frac{2}{9} \frac{U + 18\lambda + (U + 9\lambda)\cos(2\alpha)}{\lambda(2U + 3\lambda)^2} \right].
\end{aligned} \tag{B.13}$$

Finally, the $\hat{\mathcal{N}}_S^y$ term in Eq. (B.11) yields diagonal $S_i^a S_j^a$ terms with $a = x, y$ and z, in addition to a constant. Here too, in the absence of J_H the contribution is isotropic. In

the limit of $U \gg J_H$ and $U \gg \lambda$,

$$\begin{aligned}
\begin{pmatrix} 0 & 0 & 0 \\ 0 & 1 & 0 \\ 0 & 0 & 0 \end{pmatrix} &\rightarrow \frac{16}{9}\frac{t}{U}\left[\cos^2(\alpha) + \Delta\frac{2}{9}\frac{-2+\cos(2\alpha)}{\lambda}\right]\mathbf{S}_i \cdot \mathbf{S}_j \\
&\quad + \frac{8}{9}\frac{t}{U}\left[-5 + \cos(2\alpha) + \Delta\frac{4}{9}\frac{4+\cos(2\alpha)}{\lambda}\right], \\
\begin{pmatrix} 0 & 0 & 0 \\ 0 & 0 & 0 \\ 0 & 0 & 1 \end{pmatrix} &\rightarrow \frac{16}{9}\frac{t}{U}\left[\cos^2(\alpha) + \Delta\frac{2}{9}\frac{1+4\cos(2\alpha)}{\lambda}\right]\mathbf{S}_i \cdot \mathbf{S}_j \\
&\quad + \frac{8}{9}\frac{t}{U}\left[1 - 5\cos(2\alpha) + \Delta\frac{4}{9}\frac{1-8\cos(2\alpha)}{\lambda}\right].
\end{aligned} \tag{B.14}$$

We can thus write all the ME coupling constants of Eq. (B.6) as a function of the kinetic hopping integral $t = \frac{t_{pd\pi}^2}{\Delta_{pd}}$, the polarization hopping integrals, and the other physical parameters defined in the microscopic Hamiltonian.

Bibliography

[1] F. Bloch. Nuclear Induction. *Phys. Rev.*, 70:460–474, Oct 1946.

[2] F. Bloch, W. W. Hansen, and M. Packard. The Nuclear Induction Experiment. *Phys. Rev.*, 70:474–485, Oct 1946.

[3] E. M. Purcell, H. C. Torrey, and R. V. Pound. Resonance Absorption by Nuclear Magnetic Moments in a Solid. *Phys. Rev.*, 69:37–38, Jan 1946.

[4] E. Zavoisky. Spin-magnetic resonance in paramagnetics. *Fizicheskiĭ Zhurnal*, 9:211–245, 1945.

[5] S. A. Wolf, D. D. Awschalom, R. A. Buhrman, J. M. Daughton, S. von Molnár, M. L. Roukes, A. Y. Chtchelkanova, and D. M. Treger. Spintronics: A Spin-Based Electronics Vision for the Future. *Science*, 294(5546):1488–1495, 2001.

[6] I. Žutić, J. Fabian, and S. Das Sarma. Spintronics: Fundamentals and applications. *Rev. Mod. Phys.*, 76:323–410, Apr 2004.

[7] J. Fabian, A. Matos-Abiague, C. Ertler, P. Stano, and I. Zutic. Semiconductor spintronics. *Acta Phys. Slovaca*, 57:565, 2007.

[8] A. Fert. Nobel Lecture: Origin, development, and future of spintronics. *Rev. Mod. Phys.*, 80:1517–1530, Dec 2008.

[9] M. N. Baibich, J. M. Broto, A. Fert, F. N. Van Dau, F. Petroff, P. Etienne, G. Creuzet, A. Friederich, and J. Chazelas. Giant Magnetoresistance of (001)Fe/(001)Cr Magnetic Superlattices. *Phys. Rev. Lett.*, 61:2472–2475, Nov 1988.

[10] G. Binasch, P. Grünberg, F. Saurenbach, and W. Zinn. Enhanced magnetoresistance in layered magnetic structures with antiferromagnetic interlayer exchange. *Phys. Rev. B*, 39:4828–4830, Mar 1989.

[11] E. I. Rashba. Properties of semiconductors with an extremum loop. 1. Cyclotron and combinational resonance in a magnetic field perpendicular to the plane of the loop. *Sov. Phys. Solid State*, 2(6):1109–1122, 1960.

[12] M. Fiebig. Revival of the magnetoelectric effect. *Journal of Physics D: Applied Physics*, 38(8):R123, 2005.

[13] P. Curie. Sur la symétrie dans les phénomènes physiques, symétrie d'un champ électrique et d'un champ magnétique. *J. Phys.*, 3(1):393–415, 1894.

[14] L. D. Landau and E. M. Lifshitz. Electrodynamics of continuous media. 1960.

[15] I. Dzyaloshinskii. On the magneto-electrical effects in antiferromagnets. *Soviet Physics JETP*, 10:628–629, 1960.

[16] M. Date, J. Kanamori, and M. Tachiki. Origin of magnetoelectric effect in Cr_2O_3. *J. Phys. Soc. Jpn.*, 16(12):2589–2589, 1961.

[17] G. T. Rado and V. J. Folen. Observation of the Magnetically Induced Magnetoelectric Effect and Evidence for Antiferromagnetic Domains. *Phys. Rev. Lett.*, 7:310–311, Oct 1961.

[18] T. Kimura, T. Goto, H. Shintani, K. Ishizaka, T.-h. Arima, and Y. Tokura. Magnetic control of ferroelectric polarization. *nature*, 426(6962):55, 2003.

[19] J. Wang, J. Neaton, H. Zheng, V. Nagarajan, S. Ogale, B. Liu, D. Viehland, V. Vaithyanathan, D. Schlom, U. Waghmare, et al. Epitaxial $BiFeO_3$ multiferroic thin film heterostructures. *science*, 299(5613):1719–1722, 2003.

[20] N. Hur, S. Park, P. Sharma, J. Ahn, S. Guha, and S. Cheong. Electric polarization reversal and memory in a multiferroic material induced by magnetic fields. *Nature*, 429(6990):392, 2004.

[21] W. Eerenstein, N. Mathur, and J. F. Scott. Multiferroic and magnetoelectric materials. *nature*, 442(7104):759, 2006.

[22] S.-W. Cheong and M. Mostovoy. Multiferroics: a magnetic twist for ferroelectricity. *Nature materials*, 6(1):13, 2007.

[23] D. Khomskii. Trend: Classifying multiferroics: Mechanisms and effects. *Physics*, 2:20, 2009.

[24] Y. Tokura, S. Seki, and N. Nagaosa. Multiferroics of spin origin. *Rep. Prog. Phys.*, 77(7):076501, 2014.

[25] Y. Wang, J. Hu, Y. Lin, and C.-W. Nan. Multiferroic magnetoelectric composite nanostructures. *Npg Asia Materials*, 2:61 EP –, 04 2010.

[26] T.-K. Ng and P. A. Lee. Power-Law Conductivity inside the Mott Gap: Application to κ-(BEDT-TTF)$_2$Cu$_2$(CN)$_3$. *Phys. Rev. Lett.*, 99(15):156402, 2007.

[27] A. C. Potter, T. Senthil, and P. A. Lee. Mechanisms for sub-gap optical conductivity in Herbertsmithite. *Phys. Rev. B*, 87(24):245106, 2013.

[28] S. Elsässer, D. Wu, M. Dressel, and J. A. Schlueter. Power-law dependence of the optical conductivity observed in the quantum spin-liquid compound κ-(BEDT-TTF)$_2$Cu$_2$(CN)$_3$. *Phys. Rev. B*, 86(15):155150, 2012.

[29] D. V. Pilon, C. H. Lui, T.-H. Han, D. Shrekenhamer, A. J. Frenzel, W. J. Padilla, Y. S. Lee, and N. Gedik. Spin-induced optical conductivity in the spin-liquid candidate Herbertsmithite. *Phys. Rev. Lett.*, 111(12):127401, 2013.

[30] C. Wellm, J. Zeisner, A. Alfonsov, A. Wolter, M. Roslova, A. Isaeva, T. Doert, M. Vojta, B. Büchner, and V. Kataev. Signatures of low-energy fractionalized excitations in α-$RuCl_3$ from field-dependent microwave absorption. *arXiv:1710.00670*, 2017.

[31] A. Little, L. Wu, P. Lampen-Kelley, A. Banerjee, S. Patankar, D. Rees, C. A. Bridges, J.-Q. Yan, D. Mandrus, S. E. Nagler, and J. Orenstein. Antiferromagnetic Resonance and Terahertz Continuum in α-$RuCl_3$. *Phys. Rev. Lett.*, 119:227201, Nov 2017.

[32] Z. Wang, S. Reschke, D. Hüvonen, S.-H. Do, K.-Y. Choi, M. Gensch, U. Nagel, T. Rõõm, and A. Loidl. Magnetic Excitations and Continuum of a Possibly Field-Induced Quantum Spin Liquid in α-$RuCl_3$. *Phys. Rev. Lett.*, 119:227202, Nov 2017.

[33] S. Reschke, F. Mayr, S. Widmann, H.-A. K. von Nidda, V. Tsurkan, M. Eremin, S.-H. Do, K.-Y. Choi, Z. Wang, and A. Loidl. Sub-gap optical response across the structural phase transition in van der Waals layered α-$RuCl_3$. *arXiv:1803.04887*, 2018.

[34] L. Shi, Y. Liu, T. Lin, M. Zhang, S. Zhang, L. Wang, Y. Shi, T. Dong, and N. Wang. Field induced magnon excitation and in gap absorption of Kitaev candidate $RuCl_3$. *arXiv:1803.08398*, 2018.

[35] A. Kitaev. Anyons in an exactly solved model and beyond. *Ann. Phys. (Berlin)*, 321(1):2–111, 2006.

[36] E. Rashba and V. Sheka. Combinational resonance of zonal electrons in crystals having a zinc blende lattice. *Sov. Phys. Solid State*, 3(6):1257–1267, 1961.

[37] E. Rashba and V. Sheka. *Landau Level Spectroscopy*. Elsevier, New York, 1991.

[38] O. A. Tretiakov, K. S. Tikhonov, and V. L. Pokrovsky. Spin resonance in a Luttinger liquid with spin-orbit interaction. *Phys. Rev. B*, 88(12):125143, 2013.

[39] A. Bolens, H. Katsura, M. Ogata, and S. Miyashita. Synergetic effect of spin-orbit coupling and Zeeman splitting on the optical conductivity in the one-dimensional Hubbard model. *Phys. Rev. B*, 95:235115, Jun 2017.

[40] L. N. Bulaevskii, C. D. Batista, M. V. Mostovoy, and D. I. Khomskii. Electronic orbital currents and polarization in Mott insulators. *Phys. Rev. B*, 78(2):024402, 2008.

[41] A. Bolens. Theory of electronic magnetoelectric coupling in d^5 Mott insulators. *arXiv:1805.02488*, 2018.

[42] G. Baskaran, S. Mandal, and R. Shankar. Exact results for spin dynamics and fractionalization in the Kitaev model. *Phys. Rev. Lett.*, 98(24):247201, 2007.

[43] J. Knolle, G.-W. Chern, D. L. Kovrizhin, R. Moessner, and N. B. Perkins. Raman scattering signatures of Kitaev spin liquids in A_2IrO_3 iridates with A= Na or Li. *Phys. Rev. Lett.*, 113(18):187201, 2014.

[44] J. Knolle, D. L. Kovrizhin, J. T. Chalker, and R. Moessner. Dynamics of a two-dimensional quantum spin liquid: signatures of emergent Majorana fermions and fluxes. *Phys. Rev. Lett.*, 112(20):207203, 2014.

[45] J. Knolle, D. L. Kovrizhin, J. T. Chalker, and R. Moessner. Dynamics of fractionalization in quantum spin liquids. *Phys. Rev. B*, 92(11):115127, 2015.

[46] X.-Y. Song, Y.-Z. You, and L. Balents. Low-energy spin dynamics of the honeycomb spin liquid beyond the Kitaev limit. *Phys. Rev. Lett.*, 117(3):037209, 2016.

[47] J. Knolle. *Dynamics of a Quantum Spin Liquid*. Springer, Cham, 2016.

[48] G. B. Halász, N. B. Perkins, and J. van den Brink. Resonant inelastic X-ray scattering response of the Kitaev honeycomb model. *Phys. Rev. Lett.*, 117(12):127203, 2016.

[49] G. Jackeli and G. Khaliullin. Mott insulators in the strong spin-orbit coupling limit: from Heisenberg to a quantum compass and Kitaev models. *Phys. Rev. Lett.*, 102(1):017205, 2009.

[50] X. Liu, T. Berlijn, W.-G. Yin, W. Ku, A. Tsvelik, Y.-J. Kim, H. Gretarsson, Y. Singh, P. Gegenwart, and J. P. Hill. Long-range magnetic ordering in Na_2IrO_3. *Phys. Rev. B*, 83(22):220403, 2011.

[51] S. K. Choi, R. Coldea, A. N. Kolmogorov, T. Lancaster, I. I. Mazin, S. J. Blundell, P. G. Radaelli, Y. Singh, P. Gegenwart, K. R. Choi, S. W. Cheong, P. J. Baker, C. Stock, and J. Taylor. Spin waves and revised crystal structure of honeycomb iridate Na_2IrO_3. *Phys. Rev. Lett.*, 108(12):127204, 2012.

[52] F. Ye, S. Chi, H. Cao, B. C. Chakoumakos, J. A. Fernandez-Baca, R. Custelcean, T. F. Qi, O. B. Korneta, and G. Cao. Direct evidence of a zigzag spin-chain structure in the honeycomb lattice: A neutron and x-ray diffraction investigation of single-crystal Na_2IrO_3. *Phys. Rev. B*, 85(18):180403, 2012.

[53] R. D. Johnson, S. C. Williams, A. A. Haghighirad, J. Singleton, V. Zapf, P. Manuel, I. I. Mazin, Y. Li, H. O. Jeschke, R. Valenti, and R. Coldea. Monoclinic crystal structure of α-$RuCl_3$ and the zigzag antiferromagnetic ground state. *Phys. Rev. B*, 92(23):235119, 2015.

[54] J. A. Sears, M. Songvilay, K. W. Plumb, J. P. Clancy, Y. Qiu, Y. Zhao, D. Parshall, and Y.-J. Kim. Magnetic order in α-$RuCl_3$: A honeycomb-lattice quantum magnet with strong spin-orbit coupling. *Phys. Rev. B*, 91(14):144420, 2015.

[55] H. B. Cao, A. Banerjee, J.-Q. Yan, C. A. Bridges, M. D. Lumsden, D. G. Mandrus, D. A. Tennant, B. C. Chakoumakos, and S. E. Nagler. Low-temperature crystal and magnetic structure of α-$RuCl_3$. *Phys. Rev. B*, 93(13):134423, 2016.

[56] L. J. Sandilands, Y. Tian, K. W. Plumb, Y.-J. Kim, and K. S. Burch. Scattering Continuum and Possible Fractionalized Excitations in α-$RuCl_3$. *Phys. Rev. Lett.*, 114(14):147201, 2015.

[57] J. Nasu, J. Knolle, D. L. Kovrizhin, Y. Motome, and R. Moessner. Fermionic response from fractionalization in an insulating two-dimensional magnet. *Nat. Phys.*, 12:912, 2016.

[58] A. Banerjee, C. Bridges, J.-Q. Yan, A. Aczel, L. Li, M. Stone, G. Granroth, M. Lumsden, Y. Yiu, J. Knolle, et al. Proximate Kitaev quantum spin liquid behaviour in a honeycomb magnet. *Nature materials*, 15(7):733, 2016.

[59] A. Banerjee, J. Yan, J. Knolle, C. A. Bridges, M. B. Stone, M. D. Lumsden, D. G. Mandrus, D. A. Tennant, R. Moessner, and S. E. Nagler. Neutron scattering in the proximate quantum spin liquid α-$RuCl_3$. *Science*, 356(6342):1055–1059, 2017.

[60] Y. Kasahara, K. Sugii, T. Ohnishi, M. Shimozawa, M. Yamashita, N. Kurita, H. Tanaka, J. Nasu, Y. Motome, T. Shibauchi, and Y. Matsuda. Unusual Thermal Hall Effect in a Kitaev Spin Liquid Candidate $\alpha-RuCl_3$. *Phys. Rev. Lett.*, 120:217205, May 2018.

[61] R. Hentrich, M. Roslova, A. Isaeva, T. Doert, W. Brenig, B. Büchner, and C. Hess. Large Thermal Hall Effect in α-$RuCl_3$: Evidence for Heat Transport by Kitaev-Heisenberg Paramagnons. *arXiv:1803.08162*, 2018.

[62] A. Bolens, H. Katsura, M. Ogata, and S. Miyashita. Mechanism for subgap optical conductivity in honeycomb Kitaev materials. *Phys. Rev. B*, 97(16):161108, 2018.

[63] R. Kubo. Statistical-Mechanical Theory of Irreversible Processes. I. General Theory and Simple Applications to Magnetic and Conduction Problems. *J. Phys. Soc. Jpn.*, 12(6):570–586, 1957.

[64] D. Tong. Lectures on kinetic theory. *Lecture notes available at http://www.damtp.cam.ac.uk/user/tong/kinetic.html*, 2012.

[65] G. D. Mahan. *Many-particle physics*. Springer US, New York, 2013.

[66] B. S. Shastry and B. I. Shraiman. Theory of Raman scattering in Mott-Hubbard systems. *Phys. Rev. Lett.*, 65:1068–1071, Aug 1990.

[67] A. Agarwal, S. Chesi, T. Jungwirth, J. Sinova, G. Vignale, and M. Polini. Plasmon mass and Drude weight in strongly spin-orbit-coupled two-dimensional electron gases. *Phys. Rev. B*, 83:115135, Mar 2011.

[68] W. Kohn. Theory of the Insulating State. *Phys. Rev.*, 133:A171–A181, Jan 1964.

[69] D. J. Scalapino, S. R. White, and S. Zhang. Insulator, metal, or superconductor: The criteria. *Phys. Rev. B*, 47:7995–8007, Apr 1993.

[70] T. Giamarchi. Umklapp process and resistivity in one-dimensional fermion systems. *Phys. Rev. B*, 44(7):2905, 1991.

[71] T. Giamarchi and A. J. Millis. Conductivity of a Luttinger liquid. *Phys. Rev. B*, 46(15):9325, 1992.

[72] T. Giamarchi. Mott transition in one dimension. *Physica B: Condensed Matter*, 230-232:975–980, 1997.

[73] A. Shekhter, M. Khodas, and A. M. Finkel'stein. Chiral spin resonance and spin-Hall conductivity in the presence of the electron-electron interactions. *Phys. Rev. B*, 71(16):165329, 2005.

[74] M. Dresselhaus and M. Dresselhaus. Optical properties of solids. *Proceedings of the International School of Physics "Enrico Fermi"*, 1966.

[75] E. Jeckelmann, F. Gebhard, and F. H. L. Essler. Optical conductivity of the half-filled Hubbard chain. *Phys. Rev. Lett.*, 85(18):3910, 2000.

[76] E. Jeckelmann. Dynamical density-matrix renormalization-group method. *Phys. Rev. B*, 66(4):045114, 2002.

[77] D. Controzzi, F. H. L. Essler, and A. M. Tsvelik. Optical conductivity of one-dimensional Mott insulators. *Phys. Rev. Lett.*, 86(4):680, 2001.

[78] F. H. L. Essler, F. Gebhard, and E. Jeckelmann. Excitons in one-dimensional Mott insulators. *Phys. Rev. B*, 64(12):125119, 2001.

[79] A. Ovchinnikov. Excitation spectrum in the one-dimensional Hubbard model. *Zh. Eksp. Teor. Fiz.*, 57:2137, 1969. [Sov. Phys. JETP **30**, 1160 (1970)].

[80] A. Pustogow, Y. Li, I. Voloshenko, P. Puphal, C. Krellner, I. I. Mazin, M. Dressel, and R. Valentí. Nature of optical excitations in the frustrated kagome compound herbertsmithite. *Phys. Rev. B*, 96:241114, Dec 2017.

[81] Yu. A. Bychkov and E. I. Rashba. Properties of a 2D electron gas with lifted spectral degeneracy. *JETP Lett.*, 39(2):78, 1984.

[82] G. Dresselhaus. Spin-orbit coupling effects in zinc blende structures. *Phys. Rev.*, 100(2):580, 1955.

[83] I. Dzyaloshinsky. A thermodynamic theory of "weak" ferromagnetism of antiferromagnetics. *Journal of Physics and Chemistry of Solids*, 4(4):241–255, 1958.

[84] T. Moriya. Anisotropic superexchange interaction and weak ferromagnetism. *Phys. Rev.*, 120(1):91, 1960.

[85] N. Hatano, R. Shirasaki, and H. Nakamura. Non-Abelian gauge field theory of the spin-orbit interaction and a perfect spin filter. *Phys. Rev. A*, 75(3):032107, 2007.

[86] Y. Aharonov and A. Casher. Topological quantum effects for neutral particles. *Phys. Rev. Lett.*, 53(4):319, 1984.

[87] W. Witczak-Krempa, G. Chen, Y. B. Kim, and L. Balents. Correlated Quantum Phenomena in the Strong Spin-Orbit Regime. *Annual Review of Condensed Matter Physics*, 5(1):57–82, 2014.

[88] J. G. Rau, E. K.-H. Lee, and H.-Y. Kee. Spin-Orbit Physics Giving Rise to Novel Phases in Correlated Systems: Iridates and Related Materials. *Annual Review of Condensed Matter Physics*, 7(1):195–221, 2016.

[89] R. Schaffer, E. K.-H. Lee, B.-J. Yang, and Y. B. Kim. Recent progress on correlated electron systems with strong spin–orbit coupling. *Rep. Prog. Phys.*, 79(9):094504, 2016.

[90] S. V. Streltsov and D. I. Khomskii. Orbital physics in transition metal compounds: new trends. *Physics-Uspekhi*, 60(11):1121, 2017.

[91] R. L. Bell. Electric Dipole Spin Transitions in InSb. *Phys. Rev. Lett.*, 9:52–54, Jul 1962.

[92] B. D. McCombe, S. G. Bishop, and R. Kaplan. Combined Resonance and Electron g Values in InSb. *Phys. Rev. Lett.*, 18:748–750, May 1967.

[93] B. D. McCombe and R. J. Wagner. Electric-Dipole-Excited Electron Spin Resonance in InSb. *Phys. Rev. B*, 4:1285–1288, Aug 1971.

[94] M. Oshikawa and I. Affleck. Electron spin resonance in S=1/2 antiferromagnetic chains. *Phys. Rev. B*, 65(13):134410, 2002.

[95] S. Maiti, M. Imran, and D. L. Maslov. Electron spin resonance in a two-dimensional Fermi liquid with spin-orbit coupling. *Phys. Rev. B*, 93(4):045134, 2016.

[96] E. I. Rashba and A. L. Efros. Orbital mechanisms of electron-spin manipulation by an electric field. *Phys. Rev. Lett.*, 91(12):126405, 2003.

[97] A. L. Efros and E. I. Rashba. Theory of electric dipole spin resonance in a parabolic quantum well. *Phys. Rev. B*, 73(16):165325, 2006.

[98] A. Abanov, V. L. Pokrovsky, W. M. Saslow, and P. Zhou. Spin resonance in a quantum wire: Anomalous effects of an applied magnetic field. *Phys. Rev. B*, 85(8):085311, 2012.

[99] J. Sun, S. Gangadharaiah, and O. A. Starykh. Spin-Orbit-Induced Spin-Density Wave in a Quantum Wire. *Phys. Rev. Lett.*, 98:126408, Mar 2007.

[100] S. Gangadharaiah, J. Sun, and O. A. Starykh. Spin-orbital effects in magnetized quantum wires and spin chains. *Phys. Rev. B*, 78(5):054436, 2008.

[101] C. Sun and V. L. Pokrovsky. Spin correlations in quantum wires. *Phys. Rev. B*, 91:161305, Apr 2015.

[102] T. Giamarchi. *Quantum physics in one dimension*, volume 121. Oxford university press, 2004.

[103] V. Gritsev, G. Japaridze, M. Pletyukhov, and D. Baeriswyl. Competing Effects of Interactions and Spin-Orbit Coupling in a Quantum Wire. *Phys. Rev. Lett.*, 94:137207, Apr 2005.

[104] N. Mott. On metal-insulator transitions. *Journal of Solid State Chemistry*, 88(1):5–7, 1990.

[105] L. Magarill, A. Chaplik, and M. Éntin. Spin-plasmon oscillations of the two-dimensional electron gas. *Journal of Experimental and Theoretical Physics*, 92(1):153–158, 2001.

[106] E. G. Mishchenko and B. I. Halperin. Transport equations for a two-dimensional electron gas with spin-orbit interaction. *Phys. Rev. B*, 68(4):045317, 2003.

[107] A.-K. Farid and E. G. Mishchenko. Optical conductivity of a two-dimensional electron liquid with spin-orbit interaction. *Phys. Rev. Lett.*, 97(9):096604, 2006.

[108] E. H. Lieb and F. Y. Wu. Absence of Mott transition in an exact solution of the short-range, one-band model in one dimension. *Phys. Rev. Lett.*, 20(25):1445, 1968.

[109] P. Horsch and W. Stephan. Frequency-dependent conductivity of the one-dimensional Hubbard model at strong coupling. *Phys. Rev. B*, 48(14):10595, 1993.

[110] A. C. Tiegel, T. Veness, P. E. Dargel, A. Honecker, T. Pruschke, I. P. McCulloch, and F. H. L. Essler. Optical conductivity of the Hubbard chain away from half filling. *Phys. Rev. B*, 93(12):125108, 2016.

[111] S. Fujimoto and N. Kawakami. Persistent currents in mesoscopic Hubbard rings with spin-orbit interaction. *Phys. Rev. B*, 48(23):17406, 1993.

[112] K. Y. Povarov, A. I. Smirnov, O. A. Starykh, S. V. Petrov, and A. Y. Shapiro. Modes of magnetic resonance in the spin-liquid phase of Cs_2CuCl_4. *Phys. Rev. Lett.*, 107(3):037204, 2011.

[113] A. I. Smirnov, T. A. Soldatov, K. Y. Povarov, M. Hälg, W. E. A. Lorenz, and A. Zheludev. Electron spin resonance in a model $S = 1/2$ chain antiferromagnet with a uniform Dzyaloshinskii-Moriya interaction. *Phys. Rev. B*, 92(13):134417, 2015.

[114] R. Glenn, O. A. Starykh, and M. E. Raikh. Interplay of spin-orbit coupling and Zeeman splitting in the absorption lineshape of fermions in two dimensions. *Phys. Rev. B*, 86(2):024423, 2012.

[115] S. Maiti, V. Zyuzin, and D. L. Maslov. Collective modes in two-and three-dimensional electron systems with Rashba spin-orbit coupling. *Phys. Rev. B*, 91(3):035106, 2015.

[116] T. Ando, A. B. Fowler, and F. Stern. Electronic properties of two-dimensional systems. *Rev. Mod. Phys.*, 54:437–672, Apr 1982.

[117] A. Ashrafi and D. L. Maslov. Chiral Spin Waves in Fermi Liquids with Spin-Orbit Coupling. *Phys. Rev. Lett.*, 109:227201, Nov 2012.

[118] S.-S. Zhang, X.-L. Yu, J. Ye, and W.-M. Liu. Collective modes of spin-orbit-coupled Fermi gases in the repulsive regime. *Phys. Rev. A*, 87:063623, Jun 2013.

[119] V. Silin. Oscillations of a Fermi-liquid in a magnetic field. *Sov. Phys. JETP*, 6:945–950, 1958.

[120] J. H. de Boer and E. J. Verwey. Semi-conductors with partially and with completely filled 3d-lattice bands. *Proceedings of the Physical Society*, 49(4S):59, 1937.

[121] N. F. Mott. The basis of the electron theory of metals, with special reference to the transition metals. *Proceedings of the Physical Society. Section A*, 62(7):416, 1949.

[122] J. Hubbard. Electron correlations in narrow energy bands III. An improved solution. *Proc. R. Soc. Lond. A*, 281(1386):401–419, 1964.

[123] D. Khomskii. Spin chirality and nontrivial charge dynamics in frustrated Mott insulators: spontaneouscurrents and charge redistribution. *J. Phys. Condens. Matter*, 22(16):164209, 2010.

[124] B. Tsukerblat, A. Tarantul, and A. Müller. Low temperature EPR spectra of the mesoscopic cluster V_15: The role of antisymmetric exchange. *J. Chem. Phys*, 125(5):054714, 2006.

[125] K. Hwang, S. Bhattacharjee, and Y. B. Kim. Signatures of spin-triplet excitations in optical conductivity of valence bond solids. *New J. Phys*, 16(12):123009, 2014.

[126] S. Zhu, Y.-Q. Li, and C. D. Batista. Spin-orbit coupling and electronic charge effects in Mott insulators. *Phys. Rev. B*, 90:195107, Nov 2014.

[127] Y. Kamiya and C. D. Batista. Multiferroic behavior in trimerized Mott insulators. *Phys. Rev. Lett.*, 108:097202, Feb 2012.

[128] D. I. Khomskii. Electric dipoles on magnetic monopoles in spin ice. *Nature Communications*, 3:904, 06 2012.

[129] M. Trif, F. Troiani, D. Stepanenko, and D. Loss. Spin-Electric Coupling in Molecular Magnets. *Phys. Rev. Lett.*, 101:217201, Nov 2008.

[130] M. Trif, F. Troiani, D. Stepanenko, and D. Loss. Spin electric effects in molecular antiferromagnets. *Phys. Rev. B*, 82:045429, Jul 2010.

[131] Y. Huh, M. Punk, and S. Sachdev. Optical conductivity of visons in Z_2 spin liquids close to a valence bond solid transition on the kagome lattice. *Phys. Rev. B*, 87:235108, Jun 2013.

[132] L. Savary and L. Balents. Quantum spin liquids: a review. *Rep. Prog. Phys.*, 80(1):016502, 2017.

[133] C. D. Batista, S.-Z. Lin, S. Hayami, and Y. Kamiya. Frustration and chiral orderings in correlated electron systems. *Rep. Prog. Phys.*, 79(8):084504, 2016.

[134] M. Poirier, S. Parent, A. Côté, K. Miyagawa, K. Kanoda, and Y. Shimizu. Magnetodielectric effects and spin-charge coupling in the spin-liquid candidate κ-(BEDT-TTF)$_2$Cu$_2$(CN)$_3$. *Phys. Rev. B*, 85:134444, Apr 2012.

[135] N. B. Perkins, Y. Sizyuk, and P. Wölfle. Interplay of many-body and single-particle interactions in iridates and rhodates. *Phys. Rev. B*, 89(3):035143, 2014.

[136] R. Peierls. Zur theorie des diamagnetismus von leitungselektronen. *Zeitschrift für Physik*, 80(11-12):763–791, 1933.

[137] Y. Aharonov and D. Bohm. Significance of Electromagnetic Potentials in the Quantum Theory. *Phys. Rev.*, 115:485–491, Aug 1959.

[138] L.-M. Duan, E. Demler, and M. D. Lukin. Controlling Spin Exchange Interactions of Ultracold Atoms in Optical Lattices. *Phys. Rev. Lett.*, 91:090402, Aug 2003.

[139] S. R. Hassan, P. V. Sriluckshmy, S. K. Goyal, R. Shankar, and D. Sénéchal. Stable Algebraic Spin Liquid in a Hubbard Model. *Phys. Rev. Lett.*, 110:037201, Jan 2013.

[140] J. P. L. Faye, D. Sénéchal, and S. R. Hassan. Topological phases of the Kitaev-Hubbard model at half filling. *Phys. Rev. B*, 89:115130, Mar 2014.

[141] H. Katsura, M. Sato, T. Furuta, and N. Nagaosa. Theory of the Optical Conductivity of Spin Liquid States in One-Dimensional Mott Insulators. *Phys. Rev. Lett.*, 103:177402, Oct 2009.

[142] I. A. Sergienko, C. Şen, and E. Dagotto. Ferroelectricity in the magnetic E-phase of orthorhombic perovskites. *Phys. Rev. Lett.*, 97(22):227204, 2006.

[143] C. Jia, S. Onoda, N. Nagaosa, and J. H. Han. Bond electronic polarization induced by spin. *Phys. Rev. B*, 74(22):224444, 2006.

[144] C. Jia, S. Onoda, N. Nagaosa, and J. H. Han. Microscopic theory of spin-polarization coupling in multiferroic transition metal oxides. *Phys. Rev. B*, 76(14):144424, 2007.

[145] T.-h. Arima. Ferroelectricity induced by proper-screw type magnetic order. *J. Phys. Soc. Jpn.*, 76(7):073702–073702, 2007.

[146] H. Katsura, N. Nagaosa, and A. V. Balatsky. Spin current and magnetoelectric effect in noncollinear magnets. *Phys. Rev. Lett.*, 95(5):057205, 2005.

[147] M. Mostovoy. Ferroelectricity in spiral magnets. *Phys. Rev. Lett.*, 96(6):067601, 2006.

[148] I. A. Sergienko and E. Dagotto. Role of the Dzyaloshinskii-Moriya interaction in multiferroic perovskites. *Phys. Rev. B*, 73(9):094434, 2006.

[149] T. A. Kaplan and S. D. Mahanti. Canted-spin-caused electric dipoles: A local symmetry theory. *Phys. Rev. B*, 83:174432, May 2011.

[150] A. Pimenov, A. Mukhin, V. Y. Ivanov, V. Travkin, A. Balbashov, and A. Loidl. Possible evidence for electromagnons in multiferroic manganites. *Nature Physics*, 2(2):97, 2006.

[151] A. Sushkov, R. V. Aguilar, S. Park, S. Cheong, and H. Drew. Electromagnons in multiferroic YMn_2O_5 and $TbMn_2O_5$. *Phys. Rev. Lett.*, 98(2):027202, 2007.

[152] H. Katsura, A. V. Balatsky, and N. Nagaosa. Dynamical magnetoelectric coupling in helical magnets. *Phys. Rev. Lett.*, 98(2):027203, 2007.

[153] M. Cazayous, Y. Gallais, A. Sacuto, R. De Sousa, D. Lebeugle, and D. Colson. Possible observation of cycloidal electromagnons in $BiFeO_3$. *Phys. Rev. Lett.*, 101(3):037601, 2008.

[154] S. Seki, N. Kida, S. Kumakura, R. Shimano, and Y. Tokura. Electromagnons in the spin collinear state of a triangular lattice antiferromagnet. *Phys. Rev. Lett.*, 105(9):097207, 2010.

[155] Y. Takahashi, R. Shimano, Y. Kaneko, H. Murakawa, and Y. Tokura. Magnetoelectric resonance with electromagnons in a perovskite helimagnet. *Nature Physics*, 8(2):121, 2012.

[156] S. H. Chun, K. W. Shin, H. J. Kim, S. Jung, J. Park, Y.-M. Bahk, H.-R. Park, J. Kyoung, D.-H. Choi, D.-S. Kim, et al. Electromagnon with Sensitive Terahertz Magnetochromism in a Room-Temperature Magnetoelectric Hexaferrite. *Phys. Rev. Lett.*, 120(2):027202, 2018.

[157] S. Kimura, M. Matsumoto, M. Akaki, M. Hagiwara, K. Kindo, and H. Tanaka. Electric dipole spin resonance in a quantum spin dimer system driven by magnetoelectric coupling. *Phys. Rev. B*, 97:140406, Apr 2018.

[158] W. Lu, J. Tuchendler, M. von Ortenberg, and J. P. Renard. Direct observation of the Haldane gap in NENP by far-infrared spectroscopy in high magnetic fields. *Phys. Rev. Lett.*, 67:3716–3719, Dec 1991.

[159] T. M. Brill, J. P. Boucher, J. Voiron, G. Dhalenne, A. Revcolevschi, and J. P. Renard. High-Field Electron Spin Resonance and Magnetization in the Dimerized Phase of $CuGeO_3$. *Phys. Rev. Lett.*, 73:1545–1548, Sep 1994.

[160] H. Nojiri, H. Ohta, S. Okubo, O. Fujita, J. Akimitsu, and M. Motokawa. Submillimeter Wave ESR Study of Spin Gap Excitations in $CuGeO_3$. *J. Phys. Soc. Jpn.*, 68(10):3417–3423, 1999.

[161] T. Rõõm, U. Nagel, E. Lippmaa, H. Kageyama, K. Onizuka, and Y. Ueda. Far-infrared study of the two-dimensional dimer spin system $SrCu_2(BO_3)_2$. *Phys. Rev. B*, 61:14342–14345, Jun 2000.

[162] H. Nojiri, H. Kageyama, Y. Ueda, and M. Motokawa. ESR Study on the Excited State Energy Spectrum of $SrCu_2(BO_3)_2$ –A Central Role of Multiple-Triplet Bound States–. *J. Phys. Soc. Jpn.*, 72(12):3243–3253, 2003.

[163] T. Sakai and H. Shiba. Numerical Study of a Model for NENP: One-Dimensional S=1 Antiferromagnetin a Staggered Field. *J. Phys. Soc. Jpn.*, 63(3):867–871, 1994.

[164] T. Sakai. Direct Observation of Spin Gaps in Electron Spin Resonance. *J. Phys. Soc. Jpn.*, 72(Suppl.B):53–60, 2003.

[165] O. Cépas and T. Ziman. Theory of phonon-assisted forbidden optical transitions in spin-gap systems. *Phys. Rev. B*, 70:024404, Jul 2004.

[166] Z. Wang, D. Kamenskyi, O. Cépas, M. Schmidt, D. L. Quintero-Castro, A. T. M. N. Islam, B. Lake, A. A. Aczel, H. A. Dabkowska, A. B. Dabkowski, G. M. Luke, Y. Wan, A. Loidl, M. Ozerov, J. Wosnitza, S. A. Zvyagin, and J. Deisenhofer. High-field electron spin resonance spectroscopy of singlet-triplet transitions in the spin-dimer systems $Sr_3Cr_2O_8$ and $Ba_3Cr_2O_8$. *Phys. Rev. B*, 89:174406, May 2014.

[167] Y. Singh and P. Gegenwart. Antiferromagnetic Mott insulating state in single crystals of the honeycomb lattice material Na_2IrO_3. *Phys. Rev. B*, 82(6):064412, 2010.

[168] J. Chaloupka, G. Jackeli, and G. Khaliullin. Kitaev-Heisenberg model on a honeycomb lattice: possible exotic phases in iridium oxides A_2IrO_3. *Phys. Rev. Lett.*, 105(2):027204, 2010.

[169] Y. Singh, S. Manni, J. Reuther, T. Berlijn, R. Thomale, W. Ku, S. Trebst, and P. Gegenwart. Relevance of the Heisenberg-Kitaev model for the honeycomb lattice iridates A_2IrO_3. *Phys. Rev. Lett.*, 108(12):127203, 2012.

[170] I. Pollini. Electronic properties of the narrow-band material α-$RuCl_3$. *Phys. Rev. B*, 53(19):12769, 1996.

[171] K. Plumb, J. Clancy, L. Sandilands, V. V. Shankar, Y. Hu, K. Burch, H.-Y. Kee, and Y.-J. Kim. α-$RuCl_3$: A spin-orbit assisted Mott insulator on a honeycomb lattice. *Phys. Rev. B*, 90(4):041112, 2014.

[172] H.-S. Kim, V. S. V., A. Catuneanu, and H.-Y. Kee. Kitaev magnetism in honeycomb $RuCl_3$ with intermediate spin-orbit coupling. *Phys. Rev. B*, 91(24):241110, 2015.

[173] S. Trebst. Kitaev Materials. *arXiv:1701.07056*, 2017.

[174] I. I. Mazin, H. O. Jeschke, K. Foyevtsova, R. Valentí, and D. I. Khomskii. Na_2IrO_3 as a Molecular Orbital Crystal. *Phys. Rev. Lett.*, 109:197201, Nov 2012.

[175] G. L. Stamokostas and G. A. Fiete. Mixing of $t_{2g} - e_g$ orbitals in $4d$ and $5d$ transition metal oxides. *Phys. Rev. B*, 97:085150, Feb 2018.

[176] J. G. Rau, E. K.-H. Lee, and H.-Y. Kee. Generic spin model for the honeycomb iridates beyond the Kitaev limit. *Phys. Rev. Lett.*, 112(7):077204, 2014.

[177] J. G. Rau and H.-Y. Kee. Trigonal distortion in the honeycomb iridates: Proximity of zigzag and spiral phases in Na_2IrO_3. *arXiv:1408.4811*, 2014.

[178] Y. Sizyuk, C. Price, P. Wölfle, and N. B. Perkins. Importance of anisotropic exchange interactions in honeycomb iridates: minimal model for zigzag antiferromagnetic order in Na_2IrO_3. *Phys. Rev. B*, 90(15):155126, 2014.

[179] H.-S. Kim and H.-Y. Kee. Crystal structure and magnetism in α-$RuCl_3$: An ab initio study. *Phys. Rev. B*, 93(15):155143, 2016.

[180] S. M. Winter, Y. Li, H. O. Jeschke, and R. Valenti. Challenges in design of Kitaev materials: Magnetic interactions from competing energy scales. *Phys. Rev. B*, 93(21):214431, 2016.

[181] R. Yadav, N. A. Bogdanov, V. M. Katukuri, S. Nishimoto, J. van den Brink, and L. Hozoi. Kitaev exchange and field-induced quantum spin-liquid states in honeycomb α-$RuCl_3$. *Sci. Rep.*, 6:37925, 2016.

[182] W. Wang, Z.-Y. Dong, S.-L. Yu, and J.-X. Li. Theoretical investigation of magnetic dynamics in α-$RuCl_3$. *Phys. Rev. B*, 96(11):115103, 2017.

[183] S. M. Winter, A. A. Tsirlin, M. Daghofer, J. van den Brink, Y. Singh, P. Gegenwart, and R. Valenti. Models and Materials for Generalized Kitaev Magnetism. *J. Phys. Condens. Matter*, 2017.

[184] Y. S. Hou, H. J. Xiang, and X. G. Gong. Unveiling magnetic interactions of ruthenium trichloride via constraining direction of orbital moments: Potential routes to realize a quantum spin liquid. *Phys. Rev. B*, 96(5):054410, 2017.

[185] J. Kanamori. Electron correlation and ferromagnetism of transition metals. *Progr. Theor. Phys.*, 30(3):275–289, 1963.

[186] A. Georges, L. de' Medici, and J. Mravlje. Strong correlations from Hund's coupling. *Annu. Rev. Condens. Matter Phys.*, 4:137, 2013.

[187] J. C. Slater and G. F. Koster. Simplified LCAO method for the periodic potential problem. *Phys. Rev.*, 94(6):1498, 1954.

[188] S. Miyahara and N. Furukawa. Theory of antisymmetric spin-pair-dependent electric polarization in multiferroics. *Phys. Rev. B*, 93(1):014445, 2016.

[189] M. Matsumoto, K. Chimata, and M. Koga. Symmetry Analysis of Spin-Dependent Electric Dipole and Its Application to Magnetoelectric Effects. *J. Phys. Soc. Jpn.*, 86(3):034704, 2017.

[190] M. S. Dresselhaus, G. Dresselhaus, and A. Jorio. Applications of group theory to the physics of solids, 2008.

[191] P. Anderson. Resonating valence bonds: A new kind of insulator? *Materials Research Bulletin*, 8(2):153 – 160, 1973.

[192] H. Matsuura and M. Ogata. A Poor Man's Derivation of Quantum Compass–Heisenberg Interaction: Superexchange Interaction in J–J Coupling Scheme. *J. Phys. Soc. Jpn.*, 83(9):093701, 2014.

[193] S. M. Winter, K. Riedl, P. A. Maksimov, A. L. Chernyshev, A. Honecker, and R. Valenti. Breakdown of magnons in a strongly spin-orbital coupled magnet. *Nat. Commun.*, 8(1):1152, 2017.

[194] F. Zschocke and M. Vojta. Physical states and finite-size effects in Kitaev's honeycomb model: Bond disorder, spin excitations, and NMR line shape. *Phys. Rev. B*, 92:014403, Jul 2015.

[195] J. Blaizot and G. Ripka. *Quantum Theory of Finite Systems*. MIT Press, Cambridge, 1986.

[196] E. H. Lieb. Flux Phase of the Half-Filled Band. *Phys. Rev. Lett.*, 73(16):2158, 1994.

[197] B. Dóra and R. Moessner. Gauge field entanglement in Kitaev's honeycomb model. *Phys. Rev. B*, 97:035109, Jan 2018.

[198] H. Yao, S.-C. Zhang, and S. A. Kivelson. Algebraic Spin Liquid in an Exactly Solvable Spin Model. *Phys. Rev. Lett.*, 102:217202, May 2009.

[199] F. L. Pedrocchi, S. Chesi, and D. Loss. Physical solutions of the Kitaev honeycomb model. *Phys. Rev. B*, 84:165414, Oct 2011.

[200] M. Gohlke, R. Verresen, R. Moessner, and F. Pollmann. Dynamics of the Kitaev-Heisenberg Model. *Phys. Rev. Lett.*, 119:157203, Oct 2017.

[201] D. Gotfryd, J. Rusnačko, K. Wohlfeld, G. Jackeli, J. Chaloupka, and A. M. Oleś. Phase diagram and spin correlations of the Kitaev-Heisenberg model: Importance of quantum effects. *Phys. Rev. B*, 95(2):024426, 2017.

[202] J. Knolle, S. Bhattacharjee, and R. Moessner. Dynamics of a quantum spin liquid beyond integrability: The Kitaev-Heisenberg-Γ model in an augmented parton mean-field theory. *Phys. Rev. B*, 97:134432, Apr 2018.

[203] A. Banerjee, P. Lampen-Kelley, J. Knolle, C. Balz, A. A. Aczel, B. Winn, Y. Liu, D. Pajerowski, J. Yan, C. A. Bridges, A. T. Savici, B. C. Chakoumakos, M. D. Lumsden, D. A. Tennant, R. Moessner, D. G. Mandrus, and S. E. Nagler. Excitations in the field-induced quantum spin liquid state of α-$RuCl_3$. *npj Quantum Materials*, 3(1):8, 2018.

[204] M. Gohlke, G. Wachtel, Y. Yamaji, F. Pollmann, and Y. B. Kim. Quantum spin liquid signatures in Kitaev-like frustrated magnets. *Phys. Rev. B*, 97:075126, Feb 2018.

[205] D. Torchinsky, H. Chu, L. Zhao, N. Perkins, Y. Sizyuk, T. Qi, G. Cao, and D. Hsieh. Structural distortion-induced magnetoelastic locking in Sr_2IrO_4 revealed through nonlinear optical harmonic generation. *Phys. Rev. Lett.*, 114(9):096404, 2015.